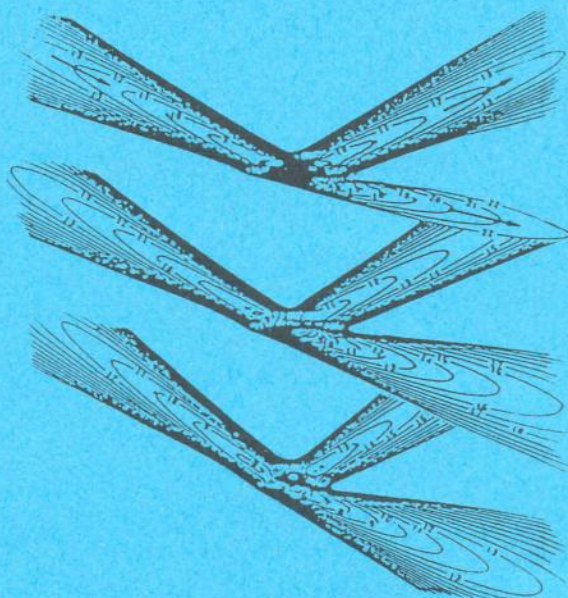


**INTERNATIONALE CONFERENCE**

**DEVELOPMENTS IN MARINE  
ACOUSTICS**

**DECEMBER 4-6 1984**

**UNIVERSITY OF NEW SOUTH WALES  
SYDNEY, N.S.W.  
AUSTRALIA**



**AUSTRALIAN ACOUSTICAL  
SOCIETY**

(i)

INTERNATIONAL CONFERENCE  
DEVELOPMENTS IN MARINE ACOUSTICS

DECEMBER 4-6 1984

University of New South Wales,  
Sydney, NSW, Australia

Sponsored by The Australian Acoustical Society and  
co-sponsored by the Australian Academy of Science

Copyright 1984 Australian Acoustical Society

ISBN 0-909882-07-X

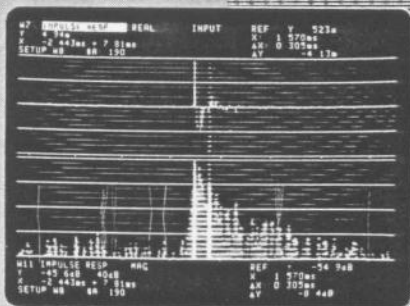
Published by

Australian Acoustical Society  
c/- Science Foundation,  
35-43 Clarence Street,  
Sydney. NSW. 2000.

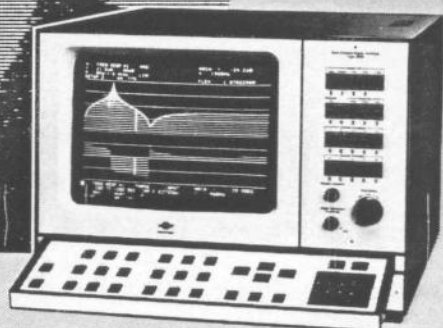
Printed by

Centatime (NSW) Pty.Ltd.,  
8 Tilford Street,  
ZETLAND. NSW. 20

# Do you know Hilbert?



The real part of the impulse response of a small loudspeaker and the log. magnitude, calculated via Hilbert transforms. Only the log. magnitude shows the many reflections of energy taking place



Dual Channel Signal Analyzer  
Type 2032/2034

Brüel & Kjær's new Dual Channel Signal Analyzers Types 2032 and 2034 incorporate automatic computation of HILBERT transforms, which enable the envelopes of Time Functions to be measured. If you want to know more about HILBERT and the many other unique capabilities of Types 2032 and 2034, please don't hesitate to ask our representative.



## Brüel & Kjær Australia PTY. LTD.

#### HEAD OFFICE:

33 Majors Bay Road, Concord, N.S.W., 2137  
P.O. Box 120, Concord, N.S.W., 2137  
Telephone: (02) 736-1755 Telex: 26246  
Cable: BRUJA SYDNEY

#### MELBOURNE OFFICE:

8/12 Pascoe Vale Road, Moonee Ponds, Vic., 3039  
P.O. Box 233 Moonee Ponds, Vic., 3039  
Telephone: (03) 370-7666-370-7166  
Telex: 33728

#### PERTH OFFICE:

P.O. Box 64, Mundaring, 6073  
Telephone: (09) 295-1658

#### QUEENSLAND OFFICE:

P.O. Box 227, Mooloolaba, Qld. 4557  
Telephone: (071) 44-4060

PREFACE

An International Conference on Developments in Marine Acoustics was held at the University of New South Wales, Sydney, Australia, from 4 to 6 December 1984. These Proceedings consist of author-supplied texts.

Marine acoustics is a field of endeavour with important implications for several disciplines, and has direct applications to such fields as oceanography, exploration, fisheries and military technology. Work in marine acoustics is being pursued by a relatively small number of scientists scattered around the world and knit together by publication, exchange visits and conferences. This conference was arranged to further this interchange by providing a forum for the presentation of recent work and by bringing together various workers in the field.

The papers presented at the conference have been categorised as follows:

- A. Sea-Floor acoustic properties;
- B. Propagation in deep water;
- C. Propagation in shallow water;
- D. Noise;
- E. Scattering; and
- F. Signal Processing

The 44 papers presented at this conference represent the work of 63 scientists in Australia, Canada, China, Italy, New Zealand, South Africa, the United Kingdom, and the United States of America.

Marshall Hall  
Conference Chairman  
21st November, 1984

# Plessey Australia Marine Systems

**Helping  
the navy keep  
its defence  
dollars in  
Australia.**

Plessey is a highly competitive, highly innovative Australian supplier of defence electronics. We've proven ourselves countless times as prime contractors to the services, including the design and development of sensors and associated equipment.

We're not only competitive and innovative. But being an Australian company, we're right here where you need us for back-up and service. And we back that even further, when necessary with the help of our overseas connections. Talk to us about systems engineering, equipment, supply, installation, commissioning and life-cycle support. With more than a thousand people and the most advanced technical facilities in Australia, we offer its defence forces a technological capability and immediacy of contact and service that no-one in this country can match. Call us and we'll prove it.

Plessey Australia Pty Limited Electronic Systems Division NSW: Faraday Park, Railway Road, Meadowbank 2114. Telephone 807 0400  
Telex: 21471 ACT: 33 Aitree Court, Phillip, 2806.  
Telex: AA62165  
Telephone: (062) 82 2900.



**PLESSEY**

ACKNOWLEDGEMENTS

Financial support for the conference was provided by the Australian Acoustical Society and the Special Minister of State of the Australian Government.

Dr. J.I. Dunlop, Treasurer of the Australian Acoustical Society, served as Secretary, Treasurer, and Facilities Co-ordinator of the Conference committee. Mr. R.A. Piesse took an active interest in the initial planning of the conference, and was supported in this effort by Mr. E.T. Weston (Messrs Piesse and Weston are both sometime councillors of the Australian Acoustical Society).

The University of New South Wales made available a lecture theatre and lecture room to serve as the venue of the conference. Secretarial activities and communications have been largely provided by the Australian Department of Defence. Additional support was provided by the University of N.S.W. And lastly (but certainly not least), the authors of the papers presented at the conference, both invited and contributed, are sincerely thanked for their fine efforts.

The following firms assisted financially by advertising in in the Proceedings:-

- (a) Bruel & Kjaer;
- (b) Hawker Pacific; and
- (c) Plessey Australia.

# Acoustics in Depth.

Sonatech, the world's largest manufacturer of deep ocean transponders, has been a primary supplier of underwater acoustics to the scientific, industrial and military communities since 1973.

Offering the broadest range of equipment from fully integrated navigation systems to simple transponder releases, the company provides applications assis-

tance for its extensive customer base and engages in continuing research in underwater acoustics.

In addition to its standard product line, Sonatech specializes in unique problem-solving designs and offers turnkey systems, worldwide service and a full range of mission support programs.

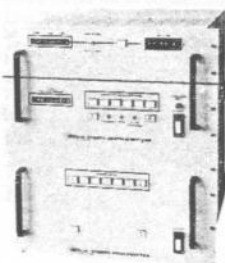
## Positioning/Tracking

- Long Baseline System — Sonatrack II
- Short Baseline System — STS
- Velocity Positioning Reference System — VPRS



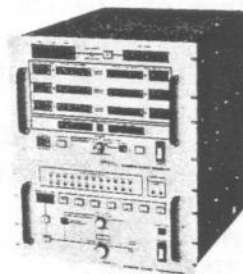
## Bathymetry

- Automatic Contour Plotting
- Depth Digitizer



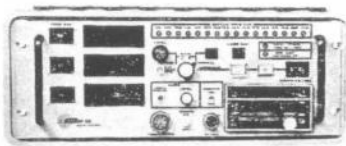
## Acoustic Telemetry

- Remote Sensor Telemetry
- Riser Angle Monitoring



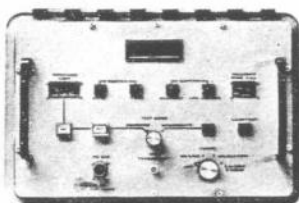
## Command/Control

- Transponders/Releases
- Remote Control



## Location/Recovery

- Submersible Emergency Locating System



## Instrumentation

- Acoustic Profiling Velocimeter
- Doppler Soil Penetrometer



## Remote Monitoring/Acoustic Pattern Recognition

- SADOT — Missile Impact Scoring



## Transponders

- Air-Surface-Sub/Launched
- Miniature
- High Power Beacons
- CTFM

We may already have the answer to your problem. Call or write today.

 **Hawker Pacific Pty. Ltd.**

P.O. Box 216 Ermington N.S.W. 2115 Tel. 648 3555

 **SONATECH, INC**

## TABLE OF CONTENTS

	Page	
<u>A : Sea-Floor Acoustic Properties</u>		
A.1	Acoustic and related properties of the Sea Floor - E.L. Hamilton	1
A.2	Use of Scholte Waves to determine the shear properties of ocean sediments - F.B. Jensen, H. Schmidt and T. Akal	8
A.3	The Inversion of Seismic Data measured at the ocean surface to determine the velocity profile of the ocean bottom - G.R. Sutton and B. Moore	14
A.4	Ray theory modelling applied to low frequency acoustic interaction with horizontally stratified ocean bottoms - M.W. Lawrence	16
A.5	Acoustic impedance measurements on marine sediments - J.I. Dunlop and P. Douglas	21
A.6	Bottom interaction of low frequency acoustic waves in the New Caledonia Basin - G.V. Frisk and E.E. Hays	28
A.7	Geological Factors in Marine Geoacoustic Modelling - C. Jenkins	30

	Page
<u>B : Propagation in Deep Water</u>	
B.1	Coupling Characteristics between two underwater acoustics ducts - M.A. Pedersen, D.F. Gordon and D. Edwards 37
B.2	Comparison between the North and South Pacific Oceans of acoustic propagation in secondary sound channels - D.G. Browning 41
B.3	Modelling ocean acoustic propagation with a wide-angle parabolic equation method - N.R. Chapman and D.J. Thomson 44
B.4	Numerical simulation of wave propagation in a randomly varying medium - C. Macaskill and T.E. Ewart 50
B.5	Intensity decay laws for near-surface sound sources in the ocean - R.N. Denham 55
B.6	Short-range, low frequency acoustic transmission in the Tasman Sea - A.F. Quill 58
B.7	Effects of wind-generated bubbles on surface-duct sound propagation at frequencies up to 20 kHz - M. Hall 60
B.8	Signal multipath propagation in bottom limited regions - R.W. Bannister, S.G.N. Payne and J.C. Hall 66

C : Propagation in Shallow Water

C.1	Efficient numerical solution technique for wave propagation in horizontally stratified environments - F.B. Jensen and H. Schmidt	73
C.2	Shallow water acoustic modelling over a sloping bottom - C.T. Tindle	79
C.3	A note on the application of normal-mode theory to shallow water propagation - M. Hall	81
C.4	Studies of optimum frequency of sound propagation in Australian shallow waters - F.P. Fessenden, D.J. Kewley and L.T. Sin Fai Lam	87
C.5	Shallow water waveguide characterization using a Hankel transform - G.V. Frisk and J.F. Lynch	93

D : Noise

D.1	Determining ambient noise due to wind and waves using measured surface source levels - A.S. Burgess and D.J. Kewley	95
D.2	Infrasonic ambient noise in the ocean - A.C. Kibblewhite and K.C. Ewans	100
D.3	Noise generation at the sea surface : recent theoretical and experimental work - D.H. Cato	101
D.4	The problems in predicting sea surface noise in the frequency band 10 Hz to 200 Hz - D.H. Cato	106
D.5	Determining the horizontal directivity of ambient noise using a towed array - R. Marrett	112
D.6	Is there a submarine volcano in the Tasman Sea? - L.H. Hall	116

E : Scattering

- E.1      A brief review of Fisheries Acoustics Part I: 119  
          Acoustic assessment of fish stocks - R.B.Mitson
- E.2      A brief review of Fisheries Acoustics Part II:  
          Acoustic Telemetry for the Study of Fish  
          Behaviour - R.B. Mitson
- E.3      Scattering from fish shoals and the determination  
          of fish density from a statistical analysis of  
          echo waveforms - P.N. Denbigh 131
- E.4      High-frequency mid-water echo sounding - J.G.H. Maxwell,  
          I.S.F. Jones and R. Coleman 137
- E.5      An assessment of second-order perturbation theory  
          for scattering of sound by a surface roughened by  
          hard, spherical, randomly distributed bosses -  
          A. Tolstoy, D. Berman, O. Diachok and I. Tolstoy 143
- E.6      Echo strength of spherical object in the presence  
          of nearby boundaries - X.L. Bao, B.S. Liu and  
          F.H. Li 151

F : Signal Processing 1

F.1	The effect of weight vector errors on the performance of an antenna array - L.C. Godara	157
F.2	A comparison of various frequency estimators - R.F. Barrett and D.R.A. McMahon	164
F.3	Measurements on the output statistics of conventionally and adaptively beamformed underwater acoustic data - D.A. Gray	169
F.4	A comparison between conventional and adaptive beamformers using underwater acoustic data - A.C. Smith and G.C.L. Searle	175
F.5	Misadjustment in adaptive beamforming using perturbation sequences - L.C. Godara and A. Cantoni	180
F.6	Leakage of interference in adaptive beamformers - D.R. Sweet	187
F.7	A new set of linear constraints for broadband time domain element space processors - M.H. Er and A. Cantoni	193

G : Signal Processing 2

G.1	On phase shifter errors in an antenna array - L.C. Godara	200
G.2	An application of a non-linear technique to the processing of underwater acoustic data - D.A. Gray	206
G.3	Systolic Architectures for sonar processing - W. Marwood and A.P. Clarke	211
G.4	Robust estimation of bearing in correlated noise - C.L. Byrne and A.K. Steele	219
G.5	A high speed side scan sonar based on wide band frequency modulated continuous transmission (CTFM) - P.T. Gough, M.J. Cusdin, A. de Roos and J.J. Sinton	225
	AUTHOR INDEX	231

## Acoustic and Related Properties of the Sea Floor

Edwin L. Hamilton

Naval Ocean Systems Center (Emeriti Program), San Diego, California 92152, U.S.A.

This review-tutorial paper is concerned with those acoustic and related properties of the sea floor that, when known, allow the geophysicist and underwater acoustician to use basic physics in understanding sound propagation in the sea floor. These data are usually presented in the form of geoacoustic models. These models guide theoretical studies, help reconcile experiments at sea with theory, and aid in predicting the effects of the sea floor on sound propagation.

A geoacoustic model details the true thicknesses and properties of sediment and rock layers in the real sea floor. The required properties are values at the sea floor (and gradients) of compressional wave (sound) velocity and attenuation, shear wave velocity and attenuation, and density. Values of these properties and their gradients are presented in tables, diagrams, and regression equations. Included in a geoacoustic model are bathymetric charts, echo-sounder records, acoustic reflection records, analyses from reflection and refraction measurements, measurements from cores (or in situ measurements), and water-mass data (e. g., sound velocity, density). Archival information from Navy files or the geological and geophysical literature is usually required. The acoustician is very much concerned with the topography, roughness, and slope of the sea floor. These properties can be studied from the above-noted records. This report, however, is concerned with the properties required for each sediment and rock layer.

It is very rare when all of the required properties to form geoacoustic models are available for any given area. It is necessary, therefore, to estimate or predict missing properties by extrapolation or computations; usually from similar sediments in the same environment elsewhere. The construction and use of geoacoustic models has been successful in many areas; especially in the deep sea. Shallow water geoacoustic modeling poses difficult problems because of vertical and horizontal variability in sediment types and properties. Rocks may be at, or near, the surface under thin sediment layers; areas may be so complex (including lava flows, fracturing, and faulting) that modeling is ineffective and reflection or bottom loss characteristics must be measured.

The general subject of geoacoustic modeling was recently summarized (Hamilton, 1980) with an extensive reference list; consequently, in this summary only those references especially pertinent to the summary will be listed.

In the presentation, frequent references will be made to the three general environments: the continental terrace (shelf and slope), the abyssal hill environment, and the abyssal plain environment. Each of these main environments usually has distinctive sediment types which, if sediment porosity is about the same, tend to have about the same acoustic properties for the same sediment type in the same environment in any ocean. In the continental terrace most of the sediments are from terrigenous sources and range from sands to silty clays. The deep-sea abyssal plains are usually composed of layers of silt-clays with thinner, intercalated layers of sands (in and near channels) and silt; these materials (turbidites) were carried along the bottom in turbidity currents and cover, smoothly, the originally rough topography. The abyssal hills are mostly covered by relatively thin layers of pelagic clay and siliceous oozes (more than 30 percent silica), with thicker deposits of calcareous oozes (more than 30 percent calcium carbonate) around the equator and on seamounts, plateaus, ridges, and islands where the sea floor is above the calcium carbonate compensation depth.

The properties of the sea floor can best be determined by in situ measurements accompanied by coring (e. g., Tucholke and Shirley, 1979), or from laboratory measurements from cores, corrected to in situ values. In the absence of in situ measurements or cores, values of necessary properties can be predicted from tables such as those in Hamilton and Bachman (1982), and in Hamilton et al. (1982). Proper use of the tables requires preliminary prediction of environment and sediment type, and final correction of tabulated values to in situ values.

In a gas-free sediment, the volume of voids (or space between mineral grains) occupied by water is expressed as porosity (volume of voids/total volume). In natural marine sediments porosity usually ranges from about 35 to about 90 percent; average values for the various sediment types in the various environments are listed in our latest tables (Hamilton and Bachman, 1982). Some average porosities of the continental shelf and slope (in percent) are fine sand, 44.5; very fine sand, 48.5; silty sand, 54; and silt-clays, 72.1. In abyssal plains silt-clays average 78.5 percent porosity, and in abyssal hills, 79.9 percent. The siliceous sediments (clayey silt and silty clay) of the Bering and Okhotsk Seas have an average porosity of 86.6 percent. These porosities are the result of distinctive mineral-grain structures which will be discussed.

The saturated bulk density of a gas-free sediment can be expressed with the equation:  $\rho_{\text{sat}} = n\rho_w + (1-n)\rho_s$ ; where  $n$  is fractional porosity,  $\rho_w$  is density of pore water, and  $\rho_s$  is the bulk density of mineral grains. Values

for sea-water density can be obtained from oceanographic tables. In our samples, the range of bulk densities of mineral grains in the continental terrace for the various sediment types is 2.66 to 2.72 g/cm<sup>3</sup>; the average for all samples (340) is 2.678 g/cm<sup>3</sup>. Averaged bulk grain densities in abyssal plain silt-clays is 2.667 g/cm<sup>3</sup>; in abyssal hills, 2.735 g/cm<sup>3</sup>; and in siliceous sediments of the Bering and Okhotsk Seas, 2.457 g/cm<sup>3</sup>.

In predicting in situ properties of the sea floor surface, it can be assumed that porosity and density are the same in situ as in the laboratory. The differences are within the margins of error of laboratory measurements. The corrections to density can be easily made (using in situ values of water density), but the increased pore-water density at a water depth of 6000 m, for example, would increase laboratory to in situ saturated bulk density by no more than about 0.03 g/cm<sup>3</sup>.

Two methods have been presented to obtain values of density with depth in the sea floor. In thicker sections in which there are sound velocity data, the velocity-density relations for the appropriate sediment-rock type can be used to establish density-depth curves (Hamilton, 1978). Another method, not involving velocity, is to use a value of density from surface core measurements and apply an appropriate gradient (for the sediment type) from generalized studies (Hamilton, 1976a).

As a result of a large number of measurements of sound velocity and related properties of cores from the sea floor, it is now possible through regression equations (Hamilton and Bachman, 1982) to empirically estimate sound velocity given mean grain size, porosity, or density; or of density and porosity given grain sizes. The inverse of these regressions are in a report by Bachman (1984).

In sediments of the sea floor, sound velocity increases from less than that in sea water in silt-clays to high velocities (greater than 1800 m/s) in low-porosity sands. The sound velocity-porosity relationships have received much attention in past studies because porosity is an easily-measured property which usually allows reasonable predictions of velocity. This is a result of the large compressibility of water in pore spaces relative to the much smaller compressibility of the mineral grains. The net effect of the varying volumes of these two constituents (and density) results in most of the abyssal hill and plain high-porosity sediments, and many of the continental terrace silt-clays having velocities less than that in sea water, but higher than would have been predicted by the Wood Equation for suspensions. These velocities (higher than to be expected in suspensions) are due to the presence of rigidity

and a frame bulk modulus in the mineral structures of the sediments. This low velocity phenomenon was noted in early laboratory studies, and has been confirmed by in situ measurements in the sea floor (e. g., Tucholke and Shirley, 1979; Tucholke, 1980). The lowest velocities measured in the higher-porosity sediments are usually no more than about three percent less than in sea water at the same temperature and pressure.

The sound velocity ratio (sediment velocity/sea-water velocity) is important when studying reflection and refraction of sound waves incident on the sea floor. This ratio is also useful in predicting in situ sediment-surface velocities because the ratio remains the same in the laboratory or at any water depth in the sea. To correct a laboratory velocity to the sea floor, simply multiply the velocity ratio by the bottom-water velocity. This has the same result as making full temperature and pressure corrections to the laboratory measurement using tables for the speed of sound in sea water.

Mean grain size in all environments, and percent clay-size material in the deep-sea environments, have been determined to be important indices to sound velocity. The relationships between grain-size data and velocity are especially important because grain size analyses can be made of dried sediment in which density, porosity, and velocity measurements cannot be made. Additionally, there is much data on grain sizes in geologic literature which can be used as indices to acoustic properties.

Interval sound velocities in sediment and rock layers in the sea floor have been determined by the sonobuoy technique for about 20 years. These measurements have allowed computations of positive velocity gradients which are important in refracting sound energy back into the water mass. Near-surface sediment velocity gradients usually range between 0.3 to 2.0 meters per second per meter, or  $s^{-1}$ ; these gradients usually decrease with depth. About two thirds of the average increase of sound velocity with depth in the sea floor is apparently caused by reductions of porosity because of pressure-induced porosity reductions and effects on the sediment mineral frame; other causes are temperature increases with depth, pore-water pressure increases, and increases in mineral frame rigidity (Hamilton, 1979a). This means that areas of fast sediment accumulation in which porosity is high have lower gradients; higher porosities and lower gradients can also be expected in sediments with strong mineral frames which resist pressure-induced porosity reductions. Recent studies have supported these conclusions. In the upper 100 m, deep-sea turbidites have average velocity gradients of  $1.2 s^{-1}$ ; the U. S. Atlantic continental rise,  $0.8 s^{-1}$ ; and

basins of the continental shelf off Sumatra,  $0.7 \text{ s}^{-1}$ . These values from sonobuoy measurements are supported by selected Deep Sea Drilling Project (DSDP) sites. Studies of other sediment types, based on selected DSDP drill holes, indicate that velocity gradients in the upper levels of siliceous sediments average about  $0.8 \text{ s}^{-1}$ ; calcareous sediments,  $0.9 \text{ s}^{-1}$ ; and pelagic clay,  $1.0 \text{ s}^{-1}$ . When regression equations are computed for velocity-depth, or travel time of sound, it is important to force the regressions through a realistic value of velocity at the sea floor (based on core measurements corrected to in situ). When this is not done, the resulting intercepts at depth or time equals zero are apt to be statistical artifacts.

In sands there is little significant reduction of porosity because of effective pressures in the upper tens of meters. The main effects on sound velocity are due to increased rigidity of the mineral structure. Sound velocity in sands increases very fast in the first few meters; a laboratory example indicated  $19 \text{ s}^{-1}$  between 1 and 2 m, and only  $1.5 \text{ s}^{-1}$  between depths of 18 and 20 m.

The effects of rigidity on sound propagation can be important; especially where conversion of compressional waves to shear waves at the sediment-basement boundary can be an important energy-loss mechanism. Given shear wave velocity and density, rigidity can be computed. Unfortunately, there are very few in situ, shear wave measurements in modern marine sediments. Japanese scientists and engineers are world leaders in in situ measurements of shear wave velocities on land. Ohta and Goto (1978) summarized about 300 low-strain data sets in silt-clays and sands from the alluvial plains of Japan. Their regression equations in m/s at depth,  $D$ , in m, were in the form:  $V_s = KD^{0.312}$  (with  $K = 79$  in silts and clays, and 100 to 112 in fine to coarse sands). These values compared well to a review involving U. S. measurements (Hamilton, 1976b). Given compressional wave velocity, shear wave velocity can be approximated (Hamilton, 1979b).

When compressional waves are reflected and refracted through the sea floor, sound energy is attenuated; consequently, sound attenuation in the sediment surface, and as a function of depth in the sea floor are important components of geoacoustic models. It is important to differentiate between intrinsic attenuation and effective attenuation. Intrinsic attenuation is due to energy losses through conversion to heat by friction between mineral grains, and, in some sediments, through relative movements of pore water and mineral frame. Effective attenuation occurs when sound enters the sea floor; especially at low frequencies and deep penetration. In this case, sound energy is lost through a number

of largely unpredictable causes; including intrinsic attenuation, reflection and refraction at interfaces (including conversion of compressional to shear waves), reflector roughness and curvature, and scattering by inhomogeneities within the sediment. It is effective attenuation which is required in geoacoustic modeling. Most of the measurements of intrinsic attenuation in silt-clays indicate an approximate first-order dependence of attenuation on frequency from a few Hz to the MHz range. The available measurements in sands between 1 and 100 kHz indicate an approximate  $f^1$  relationship, with no inflection in this frequency range which can be construed as a change from  $f^2$  at low frequencies to  $f^{1/2}$  at high frequencies as required by the Biot-Stoll equations. There have been laboratory measurements in clean, highly permeable sands of attenuation at low frequencies (less than 1 kHz) which are in accord with the Biot-Stoll equations (e. g., Stoll, 1979), but there are no in situ measurements of attenuation of compressional waves in this low-frequency range in sea-floor, poorly-sorted, natural sands of low permeability which confirm or deny an  $f^2$  dependence.

Very little data are available to determine effective attenuation as a function of depth in the sea floor. The available measurements vary widely from very low to higher attenuation-depth functions (Hamilton, 1976c; Mitchell and Focke, 1980; Frisk et al., 1981; Jacobson et al., 1981). These differences are probably not errors, but are due to the differences in sediment types, consolidation with depth, layering, reflectors, and other causes of effective attenuation. As with sound velocity, each sediment and rock layer is apt to be unique, and the best that can be done for predictions of effective attenuation and its gradients are to gather data from similar sediment types and geomorphic areas, examine the data statistically, and report empirical averages and variations.

When reflecting sound waves are partially converted to shear waves, the shear energy is rapidly attenuated. There are very little data on attenuation of shear waves in natural marine sediments; most data are from land measurements. The available information was summarized in Hamilton (1976d).

The floor of the world's ocean cannot be defined by any single model or even a small number of models. Therefore, it is important that acoustic and geophysical experiments at sea be supported by a particular model, or models, of the area. Given those records and measurements noted in the second paragraph of this summary, it is possible to extrapolate geoacoustic models over wider areas within geomorphic provinces. Using the data and techniques discussed above and in the references, it is possible to estimate or predict missing properties.

## REFERENCES

- Bachman, R. T., 1984, Acoustic and physical property relationships in marine sediments, in preparation.
- Frisk, G. V., Doust, J. A., and Hays, E. E., 1981, Bottom interaction of low-frequency acoustic signals---, *J. Acoust. Soc. Am.*, v. 69, p. 84-94.
- Hamilton, E. L., 1956, Low sound velocities in high-porosity sediments, *J. Acoust. Soc. Am.*, v. 28, p. 16-19.
- Hamilton, E. L., 1976a, Variations of density and porosity with depth in deep-sea sediments, *J. Sedimentary Petrology*, v. 46, p. 280-300.
- Hamilton, E. L., 1976b, Shear-wave velocity versus depth in marine sediments: a review, *Geophysics*, v. 41, p. 985-996.
- Hamilton, E. L., 1976c, Sound attenuation as a function of depth in the sea floor, *J. Acoust. Soc. Am.*, v. 59, p. 528-535.
- Hamilton, E. L., 1976d, Attenuation of shear waves in marine sediments, *J. Acoust. Soc. Am.*, v. 60, p. 334-338.
- Hamilton, E. L., 1978, Sound velocity-density relations in sea-floor sediments and rocks, *J. Acoust. Soc. Am.*, v. 63, p. 366-377.
- Hamilton, E. L., 1979a, Sound velocity gradients in marine sediments, *J. Acoust. Soc. Am.*, v. 65, p. 909-922.
- Hamilton, E. L., 1979b,  $V_p/V_s$  and Poisson's ratios in marine sediments and rocks, *J. Acoust. Soc. Am.*, v. 66, p. 1093-1101.
- Hamilton, E. L., 1980, Geoacoustic modeling of the sea floor, *J. Acoust. Soc. Am.*, v. 68, p. 1313-1340.
- Hamilton, E. L., and Bachman, R. T., 1982, Sound velocity and related properties of marine sediments, *J. Acoust. Soc. Am.*, v. 72, p. 1891-1904.
- Hamilton, E. L., Bachman, R. T., Berger, W. H., Johnson, T. C., and Mayer, L. A., 1982, Acoustic and related properties of calcareous deep-sea sediments, *J. Sedimentary Petrology*, v. 52, p. 733-753.
- Jacobson, R. S., Shor, G. G., Jr., and Dorman, L. M., 1981, Linear inversion of body wave data-Part II: attenuation, *Geophysics*, v. 46, p. 152-162.
- Mitchell, S. K., and Focke, K. C., 1980, New measurements of compressional wave attenuation in deep ocean sediments, *J. Acoust. Soc. Am.*, v. 67, p. 1582-1589.
- Ohta, Y., and Goto, N., 1978, Empirical shear wave velocity equations in terms of characteristic soil indexes; *Earthquake Engin. and Struct. Dynamics*, v. 6, p. 167-187.
- Stoll, R. D., 1979, Experimental studies of attenuation in sediments, *J. Acoust. Soc. Am.*, v. 66, p. 1152-1160.
- Tucholke, B. E., 1980, Acoustic environment---western N. Atl. Ocean, determined from---sediment cores, *J. Acoust. Soc. Am.*, v. 68, p. 1376-1390.
- Tucholke, B. E., and Shirley, D. J., 1979, Comparison of lab. and in situ measurements-on sediment cores ---*J. Geophys. Res.*, v. 84, p. 687-695.

USE OF SCHOLTE WAVES TO DETERMINE  
THE SHEAR PROPERTIES OF OCEAN SEDIMENTS

by

Finn B. Jensen, Henrik Schmidt, and Tuncay Akal  
SACLANT ASW Research Centre, 19026 La Spezia, Italy

### Introduction

It is well-established that shear rigidity of the ocean bottom affects propagation of waterborne sound through the coupling of energy into shear waves. This coupling mechanism is particularly important in low-frequency shallow-water acoustics, where the excitation of shear waves in the bottom often becomes the dominant loss mechanism for waterborne sound [1]. Under these circumstances a realistic physical model of the ocean bottom is a viscoelastic solid described by compressional and shear-wave velocities, the attenuation factors associated with these waves, and the material density.

While density and the compressional-wave properties (speed and attenuation) in sediments can be determined by direct methods, the shear-wave properties are difficult to measure. This is because of the usually high attenuation of these waves and because it is difficult to generate a wave that consists of predominantly transverse particle motion. The shear-wave speed and attenuation can be indirectly determined, however, through the measured propagation characteristics of the ocean-bottom interface wave, whose existence is intrinsically related to the shear properties of the sediments.

We shall review the characteristics of seismic interface waves, give some simple formulas that relate their speed and attenuation to those of shear bulk waves, provide examples from the literature of indirectly determined shear speeds in sediments, and, finally, demonstrate how the use of a sophisticated numerical model of seismic wave propagation allows us to reconstruct from seismic records the shear speed and shear attenuation profiles in ocean sediments.

#### 1. Seismic Interface Waves

This particular wave type — named boundary, surface, or interface wave — is a guided wave propagating along the interface between two media with different shear speeds [2,3]. The wave is generally given different names according to the media properties involved [4]. Hence when propagating

on a free surface of a solid it is called a Rayleigh wave, while it is a Scholte wave when propagating along a liquid/solid interface, and a Stoneley wave when associated with a solid/solid interface. Note that at least one of the media must be a solid for the interface waves to exist. In the case of a water/sediment interface, the pertinent wave type is a Scholte wave with the following characteristics:

- The wave propagates along the sea floor with exponentially decaying amplitude away from the guiding interface (wave is evanescent in both media).
- Particle motion is elliptical in the depth/range plane.
- There is no low-frequency cutoff.
- Propagation speed and attenuation are closely related to the shear properties of the sediment.

For a simplified environment consisting of two homogeneous media in contact, the Scholte wave is non-dispersive. Its propagation speed ( $c_{sch}$ ) and attenuation ( $\delta_{sch}$ ) then relate in an extremely simple manner to the sediment shear properties as:

$$c_{sch} = 0.9 \cdot c_s, \quad \delta_{sch} = 1.1 \cdot \delta_s, \quad (1)$$

where the attenuation is in decibels per unit length. These formulas, determined from numerical simulations to be accurate to within a few percent for unconsolidated sediments (clay, silt, sand) with low shear speeds, indicate that the Scholte-wave properties are virtually independent of densities and compressional-wave properties in the two media. Consequently the Scholte interface wave is ideal for determining the shear properties of the ocean bottom.

For a realistic environment with sediment layering, the Scholte wave becomes dispersive and, in addition, a finite number of ducted shear modes will be present. Figure 1 shows dispersion curves for a solid layer of low shear speed on a high-speed solid substratum. The fundamental mode ( $M_0$ ) is an interface wave that in the low-frequency limit  $kH \rightarrow 0$  propagates as a Rayleigh wave on the substratum, and in the high-frequency limit  $kH \rightarrow \infty$  propagates as a Rayleigh wave on the upper layer. The higher-order modes are ducted shear modes in the upper layer. They all have a cutoff frequency where they propagate with the shear speed of the substratum. In the high-frequency limit

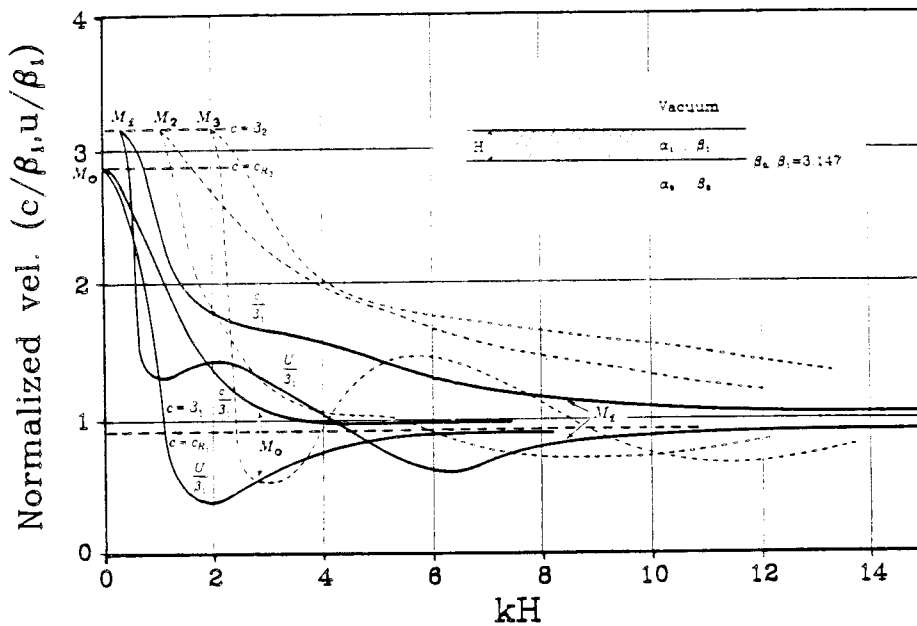


Fig. 1 Dispersion curves for elastic layer over semi-infinite elastic solid (Tolstoy and Usdin [2]).

these modes propagate with the shear speed of the upper layer. In this case there is no Stoneley wave present; this is due to the stringent conditions for the existence of this type of wave, which is found only when the change in shear speed across a solid/solid boundary is less than 10%.

In the following section we show how the complex information contained in experimentally determined dispersion curves similar to those of Fig. 1 can be used to extract shear information for the ocean bottom. Such an analysis generally requires the use of a numerical model. However, if experimental results show negligible dispersion, we can use the simple formulas of Eq. (1) to determine shear properties for the upper sediment layer. No dispersion means that the sediment is homogeneous to a depth of 1 to 2 wavelengths, which is the approximate penetration depth of the Scholte wave.

## 2. Sediment Shear Properties

Over the past 20 years various investigators [5-10] have used Scholte waves to determine the shear properties of unconsolidated sediments. These experimental results are summarized in Table 1. Note that experiments were done in water depths ranging from 1 to 985 m, over sandy or silty bottoms, and for frequencies between 3 and 35 Hz. The measured Scholte-wave attenuations (with geometrical spreading removed) are seen to vary more than two orders of magnitude, with the highest attenuation being associated with the highest centre frequency. The inferred shear speeds are seen to be between 85 and 195 m/s, which is in excellent agreement with the values quoted by Hamilton [11].

Table 1 Interface wave experiments

Investigators	Year	Water depth	Bottom type	Centre freq.	Measured att.	Inferred shear speed	Inferred shear att.
		m	-	Hz	dB/km	m/s	dB/ $\lambda_s$
Bucker, Whitney, Keir [5]	1964	1	sand	20	300	100	1.4
		20	sand	25	200	195	1.4
Hamilton et al. [6]	1970	390	silt	-	-	100	-
		985	silt	-	-	90	-
Schirmer [7]	1980	130	sand	4.5	7	120	0.2
Essen et al. [8]	1981	1	silt	4	-	85	-
Holt, Hovem, Syrstad [9]	1983	-	sand	35	600	150	2.3
Schmalfeldt, Rauch [10]	1983	20	-	3	10	100	0.3
		30	-	3	2	150	0.1

Assuming the shear attenuation to be linear with frequency [11], we can conveniently express it in decibels per wavelength. This has been done in the last column of Table 1, using the simple formula of Eq.(1) to relate measured attenuation of the Scholte wave with the bulk shear-wave attenuation. We obtain values that still vary more than one order of magnitude (0.1 to 2.3 dB/ $\lambda_s$ ), whereas Hamilton [11], based on sparse in-situ measurements for silt and sand sediments, quotes attenuation values around 1 to 2 dB/ $\lambda_s$ . Note, however, that the very low attenuation values (0.1 to 0.3 dB/ $\lambda_s$ ) are all associated with low-frequency experiments (3 to 4.5 Hz) where the shear wavelength is large (25 to 50 m) giving penetration depths of 50 to 100 m for the Scholte wave. Hence these attenuations are averaged over the upper 50 to 100 m of the bottom, and knowing that the shear attenuation decreases with depth, it is not surprising that the low-frequency experiments result in lower mean values for the shear attenuation.

To demonstrate how shear speed and shear attenuation profiles can be determined from Scholte wave experiments in connection with a sophisticated propagation model, we turn to the experimental record in Fig. 2a. Here we see stacked time signals for the horizontal particle velocity, as recorded by a geophone on the ocean bottom [10]. The source was an explosive charge detonated near the sea floor. We note some dispersed low-frequency arrivals with group velocities between 78 and 235 m/s. Figure 2b is a synthetic seismogram generated by a numerical model [12] for a realistic bottom layering. The dispersion characteristics are seen to be in excellent agreement with the experimental data, while there is some disagreement in the details of the signal shapes. The model environment used is given in Fig. 3a. It consists of 3 sediment layers with different shear-speed gradients and a constant attenuation of 0.25 dB/ $\lambda_s$ . For simplicity, the compressional-wave properties were taken to be constant throughout the bottom. It should be

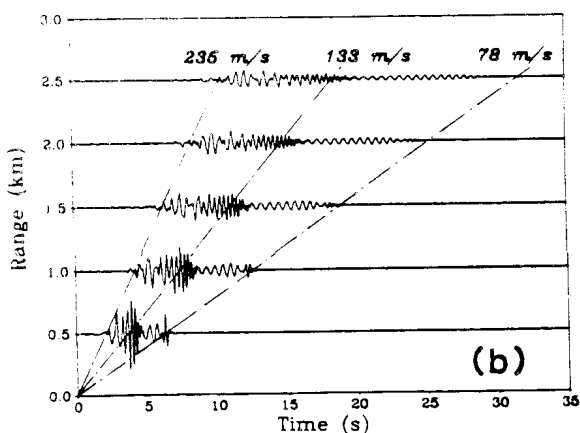
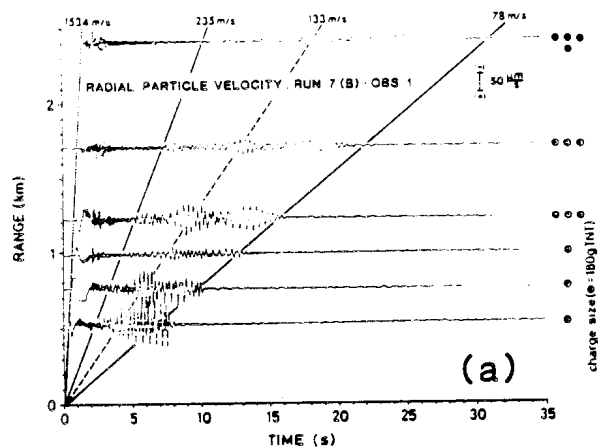


Fig. 2 Experimental and synthetic seismograms for the horizontal particle velocity of the sea floor.

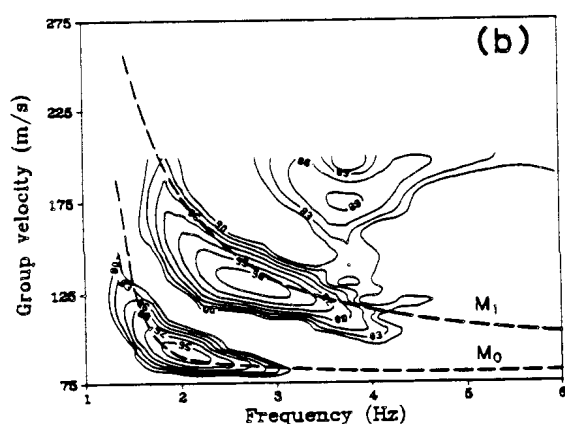
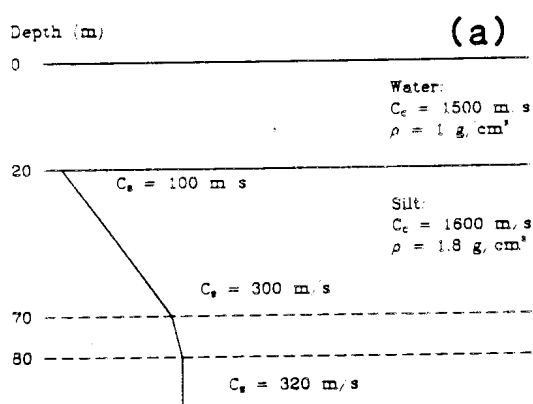


Fig. 3 Model environment and dispersion curves associated with the seismograms of Fig. 2.

emphasized that these shear speeds (100 to 320 m/s) and shear speed gradients ( $<4$  m/s/m) are in good agreement with values given by Hamilton [11].

Figure 3b shows experimental and theoretical dispersion curves. The contours were obtained by applying a sliding narrowband filter to the experimental data [10]. We see that energy is arriving on three discrete modes, of which the slowest arrival is the Scholte wave ( $M_0$ ). The dashed lines show the computed dispersion curves for the model environment. Note the good agreement between theory and experiment for both the Scholte wave ( $M_0$ ) and the first shear mode ( $M_1$ ).

Better agreement on signal shapes in Figs. 2a and 2b could probably be obtained by introducing a realistic shear-attenuation profile in the bottom. More results on the modelling of seismic waves in sediments are given in [13].

### 3. Summary

Shear properties of ocean sediments are difficult to obtain by direct measurements. However, both shear speed and shear attenuation profiles can be inferred from the propagation of Scholte waves, as successfully done by various investigators over the past 20 years.

## References

1. T. AkaI and F.B. Jensen, Effects of the sea-bed on acoustic propagation. In: N.G. Pace (Ed.), Acoustics and the Sea-Bed. Bath Univ. Press, Bath, UK (1983): pp. 225-232.
2. W.M. Ewing, W.S. Jardetzky and F. Press, Elastic Waves in Layered Media. McGraw-Hill, New York, NY (1957).
3. I. Tolstoy and C.S. Clay, Ocean Acoustics: Theory and Experiment in Underwater Sound. McGraw-Hill, New York, NY (1966).
4. D. Rauch, Seismic interface waves in coastal waters: a review, Rep. SR-42. SACLANT ASW Research Centre, La Spezia, Italy (1980).
5. H.P. Bucker, J.A. Whitney and D.L. Keir, Use of Stoneley waves to determine the shear velocity in ocean sediments. J. Acoust. Soc. Amer. 36, 1595-1596 (1964).
6. E.L. Hamilton, H.P. Bucker, D.L. Keir and J.A. Whitney, Velocities of compressional and shear waves in marine sediments determined in situ from a research submersible. J. Geophys. Res. 75, 4039-4049 (1970).
7. F. Schirmer, Experimental determination of properties of the Scholte wave in the bottom of the North Sea. In: W.A. Kuperman and F.B. Jensen (Eds.), Bottom-Interacting Ocean Acoustics. Plenum, New York, NY (1980): pp. 285-298.
8. H.H. Essen, H. Janle, F. Schirmer and J. Siebert, Propagation of surface waves in marine sediments. J. Geophysics 49, 115-122 (1981).
9. R.M. Holt, J.M. Hovem and J. Syrstad, Shear modulus profiling of near bottom sediments using boundary waves. In: N.G. Pace (Ed.), Acoustics and the Sea-Bed. Bath Univ. Press, Bath, U.K. (1983): pp. 317-325.
10. B. Schmalfedt and D. Rauch, Explosion-generated seismic interface waves in shallow water: experimental results, Rep. SR-71. SACLANT ASW Research Centre, La Spezia, Italy (1983).
11. E.L. Hamilton, Geoacoustic modeling of the sea floor. J. Acoust. Soc. Amer. 68, 1313-1340 (1980).
12. H. Schmidt and F.B. Jensen, Efficient numerical solution technique for wave propagation in horizontally stratified ocean environments, Rep. SM-173. SACLANT ASW Research Centre, La Spezia, Italy (1984).
13. H. Schmidt, Excitation and propagation of interface waves in a stratified sea-bed. In: N.G. Pace (Ed.), Acoustics and the Sea-Bed. Bath Univ. Press, Bath, UK (1983): pp. 327-334.

THE INVERSION OF SEISMIC DATA MEASURED AT THE OCEAN SURFACE  
TO DETERMINE THE VELOCITY PROFILE OF THE OCEAN BOTTOM

G.R. SUTTON\* and B. MOORE\*

In oil exploration, seismic surveys using towed arrays and air guns are conducted to record acoustic data which are then processed to yield information of the structure and lithology of the ocean bottom. The collection and processing of the data are generally conducted by a seismic processing company on behalf of an oil company. The processed data are then combined by interpreters within the oil company with other information about the geology of the area and well data, if any, to decide on further action. The further action may involve the collection of additional seismic data, further seismic processing or drilling a well. Although the physics involved in oil exploration is similar to that in the world of underwater acoustics, the objectives are different, resulting in somewhat different processing or analysis procedures. A typical seismic processing sequence follows:

FILTERING  
DECONVOLUTION  
VELOCITY ANALYSIS  
C.D.P. STACKING  
MODELLING

The single most important unknown in seismic processing is the velocity profile. If the velocity were known accurately, the seismic problem in oil exploration basically would be solved. Consequently much effort has gone into the determination of velocity over the years. In the absence of well data, the initial estimates of velocity are determined from trial and error procedures based on what is known in the industry as Normal Moveout (NMO). This refers to the expected arrival times of a reflection from a reflecting interface being greater at the larger off-set hydrophones of the array. The final estimate of the velocity profile is basically that which "optimizes" the C.D.P. stack.

After processing, refinements to this coarse velocity profile are often attempted. These methods involve a top-down ray tracing procedure. In other words, rays are traced from the surface to determine the spatial locations of the next horizon of interest and the interval velocity, the procedure then being repeated as many times as there are layers of interest.

\*School of Mathematical Sciences, NSW Institute of Technology.

The difficulty with these methods is that they cause the error in the determination of the interval velocity to increase with depth. To overcome this difficulty generalized linear inversion techniques are being used and it is this technique which is used in our approach to the problem. Before detailing our approach, it should be noted that direct inversion of seismic reflectivity data has been attempted. This has been successful in synthetic models but is time-consuming and is currently not used in the industry. In such direct approaches to the problem, horizontal layering is assumed and the model is basically one-dimensional. In our approach, we permit lateral velocity variations and consequently our model could be viewed as two-dimensional.

In any inversion method a knowledge of a forward model that models the generation of the data to be inverted is essential. This forward model is a function that can be either an empirical relationship or a mathematical model of the process. In our approach the forward model generates horizon times, normal moveout velocities and dips from a two-dimensional interval velocity model. Consequently, it is a nonlinear function of many variables that cannot be inverted analytically. The numerical technique used for the inversion is based on a Taylor series expansion of the forward model. We have

$$F(\underline{V}_T) = F(\underline{V}_E) + \frac{\partial F(\underline{V}_E)}{\partial \underline{V}_E} (\underline{V}_T - \underline{V}_E) + \frac{\partial^2 F(\underline{V}_E)}{\partial \underline{V}_E^2} \frac{(\underline{V}_T - \underline{V}_E)^2}{2!} + \dots$$

$\underline{V}_T$  - velocity profile to be solved for

$\underline{V}_E$  - estimate of velocity profile

F - forward modelling function

It is required to solve this equation for  $\underline{V}_T - \underline{V}_E$  which would indicate how to correct  $\underline{V}_E$  to make it  $\underline{V}_T$ . However, this is not possible and an approximation must be made. The approximation is to linearize the equation. We have

$$F(\underline{V}_T) - F(\underline{V}_E) = \frac{\partial F(\underline{V}_E)}{\partial \underline{V}_E} (\underline{V}_T - \underline{V}_E).$$

It is the application of this equation in the determination of our two dimensional velocity model that will be addressed in this paper.

RAY THEORY MODELLING  
APPLIED TO LOW FREQUENCY ACOUSTIC INTERACTION  
WITH HORIZONTALLY STRATIFIED OCEAN BOTTOMS

Martin W. Lawrence  
R.A.N. Research Laboratory  
PO Box 706, Darlinghurst, 2010  
Australia.

This paper addresses the application of ray theory to interaction of low frequency harmonic acoustic waves from a point source with a horizontally stratified ocean bottom. Conventional ray tracing techniques are used with a number of added complexities, one of which is that ray splitting occurs at discontinuous interfaces. Each split ray is then separately followed and the total pressure field is obtained by coherently summing the field due to each ray family.

Depth is divided into segments in each of which the sound speed, sound absorption and density vary linearly (or are constant) with depth. Discontinuities in any of these properties may occur at the interfaces between these depth segments.

An entirely "local" ray treatment is adopted. Rays are traced from one interface to the next and the changes that occur to the ray are calculated as the ray is followed. This approach allows determination of the location at which various effects are being generated, in contrast to those models which first calculate a plane wave reflection coefficient for the entire seafloor. The acoustic field is calculated along a piecewise linear receiver trajectory.

"Low frequency" is included in the title because (i) layers are considered that are not thick with respect to a wavelength and (ii) frequency dependent effects (such as caustic corrections) are considered.

An ocean surface reflector can be included or not, to fit the experimental circumstances (pulsing of the harmonic source can be used in deep water, with deep source and receiver, in order to remove the effect of surface reflections). The surface reflector, if included, is modeled as an ideal pressure release boundary. If a surface reflector is not included, the top layer extends to infinity. The bottom layers always extends to infinity. All layers are treated as fluids; shear wave conversion is not considered.

In order to achieve good agreement between results from this model and normal mode results (for cases that could be handled by normal

mode techniques), it proved necessary to include corrections in the vicinity of caustics, and to incorporate beam displacement. The interaction of these two effects produces some of the most interesting effects of the model.

When the derivative of range with respect to ray angle at the source goes to zero, simple ray theory predicts infinite energy. Due to the nature of the ocean seafloor sound-speed environment, such caustics frequently occur. Dealing with this problem requires (i) a more accurate expression for spreading loss, in a boundary region surrounding the caustic, and (ii) appropriate adjustment in phase of a ray after touching a caustic.

For a simple caustic there are two eigenrays to each point on the insonified side of the caustic, one of which has touched the caustic, and the other has yet to touch. The caustic separates the insonified region from the shadow zone.

### Beam Displacement

Beam displacement is the effective lateral displacement along a surface of a bounded plane wave on reflection from that surface. Beam displacement can be shown to arise quite naturally from a decomposition of plane waves. Each ray in ray theory can be regarded as a bounded beam, for example in determination of intensity in terms of beam area. Thus a ray will be subject to beam displacement on reflection. The incorporation of beam displacement will improve ray calculations by allowing for these boundary effects.

The displacement of a beam is given by

$$d = -\partial\phi/\partial k_r \quad (1)$$

where  $\phi$  is the phase shift on reflection and  $k_r$  is the horizontal wave-number. For lossless media, phase shift on reflection only varies with  $k_r$  for the case of total reflection. Large beam displacements occur near the critical angle giving rise to the formation of a caustic.

### Caustic Corrections

On the insonified side of the caustic, the acoustic pressure (with a time factor  $\exp(-i\omega t)$  suppressed) may be described by the following equation

$$pe^{i\phi} = \left[ (p_2 + p_1)\pi^{1/2} x^{1/4} \text{Ai}(-x) + i(p_2 - p_1)\pi^{1/2} x^{-1/4} \text{Ai}'(-x) \right] e^{i(\phi_{av} \pm \frac{\pi}{4})}, \quad (2)$$

where  $p$  is the pressure amplitude, and  $\phi$  is the associated phase, at a particular receiver range.  $Ai$  and  $Ai'$  are the Airy function and its derivative (with respect to its argument  $x$ ).  $p_1$  and  $p_2$  are pressure amplitudes of the two ray arrivals at this same range, calculated by standard geometrical acoustics, while  $\phi_1$  and  $\phi_2$  are the corresponding phases. Further,  $x$  and  $\phi_{av}$  are defined by

$$x = \left[ \frac{3}{4}(\phi_2 - \phi_1) \right]^{2/3}, \quad \phi_2 > \phi_1, \quad (3)$$

$$\phi_{av} = \frac{1}{2}(\phi_2 + \phi_1). \quad (4)$$

Note that Eq. (2) asymptotically (for large  $x$ ) approaches the simple sum of the two geometric acoustic arrivals, provided that: (i) for the minus sign in Eq. (2) the phase of arrival 2 is reduced by  $\pi/2$ , i.e.

$$pe^{i\phi} \rightarrow p_2 e^{i(\phi_2 - \frac{\pi}{2})} + p_1 e^{i\phi_1}, \quad x \rightarrow \infty, \quad (5)$$

and (ii) for the plus sign in Eq. 2 the phase of arrival 1 is increased by  $\pi/2$ , i.e.

$$pe^{i\phi} \rightarrow p_2 e^{i\phi_2} + p_1 e^{i(\phi_1 + \frac{\pi}{2})}, \quad x \rightarrow \infty. \quad (6)$$

The condition that  $\phi_2 > \phi_1$  ensures that the Airy function argument will be a real number. This condition establishes which arrival will be called ray 2, and which ray 1.

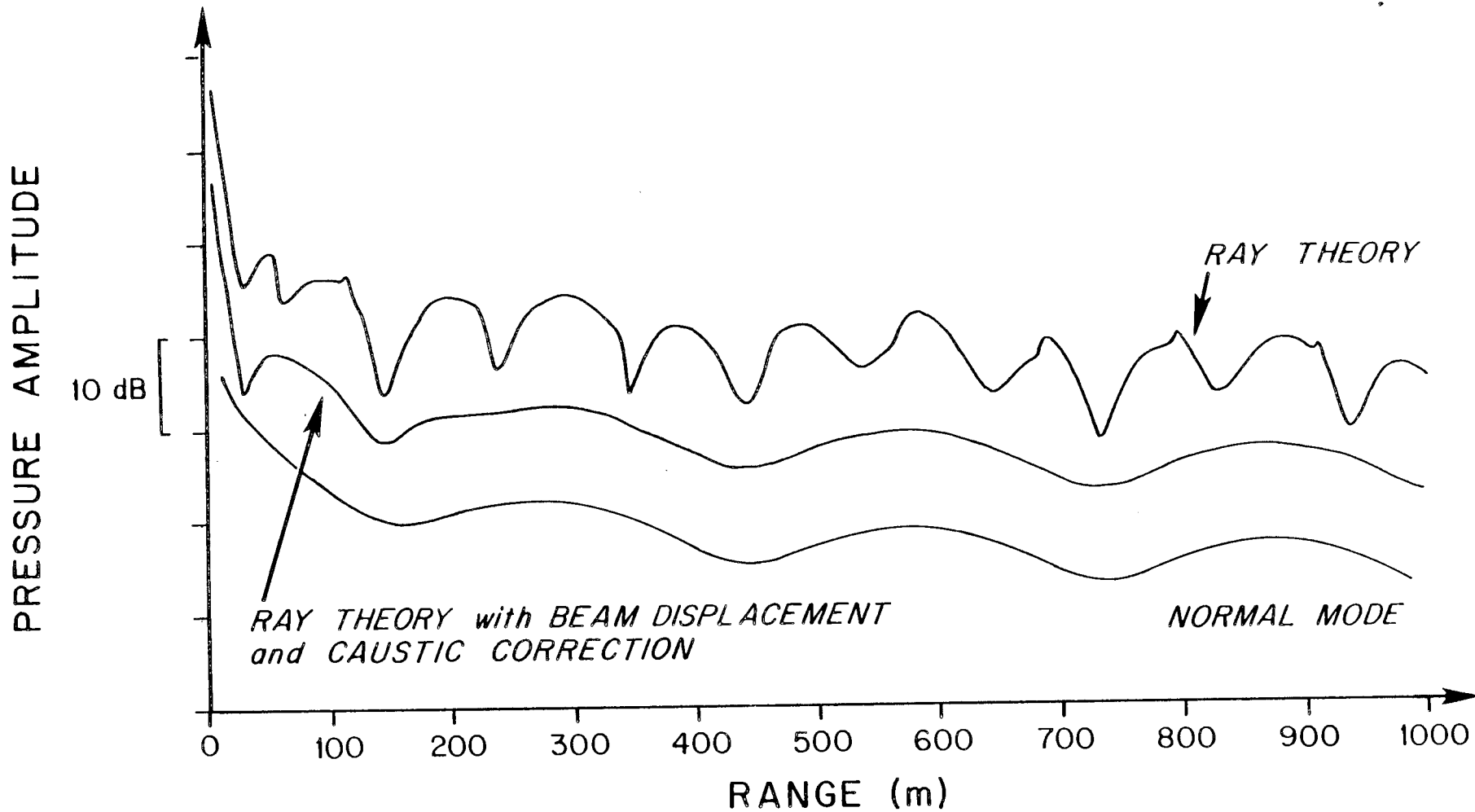
Using somewhat lengthy arguments, it can be shown for the simplest cases that for a refraction induced caustic, the larger phase occurs for the ray that has touched the caustic. The association of a  $\pi/2$  phase shift with touching of a caustic is a well known phenomenon. Thus this case corresponds to Eq. 5. However for beam-displacement induced caustics, similar arguments show that the larger phase occurs for the ray that has not touched the caustic. Thus this case corresponds to Eq. 6.

One direct implication of this result is that a ray touching a caustic loses  $\pi/2$  phase for a refraction caustic, but gains  $\pi/2$  phase for a beam displacement caustic.

These results have been incorporated in a computer program, together with a related treatment of the shadow zone of a caustic. Calculations using this program have shown many cases in which the above effects are

significant. The results from one example are shown in Fig. 1 for a frequency of 50 Hz. Note that the curves are offset from each other by 10 dB. This example is a Pekeris waveguide of 50 m depth, source and receiver at 25 m depth, sound speeds and densities constant at 1500 and 2000 m/s and 1.0 and 1.5 g/cm<sup>3</sup> for water and sediment respectively. It is evident that good agreement with the normal mode result requires inclusion of beam displacement and the resulting caustics.

The majority of this work took place during the author's exchange posting to the Woods Hole Oceanographic Institution. I thank my colleagues there for many stimulating discussions.



## ACOUSTIC IMPEDANCE MEASUREMENTS ON MARINE SEDIMENTS

J.I. Dunlop P. Douglas

School of Physics,  
University of New South Wales,  
P.O. Box 1, Kensington, NSW. 2033.Introduction

In many applications of underwater acoustics e.g. shallow water propagation or sonar depth sounding the sea floor plays an important role. As the acoustic impedance mismatch at the water sea-floor interface is usually not great there is a need for accurate measurement of its acoustic properties - the acoustic velocity, damping and density. Measurement of the acoustic velocity of a marine sediment may be accomplished with considerable precision using several types of measurement - duct propagation, critical angle or transit times of high frequency pulses between transducers inserted directly into the medium. Attenuation constants can also be obtained using the latter method but the precision is low and in particular there is a need for values at low frequencies which are usually obtained from extrapolation of measurements at high frequencies. More serious difficulties are posed to the direct measurement of bulk density, the effects of removing the sample greatly reducing the accuracy.

These acoustic properties can also be deduced from measurements of the acoustic impedance of the medium. Shirley (1977) developed a technique for in situ measurement of acoustic impedance by determining the effects of acoustic loading on the measured electrical impedance of an acoustic transducer immersed in the sediment. This technique was capable of measuring the acoustic impedance of sediments in the laboratory at a frequency of 65 kHz. Another technique (Dunlop 1981) makes use of the acoustic impedance tube for determining the acoustic properties of marine sediments.

In this paper, an extension of this technique will be discussed, and some field measurements presented.

The Acoustic Impedance Tube

An acoustic impedance tube consists of a rigid walled tube or duct along which acoustic waves propagate, to impinge on a sample fixed to

2.

to the closed end of the tube. Depending on the structure of the sample some fraction of the waves are reflected back along the tube and combine with the incident waves. Measurement of this acoustic field in front of the sample can yield information on the acoustic characteristics of the sample.

In its normal mode of operation the tube is operated with a rigid termination on which the sample is placed. For measurements on marine sediments this is readily accomplished in the laboratory, but at the expense of disturbing the sediment sample. The impedance tube may however be operated in the open end mode when it may be used for in-situ measurement of marine sediment.

Three possible configurations of deployment of the tube are shown in Fig. 1, namely the closed tube, open flanged tube and open protruding tube. In the case of the closed end Fig. 1a the acoustic impedance ( $Z$ ) at the surface of the sample is given by

$$Z = Z_0 \coth \gamma \ell \dots\dots\dots(1)$$

where  $Z_0$  is the characteristic impedance of the medium and  $\gamma$  the propagation constant. The length of the material above the rigid backing plate is  $\ell$ .

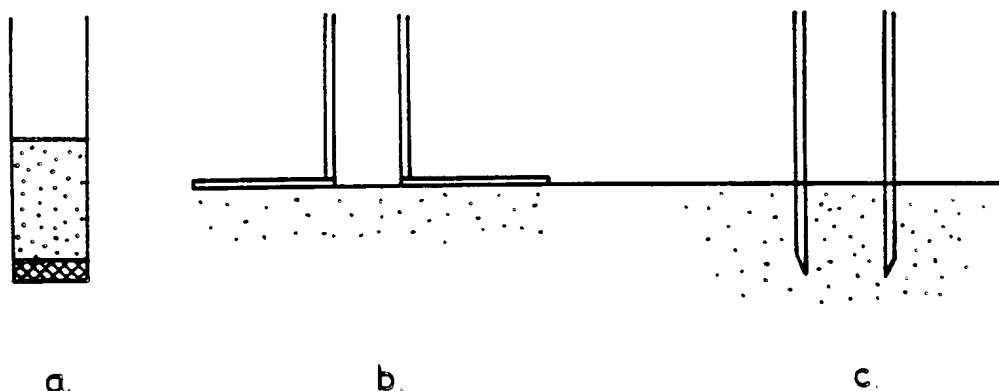


Fig. 1. Impedance tube configurations (a) closed tube (b) Open flange (c) open protrusion.

In the case of open flanged end, Fig. 1b, the acoustic impedance at the end of the tube is the radiation impedance ( $Z_R$ ) into the marine sediment. This may be derived to be (Kinsler & Frey 1963)

$$Z_R/Z_0 = R(2\gamma a) + j X(2\gamma a) \dots\dots\dots(2)$$

where  $a$  is the radius of the tube and the functions  $R$  and  $X$  are given as

3.

$$R(y) = y^2/2.4 - y^4/2.4^2.6 + y^6/2.4^2.6^2.8 - \dots$$

$$X(y) = 4/\pi(y/3 - y^3/3^2.5 + y^5/3^2.5^2.7 - \dots)$$

The third configuration employed, Fig. 1c, is that of an open end protruding into the sediment. The measured impedance at the surface of the sediment may be approximated by

$$Z/Z_o = \frac{Z_R \cosh \gamma \ell + Z_o \sinh \gamma \ell}{Z_R \sinh \gamma \ell + Z_o \cosh \gamma \ell} \dots\dots\dots(3)$$

The measured impedance for all three configurations is a function of  $Z_o$  the characteristic impedance of the medium and  $\gamma$  the propagation constant in the medium. Both of these parameters are affected by the nature of the medium which in the case of interest here is a granular-fluid mixture of varying density and porosity.

Acoustic Propagation in a Marine Sediment

The theory of wave propagation in saturated granular media has been formulated by several workers (e.g. Stoll 1974). In its simplest terms the theory assumes a wave propagating in a fluid modified by the presence of solid grains. A major mechanism for dissipation is viscous flow of the fluid in the pores between the particles, so that the system might be compared to a rigid porous material as a first approximation. There are other loss mechanisms however e.g. the elastic properties of the solid frame, losses due to grain to grain contact.

The characteristics of rigid porous materials has been expounded by Zwikker & Kosten (1949) in terms of a dissipation loss angle  $\delta$  denoting the phase difference between acoustic pressure and density variation or acoustic velocity, and a structure factor  $k$ . The acoustic characteristics of a material are modified accordingly to become

$$\gamma = j \frac{\omega \sqrt{k}}{c} (1 - j \delta/2)$$

and  $Z_o = \rho c / k (1 - j \delta/2)$

4.

Substitution of these expressions for  $\gamma$  and  $Z_0$  in the impedance equations 1, 2, 3 will then produce impedance plots as a function of frequency. Various values may be substituted for the parameters  $\delta$  and  $k$  until good agreement is obtained between these impedance plots and the measured impedance values.

A similar model by Beranek (1960) gives

$$\gamma = j\omega\sqrt{\rho_0 k Y / K} \sqrt{1 - jR_1 / \rho_0 \omega k}$$

and

$$Z_0 / \rho_0 c = -j K Y / \omega Y$$

where  $R_1$  is the alternating flow resistance,  $k$  a structure factor,  $Y$  the porosity,  $K$  the modulus of the fluid and  $\rho_0$  its density.

### Apparatus

Steel tubing, internal diameter 89 mm and wall thickness 7 mm was used to construct the various tubes employed. The sound field in front of the measurement end of the tube was measured using Bruel and Kjaer type 8103 hydrophones inserted into the tube through grommets in the side walls. The impedance ( $Z$ ) at the end of the duct may be derived from  $P_{12}$  the ratio of the sound pressure and  $\phi_{12}$  the phase difference between points  $x_1$  and  $x_2$  (Seybert & Ross 1977).

The tube was excited by limited band noise from a HP3582A spectrum analyser and the signals from the detection hydrophones processed by the analyser to yield  $P_{12}$  and  $\phi_{12}$ . This was then transferred to a computer for computation and plotting of the impedance as a function of frequency.

### Results

Typical results of acoustic impedance measurements on sand sediment using the three different techniques are shown in Fig. 2 (closed tube), Fig. 3 (open flange tube) and Fig. 4 (open protruding tube). Also shown on the diagrams are calculated plots using the respective impedance functions given by equations 1, 2, 3.

The closed tube results (Fig. 1) were obtained in the laboratory following reconstitution of the sediment in the tube. The measured impedance shows considerable irregularity which altered during the consolidation of the sediment. The match with the theoretical curve is moderately good and the values of  $c$  and  $\alpha$  obtained are in the expected region.

The open flange measurement was obtained from a remote measurement on a sandy sea floor in 5 m of water. The measured impedance curve exhibits artifacts and distortions, and no sensible value of  $k$  can be obtained. The low damping value suggests that the upper layer of sediment is very similar to water in its acoustic characteristics.

The open protruding tube measurements were obtained for reconstituted sediment in a tank. The impedance curve produced is smooth and can be matched very well with a theoretical curve. In the results shown the Beranek model was used. The value of  $k$  obtained is much lower than expected and the high value of flow resistance obtained suggests that the model used, that of a rigid porous material may not be appropriate.

### Conclusion

It is possible to measure the impedance properties of the sea floor using modified acoustic impedance tube techniques. The protruding tube technique offers most promise of being developed to investigate the upper layers to a depth of possibly 1 m depending on consolidation.

### References

- Beranek L.L. ; Noise Reduction, McGraw-Hill N.Y. 1960.
- Dunlop J.I. & Whichello A; Acoustic Impedance of Marine Sediments, Marine Geophy. Res. 5 157-163 (1981).
- Kinsler L.E. & Frey A.R.; Fundamentals of Acoustics, John Wiley 2nd. Ed. 1962.
- Seybert A.F. & Ross D.F.; Experimental Determination of Acoustic Properties using a two Microphone Random Excitation Technique, J. Acoust. Soc. Am. 61(5) 1362 (1977).
- Shirley D.J.; Method for Measuring In-situ Acoustic Impedance of Marine Sediments, J. Acoust. Soc. Am. 62(4) 1028-1032 (1977).
- Stoll R.D.; Physics of Sound in Marine Sediments, Ed. L. Hampton, Plenum Press (1974).
- Zwikker C.B. & Kosten C.W. ; Sound Absorbing Materials, Elsevier Am. (1948).

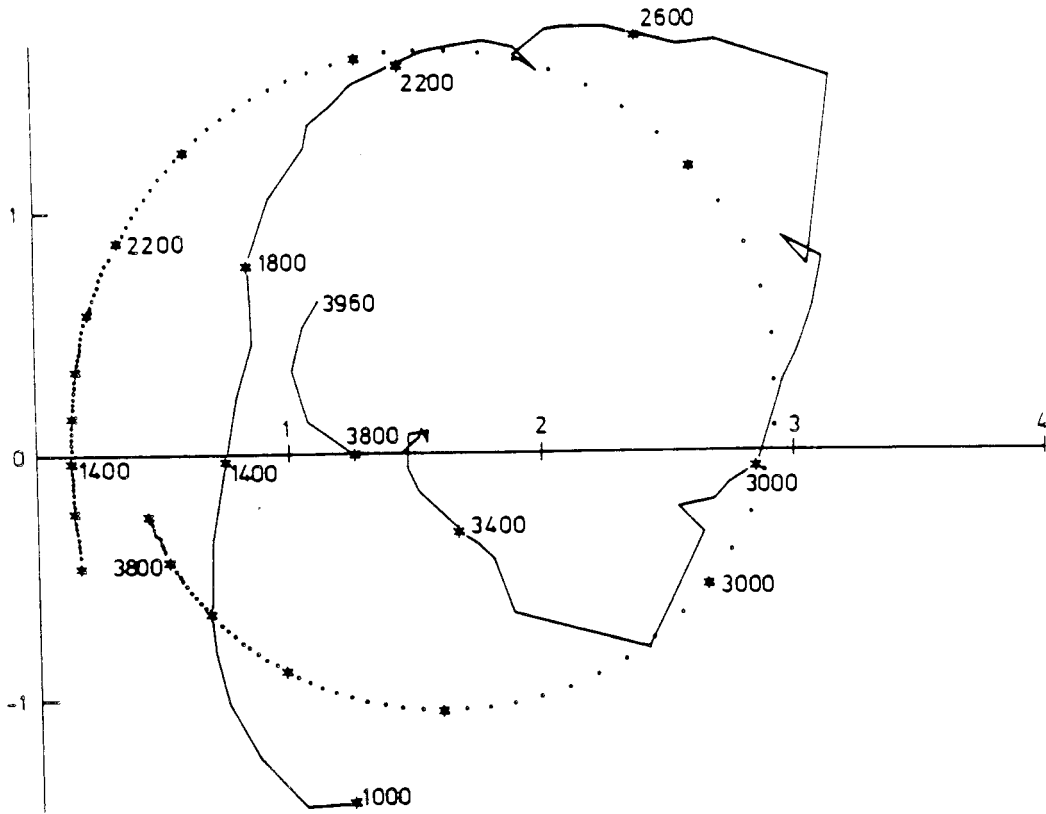


Fig. 2. Impedance values of a 266 mm sample of sand in the closed impedance tube (-). Calculated impedance curve of  $Z = Z_0 \coth \gamma l$  with  $k = 0.8$  and  $\delta = 0.2$  (.....).

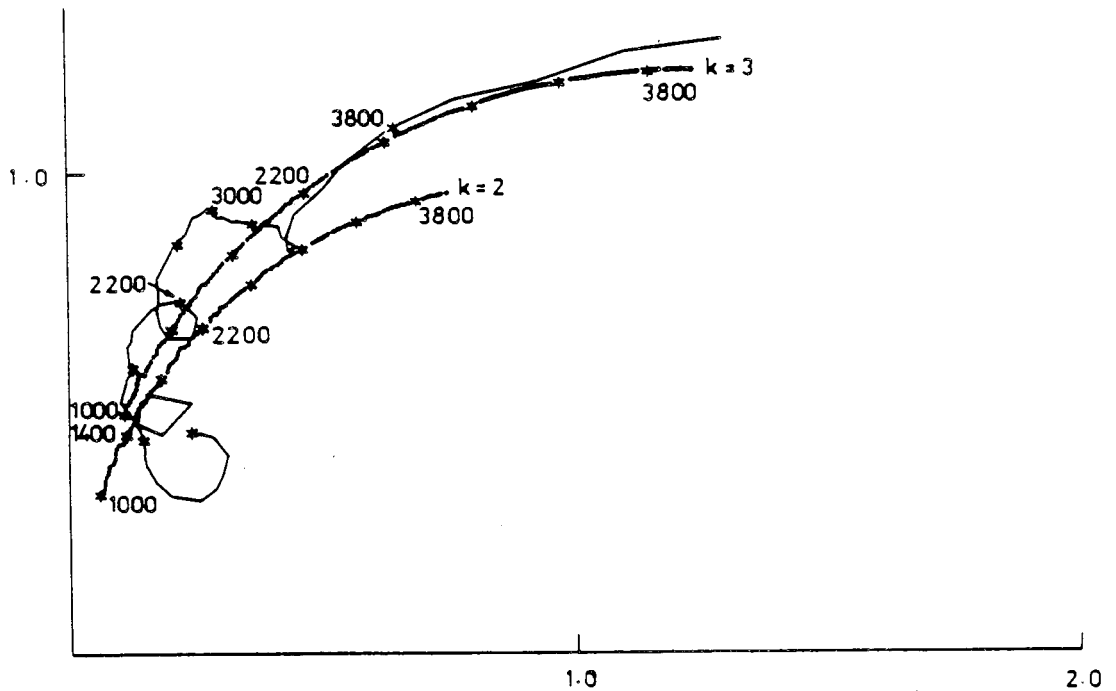


Fig. 3. Impedance values of open flange on sand sea floor (-). Calculated impedance curves of  $Z/Z_0 = R(2ka) + jX(2ka)$  with  $\delta = 0.05$  (...).

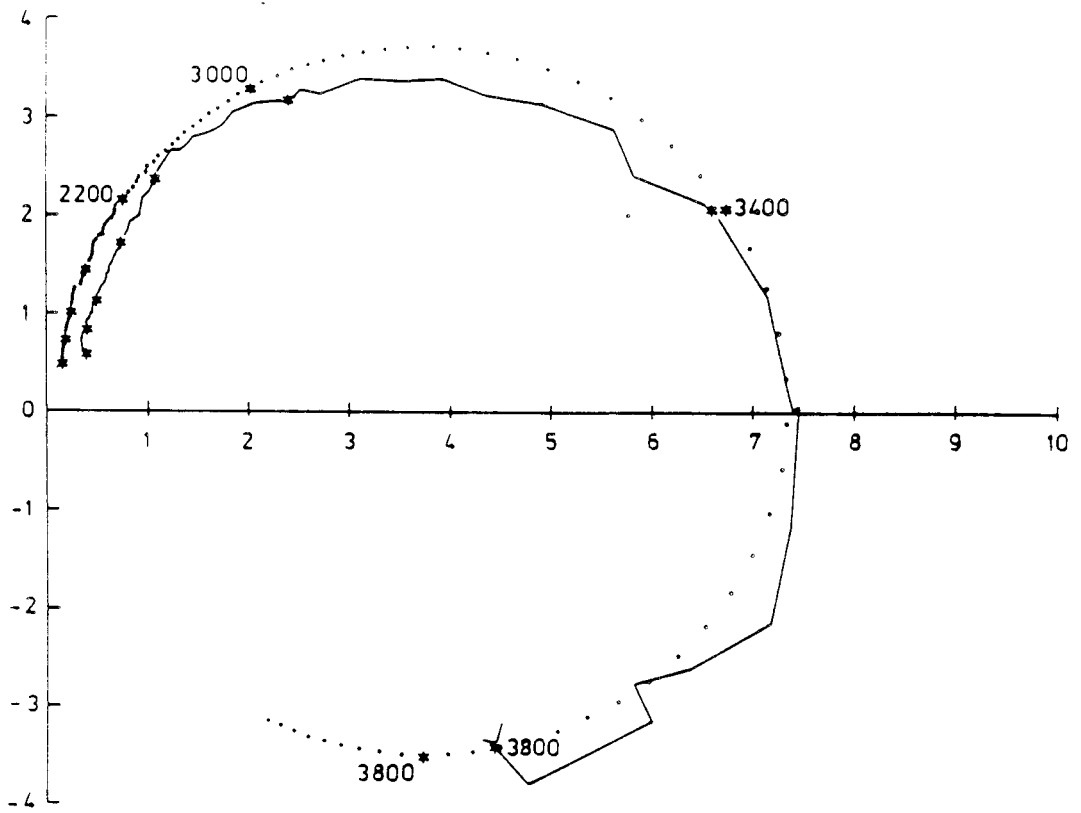


Fig. 4. Impedance values of open pipe protruding 191 mm into sand sediment (-). Calculated impedance curves employing Beranek model with  $k = 0.225$  and  $R_1 = 600,000$  (...)

BOTTOM INTERACTION  
OF LOW FREQUENCY ACOUSTIC WAVES  
IN THE NEW CALEDONIA BASIN

George V. Frisk,<sup>1</sup> Earl E. Hays<sup>1</sup> and Martin W. Lawrence<sup>2</sup>

<sup>1</sup> Woods Hole Oceanographic Institution  
Woods Hole, Massachusetts, USA 02543

<sup>2</sup> RAN Research Laboratory  
PO Box 706  
Darlinghurst, NSW, Australia 2010

In May 1983 an acoustic experiment was conducted in the New Caledonia Basin using the HMNZS Tui. The sea floor in this region is at a depth of 3200 m, is calcareous ooze, and is very flat. The acoustic experiment was performed in the vicinity of the Deep Sea Drilling Program Site 206.

The experiment consists of measuring the complex acoustic field (i.e. both amplitude and phase) from a single harmonic source, as the separation between source and receiver is varied. Both the source and the receiver are positioned near to the sea floor, so that (by pulsing the acoustic signal from the source) the reflection from the water surface may be gated out. The acoustic signal at the receiver is thus a combination of direct and bottom interacting energy.

In the New Caledonia Basin experiment the source, at frequency 220 Hz, was located at the water-sediment interface. The receiver was lowered from the ship until it was a few tens of metres from the sea floor. Due to drift of the ship, the receiver lowering path is at an angle to the vertical, and when the lowering ceases the receiver continues to move with respect to the source. Useful data (without interference from surface reflections) can be collected from approximately midwater depth (~1600 m) on the lowering and then throughout the horizontal drift, out to ranges approaching 10 km.

By means of high frequency pingers on the source, the receiver and the ship, measurements were made which allowed the geometry of the experiment to be estimated.

A number of lowerings and horizontal drifts were made, each with the source in the same location. The height of drift above the bottom was varied from one run to the next. The quality of the data collected depended on the drift rate of the ship, which in turn depended (mainly) on the wind strength. For 3 lowerings and 2 horizontal drifts, the rate of drift was  $\frac{1}{4}$  to  $\frac{1}{2}$  knots. It is these data sets which have been analysed most extensively

The geometry of the horizontal drifts is such that the receiver travels through the direct path shadow zone boundary. That is, the field is sampled in regions with illumination from both direct and bottom interacting paths and subsequently (at greater range) with illumination only from bottom interacting paths. The direct path shadow zone occurs because of the positive sound speed gradient in the water column near the sea floor.

Acoustic properties of the sea floor have been inferred by an indirect inverse technique. That is, a geoacoustic profile is assumed for the sea floor; this profile is used to generate a synthetic pressure field for comparison with the measured field. The geoacoustic parameters are then varied while searching for improved agreement between synthetic and measured pressure fields.

The synthetic fields have been generated by a ray theory technique which allows for spreading loss, refraction, reflection, absorption and some full wave effects such as corrected caustics and beam displacement.

The acoustic paths which dominate in producing the horizontal drift data are paths at small angles to the horizontal. Thus the horizontal drifts depend sensitively on the properties in the top hundred or so metres of the sediment pile. The lowering data, however, involves steeper ray paths and thus probes the sea floor to a greater depth. Spatial oscillation periods on the lowering data reveal reflector depths.

Geoacoustic data for this region can also be inferred by other means. During the Tui cruise single-trace seismic records were made and a core obtained. During the Deep Sea Drilling Program measurements were made as follows : sonobuoy refraction, core-sample sound speed, core density and seismic profiling. The geoacoustic parameters inferred by the technique described here are not inconsistent with those derived from other techniques, but in some areas are more restrictive of the possible parameter values.

The location of the source at the water-sediment interface has complicated the analysis. However this unique data set contains many interesting features. One of which is the reproduction from one lowering to the next of the same bumps and wiggles in the pressure field amplitude (from two lowerings that occurred along almost the same track).

GEOLOGICAL FACTORS IN MARINE GEOACOUSTIC MODELLING \*

Chris Jenkins

Ocean Sciences Institute,  
University of Sydney.

The aim of this contribution is to bring attention to some important geological controls on acoustic response patterns of the deep seafloor. Examples are drawn from the Tasman Sea east of N.S.W. A documentation of South-West Pacific and Australasian seafloor geology and geophysics - including geoacoustics - is being undertaken by the Ocean Sciences Institute at Sydney University and the examples presented here are currently a focus of research at the unit.

a. Bottom-current modification of sea-floor properties.

Geoacoustic properties can be strongly affected by the erosion and deposition due to bottom currents at abyssal depths. These currents are responsible for ripples and other (erosional) elements of bottom roughness, the seafloor exposure of lithified sediments and even basement in deeply eroded zones, and strong acoustic layering within thick sediment drifts. The pronounced variations in seafloor sonic velocity and density which are produced by current activity, are independent of the sediment compositions in an area (e.g. terrigenous or pelagic) and are not acknowledged in existing syntheses of typical velocity and density profiles for the deep sea.

The Tasman Sea is a virtual cul-de-sac for the global circulations at abyssal depths, but even so, bottom currents have been responsible for the strong modification of turbidite fans, the construction of

sediment drifts 500km in size, and locally the deep erosion of sediment cover. An economical means of defining the pattern of bottom-current effects in such a basin is through a seismic interpretation of near-surface (late Neogene) stratigraphy at 10-200 Hz frequencies (Fig. 1). For most of the Tasman Sea good seismic cover exists and this has allowed erosional/depositional provinces under the abyssal circulation to be defined. Geoacoustic properties are expected to show good correlation with those provinces, with raised sonic velocities ( $V_p$ ) and densities, and considerable surface roughness in eroded zones, but low  $V_p$  and densities on active sediment drifts and pelagic-drape areas.

#### b. Bottom Roughness.

The scattering of sound by sediment-surface roughness elements is crucial to attenuation studies. Roughness reflects a host of surface sedimentary, tectonic and biological elements. For example, on turbidite fans, sediment distributary channels, channel levee-banks, large flute-scours, hummocky sediment waves and ripples contribute to a definite gradient of roughness which decreases with distance away from source points for the sediments - the openings of submarine canyons (Figure).

On a finer scale relevant to frequencies at 1-5kHz, the mounds built by burrowing animals cause appreciable scattering in pelagic and turbidite areas (Figure).

#### c. Sediment trends: grainsize and composition.

As shown by Hamilton (1980) and others, the acoustic impedance, sonic velocity, attenuation factors and burial characters of a sediment are statistically related to its composition and grainsize which in turn undergo systematic changes across any continental margin and ocean basin.

The nature of surface sediment changes across the Tasman Sea and Australian margin is shown in a west-east transect offshore of N.S.W. at 30-32° S latitude (Figure). Grainsize trends on terrigenous sediments, characters of the pelagic carbonates and the influence of deep-water dissolution on the foram fraction (and therefore grainsizes) are available from this transect.

d. Sonic properties with depth in nanno/foram oozes.

In spite of the simplicity of the main chemical system involved (CaCO<sub>3</sub>/MgCO<sub>3</sub>), it remains a difficult problem to predict sound velocities inside thick calcareous ooze sequences. In the Australasian region where submerged platforms accumulating this type of ooze are common (e.g. the Lord Howe Rise), characterizing the V<sub>p</sub> and densities with depth as ooze changes to chalk then limestone, is an important marine geoacoustical problem.

The Deep Sea Drilling Project provides excellent data on sonic properties through many thick carbonate ooze sequences close to Australia, including some obtained with modern, continuous, low-disturbance hydraulic piston-coring. It is apparent that in each case (see Fig. 2) little change in V<sub>p</sub> or densities takes place for the first 200-500m, and that little else besides gravitational compaction is at work. Laughton (1954) with Nafe & Drake (1963), proposed that here,  $V_p = 0.44\sqrt{z+1.65}$  where V<sub>p</sub> is the compressional sound velocity and z the depth of burial.

In every case following this regular zone, dramatic and erratic changes to V<sub>p</sub> and density set in which must be due to some other processes. This change is measured at widely varying depths at different D.S.D.P. sites and furthermore, is not easily correlated to

the visually observed changes from ooze to chalk in the cores. A detailed explanation for the change and a system where its level can be predicted is the goal of recent efforts in this field. Broadly speaking the level corresponds to dissolution and cementation events through the stratigraphy. Below it strong acoustic reflections form through these chemical changes.

A current O.S.I. study is investigating the roles of latitude, ooze texture, palaeo-water-depths, overburden pressures and sediment chemistry as controls on the depth of this geoacoustically important level. Results so far suggest that  $MgCO_3$  and  $SiO_2$  appear to retard and accelerate respectively the onset of cementation with depth, and that the two components might be in turn determined by latitudinal controls on foram/nannoplankton/radiolarian ratios.

#### e. High Sonic Velocity Units Surrounding Seamounts.

Seamount peaks have an effect on seafloor acoustic properties which can extend for many times the radius of the peak itself. Volcanic materials with high sonic velocities, high attenuations and great roughness may spread from seamounts for up to 100 km at the time of eruption as units of basalt, tuff and intrusive basalts or gabbros. Even after they become buried in the seafloor sedimentary sequence they can serve as special high-velocity sound channels over wide areas. In another variation, moat scouring around the seamount base by deep currents which intensify around the peak, may leave this volcanic apron actually exposed for wide areas (20 km) surrounding the seamount.

In the Tasman Sea, the Derwent-Hunter seamount of about 15 m.y. age shows these features to advantage (Figure). The tapering unit of volcanics now buried, shows classic features, with proximal to distal changes from a thick, rough, lava-bearing unit, to well stratified

sand-silt-clay grade ashes further away. Sonic velocities in the ashes are probably high because of mineral alterations. Rough sill-like (horizontal) intrusives, very probably with acoustic velocities of 4-6 km/sec are featured inside the pre-volcanic pelagic sequence. Current-scour moating is evidenced east of the mount.

\* The author will be at sea during December and this paper is presented as a display at the conference.

O.S.I. reports of interest.

Beavis, A.R. & Jenkins, C.J. 1984. Bottom photography in the Tasman Sea. Cook 1-84 SEAMAP cruise.

Hubble, T.C.T. & Jenkins, C.J. 1984. Sediment cores from the N.S.W. continental slope off Port Stephens, Port Macquarie and Coffs Harbour (31\*-33\*S).

Jenkins, C.J. 1984. A geoacoustic model of the continental slope of northern N.S.W. at 31\*S latitude, and of the Derwent-Hunter Seamount, 31\*S, 156\*E.

Jenkins, C.J. 1984. Erosion and deposition at abyssal depths in the Tasman Sea. A seismic-stratigraphic study of the bottom-current patterns.

Packham, G.H. 1983. Morphology and acoustic properties of the N.S.W. slope with special reference to the Coffs Harbour - Point Plomer and Montague Island - Green Cape areas.

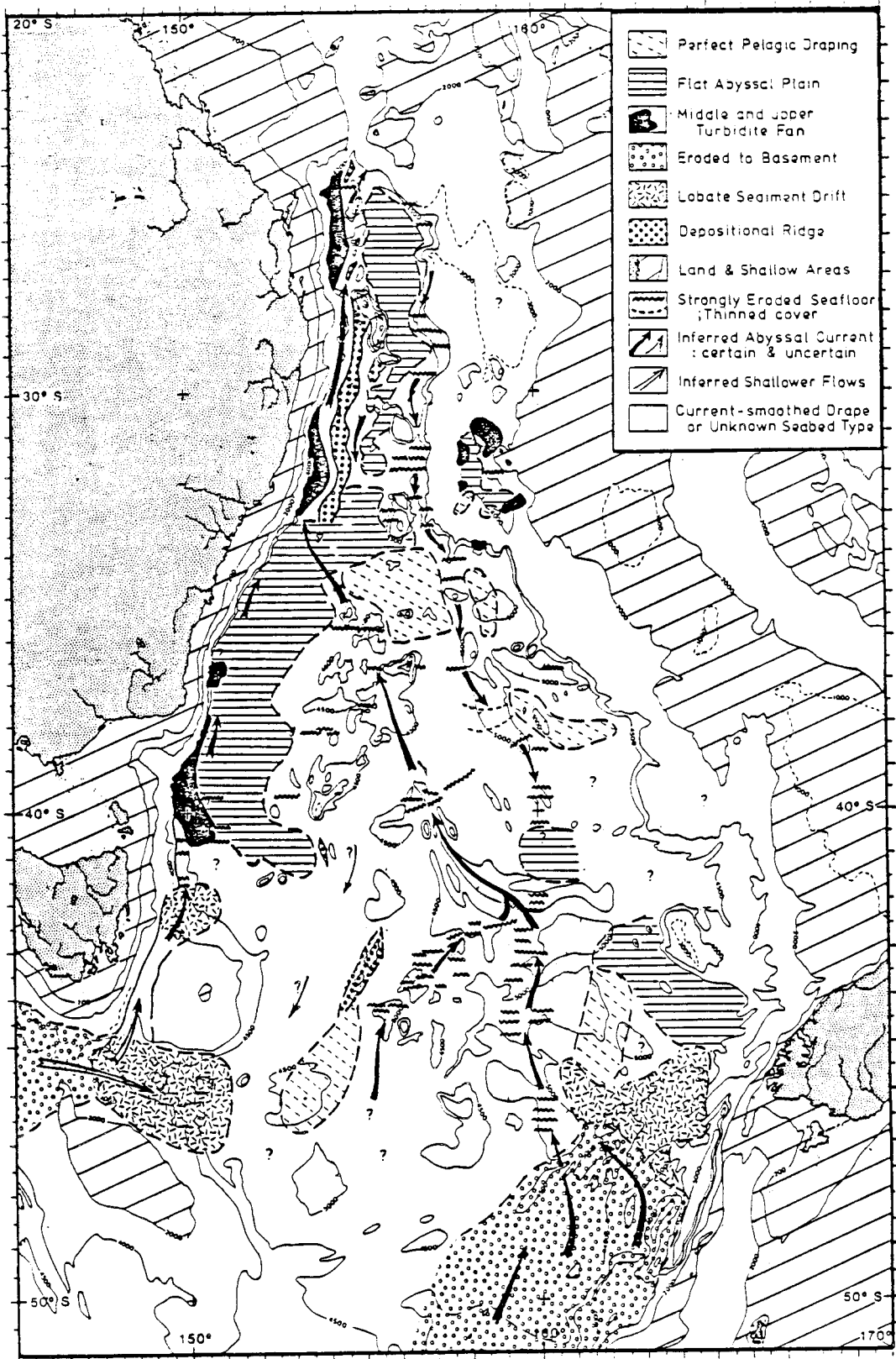


FIGURE 1. Deep ocean environments and bottom-currents, Tasman Sea; based on seismic interpretation of the late Neogene.

D.S.D.P. 289

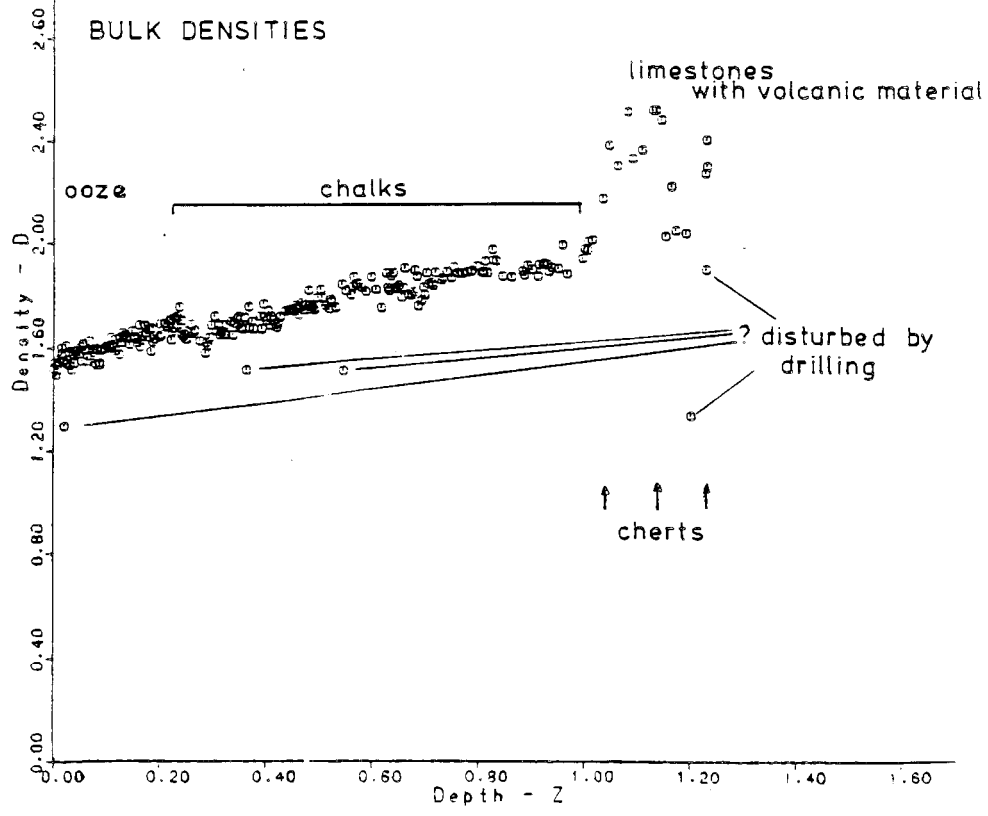
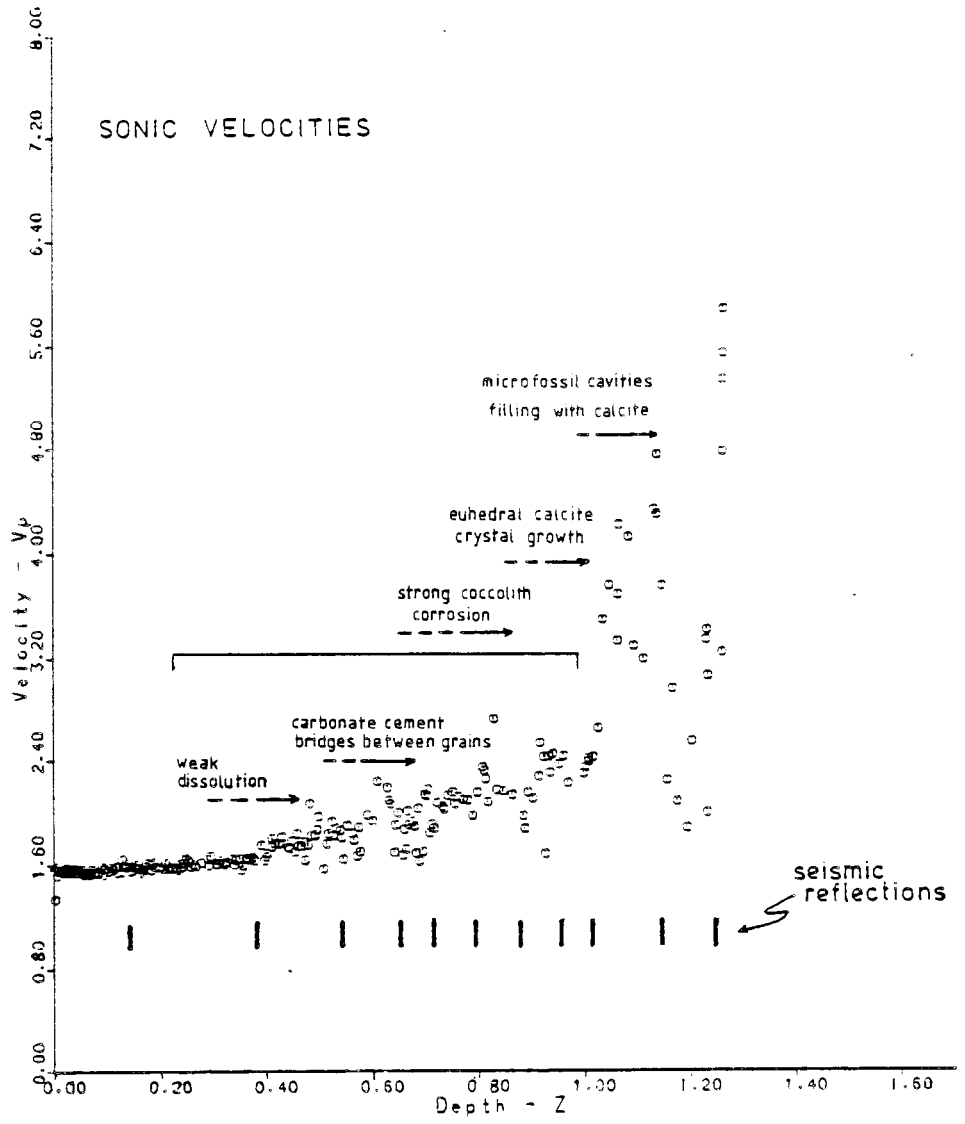


FIGURE 2. Aspect of sonic velocity & density logs, DS0 289, Ontong Java Plateau.

## Coupling Characteristics Between Two Underwater Acoustic Ducts

by

M. A. Pedersen, D. F. Gordon and D. Edwards

Naval Ocean Systems Center

San Diego, CA 92152

The major objective of this paper is to determine optimum propagation conditions for two adjacent refractive underwater acoustic ducts, subject to the constraint that the source must be located within the upper duct and the receiver within the lower duct. We will refer to this configuration as cross-duct propagation as opposed to in-duct propagation where both source and receiver are located in the same duct. The two refractive ducts have different axial sound speeds and different shapes. There is a relative maximum in sound speed between the ducts, which acts as a barrier to cross-duct propagation. The chief investigative tools are the numerical and analytic results of normal mode theory. However ray theory is used as well to assist in the analysis. The theoretical model of the sound speed profile is a piecewise function of the form of Eq. (1a). Here  $Z_i$ ,  $C_i$  and  $\gamma_i$  represent respectively the interface depth, sound speed and sound speed gradient at the top of layer  $i$ .

The most important parameter in the investigation of coupling between ducts is the phase velocity which is addressed in Eqs. (1) to (6). The phase velocity of normal mode theory is given by Eq. (1), where  $\lambda_n$  is the wave number for mode  $n$  and is obtained by iterating the eigenvalue equation. Initial values for starting this iteration may be obtained from Eq. (2), where the  $C_{mn}$  are roots of the phase integral equation of ray theory given by Eq. (3). Here  $\tilde{R}$  and  $\tilde{T}$  are the cycle range and associated travel time respectively, while  $E_b$  and  $E_s$  are both  $\pi/2$  for our application. Equations (4) to (6) present the closed form solution to Eq. (3) for a single refractive duct. Here  $C_a$  is the axial sound speed while  $\gamma_{1a}$  and  $\gamma_a$  are slopes at the axis for the upper and lower branches respectively. Equation (4) is used to generate two sets of  $C_{mn}$  --one for each single duct. These two sets provide good approximations to the mode eigenvalues for the double duct configuration, although the mode number  $n$  of Eq. (1) for the double duct is not the same as the  $n$  of Eq. (6).

Plots of Eq. (4) as a function of frequency for each of the two single ducts are in reasonable agreement with the normal mode results of Eq. (1) as obtained by iterating the eigenvalue equation for the double duct configuration. The major difference occurs at frequencies where the results of Eq. (4) for one duct cross the results for the other duct. A detailed examination shows that the results of Eq. (1) for adjacent modes never cross

each other but veer away from each other after forming a point of closest approach. The case of greatest interest for our particular sound speed profile is that of modes 2 and 3 in which the phase velocities approach within 0.17259 m/s of each other at a frequency of 54.43 Hz.

Now the frequencies of maximum cross-duct propagation can be associated with the frequencies of closest approach for adjacent modes. However we need to develop a rigorous numerical measure of cross-duct propagation as follows in Eqs. (7) to (13).

Equation (7) is the standard expression for the propagation loss with coherent summation of modes, where the depth functions are indicated in Eq. (8). Equation (9) presents the propagation loss for mode  $n$ . In our applications the last term of Eq. (9) may be ignored, because our modes are strongly trapped with insignificant damping. Equation (10) presents the first term of Eq. (9). In Eq. (11) the depth function is maximized for a source in the upper duct, while in Eq. (12) the depth function is maximized for a receiver in the lower duct. The desired result is Eq. (13), the duct coupling function, which in essence is Eq. (10) for optimum source and receiver depths.

The duct coupling function of Eq. (13) was evaluated numerically for frequencies from 20 to 90 Hz for modes 1 to 8. The most significant feature of this evaluation are relative minima which occur for modes 2 and 3 at respective frequencies of 53.34 and 53.23 Hz. The minimum loss associated with mode 3 is about 1 dB less than that for mode 2. Thus we chose 53.23 Hz as a frequency to evaluate for optimum cross-duct propagation. For comparison purposes we also chose to evaluate a frequency of 64 Hz. At this frequency the most important mode is mode 6 for which the value of  $H_{noM}$  is about 13 dB greater than that for the mode 3 minimum at 53.23 Hz.

At the critical frequency (53.23 Hz) the phase relationship between the depth functions of modes 2 and 3 plays an important role. When both source and receiver are in the upper duct these depth functions are in phase. However when the source is in the upper duct and the receiver is in the lower duct the phase differs by  $\pi$  radians. The consequences of this are best illustrated by Eqs. (14) to (18). Equation (14) is an expression for the coherent addition of modes  $n-1$  and  $n$ . In our application  $H_{no}$  is taken as  $H_{noM}$  for mode 3. Equation (15) represents a modulation term and is equivalent to the cosine law of elementary trigonometry. Equation (16) is in essence the ratio of mode amplitudes. Equation (17) represents the phase difference between the modes at zero range. Equation (18) is the mode interference distance which may be expressed in terms of the phase velocities of adjacent modes and the frequency. For our example this distance is 223.8 km. Thus critical ranges are given by multiples of 111.9 km. For cross-duct propagation, Eq. (14) predicts minimum losses at odd multiples of 111.9 km and

maximum losses at even multiples. For in-duct propagation the minima and maxima occur at even and odd multiples respectively.

The propagation loss of Eq. (7) was then evaluated out to a range of 400 km for both cross-duct and in-duct configurations. The first 23 modes were summed as these represent all the trapped modes for the double duct structure. Comparisons were made between these detailed evaluations and the results of Eq. (14) and showed excellent agreement. The propagation characteristics are essentially determined by the interference pattern between modes 2 and 3 with the contributions of the remaining 21 modes producing a rapid perturbation about the result of Eq. (14).

In addition a propagation loss contour plot was generated by evaluating Eq. (7) for 41 receiver depths from 5 to 1000 m. The range interval of 80 to 140 km was chosen to bracket 111.9 km where cross-duct propagation is enhanced and in-duct propagation is suppressed. The propagation losses for receivers in the upper duct generally exceed 90 dB. The smallest propagation losses are less than 80 dB, occur for receivers in the lower duct, and are centered near the antinodes of the depth function of mode 3. These contour plots confirm our analysis. The propagation at 53.23 Hz is dominated by mode 3 with mode 2 producing a modulation with a period of 223.8 km, and the remaining modes producing a relatively minor perturbation.

The final step in the analysis was the evaluation of propagation loss at 64 Hz. Here 27 modes were coherently summed. The propagation loss for cross-duct propagation was more than 10 dB greater than that for in-duct propagation for ranges from 0 to 400 km. A contour plot was also generated for the range interval from 80 to 140 km. The plots indicate little evidence of cross-duct propagation. The acoustic field for receivers in the lower duct can be associated with the convergence zone structure formed by steep-angle rays which form an apex in the upper layer of the duct and a nadir in the lower layer of the lower duct. The acoustic field for receivers in the upper duct is dominated by low-angle energy which is confined to the upper duct. However this field has range periodic bursts of modulation that can be associated with the convergence zone structure.

In conclusion there is little coupling between two ducts except for frequencies where the eigenvalues of adjacent modes approach each other. At these critical frequencies there is a range periodic transfer of energy back and forth between the ducts, with the period determined by the frequency and the difference in phase velocity between the adjacent modes. Ray theory provides good starting values for eigenvalue iteration and enables one to interpret normal mode results associated with the convergence zone structure. However the cross-duct coupling phenomenon at 53.23 Hz is beyond the pale of simple ray theory.

$$C^{-2} = C_i^{-2} - 2\gamma_i C_i^{-3} (Z - Z_i). \quad (1a)$$

$$C_{pn} = \omega / \text{Re } \lambda_n. \quad (1)$$

$$\text{Re } \lambda_n = \omega / C_{mn}. \quad (2)$$

$$\omega(\tilde{T}-\tilde{R}/C_m) = E_b + E_s + (n-1) 2\pi. \quad (3)$$

$$C_{mn} = C_a(1-f^{-2/3}\gamma)^{-1/2}, \quad (4)$$

$$\gamma = \gamma_n(\gamma_a^{-1} + |\gamma_{1a}|^{-1})^{-2/3}, \quad (5)$$

$$\gamma_n = [3(n-1/2)/2]^{2/3}. \quad (6)$$

$$H = -20 \log \left| \sum_n H_0^{(2)}(\lambda_n r) U_n(Z, Z_s) \right| - 20 \log \pi. \quad (7)$$

$$U_n(Z, Z_s) \equiv U_n(Z) U_n(Z_s) / D_n. \quad (8)$$

$$H_n \approx H_{no} + 10 \log r + 8.686 \text{Im } \lambda_n r. \quad (9)$$

$$H_{no} = -20 \log |U_n(Z, Z_s)| + 10 \log |\lambda_n| - 7.98. \quad (10)$$

$$|U_{nM}(Z)| \equiv \text{MAX}_{Z_s} |U_n(Z, Z_s)|, \quad Z_s \text{ in upper duct.} \quad (11)$$

$$|U_{nmM}| \equiv \text{MAX}_Z |U_{nM}(Z)|, \quad Z \text{ in lower duct.} \quad (12)$$

$$H_{noM} = -20 \log |U_{nmM}| + 10 \log |\lambda_n| - 7.98. \quad (13)$$

$$H_c = H_{no} + 10 \log r - 10 \log M_o. \quad (14)$$

$$M_o = 1 + \beta^2 + 2\beta \cos(\Delta\theta + 2\pi r/R_{n, n-1}). \quad (15)$$

$$\beta = (C_{p, n-1}/C_{pn})^{1/2} |U_{n-1}(Z, Z_s)| / |U_n(Z, Z_s)|. \quad (16)$$

$$\Delta\theta = \arg \{ U_{n-1}(Z, Z_s) \} - \arg \{ U_n(Z, Z_s) \}. \quad (17)$$

$$R_{n, n-1} = 2\pi(\text{Re } \lambda_n - \text{Re } \lambda_{n-1})^{-1} = C_{pn} C_{p, n-1} / f(C_{pn} C_{p, n-1}). \quad (18)$$

Comparison Between the North and South  
Pacific Oceans of Acoustic Propagation  
in Secondary Sound Channels

David G. Browning  
New London Laboratory - Code 3331  
Naval Underwater Systems Center  
New London, CT 06320 U.S.A.

Introduction

It is well-known that a deep sound channel (DSC) exists throughout the major ocean basins, allowing long range sound propagation via totally refracted paths. For some practical applications, however, the axis of this channel may be too deep (typically 1000 meters) to be fully utilized. Secondary sound channels (SSC), although generally less robust and extensive, occur at shallower, more readily accessible depths. In many ocean regions secondary sound channels can be used to advantage at frequencies above 100 Hz. This paper describes the relative importance of each of the principal secondary sound channel generation mechanisms for both the North Pacific and South Pacific Oceans.

Principal Causes of Secondary Sound Channel Formation

There appear to be three principal causes of secondary sound channel formation in the Pacific Basin: water mass intrusions, circulation instabilities, surface layer/temperature inversions. The circulation in a large basin can cause a water mass to displace or intrude into an adjacent water mass. Such an intrusion can result in a relatively strong and stable secondary sound channel formation. Swifter currents can churn globs of water, circulation instabilities, into the adjoining water mass forming weaker and less stable secondary sound channels. The third mechanism does not depend on circulation but rather on a net influx of freshwater due to precipitation or continental run-off. This results in a strengthened mixed surface layer which can produce a secondary sound channel or half-channel.

Water Mass Intrusion

A large counter-clockwise circulation gyre covers the entire South Pacific Ocean. Cold water, with a shallow sound channel axis, flows from the Antarctic Circumpolar Current northward up along the South American coast displacing subtropical water which has a deep sound channel axis. Away from the coast, however, the cold water only intrudes into the subtropical water, resulting in a secondary sound channel formation throughout a large area of the South Pacific. Although only limited data exists, this SSC formation appears to be a permanent feature. To a lesser extent, this same situation occurs along the edge of the Antarctic

Circumpolar Current. This mechanism does not seem to be prevalent in the North Pacific Ocean because the main circulation gyre extends from the equator to only 40° North latitude thus denying itself to cold Arctic water.

### Circulation Instabilities

Secondary sound channels caused by circulation instabilities occur along the continental margins of both the North and South Pacific Oceans, where strong boundary currents and freshwater outflows occur. They can be numerous but are usually weak and of short duration- both in time and space.

### Surface Layer/Temperature Inversion

During winter most ocean areas have a surface mixed layer due to the action of storms. This results in a half channel (or surface duct). If the region generally has more freshwater influx (precipitation, run-off) than evaporation, this surface layer becomes a permanent feature as a reduced salinity mixed layer, isolated from the rest of the water column by a strong halocline directly beneath it. In the high rainfall areas of the North and South Pacific near the equator this results in a secondary half-channel year round. This mechanism again is dominant in the subarctic regions (Abundant rainfall, low evaporation), which comprise a much larger area in the North Pacific, the entire area above 40° North latitude, than in the South Pacific. In the subarctic region, although the mixed reduced salinity layer persists through the summer, a temperature gradient develops due to surface heating. This gradient does not extend to the bottom of the layer, however leaving a temperature inversion there and producing a full secondary sound channel.

### Summary

The dominant secondary sound channel mechanism in the South Pacific Ocean is water mass intrusion. This results in a large region with a SSC axis depth of 500 meters over a DSC with an axis at 1000 meters.

In the North Pacific the dominant mechanism is surface layer/temperature inversion occurring throughout a large subarctic region. Here the SSC axis depth is approximately 100 meters, overlaying a DSC whose axis varies from less than 200 to over 400 meters.

### References

1. Ewing, M. & Worzel, J.L., Geol. Soc. Am. Mem. 27, 1-15 (1948).
2. Browning, D. G., Bannister, R. W., Denham, R. N., Guthrie, K. M., Nature 282 (5741), 820-822 (1979).

3. Kibblewhite, A. C., Shirtcliffe, T. G., Stanton, B. R., J. Acoust. Soc. Am. 62, 308-319 (1977).
4. Bannister, R. W., Browning, D. G., Denham, R. N., Guthrie, K. M., Kibblewhite, A. C., J. Acoust. Soc. Am. 55, 417(A), (1974).
5. Roden, G. I., J. Geophys. Res. 69, 2899-2914, (1964).
6. Dodimead, A. J., Favorite, F., Hirano, T., Int. Nor. Pac. Fish. Comm. Bul. 13, (1962).
7. Chow, R. K., Browning, D. G., J. Acoust. Soc. Am. 72, S57(A), (1982).
8. Dunlap, C. R., Browning, D. G., Powell, J. W., J. Acoustic Soc. Am. 76, S84(A), (1984).

Modelling ocean acoustic propagation with a wide-angle  
parabolic equation method

N.R. Chapman and D.J. Thomson  
Defence Research Establishment Pacific  
Victoria, B.C., Canada

Abstract

We present in this paper a comparison between long range propagation loss data and model predictions obtained using a new wide-angle parabolic equation. The wide-angle approximation provides a better representation of the Helmholtz equation, and the method retains the use of the split-step marching algorithm. Also, the new equation is less sensitive to the reference wavenumber. The comparison with the data indicates that the wide-angle model predictions are in very good agreement with the measurements, and provide a significant improvement over the predictions based on the standard parabolic equation.

Introduction

Numerical predictions based on the parabolic approximation for the acoustic wave equation provide the capability for modelling low-frequency sound propagation in range-dependent ocean environments.<sup>1,2</sup> This capability arises because the parabolic equation (PE) is first order in range and can be solved efficiently by noniterative numerical marching algorithms. A particular technique, the split-step algorithm,<sup>2</sup> which is based on split operator and discrete Fourier transform methods, has received widespread use. Two conditions are necessary for the validity of the parabolic approximation: 1) local variations in the acoustic index of refraction must be small, and 2) propagation to long ranges must be dominated by small-angle rays. Even for ocean environments that support these conditions however, the parabolic approximation introduces errors in the phase velocity of the propagating normal modes.<sup>3</sup> These errors are intrinsic to the approximations underlying the PE method and lead to inaccuracies in modelling long range propagation.

We have recently introduced a wide-angle parabolic approximation that provides a better representation of the Helmholtz equation.<sup>4,5</sup> This approach extends the standard PE method to include wide angles of propagation and in addition retains the use of the split-step marching algorithm to advance the solution in range. The capability for correctly modelling wide angles is important for making predictions in range-dependent environments where, for instance, interaction with a sloping bottom can generate steep angle reflections. The results of a simple error analysis and our numerical experience with test cases indicate that the wide-angle PE provides a significant improvement over the standard PE, even for conditions where the standard PE is assumed to be adequate.<sup>4</sup> In addition, since the new approximation is less sensitive to the reference wavenumber,  $k_0$ , it overcomes the problem encountered with the standard PE of choosing the best value of  $k_0$  by trial and error.

In this paper we present numerical predictions using the wide-angle PE for long range propagation in a range-dependent environment, and compare the results with measured propagation loss. We also demonstrate the sensitivity of both the wide-angle and the standard PE to the reference value of  $k_0$ . These results show that the wide-angle PE provides accurate model predictions for ocean acoustic propagation problems.

### The Wide-Angle Parabolic Equation

Let  $p(r,z)\exp(-i\omega t)$  represent the cylindrically symmetric, harmonic acoustic field for  $z>0$  of a coordinate system  $(r,\theta,\phi)$ . For  $r>0$  the pressure,  $p(r,z)$ , in the far field ( $k_0 r \gg 1$ ) due to a point source at  $r=0$ ,  $z=z_0$  can be determined from

$$\partial u / \partial r = ik_0 Q u \quad (1)$$

where  $p(r,z) = u(r,z)/r^{1/2} \quad (2)$

and  $Q = (1+\epsilon+\mu)^{1/2} \quad (3)$

with  $\epsilon = n^2 - 1 \quad (4)$

and  $\mu = \frac{1}{k_0^2} \frac{\partial^2}{\partial z^2} \quad (5)$

Here  $n(r,z) = c_0/c(r,z)$  is the acoustic index of refraction, and  $k_0 = \omega/c_0$  is a suitable reference wavenumber. While strictly valid only for layered (range-independent) media, equation 1 is regularly used to model propagation in range-dependent environments. The numerical implementation via the split-step algorithm requires that the square root operator  $Q$  be specified in such a way that cross products of  $\epsilon$  and  $\mu$  do not occur. This specification can only be made approximately, with different approximations leading to different parabolic equations.

The two approximations which we present take the form

$$Q_1 = 1 + 1/2(\epsilon + \mu) \quad (6)$$

and  $Q_2 = (1+\mu)^{1/2} + (1+\epsilon)^{1/2} - 1 \quad (7)$

Clearly, both these approximations lead to parabolic equations that are amenable to solution by the split-step Fourier algorithm. This feature does not hold true for the rational linear approximation for  $Q$  which forms the basis of wide-angle PEs solved by finite difference methods.<sup>6</sup> The approximation  $Q_1$ , which leads to the standard PE, is obtained by expanding  $Q$  in a Taylor series and truncating after the second term. Justification for dropping the higher order terms rests on the requirement that the norm  $|\epsilon + \mu|$

is in some sense small. This leads to the interpretation that  $Q_1$  is suitable for small angles of propagation and small variations in  $n$ . The approximation  $Q_2$  is the wide-angle decomposition. The results of a simple error analysis show that although this approximation is restricted to small variations in  $n$ , there is no limitation to small angles.<sup>4</sup> The sensitivity to  $k_0$  can be compared for the two approximations using the differences  $E_i = Q^2 - Q_i^2$ ,  $i=1,2$  as error measures. For a single Fourier component of the field,  $u = \exp ik_0(r \cos \theta + z \sin \theta)$ , it follows that  $|\mu| = \sin^2 \theta$  and we obtain the error bounds

$$|E_1| \leq 1/4 [|\delta n| (2 + |\delta n|) + \sin^2 \theta]^2$$

and  $|E_2| \leq 2|\delta n| |\cos \theta - 1|$  .

Here we have set  $n=1+\delta n$  and assumed  $\delta n$  to be a constant. Expressing  $n$  in terms of the deviation about  $k_0$ ,  $n = 1 + \delta k/k_0$ , we can associate  $|\delta n|$  with  $|\delta k/k_0|$ , or  $|\delta c/c_0|$ . The errors are plotted vs  $\delta c/c_0$  in Figure 1; it is evident that the wide-angle approximation is less sensitive to the reference wavenumber for realistic ocean conditions.

For numerical implementation of  $Q_2$  we make the envelope transformation,

$$u(r,z) = \Psi(r,z) \exp ik_0 r, \quad (8)$$

and use the operator identity

$$(1+\mu)^{1/2} = 1 + \frac{\mu}{1+(1+\mu)^{1/2}}, \quad (9)$$

to obtain the wide-angle PE

$$\frac{\partial \Psi}{\partial r} = \frac{ik_0 \mu \Psi}{1+(1+\mu)^{1/2}} + ik_0(n-1)\Psi \quad (10)$$

For small angles ( $|\mu| \ll 1$ ) equation 10 reduces to

$$\frac{\partial \Psi}{\partial r} = \frac{1}{2k_0} \frac{\partial^2 \Psi}{\partial z^2} + ik_0(n-1)\Psi \quad (11)$$

This equation exhibits the same angle dependence as the split operator  $Q_1$ , but differs in the form of the refracting term which is given by  $ik_0(n^2-1)/2$  for the standard PE. Also, for uniform media ( $n=1$ ) the wide-angle PE gives an exact representation of the Helmholtz equation; note that this is not true for the standard PE. As discussed elsewhere however, the improvement provided by the wide-angle PE depends on both terms on the right hand side of equation 10 and not just the angle-dependent term.<sup>4</sup> Application of

split-step Fourier methods to solve equation 10 is straightforward, and the implementation correct to  $O(\Delta r^2)$  is given by

$$\Psi(r+\Delta r, z) = \exp\left(\frac{iA\Delta r}{2}\right)\exp(iB\Delta r)\exp\left(\frac{iA\Delta r}{2}\right)\Psi(r, z) \quad (13)$$

where

$$A = \frac{\partial/\partial z^2}{(k_0^2 + \partial/\partial z^2)^{1/2} + k_0} \quad (14)$$

and

$$B = k_0(n-1) \quad (15)$$

#### Comparison with Measured Propagation Loss

The measurements presented for comparison with the wide-angle PE predictions were obtained with small explosive charges during an experiment in the Northeast Pacific Ocean involving DREP and a number of US defence laboratories.<sup>7</sup> The sound speed profiles measured during the experiment and the bathymetry are shown in Figure 2. This ocean environment was used to obtain the model predictions. The wide-angle PE prediction (solid curve) is compared to the data in Figure 3; the agreement with the measurements is clearly very good, with accurate representation of the convergence zones out to very long ranges. Comparison with the prediction based on the standard PE (broken curve) illustrates that the wide-angle PE provides an improvement even for an ocean environment where long range propagation is dominated by shallow-angle rays.

#### References

1. F.D. Tappert, "The parabolic approximation method" in Wave Propagation and Underwater Acoustics, edited by J.B. Keller and J.S. Papadakis (Springer-Verlag, New York, 1977).
2. R.H. Hardin and F.D. Tappert, "Applications of the split-step Fourier method to the numerical solution of non linear and variable coefficient wave equations", SIAM Rev 15 (423) (1973).
3. S.T. McDaniel, "Propagation of normal modes in the parabolic approximation", J. Acoust. Soc. Am. 62 (307-311) (1975).
4. D.J. Thomson and N.R. Chapman, "A wide angle split step algorithm for the parabolic equation", J. Acoust. Soc. Am. 74 (1898-1854) (1983).
5. M.D. Feit and J.A. Fleck, "Light propagation in graded-index fibers", Appl. Opt. 17, 3990-3998 (1978).
6. J.F. Claerbout, "Fundamentals of Geophysical Data Processing", p. 206, McGraw-Hill, New York, 1976.
7. R.K. Chow and R.G. Turner, "Attenuation of low-frequency sound in the Northeast Pacific Ocean", J. Acoust. Soc. Am. 72, 888-891 (1982).

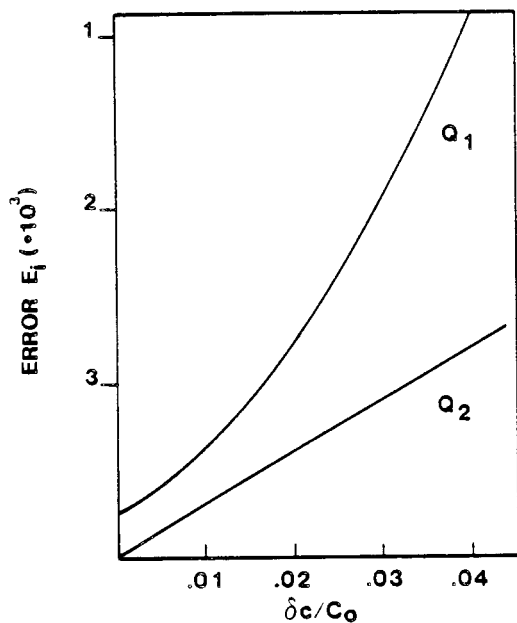


Figure 1. Error bounds  $|E_1|$  and  $|E_2|$  versus  $|\delta c / c_0|$  for the two square root approximations  $Q_1$  and  $Q_2$ .  $\epsilon = 10^0$ .

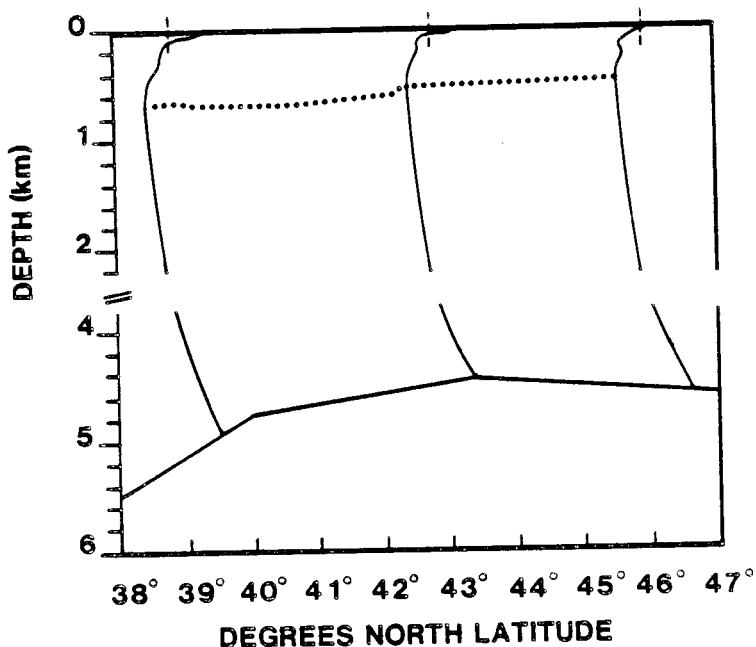


Figure 2. Measured sound speed profiles and average bathymetry for the experiment. The broken line in the profiles represents  $c = 1500$  m/s, and the sound speed minima (dotted curve) are roughly 1470 m/s.

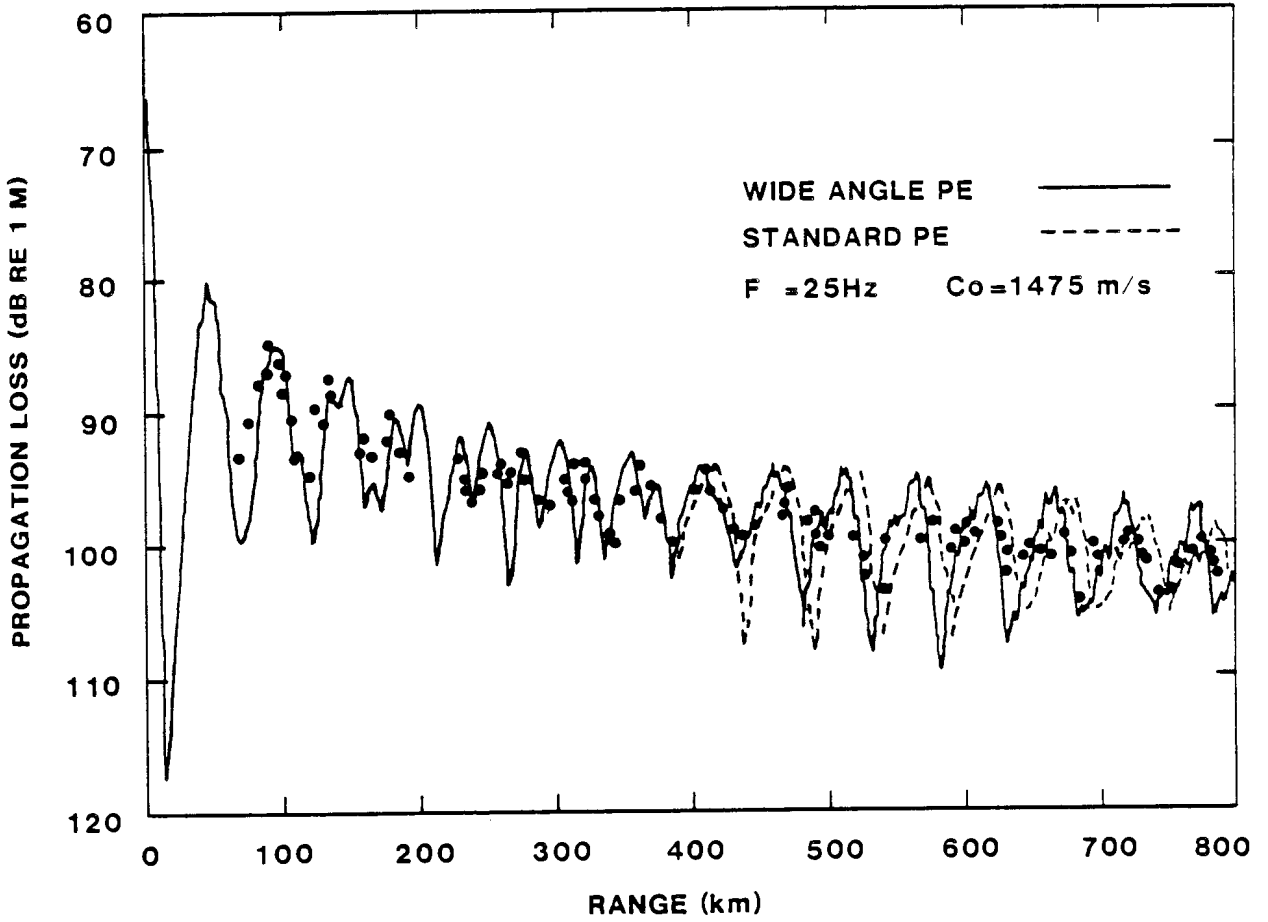


Figure 3. Wide-angle (-) and standard (---) PE predictions at 25 Hz with  $c_0 = 1475$  m/s, and source/receiver depths of 91 m/400 m. The measurements (closed circles) are 1/3 octave band averages at 25 Hz.

"Numerical simulation of wave propagation in a randomly varying medium"

C. Macaskill, Department of Applied Mathematics, University of Sydney  
and

T.E. Ewart, Applied Physics Laboratories, University of Washington, U.S.A.

## §1. Introduction

When sound is transmitted in the deep ocean at frequencies greater than a few hundred hertz it is found that significant fluctuations are observed in the signal over transmission ranges of a few kilometres or more. It is thought that for rays that do not intersect either the surface or the sea bottom, most of this variability is due to the presence of internal waves in the ocean. The internal waves, with typical horizontal scales of a few kilometres, vertical scales of a few hundred metres, and time scales of the order of a few hours, give rise to space and time fluctuations of the temperature field, and hence of the speed of sound, or refractive index. The propagating sound field thus encounters a randomly varying medium and it is the interaction of the sound with the medium that gives rise to the observed fluctuations.

In addition to the random variations of sound speed described above, there is also present in the ocean a mean sound channel which can cause bending of the ray paths and associated deterministic variations of intensity. For the acoustic frequencies being considered here, such problems, in the absence of a random component of refractive index, can be treated using the parabolic equation method. In this paper it is proposed that parabolic equation methods can be extended to take into account random fluctuations. The general approach is to solve the parabolic problem for a sequence of realizations of the random medium and then to average over these realizations to obtain predictions for the mean intensity  $\langle I \rangle$ , or the mean squared intensity  $\langle I^2 \rangle$  or indeed for the probability distribution of intensity, when both channelling and random variability are important. This idea is not new: Flatté and Tappert (1975) employed similar concepts. However, there is now a better understanding of the propagation problem in the presence of fluctuations (e.g. Dashen, 1979, Uscinski, 1982) and so it is possible to test the numerical methods against theory, thus allowing the simulation method to be used with more confidence for situations where there are no theoretical results available.

## §2. Numerical Method

The parabolic equation for the envelope of acoustic pressure is

$$\frac{\partial p}{\partial x} = -\frac{i}{2k} \frac{\partial^2 p}{\partial z^2} - ikn_s(z)p - ik\mu Wp \quad (1)$$

where  $p = p(x, z, t)$ ,  $\mu W = \mu W(x, z, t)$  is the fluctuating part of the refractive index,  $n_s(z)$  is the deterministic refractive index variation and  $k$  is the wavenumber of the incident acoustic field.  $(x, y, z)$  are cartesian co-ordinates with  $x$  horizontal and  $z$  vertical. The  $y$ -dependence of  $p$  has been neglected as scattering angles are usually very small in the horizontal, relative to those in the vertical, due to the anisotropy of the internal wave field. There are no time operators in eqn. (1) because the time taken for sound to travel through the medium is so small in comparison with the time scales of internal waves.

It is convenient to rewrite eqn. (1) as

$$\frac{\partial p}{\partial X} = -\frac{i}{2} \frac{\partial^2 p}{\partial Z^2} - ik^2 L_V^2 n_s(Z L_V) p - ik^2 L_V^2 \mu W p \quad (2)$$

where  $Z = z/L_V$ ,  $X = x/kL_V^2$  with  $L_V$  the vertical correlation length of irregularities in the ocean. Equation (2) is a stochastic p.d.e. The split-step FFT algorithm of Tappert and Hardin (1974) or finite difference methods may be used to solve this equation numerically once a suitable technique has been obtained for dealing with the random term.

In Macaskill and Ewart (1984) a method is described where the randomly varying part of the medium is modelled as a sequence of phase-changing screens, statistically independent and with normalized correlation function,

$$f(\zeta) = \int_{-\infty}^{\infty} \rho(\xi, \zeta) d\xi / \int_{-\infty}^{\infty} \rho(\xi, 0) d\xi \quad (3)$$

with  $\mu^2 \rho(X_1 - X_2, Z_1 - Z_2) = \mu^2 \rho(\xi, \zeta)$  being the correlation function of refractive index fluctuations. The distance between the screens is then  $L_p$ , the integral horizontal correlation length, where

$$L_p = \int_{-\infty}^{\infty} \rho(\xi, 0) d\xi \quad (4)$$

The split-step algorithm can be used in the following way. Take  $X_\ell = \ell \Delta X$ ,  $\ell = 0, 1, \dots, M$ , and  $Z_j = (j-1 - N/2) \Delta Z$ ,  $j = 1, 2, \dots, N$  so that there are  $(M+1)$  mesh points in the horizontal and  $N$  in the vertical. Set  $\Delta x$ , the

distance between horizontal mesh points, equal to  $L_p$ . Let  $U_\ell(Z)$  be a realization of the process with correlation function  $f(Z_1-Z_2)$  and obeying Gaussian statistics, which is easily generated by a variety of techniques, so that  $U_\ell$  represents the random part of the medium between  $X_{\ell-1}$  and  $X_\ell$ . The phase modulation introduced by the medium, and diffraction effects, are considered separately, in the spirit of the split-step algorithm.

Assume the pressure at range  $\ell\Delta X$  is known and equal to  $p_\ell(Z)$ . Then,

$$\tilde{p}_\ell(Z_j) = p_\ell(Z_j)\exp[-ik_\mu L_p U_\ell(Z_j) - ik^2 L_V^2 n_s(Z_j L_V)\Delta X] \quad (4)$$

for  $j = 1, \dots, N$ , and eqn. (4) gives the phase modulation introduced by the medium as the sound travels a distance  $\Delta X$  from  $X_\ell$  to  $X_{\ell+1}$ . The pressure at the next range point,  $p_{\ell+1}(Z)$ , is then determined by FFT techniques from the solution of

$$\frac{\partial p}{\partial X} = -\frac{i}{2} \frac{\partial^2 p}{\partial Z^2} \quad (5)$$

over  $(X_\ell, X_{\ell+1})$ , with initial condition  $p = \tilde{p}_\ell$ . An initial condition  $p_0$  is required at  $X = 0$ . The solution procedure involves applying (4) and then (5) at each range step, so as to obtain  $p_1(Z)$ ,  $p_2(Z)$  and so on until the desired range  $X$  is reached. This process gives one realization of the random sound field.

Clearly  $\Delta X$  must be small enough so as to ensure minimal numerical error. But  $L_p$  is equivalent to  $\Delta X k L_V^2$ . The essence of the present method lies in the fact that so long as the random phase modulation introduced by a single slice of medium is small, i.e.  $k_\mu L_p \ll 1$ , then, for example, 20 screens of strength  $q$ , say, in a distance  $X$  give essentially the same ensemble averaged results for the propagating field as do 10 screens of strength  $2q$  in the same distance.

The complete algorithm is as follows. For some given initial distribution  $p$  at  $X = 0$  step out the sound field to the required range  $X$  using a given batch of independent screens with a suitable correlation function  $f(\zeta)$  and the appropriate form of the channelling term  $n_s$ . This procedure is then repeated, each time with a new batch of screens, and a running average of the moments of intensity, as a function of  $X$  and  $Z$ , is thus obtained. Error estimates are made by taking the standard deviation of any given quantity over the ensemble of realizations and dividing by the square root of the number of realizations.

### §3. Results

#### (i) Initially plane wave, no channelling.

In the absence of channelling, the propagating field is statistically homogeneous in the vertical and so averages may be taken over all points  $Z_j$ . This means that good estimates of the higher order moments of intensity  $\langle I^n \rangle$  may be obtained (in this case  $\langle I \rangle \equiv 1$  everywhere). In addition, the correlation function of intensity  $\langle I_1 I_2 \rangle$  may be obtained and comparisons made with approximate theoretical results (Uscinski, 1982, Macaskill, 1983). Results have been obtained for media with  $f(\zeta) = e^{-\zeta^2}$  (Gaussian) and with  $f(\zeta) = (1 + |\zeta|e^{-|\zeta|})$  (fourth order power-law spectrum). Good agreement is obtained. The higher order moments  $\langle I^3 \rangle$ ,  $\langle I^4 \rangle$ , etc. agree qualitatively with those found in experiments in optics and underwater acoustics but better modelling of the medium is required before more exact comparisons can be made.

#### (ii) Initial beam with channelling.

In this case an initial profile  $p = e^{-Z^2/2D^2}$  is taken, with  $D$  some characteristic scale of the sound source. The channelling term is included, with  $k^2 L_V^2 n_s(ZL_V) = -bZ^2$ , for example, for a parabolic channel, where  $b$  is a constant determining the strength of the channelling. All results have been obtained for a medium with a Gaussian correlation function. In these problems the mean intensity  $\langle I \rangle$  is an interesting quantity. For the case of a parabolic channel, the mean intensity in the presence of scattering can be predicted theoretically (Beran and Whitman, 1975). This exact result can be used to check the simulations and satisfactory agreement is found. The simulation method also gives results for more complicated channelling situations, where there are no exact solutions. As yet no accurate results have been obtained for the higher moments  $\langle I^2 \rangle$ ,  $\langle I^3 \rangle$ , etc. due to the excessive number of realizations required, as in this case averages over the vertical direction cannot be taken, since the mean intensity varies with  $Z$ .

### §4. Conclusion

The above results have demonstrated the viability of the simulation approach. The next step is to try to simulate realistic ocean scattering experiments, like those described in Ewart (1976) and Ewart and Reynolds (1984). This will necessitate changing  $f(\zeta)$  so that it more closely represents internal waves and also including the time variability of the ocean. Therefore each 'screen' will have to model a two-dimensional random function with the

correct space-time correlation function. Such a representation is easily obtained. The only real difficulty is the increase in the amount of computer time required, which will be directly proportional to the number of mesh points used in the time direction.

T.E. Ewart was supported by the Office of Naval Research, Code 422P0. C. Macaskill was supported by the Ministry of Defence (Procurement Executive).

## §5. References

- Beran, M.J. and Whitman, S.M. 1975 "Scattering of a finite beam in a random medium with non-homogeneous background", J. Math. Phys. 16, 214.
- Dashen, R. 1979 "Path integrals for waves in random media", J. Math. Phys. 20, 894.
- Ewart, T.E. 1976 "Acoustic fluctuations in the open ocean - a measurement using a fixed refracted path", J. Acoust. Soc. Am. 60, 46.
- Ewart, T.E. and Reynolds, S.A. 1984 "The Mid-Ocean Acoustic Transmission Experiment - MATE", J. Acoust. Soc. Am. 75, 785.
- Flatté, S.M. and Tappert, F. 1975 "Calculation of the effect of internal waves on oceanic sound transmission", J. Acoust. Soc. Am. 58, 1151.
- Macaskill, C. 1983 "An improved solution to the fourth moment equation for intensity fluctuations", Proc. R. Soc. Lond., Series A, 386, 461.
- Macaskill, C. and Ewart, T.E. 1984 "Computer simulation of two-dimensional random wave propagation", IMA Journal of Applied Mathematics 33, 1.
- Tappert, F.D. and Hardin, R.H. 1974 *Proceedings of the Eighth International Congress on Acoustics*, Vol. II, p. 452. London: Goldcrest.
- Uscinski, B.J. 1977 *The Elements of Wave Propagation in Random Media*. New York: McGraw-Hill.
- Uscinski, B.J. 1982 "Intensity fluctuations in a multiple scattering medium. Solution of the fourth moment equation", Proc. R. Soc. Lond., Series A, 380, 137.

## INTENSITY DECAY LAWS FOR NEAR-SURFACE SOUND SOURCES IN THE OCEAN

by

R N Denham

Defence Scientific Establishment, Ministry of Defence,  
Auckland Naval Base Post Office, Auckland, New Zealand.

The formulae derived for the acoustic intensity decay with range in shallow water by Marsh and Schulkin<sup>1</sup> and Weston<sup>2</sup> have been adapted to describe the intensity-range variation in several deep water situations. The modified equations take account of the surface decoupling loss which occurs at frequencies below 100 Hz for source depths less than 25 m<sup>3</sup>.

The first example is the Argo Abyssal Plain in the northeastern Indian Ocean where the sound speed at the surface is only slightly less than the sound speed at the base of the water column. It is also assumed that the bottom loss is such that there is a critical grazing angle  $\phi_c$  with high losses for angles  $\phi > \phi_c$  and small losses given by  $\alpha\phi$  dB per bounce for  $\phi < \phi_c$ . For water of constant depth H we then have the set of equations

$$PL = 60 - 10 \log_{10} \{DF + 4 \sin^2 (k_0 h_s \sin \phi_c) \exp(-a_b r)\} \quad (1)$$

$$+ 20 \log_{10} r + a_w r, \quad r \leq r_{ab}$$

$$PL = 60 - 10 \log_{10} \{DF + 4(r_{ab}/r) \sin^2 (k_0 h_s \sin \phi_c) \exp(-a_b r)\} \quad (2)$$

$$+ 10 \log_{10} r r_{ab} + a_w r, \quad r_{ab} \leq r \leq r_{bc}$$

$$PL = 60 - 10 \log_{10} \{DF + 4(r_{ab}/r_{bc}) \sin^2 (k_0 h_s \sin \phi_c) \exp(-a_b r)\} \quad (3)$$

$$+ 10 \log_{10} r_{ab} - 15 \log_{10} r_{bc} + 25 \log_{10} r + a_w r, \quad r \geq r_{bc}$$

where

$$DF = 1 - (\sin(2k_0 h_s \sin \phi_c) / 2k_0 h_s \sin \phi_c), \quad (4)$$

$r_{ab} = H/2\phi_c$ ,  $r_{bc} = 6.8H/(\alpha\phi_c^2)$ ,  $k_0$  is the wave number,  $h_s$  is the source depth,  $a_w$  is the intrinsic attenuation of the water column and  $a_b$  is the sediment

attenuation. In deriving Eq. (3), it is assumed that  $k_0^2 h_s^2 H(0.1151\alpha r)^{-1} < 1$ . In Eqs (1) and (2), the "continuous" modes<sup>4</sup> with equivalent grazing angle greater than  $\phi_c$  have also been allowed for. It is found that at frequencies of 25 Hz and 50 Hz the mean difference in measured and predicted levels is less than 2 dB and rms level differences are less than 4 dB over the Argo Abyssal Plain.

The second example chosen is the South Tasman Sea in winter<sup>5</sup> where there is a sound speed excess of 30 m/s at the base of the water column giving RSR propagation for shallow sources. In this case Eqs (1) - (3) are replaced by

$$PL = 60 + 20 \log_{10} r - G(h_s, r) + a_w r, \quad r \leq 10 \text{ km} \tag{5}$$

$$PL = 70 + 10 \log_{10} r - G(h_s, r) + a_w r, \quad 10 \leq r \leq 480 \text{ km} \tag{6}$$

$$PL = 70 + 10 \log_{10} r - G(h_s, 480) + a_w r, \quad r \geq 480 \text{ km} \tag{7}$$

where  $G(h_s, r) = 10 \log_{10} \{1 - \exp(-a^2)\}$ ,  $a^2 = (k_0 h_s)^2 H / r Q$ ,  $Q = 0.1151\alpha$ , and  $\alpha = 0.05 (f_{\text{Hz}}/25)$  dB/degree. In Eqs (5) - (7) we assume a skip distance  $S$  of 60 km with a change in decay law at  $r = 8S$  as in the Marsh-Schulkin model. Equations (5) - (7) give a mean difference between measured and predicted levels of about 1 dB at both 25 Hz and 50 Hz and an rms level difference of 3 dB out to a range of 600 km.

In contrast to the South Tasman Sea the propagation in the South Fiji Basin in summer is bottom limited<sup>6</sup>. In this case the Marsh-Schulkin model has been modified to give

$$PL = 60 + 20 \log_{10} r - G(h_s, r) + (a_T + a_w)r, \quad r < H \tag{8}$$

$$PL = 60 + 5 \log_{10} H + 15 \log_{10} r - G(h_s, r) + (a_T + a_w)r, \quad H \leq r \leq r_1 \tag{9}$$

$$PL = 60 + 5 \log_{10}(r_1 H) + 10 \log_{10} r - G(h_s, r) + (a_T + a_w)r, \quad r \geq r_1 \tag{10}$$

In Equations (8-10),  $r_1=8S$  where  $S$  is the skip distance of the ray with zero grazing angle at the surface and  $a_T$  is the ratio of the bottom loss (dB/bounce) of the limiting ray and  $S$ . It is found that  $\alpha$  is a more complicated function of frequency and depends on the horizontal radial chosen. With the appropriate values of  $\alpha$  and frequencies below 100 Hz the mean difference between measured and predicted levels is within 1 dB and the rms level difference is 5 dB or less.

#### REFERENCES

- 1 H W Marsh and M Schulkin, "Shallow-water transmission", J. Acoust. Soc. Am. 34, 863-864 (1962).
- 2 D E Weston, "Intensity-range relations in oceanographic acoustics", J Sound Vib. 18, 271-287 (1971).
- 3 R W Bannister and M A Pedersen, "Low-frequency surface interference effects in long-range sound propagation, J. Acoust. Soc. Am. 69, 76-83 (1981).
- 4 C T Tindle, "Virtual modes and mode amplitudes near cut off", J. Acoust. Soc. Am. 65, 1423-1428 (1979).
- 5 A C Kibblewhite and R N Denham, "Long-range sound propagation in the South Tasman Sea", J. Acoust. Soc. Am. 41, 401-411 (1967).
- 6 R N Denham, R W Bannister, K M Guthrie and D G Browning, "Low-frequency sound propagation in the South Fiji Basin", J. Acoust. Soc. Am. 75, 406-412 (1984).

ANNE F. QUILL  
RANRL

Two propagation experiments were conducted in the Tasman Sea, south-east of Sydney. The sound source towed from HMAS COOK was a BTL "white" projector which has a resonance frequency of 92.3 Hz. The acoustic signal was received on a deep (146 m) low-noise receiver although some measurements were made at 67 m. The experiments were conducted in deep water with an approximate bottom depth of 4850 m. In one experiment the maximum range between the source and receiver was 28nm. In the other experiment the distance between the source and receiver was 60nm.

The aims of the propagation experiments were to make measurements of the mean propagation loss in the experimental area and to determine the variability of propagation loss about a mean value with increasing range. Comparisons between propagation loss experimental data and the results obtained from two acoustic propagation models (a normal-mode model and FACT 9H) were made.

For the deep water short-range experiment there is an initial decrease in propagation loss out to 7nm. There is evidence of a null in propagation loss at about 11nm and a subsequent decrease in propagation loss which reaches a minimum value of 81 dB at about 17nm. For longer ranges, out to 26nm, there is a rapid increase in propagation loss with range. Similar early trends which are evident in Fig.1 are found in Fig.2.

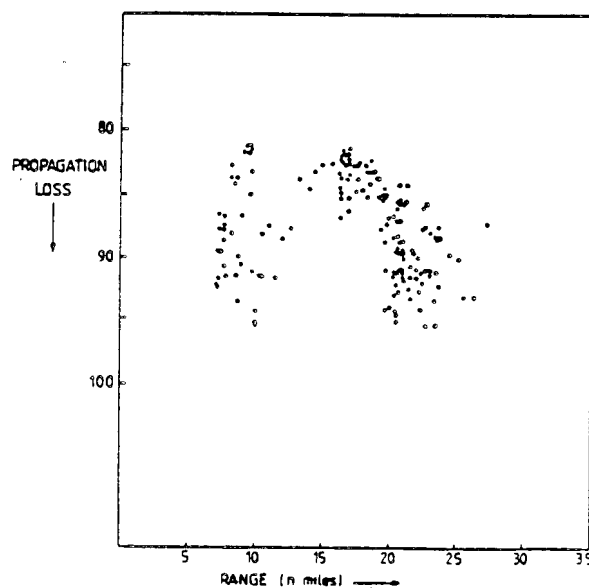


Fig.1 - Propagation loss versus Range. Serial 4a, Site B, deep water, source at 18 m, receiver at 146 m.

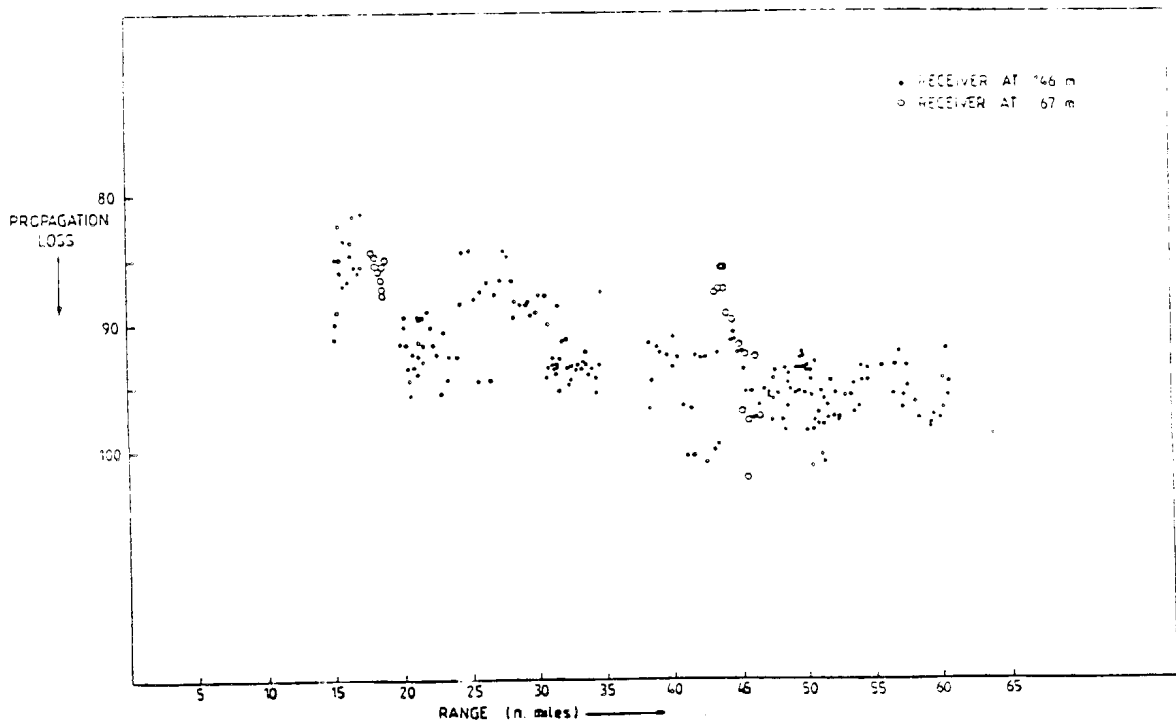


Fig.2 - Propagation loss versus Range. Serial 6, deep water, source at 18 m receiver at 67 m and 146 m.

Fig.2 is a diagram of the experiment extended out to 60nm; between 15-18nm there is a rapid increase in propagation loss with a maximum value of 96 dB. A gradual levelling off with range occurs after 35nm. There is no convergence zone improvement, this is indicative of a highly reflecting ocean bottom. Scatter about the mean propagation loss value is least between the ranges 29-34nm. The largest deviation from the mean occurs at about 45nm and is due to the inclusion of the shallow receiver (67m) data points.

The general variation of loss with range is relatively smooth for both the theoretical and the experimental data although severe nulls which are predicted in the normal-mode model are not observed in the data. Normal-mode theory is known to be more appropriate at long ranges than ray theory because of the greater attenuation with distance of the higher order modes, only a few modes need to be taken in order to describe the transmission. The deep nulls which the model predicts are probably due to interference effects. Potential causes of discrepancies between model and experimental results include an inaccurately specified sound-speed profile, inaccurately specified source and receiver depths and the interference effects of higher-order modes of short ranges.

EFFECTS OF WIND-GENERATED BUBBLES ON SURFACE-DUCT SOUNDPROPAGATION AT FREQUENCIES UP TO 20 kHz

Marshall Hall

RAN Research Laboratory  
PO Box 706, Darlinghurst, NSW 2010

The effects of wind-generated bubbles on surface-duct sound propagation have been calculated theoretically for frequencies up to 20 kHz. The main differences between the present and previous <sup>1</sup> calculations are:

- (i) the model of the bubble population density is more detailed;
- (ii) there are no approximations in the acoustic model; and
- (iii) the resulting model is applied to transducer depths that are of practical interest.

I The Acoustic Model

The speed of propagation ( $c$ ) of a sound wave of frequency  $f$  in a medium containing a bubble population density of  $N$  free bubbles per unit volume per unit radius ( $a$ ) is given by <sup>2</sup>

$$1/C^2 = 1/C_0^2 + 1/\pi f^2 \cdot \int_0^\infty \frac{aN(a)}{a_R^2/a^2 - 1 + i\delta} da \quad (1)$$

where  $C_0$  is the speed of sound if no bubble is present;  
 $a_R$  is the resonance radius; and  
 $\delta$  is the damping constant. ( $C$  would be real if  $\delta = 0$ )

The rate of attenuation of a sound wave (in decibels per unit distance) is given by

$$\alpha = (20/\ln 10) \cdot 2\pi f \cdot \text{Im}(1/C) \quad (2)$$

The resonance radius is given by <sup>3</sup>

$$a_R = a_0 \left[ 1 + \frac{3\gamma-1}{2\phi a_0} + \left( \frac{3\gamma-1}{2\phi a_0} \right)^2 \right]^{-1/2} \quad (3)$$

where  $\gamma$  is the ratio of specific heats of the gas in the bubbles;

$$\phi = (\pi f/D)^{1/2} \quad (4)$$

with  $D$  the thermal diffusivity of the gas;

and  $a_0$  is given by <sup>2</sup>

$$a_0 = \frac{1}{2\pi f} \left[ \frac{3\gamma P_0}{\rho} \right]^{1/2} \quad (5)$$

in which  $P_0$  is the hydrostatic pressure at the bubble

and  $\rho$  is the density of the medium

The damping "constant" is given by <sup>2</sup>

$$\delta = (a_R^2/a^2)\beta + 2\pi f a/C_0 \quad (6)$$

where  $\beta = \text{Im}(B)/\text{Re}(B)$  (7)

in which  $B$ , the bulk modulus of the bubbles if viscosity and surface tension are neglected, is given by <sup>3</sup>

$$B = \gamma P_0 \left[ \frac{1 - \frac{3i(\gamma-1)}{2\phi^2 a^2} \left[ (1+i)\phi a \coth(\overline{1+i}\phi a) - 1 \right]}{\right]^{-1} \quad (8)$$

## II The Bubble Model

The assumed model for the population spectrum density of bubbles per unit radius ( $a$ ) was obtained as an empirical fit to data measured by Johnson and Cooke. <sup>4</sup> The resulting expression is

$$N(a) = N_0 G(a,z) \cdot Y(z,w,\Delta\theta) \cdot U(w) \quad (9)$$

$$\text{where } N_0 = 1.6 \times 10^{10} \text{ m}^{-4} \quad (10)$$

$$G(a, z) = \begin{cases} (a_1/a_1)^2 & , & a < a_1 \\ 1 & , & a_1 < a \leq a_2 \\ (a_2/a)^p & , & a > a_2 \end{cases} \quad (11)$$

in which

$$a_1(z) = 34 + 1.24 z \text{ (}\mu\text{m)} \quad (12)$$

$$a_2(z) = 1.6a_1 \quad (13)$$

$$\text{and } p(z) = 4.37 + (z/2.55)^2 \quad (14)$$

(In ref 1,  $p$  was assumed to be a fixed value of 4; and in ref 5, a value of 5 was suggested.)

$$Y(z, w, \Delta\theta) = \exp(-z/L)$$

where, based on data measured by Thorpe <sup>6</sup>

we set

$$L = 0.94 (1 - \Delta\theta/10) (w/13) \text{ m} \quad (15)$$

where  $w$  is the wind-speed (m/s) and  $\Delta\theta$  is the air-sea temperature difference (C°).

Equation 14 was obtained by fitting a parabola to the data measured <sup>4</sup> at depths of 0.7, 1.8 and 4.0 m. Since the value of  $Y$  is small at depths greater than 2m, the value of  $p$  at such depths will not usually be critical. A convenient approximation valid for shallower depths is to set

$$p(z) \approx 4.2 + z/2.7 \quad (16)$$

From equation 16 we can obtain an approximate value for the effective depth constant ( $L'$ ) of  $N$ :

$$\frac{1}{L'} \approx \frac{1}{L} + \frac{\ln(a_R/a_2)}{2.7} \quad (17)$$

For the factor  $U$  that depends only on wind - speed, extrapolation of data in ref 6 to the surface yields the conclusion that  $N(z=0) \propto w^3$ . We therefore write

$$U(w) = (w/13)^3 \quad (18)$$

(In ref 1, this index (called  $q$ ) was set equal to 2 rather than 3; and in ref 5 a value of 4.5 was suggested. The latter hypothesis was based on data at only two wind-speeds, whereas ref 6 reports data measured at 9 wind-speeds).

### III Acoustic Calculations

#### A. Values for Change in sound-speed and Attenuation.

For frequencies up to 20 kHz, the change in sound-speed ( $\Delta c$ ) is negative; the magnitude of the change decreases with increasing frequency and increases with increasing wind-speed. For a wind-speed of 15 m/s for example,  $\Delta c$  at the sea-surface varies from -26 m/s at 1.3 kHz to -14 m/s at 20 kHz. The rate of attenuation ( $\alpha$ ) increases with both frequency and wind-speed. For a wind-speed of 15 m/s, the value of  $\alpha$  at the surface increases from 1 dB/m at 5 kHz to 6.6 dB/m at 20 kHz.

For depths below the surface, values of  $\Delta c$  and  $\alpha$  that were required for the calculations were obtained from the model.

Approximate values for depths up to 2m may be calculated by assuming that the bubble population density decays exponentially from the surface with a depth constant ( $L'$ ) given by equation 17. For example, if  $w = 15$  m/s,  $\Delta\theta = 0$ , and  $f = 20$  kHz; then

$$1/L' = 0.922 + 0.390 \text{ m}^{-1}$$

whence  $L' = 0.762\text{m}$

### B. Total Attenuation of the Limiting Ray

The total one-way attenuation (A) due to bubbles of a ray from the surface to its nadir (an iso-thermal surface duct is assumed) is given by

$$A = \int_0^H \alpha(z) \operatorname{cosec} \phi(z) dz \quad (19)$$

where H is the depth of the nadir of the ray and  $\phi$ , the angle of the ray to the horizontal, is given by

$$\cos \phi(z) = \operatorname{Re}[c(z)]/c(H) \quad (20)$$

[It is of interest that if bubble-induced refraction is neglected then the value of  $\phi$  would be too small and the result obtained for A from equation 19 would be too large]

Values of A have been calculated for the case of  $w = 15$  m/s and  $H = 60$ m. As frequency increases from 5 to 20 kHz, A increases "quasi-exponentially" from 8 dB to 61 dB (If bubble-induced refraction were neglected, then the results would be 25 and 170 dB respectively). At wind-speeds of up to 10 m/s, the present model gives results (for attenuation from the surface) that are similar to the results presented in ref 1 (for attenuation from a depth of 1 metre). The main factor that increases their results to offset the omission of 1 metre of the water column is their assumption that  $p = 4$ . Because of the present assumption that  $q = 3$  rather than 2, the present model would predict higher attenuation than ref 1 at higher wind-speeds.

### C. Dependence of Total Attenuation on Source Depth.

The effect of varying the source depth on total attenuation is determined by varying the lower limit of integration in equation 19. The attenuation decays "quasi-exponentially" as the source depth increases, as the following results (for a frequency of 20 kHz and 15-m/s wind-speed) show:

Source Depth(m) \ $\Delta S$ (C°)	<u>Total Attenuation (dB)</u>		
	-6	0	+6
0	78	61	31
1	38	25	11
2	16	8	1
3	6	2	0
4	3	0	0

#### IV CONCLUSION

At frequencies up to 20 kHz, wind-generated bubbles are unlikely to cause any noticeable attenuation of downward travelling rays emanating from sources deeper than about 4m.

#### REFERENCES

1. J.C. Novarini and D.R. Bruno, "Effects of the sub-surface bubble layer on sound propagation," J. Acoust. Soc. Am. 72, 510-514(1982).
2. Anon. "The Physics of Sound in the Sea," Summary Technical Report (National Defense Research Committee, Washington DC, 1946), pp 462-473.
3. C. Devin, "Survey of Thermal, Radiation, and Viscous Damping of Pulsating Air Bubbles in Water," J. Acoust. Soc. Am. 31, 1654-1667 (1959).
4. B.D. Johnson and R.C. Cooke, "Bubble populations and spectra in coastal waters : a photographic approach," J. Geophys. Res. 84(c7), 3761-3766(1979).
5. J. Wu, "Bubble population and spectra in near-surface ocean : summary and review of field measurements." J. Geophys. Res. 68, 457-463(1981).
6. S.A. Thorpe, "On the clouds of bubbles formed by breaking wind-waves in deep water, and their role in air-sea gas transfer," Phil. Trans. R. Soc. Lond. A 304, 155-210 (1982).

SIGNAL MULTIPATH PROPAGATION  
IN BOTTOM LIMITED REGIONS

by

- R W Bannister - Defence Scientific Establishment  
Auckland, New Zealand
- S G M Payne - Applied Research Laboratories  
University of Texas at Austin,  
Austin, Texas
- J C Hall - Naval Ocean Systems Center,  
San Diego, California

Introduction

In recent times there have been several reports describing the multipath nature of long range acoustic transmission (for example, references 1-5). In some of these (for example, references 1, 2, 4) waterborne paths have been emphasized in support of an ocean monitoring scheme using acoustic tomography. In others, (for example, reference 5) a high resolution of bottom reflected paths has been used to determine bottom reflection loss. A further series of reported data (for example, reference 3) has been concerned with interpretation of multipath arrivals received on a bottom slope-mounted hydrophone system placed where the major part of the transmission path has no bottom interactions.

The purpose of this paper is to address a different aspect of the problem. Although much of the region surrounding New Zealand is relatively deep (2000-4000m), convergence zones are not supported for shallow source depths. Acoustic transmission properties are therefore dominated by bottom interacting paths. Furthermore, this same bottom-limited region has abundant bathymetric features resulting from tectonic activity in the area. The situation of interest is therefore one of bottom limited transmission between shallow sources and receiver over bathymetric slopes. This paper reports on various recent measurements of the vertical arrival structure of the multipath field as well as associated time dispersion. To begin with the measurement technique is described. The data, together with acoustic modelling results are then presented for transmission paths which include bathymetric features.

### The measurement technique

The analysis process is based upon the cross correlation between two hydrophones spaced vertically in the watercolumn 45m apart. Explosive charges detonated at various ranges from this system are used as the source.

The use of explosive transients has a number of advantages. Firstly, their source level is high, ensuring strong signal-to-noise ratios at the receiver. The transient nature of the signal produces a series of discrete arrivals which can separately be resolved in angle. This greatly simplifies the process of determining the vertical angular field. Data obtained from this analysis process are averaged in frequency over the total bomb spectrum (40-60 Hz).

### The modelling of vertical signal multipath

In order to interpret the data as measured above, some acoustic modelling is required. The measured parameters are power, angle and arrival time for each discrete arrival from the transient source. Eigenray analysis has been used to model these parameter sets and, over flat bathymetry, good agreement can be demonstrated. This has also been shown by other workers (references 1-5) using ray theory models.

The prediction has been extended to encompass bathymetric slopes. When the seafloor has complex gradients, it has been found that much care is necessary in selecting eigenrays. The approach being pursued by the authors is to implement a modern ray-trace model (MEDUSA, reference 6). This model was developed to identify multipath arrivals from bottom bounce signals with sufficient accuracy so as to be able to infer bottom loss. Much care has been taken to construct robust ray-tracing and eigenray interpolation algorithms.

In many ways it may seem desirable to use wave-theory models such as a modified parabolic equation system. Certainly, this is more defensible at low frequencies, although in deep water (2000-4000m) environments, ray-like effects are observed. Wave models implicitly take care of all necessary acoustic processes and produce a sound field as a function of depth and range.

The problem arises, however, in interpreting the predicted field in terms of the power, angle and arrival time sets which are needed to match and interpret the measured data. This is commonly done by beamforming a pseudo-array placed within the sound field. The difficulty is that the array must span a large part of the watercolumn in order to give adequate angular resolution. This produces an unacceptable depth averaging of the vertical arrival structure. While this can be offset to some degree by using high resolution processing techniques, further problems arise from the steady-state acoustic field being difficult to resolve into discrete angles.

One possible solution to this dilemma may be to use the relationships reported by Cavanagh (reference 7) between depth and angular dependence of the sound field.

### The results

Examples of results to date are shown in figure 1. The figure refers to a transmission path whose bathymetric section is shown in the lowest panel. The soundspeed profile is such that there is a 600m depth excess for near surface sources over the deep part of the transmission path. The figure relates to transmission from an 18m source for which little waterborne energy is to be expected. This can be seen from part (c) of figure 1, which plots arrival angle versus source-receiver range, as predicted by using the MEDUSA model. Waterborne paths (annotated with the + symbol) are received over a small angle increment between 10 and 12 degrees. These angles correspond to shallow angles (<10 degrees) at the source so that they are subject to surface dipole losses in the order of 10 dB at 25 Hz. Hence at these low frequencies, little energy is transmitted by waterborne paths. This is consistent with the measured arrival angle structure given in part (b) of figure 1.

Over the flat portion of the path, then, bottom bounce energy dominates. Again this is predicted in part (c) of figure 1 where bottom bounce families are distinguished by a numeral indicating the number of bottom interactions. The measured angular structure reflects this process, part (b) of figure 1.

Propagation loss over the flat part of the path is straightforward and can be simply predicted by average decay laws (reference 9). This is shown in part (a) of figure 1.

As the source progresses up the bathymetric slope, however, more complex transmission mechanisms become effective. The result in general terms is a received level "enhancement", shown in part (a) of figure 1 as a lift above that predicted in the absence of a bathymetric gradient. The signal level recovers towards a transmission loss appropriate for solely waterborne paths ( $70 + 10 \log R$ ). At the same time, received energy is confined to within  $\pm 10$  degrees of the horizontal (part (b) of figure 1).

Some insight into the enhancement process can be gained from the modelled results. Early interactions with the slope (ranges 280 km - 350 km) are complicated by the peak and trough in bottom contour. An examination of this range bracket in part (c) of figure 1 indicates that received angles can fall in the range 10-15 degrees. These consist of a mixture of paths, some having bounced from the bottom over the whole path (8, 9 bounces) and some having one or two bounces on the slope, followed by waterborne paths.

It can be shown that the rays which interact with the bottom over the whole path originate at high angles at the source (40 degrees). Such families have negligible surface decoupling loss (reference 8) at 25 Hz. By comparison, the families of rays launched into waterborne paths have low (10 degree) angles at the source. These families will have a dipole loss in the order of 10 dB at 25 Hz. Hence in this early slope interaction there is a frequency dependent tradeoff between these two ray families. In general terms it can be shown that below 50 Hz, the bottom bounce families predominate over the slope induced waterborne paths.

Beyond 350 km range the situation simplifies. Part (c) of figure 1 indicates that ray paths in this upper part of the slope consist of slope induced waterborne paths following various numbers of bounces on the slope.

It can be shown that as the number of bounces increases the launch angle at the source also increases. Thus at low frequency, as the source proceeds up the slope, progressively less surface decoupling loss is applied to the ray. This tends to offset the effect of accumulating bottom loss and will sustain the enhancement.

## Summary

These general effects are borne out in measured data and may be summarised as follows:

- a Over the flat part of the transmission path, bottom bounce paths predominate. Received angles in the range  $\pm$  (10-50) degrees are measured and propagation loss is predictable by simple models.
- b Over the slope, an enhancement in received signal level can be observed. There is little energy loss over the entire slope region (100 km) at frequencies below 50 Hz.
- c Initial interactions with the bottom slope immediately produce the enhancement. The vertical signal multipath in this range region still contains some rays received at angles above 10 degrees indicating bottom bounce transmission.
- d For sources further up the slope, the received vertical angles are less than 10 degrees, consistent with slope induced waterborne paths.

## Acknowledgements

The participation of technical staff at DSE is gratefully acknowledged. Their design, construction and operation of the multi-element array system used to obtain these data made a significant contribution to this paper.

## References

- 1 J L Spiesberger et al. Stability and identification of ocean acoustic multipaths. JASA 67(6) 2011-2017 June 1980.
- 2 P F Worcester. An example of ocean acoustic multipath identification at long range using both travel time and vertical arrival angle. JASA 70(6) 1743-1747 Dec 1981.
- 3 J Northrop and R C Shockley. Long range Pacific acoustic multipath identification. JASA 75(6) 1760-1765 June 1984.
- 4 G R Legters et al. Long range Atlantic acoustic multipath identification. JASA 73(5) 1571-1580 May 1973.
- 5 S K Mitchell et al. Multipath analysis of explosive source signals in the ocean. JASA 67(5) 1590-1597 May 1980.
- 6 T L Foreman. Ray modelling methods for range dependent ocean environments. Thesis presented to University of Texas at Austin, December 1983.
- 7 R C Cavanagh and W W Renner. Vertical directionality and depth dependence of averaged acoustic signals and noise. JASA 68(5) 1467-1474 Nov 1980.
- 8 R W Bannister and M A Pedersen. Low frequency surface interference effects in long-range sound propagation. JASA 69(1) 76-83 Jan 1981.
- 9 R N Denham. Intensity decay laws for near surface sound sources in the ocean. Presented to this Conference.

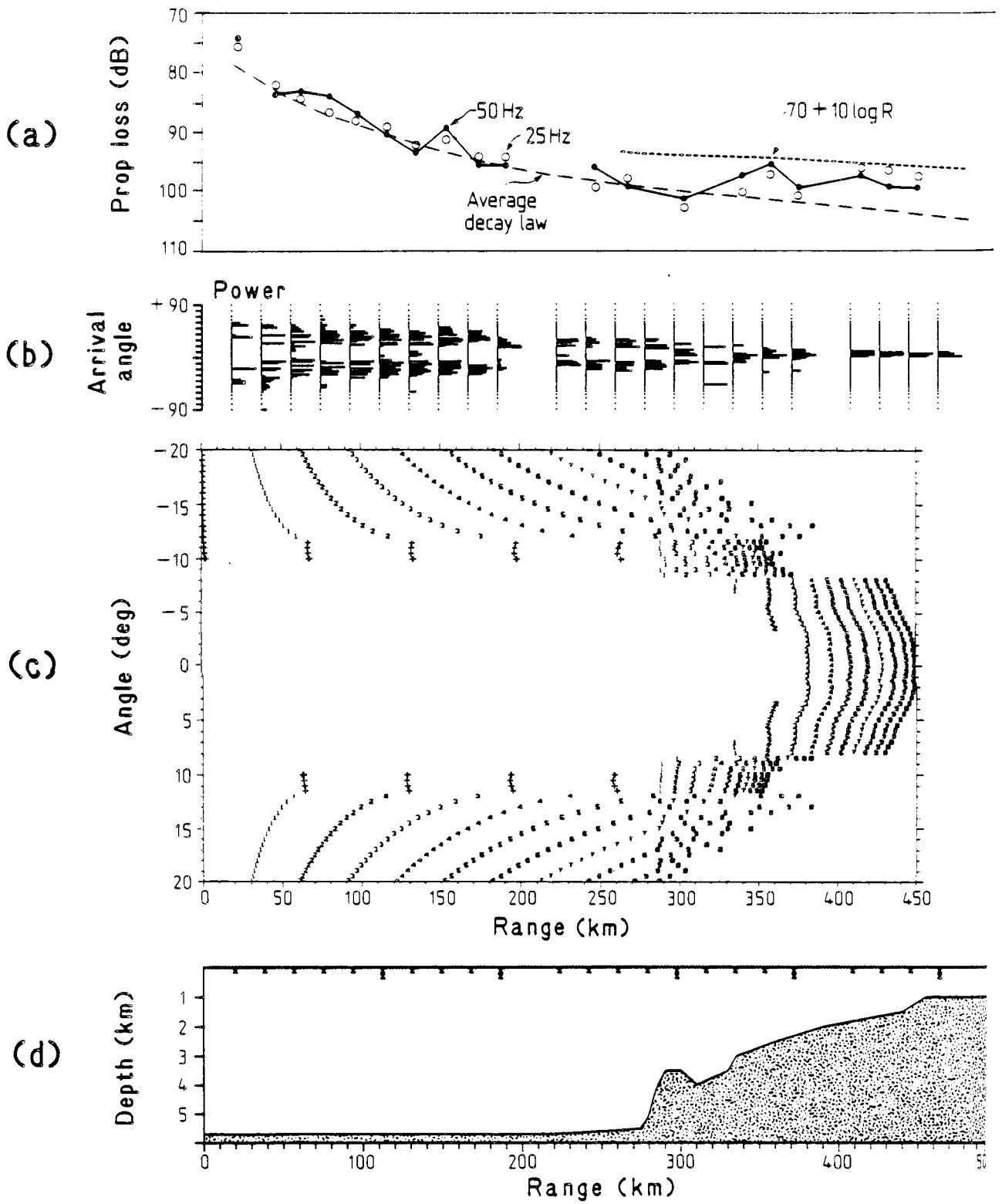


Figure 1

EFFICIENT NUMERICAL SOLUTION TECHNIQUE FOR WAVE PROPAGATION  
IN HORIZONTALLY STRATIFIED ENVIRONMENTS

by

Finn B. Jensen and Henrik Schmidt  
SACLANT ASW Research Centre, 19026 La Spezia, Italy

Introduction

A numerical model providing a full wave solution to propagation problems in horizontally stratified fluid/solid environments is presented. During the last decade a number of similar models have been developed, known in underwater acoustics as Fast Field Programs [1,2,3] and in seismology as full wave-field models [4]. These models are, however, in general based on the Thomson-Haskell matrix method, which allows for field calculations for only one source/receiver combination at a time. Hence calculation of the field as a function of depth and of fields produced by vertical source arrays need several separate runs, with the calculation time being proportional to the number of sources and receivers.

The model described here, which is a general numerical implementation of a solution technique proposed by Ewing et al [5], offers a number of important advantages over the Thomson-Haskell technique. First there are no restrictions on the number of sources, as the fields produced by more sources within a layer are simply superimposed. Second, any number of receiver depths can be treated with one solution, since the field is found in all layers simultaneously. Thus the spatial distribution of the field produced by a single source or by a beam-generating vertical array can be determined in a computationally efficient manner. Third, even for only one source/receiver combination, the computer code based on this solution technique is an order of magnitude faster than existing codes based on the Thomson-Haskell technique.

1. Solution Technique

For an environment consisting of isotropic, homogeneous viscoelastic layers, the field solution of time dependence  $\exp(i\omega t)$ , in the absence of sources, can be written in integral form as [5]:

$$\phi(x,z) = \int_{-\infty}^{\infty} [A^-(s)e^{-z\alpha(s)} + A^+(s)e^{z\alpha(s)}] e^{-isx} ds \quad (1)$$

$$\psi(x,z) = \int_{-\infty}^{\infty} [B^-(s)e^{-z\beta(s)} + B^+(s)e^{z\beta(s)}] e^{-isx} ds, \quad (2)$$

where  $\phi$  and  $\psi$  are plane-geometry displacement potentials for compressional and shear waves, respectively. The x-axis is parallel to the layer interfaces, while the z-axis is perpendicular to the interfaces and positive downwards. In Eqs. (1) and (2) the A's and B's are arbitrary functions in the horizontal wavenumber  $s$ , while

$$\alpha(s) = \sqrt{s^2 - h^2}, \quad \beta(s) = \sqrt{s^2 - k^2} \quad (3)$$

with  $h$  and  $k$  being the wavenumbers for compressional and shear waves, respectively. Note that Eqs.(1) and (2) are just decompositions of the displacement fields in up and downgoing plane waves integrated over all angles (horizontal wavenumbers).

To obtain expressions for the total field in a layer, we must add source contributions given by the following integral representation [5]:

$$\phi(x,z) = -\int_{-\infty}^{\infty} \frac{e^{-|z-z_s|} \alpha(s)}{\alpha(s)} e^{-isx} ds, \quad \psi(x,z) \equiv 0 \quad (4)$$

which is valid for a compressional line source positioned at  $(0, z_s)$ . If more than one source is present in a layer, the kernel in Eq. (4) is replaced by a sum over the number of sources.

The field at each layer interface now has two different integral representations, one from the layer above and one from the layer below. The boundary conditions (continuity of displacements and stresses) must be satisfied at all ranges  $x$ , and thus must be satisfied by the kernels in the integral representations as well, leading to a linear system of equations in the unknown arbitrary functions  $A^+$ ,  $A^-$ ,  $B^+$ , and  $B^-$ .

The main computational effort goes into solving for the A's and B's at a discrete set of horizontal wavenumbers. The stress and displacement fields can then be found at any depth by evaluation of the integral transforms, Eqs. (1) and (2), which is done by an FFT. Details of the numerical implementation including stability considerations are given in [6].

## 2. Numerical Examples

We present numerical solutions to two important propagation problems in underwater acoustics. First we consider low-frequency propagation in a shallow-water duct. This problem will be solved in cylindrical geometry, with environmental parameters as follows: 100 m water depth with a speed of 1500 m/s, a solid bottom with compressional speed of 1800 m/s, shear speed of 600 m/s, compressional attenuation of 0.1 dB/ $\lambda$ , and shear attenuation of 0.2 dB/ $\lambda$ . The density ratio between bottom and water is 2.0. We have intentionally used a solid bottom in order to demonstrate that the often-

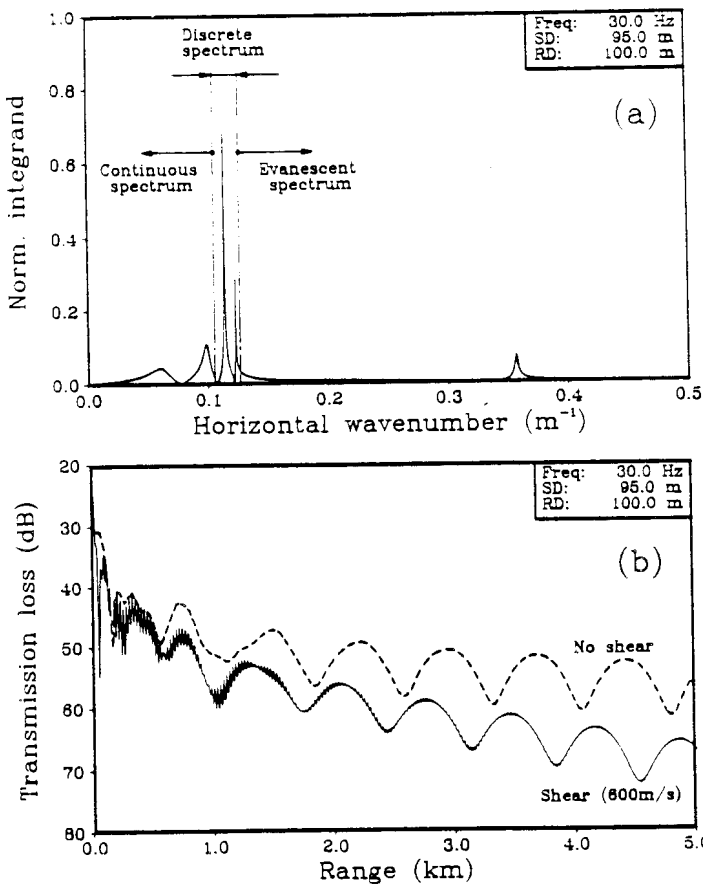


Fig. 1 Horizontal wavenumber spectrum for shallow water case at 30 Hz (a), and associated transmission loss curves (b).

neglected shear properties are of considerable importance in low-frequency ocean acoustics.

A full-spectrum solution at 30 Hz is displayed in Fig. 1 for a source at 95 m and a receiver at 100 m (on the bottom). The propagating energy versus horizontal wavenumber is shown on the integrand plot of Fig. 1a, which displays the kernel of Eq.(1) with source contributions included. We see from the integrand that there are five peaks in the spectrum corresponding to five preferred modes of propagation. There are two discrete modes, two continuous (virtual) modes, and one evanescent mode, which can be shown to be an interface wave of the Scholte type propagating along the sea floor. The two discrete modes dominate propagation beyond the nearfield, as shown in the lower transmission-loss curve (shear = 600 m/s) of Fig. 1b. The two highly attenuated virtual modes are responsible for the irregularities of the interference pattern at short ranges, while the interface mode causes the "high-frequency" noise on the propagation-loss curve. The above detailed analysis of the contributions of the various spectral components to the propagation-loss curve can be demonstrated explicitly by solving for just selected parts of the wavenumber spectrum.

A full-spectrum calculation without shear shows much better propagation at long ranges, but with essentially the same interference structure (Fig. 1b). Hence the effect of shear is to increase losses for waterborne propagation.

More details on the importance of shear in low-frequency ocean acoustics is given elsewhere [7].

The numerical model is extremely well suited for solving low-frequency guided wave-propagation problems. A full-spectrum solution is readily available with minimum computational effort. Hence the results of Fig.1 are obtained in 65 s on a VAX-11/750 and in just 5 s on an FPS-164 array processor. These computation times relate to the use of 2048 integration points along the wavenumber axis.

In the second example we study the reflection and transmission of a narrow beam of sound at a water/bottom interface. This example has been chosen to demonstrate that directional sources (beams) are handled by the numerical model in a computationally efficient manner. The beam is generated by a vertical source array composed of a number of equidistantly spaced line sources (plane geometry), and the resulting acoustic field is found by superposition of the contributions from the individual sources. The beam direction is varied by appropriately phasing the source elements, and the intensity distribution across the beam can be selected by applying an amplitude weighting across the array. By varying the array distance from the interface and the number of source elements (half-wavelength spacing), a beam of arbitrary width can be generated. Moreover, beams can be focused or defocused by phasing the sources appropriately.

The interest in the beam-reflection problem goes back to an experimental study by Muir et al [8], where it was shown in a laboratory experiment that a narrow beam of sound impinging on the bottom at grazing angles below the critical angle will not be totally reflected as predicted for an infinitely wide plane wave. Instead there is significant energy being transmitted into the bottom, this energy increasing as the incident beam narrows. We shall solve the beam reflection/transmission problem in plane geometry for an environment similar to the one used by Muir et al [8]. We consider a water halfspace overlying a fluid-bottom halfspace. The sound speeds are 1450 m/s in the water and 1675 m/s in the bottom, giving a critical (grazing) angle of exactly  $30^\circ$ . The density ratio between bottom and water is 2.0 and we neglect attenuation in the bottom. Calculations are done for a frequency of 20 kHz, which gives an acoustic wavelength ( $\lambda$ ) in the water of 7.25 cm. We have chosen a source array of 121 elements with  $\lambda/2$  spacing, giving an array length of 4.25 m. A gaussian amplitude weighting was applied across the array, producing a gaussian beam with low sidelobe levels.

Calculated field solutions are given in Fig. 2 for a focused beam that is  $2.5 \lambda$  wide at the interface. The beamwidth is measured across the beam between the 3-dB down points. The arrows in the upper part of Fig. 2 indicate the beam directions; also shown are the angles of incidence ( $\theta_i$ ), reflection

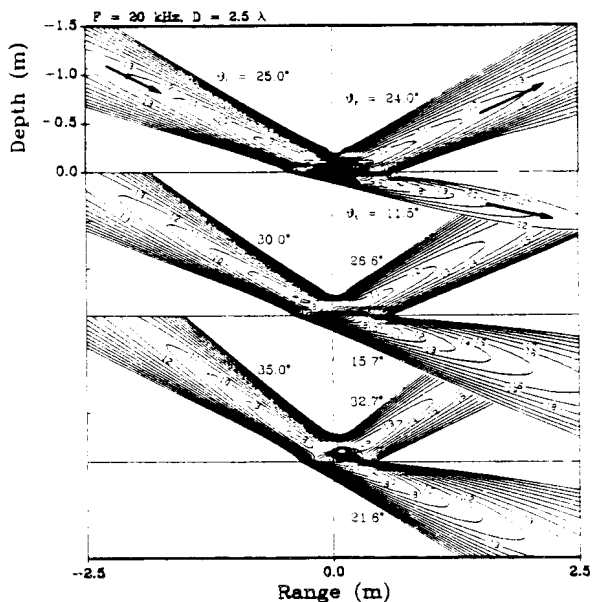


Fig. 2 Reflection and transmission of narrow beam of sound ( $D=2.5\lambda$ ) at water/bottom interface. The critical angle is  $30^\circ$  and there is no attenuation in the bottom.

( $\theta_r$ ), and transmission ( $\theta_t$ ), all measured along the direction of maximum amplitude in a beam with respect to horizontal. Three cases are considered,  $\theta_i = 25.0^\circ, 30.0^\circ, 35.0^\circ$ , with the critical angle being  $30^\circ$ . Hence the upper beam is incident at  $5^\circ$  below the critical angle, and a transmitted beam is still present in the bottom ( $\theta_t = 11.5^\circ$ ). With increasing angle of incidence more energy is propagated into the bottom (contours show losses in arbitrary dB's). We also notice that the angle of reflection is lower than the angle of incidence (non-specular reflection).

A full understanding of the observed beam behaviour can be obtained by comparing the spectral content of the incident beam with the angular reflectivity characteristics of the interface, as shown in Fig. 3. The upper figure displays angular spectra for beams of different widths and incident at the critical angle. Note that the narrow beam has the widest spectrum, while the spectral width decreases with increasing beamwidth. In this angular representation an infinitely wide plane wave becomes a delta function with only one direction of propagation. The lower figure shows the plane-wave reflection loss and phase shift versus angle at the interface, indicating perfect reflection below  $30^\circ$  with a phase shift, and an increasing reflection loss above  $30^\circ$  with no phase shift. Comparing Figs. 3a and 3b shows that the left (hatched) half of the beam spectra are perfectly reflected (though with a phase shift) while the right half is partly transmitted. Thus in practice we need to weight the incident beam spectrum with the reflectivity characteristics of the interface in order to get the spectrum for the reflected or transmitted beam. The above simple argument explains qualitatively what to expect. For example, the hatched part of the spectrum

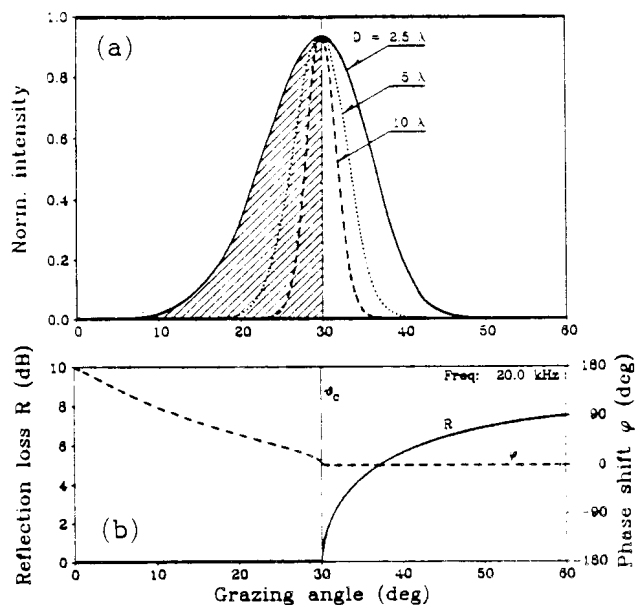


Fig. 3 Angular spectra of incident beams of different half-power widths (a), and reflectivity characteristics at water/bottom interface (b).

will be entirely reflected, while the right half will be partly transmitted. The different weightings put on the two half-spectra mean that the peak energy in the reflected beam moves to smaller angles ( $\theta_r < \theta_i$ ), as also observed in Fig. 2. On the other hand, only energy in the right half of the spectrum will be transmitted, and the beam direction ( $\theta_t$ ) can be determined from the peak in the transmitted spectrum. It is clear from Fig. 3 that even though each spectral component is reflected and transmitted according to Snell's law, the total beam, in which phase and amplitude weightings are applied to the broad spectrum, cannot be expected to be so.

The computational efficiency of the numerical code is particularly evident for this case, in which field calculations from 121 sources have been made on a spatial grid of 50 x 512 points. Each contoured beam plot in Fig. 2 takes 6 min on a VAX-11/750 and 21 s on an FPS-164. Not only are these acceptable calculation times, but this code seems to be the only one capable of doing these types of calculations.

### 3. Conclusions

We have presented an efficient numerical solution technique for wave propagation in horizontally stratified viscoelastic media. The model provides a full wave solution for the field generated by a single source as well as for that generated by a vertical source array. It allows the spatial distribution of the acoustic field to be evaluated at least one order of magnitude faster than with existing models based on the Thomson-Haskell solution technique. The computational examples clearly demonstrate the model's versatility in providing exact solutions to a wide range of guided and non-guided propagation problems in underwater acoustics.

### References

1. F.R. DiNapoli, Fast field program for multilayered media, Rep. 4103. US Naval Underwater Systems Center, New London, CT (1971).
2. H.W. Kutschale, Rapid computation by wave theory of propagation loss in the Arctic Ocean, Rep. CU-8-73. Columbia University, Palisades, NY (1973).
3. F.R. Dinapoli and R.L. Deavenport, Theoretical and numerical Green's function solution in a plane multilayered medium. J. Acoust. Soc. Amer. 67, 92-105 (1980).
4. B.N.L. Kennett, Seismic Wave Propagation in Stratified Media. Cambridge University Press, Cambridge (1983).
5. W.M. Ewing, W.S. Jardetzky and F. Press, Elastic Waves in Layered Media. McGraw-Hill, New York, NY (1957): chapter 4.
6. H. Schmidt and F.B. Jensen, "Efficient Numerical Solution Technique for Wave Propagation in Horizontally Stratified Ocean Environments," Rep. SM-173, SACLANT ASW Research Centre, La Spezia, Italy (1984).
7. T. Akal and F.B. Jensen, Effects of the sea-bed on acoustic propagation, Rep. SM-167. SACLANT ASW Research Centre, La Spezia, Italy (1983).
8. T.G. Muir, C.W. Horton and L.A. Thompson, The penetration of highly directional acoustic beams into sediments. J. Sound Vib. 64, 539-551 (1979).

SHALLOW WATER ACOUSTIC MODELLING OVER A SLOPING BOTTOM

C.T. TINDLE

Physics Department, University of Auckland, Private Bag, Auckland, New Zealand

The problem of finding the acoustic field in shallow water over a sloping bottom is receiving much attention for two reasons. Firstly the problem has practical importance because the real ocean bottom is rarely horizontal especially in shallow water. Secondly, the problem is of theoretical interest because the wave equation governing propagation becomes non separable and there is no exact formalism applicable to the general case.

Exact solutions to general underwater sound propagation problems exist only for horizontally stratified cases and a variety of theoretical methods and computer programs are available. The extension of these methods to range dependent problems involves approximations.

Ray theory is well known to be a high frequency approximation to wavefront propagation but recent work <sup>1</sup> has shown that if beam displacement is included ray theory can be accurate in low frequency situations. Beam displacement is the lateral displacement of a ray which suffers total internal reflection and arises when the phase of the reflection coefficient is a function of the angle of incidence. Beam displacement is easily calculated from the phase of the reflection coefficient even if this is only known numerically.

The extension of ray theory with beam displacement to propagation over a sloping bottom is very interesting because the extension requires no analytic or numerical approximation. Therefore the accuracy of ray theory with beam displacement is expected to be the same as it is for a horizontal bottom. The accuracy has been tested for a horizontal bottom against

exact results <sup>1</sup> and is very good. Any slight differences would not be significant in comparison with experimental data.

The extension of ray theory with beam displacement to the sloping bottom situation is achieved with some simple geometric considerations.

Calculations have been performed for the "Pekenis" model of two homogeneous fluids modified to include a sloping interface. It is clear that even a small slope such as  $1^\circ$  has a dramatic effect on the acoustic field in shallow water. In shallow water of constant depth the sound field as a function of range shows quasiperiodic smooth fluctuations as normal modes interfere. These characteristic smooth fluctuations are also features of the field over a sloping bottom but the detail and spacing changes rapidly as the bottom slope is increased.

It is interesting to compare the results of ray theory with beam displacement to adiabatic normal mode calculations. Adiabatic normal mode theory is an approximation which assumes that a normal mode adjusts to the local water depth without coupling of energy to other modes. In a number of cases for down slope propagation the adiabatic normal mode results agree well with our calculations even for slopes of up to  $5^\circ$ .

The cases where adiabatic normal mode results differ from our ray calculations occur when there are normal modes which are not quite trapped in the water depth at the source and which are therefore not included in the calculation. As the water depth increases these modes become trapped and contribute to the acoustic field. The adiabatic mode calculation can be made to agree with the ray results if it is assumed that the mode near cutoff propagates initially as a virtual mode which becomes trapped as the water depth increases.

It is concluded that Ray theory with beam displacement is a useful method of calculating the acoustic field in shallow water over a sloping bottom.

1 C.T. TINDLE, Ray calculations with beam displacement,  
J. Acoust. Soc. Am. 73 1581-1586 (1983).

A NOTE ON THE APPLICATION OF  
NORMAL-MODE THEORY TO SHALLOW WATER PROPAGATION

Marshall Hall

RAN Research Laboratory  
PO Box 706 Darlinghurst NSW 2010

If the slope of the sea floor and the horizontal gradient of the slope are both small then coupling between well-trapped waterborne acoustic normal modes is negligible.<sup>1</sup> The acoustic field can then be determined by calculating separately the contributions of the significant modes and adding them together. The modes are damped with range (by friction in the sea floor) to an extent that increases with mode number. At sufficiently long ranges therefore, only the first mode will be significant.

A. RELATIVE INTENSITY

A rigorous derivation of an expression for relative intensity in a range-dependent medium, based on the "no-coupling" hypothesis, has been presented<sup>2</sup>. The result is, however, somewhat complicated. If we make the simplifying assumption that the contributions of the modes are similar to that for a stratified medium (except that we allow the eigenvalues to vary with distance rather than remain constant) then the acoustic intensity at a receiver at  $(x_r, y_r, z_r)$  relative to that at unit distance from a source at  $(x_s, y_s, z_s)$  is given by<sup>3</sup>

$$ri \approx |\psi|^2$$

where

$$\psi = i\pi \sum_{n=1}^{\infty} H_0^{(2)}(K_n R) U_n(z_s) U_n(z_r) / \int_0^{\infty} U_n(z)^2 dz \quad (1)$$

in which  $R$  is the length in the x-y (horizontal) plane of the path travelled;

$K_n$  is the (complex) wavenumber eigenvalue of the n'th mode and  $U_n(z)$  is the amplitude of the depth function at depth  $z$ ;

Substituting <sup>4</sup>

$$H_0^{(2)}(K_n R) \approx \left[ 2/(\pi K_n R) \right]^{1/2} \exp(-iK_n R + i\pi/4) \quad (2)$$

and <sup>5</sup>

$$\int_0^\infty U_n(z)^2 dz = H/2 \quad (3)$$

where  $H$  is the bottom depth

yields

$$\psi = \sum (8\pi/K_n R)^{1/2} U_n(z_s)U_n(z_r) / (H_s H_r)^{1/2} \exp(-iK_n R) \quad (4)$$

where  $H_s, H_r$  are the bottom depths at the positions of the source and receiver respectively.

It can be seen from equation 4 that dependence of relative intensity on range comprises two factors:

- (i) cylindrical spreading; and
- (ii) damping (if the  $K_n$  are complex).

#### B. Eigenvalues of the Modes

The real part of the eigenvalue of a mode is often described by its "phase velocity",  $P_n$ , which is defined by

$$P_n = \omega \operatorname{Re}(1/K_n) \quad (5)$$

where  $\omega$  is the angular frequency.

The imaginary part of the wavenumber eigenvalue is the rate of damping of a mode with horizontal range in nepers per unit distance. The damping coefficient ( $\Gamma$ ) in decibels per unit distance is given by

$$\Gamma_n = (20/\ln 10) \operatorname{Im}(K_n) \quad (6)$$

(1) Iso-speed profile.

We consider a sound-speed profile defined by

$$c(z) = \begin{cases} C_w & , 0 < z < H \\ C_p & , z > H \end{cases} \quad (7)$$

in which  $C_p$  is complex and  $\text{Re}(C_p) > C_w$ .

For this profile, it can be shown (from the results presented in ref 5) that  $K_n$  is approximately given by

$$K_n^2 = k_w^2 - [n(\pi - \epsilon)/H]^2 \quad (8)$$

where

$$\epsilon = \pi \rho_b / \rho_w [ H ( k_w^2 - k_p^2 )^{1/2} + \rho_b / \rho_w ]^{-1} \quad (9)$$

in which

$\rho_b$ ,  $\rho_w$  are the densities of the sea-floor and sea-water respectively

$$k_w = \omega / C_w \quad (10)$$

and

$$k_p = \omega / C_p \quad (11)$$

The fact the  $\epsilon$  varies with  $H$  is an important consequence of realistic sound-speed profiles. Early models of shallow-water propagation implied that  $\epsilon$  was a constant (either 0 or  $\pi/2$ , depending on whether  $C_p$  was assumed to be 0 or  $\infty$ ).

From equation 8 it can be seen that if  $H$  is increased then  $P_n$  decreases (If  $\epsilon$  were independent of  $H$  the variation would be larger).

Since  $C_p$  is complex,  $k_p$ ,  $\epsilon$  and  $K_n$  are also complex. The imaginary part of  $\epsilon$ , which is negative, varies inversely with  $H$ ;  $\Gamma_n$  therefore decreases rapidly as  $H$  increases.

In water of variable depth, the value of each  $K_n$  also varies, and equation 4 would be evaluated using their average values along an acoustic path. These averages would be calculated by expressing  $K_n$  as a function of position in the x-y plane and integrating along the path. (The method of determining the acoustic path will be discussed later).

(2) Stratified profile.

For the stratified case, we consider a sound-speed profile defined by

$$C(z) = \begin{cases} C_w + \Delta C & , 0 < z < H/2 \\ C_w - \Delta C & , H/2 < z < H \\ C_p & , z > H \end{cases} \quad (12)$$

It can be shown (based on the perturbation results obtain by ref 5) that  $K_n$  is now approximately given by

$$K_n^2 \approx k_w^2 - [n(\pi - \epsilon)/H]^2 + 2k_w^2 \epsilon \Delta C [1 - (-1)^n] / \pi C_w \quad (13)$$

We see from equation 13 that if  $\Delta C > 0$  then the result of the stratification is (for odd values of n) to decrease  $P_n$  and to increase  $\Gamma_n$ .

### C. DEPTH FUNCTIONS

(1) Iso-speed profile

The depth function of the n'th mode in an iso-speed profile is approximately given by <sup>5</sup>

$$U_n(z) = \sin [ n(\pi - \epsilon)z/H ] \quad (14)$$

For well-trapped modes,  $\epsilon$  is small (less than 0.5) and the maximum value of the first mode, for example, occurs near  $z = H/2$ .

## (2) Stratified profile

The depth function for the sound-speed profile defined by equation 12 can be obtained either from the perturbation theory series (in terms of the modes for the iso-speed profile)<sup>5</sup>; or, since the eigenvalue  $K_n$  is known (equation 13) the depth function can also be determined more directly.

As was shown in ref 5, the main effect of the stratification with  $\Delta C > 0$  is to increase the depth at which the maximum of the depth function occurs. (For typical cases, the depths of the maxima are around  $0.7H$ ).

## D. HORIZONTAL REFRACTION

If the bottom depth is not constant then unless the source and receiver are directly upslope or downslope from each other, the mode path(s) (in the horizontal plane) joining the source and receiver will not be a straight line. Because of the variation of phase velocity with bottom depth and hence horizontal position, the mode path undergoes horizontal refraction. The effective sound speed, from which refraction in the horizontal plane can be determined, is the phase velocity of the mode.<sup>6</sup> Since phase-velocity decreases as bottom-depth increases, mode paths are refracted towards deeper water.

If the bottom-depth ( $H$ ) is a function only of distance off-shore ( $y$ ), then the mode path can be determined from Snell's Law:

$$P_v = P(y)/\sin \beta(y) \quad (15)$$

where  $\beta$  is the angle between the ray and the  $y$ -axis,

and  $P_v$ , a constant for a ray, is its vertex velocity (where  $\beta = \pi/2$ )

[If the path is directly upslope or downslope, then  $\beta = \pi$  or  $0$  (respectively),  $P_v = \infty$ , and  $\beta$  therefore remains at  $\pi$  or  $0$ .]

A practical procedure for determining the mode path is to divide the y-axis into intervals in each of which  $P(y)$  can be approximated by linear segments. Within each such interval the ray path would be circular with a radius of curvature given by

$$\rho = \frac{P}{v \frac{dP}{dy}} \quad (16)$$

The displacement  $X_i$  parallel to the coast (the x-axis) of a ray passing through an interval ( $y_i$  to  $y_{i+1}$ ) would be

$$X_i = \rho_i (\cos \beta_{i+1} - \cos \beta_i) \quad (17)$$

#### REFERENCES

1. F.B. Jensen and W.A. Kuperman, "Range-dependent bottom-limited propagation modelling with the parabolic equation", in Bottom Interacting Ocean Acoustics, edited by W.A. Kuperman and F.B. Jensen (Plenum Press, New York, 1980) pp 451-466.
2. A.D. Pierce, "Extension of the Method of Normal Modes to Sound Propagation in an Almost-Stratified Medium", J. Acoust. Soc. Am. 37, 19-27 (1965).
3. "Propagation of Short Radio Waves" edited by D.E. Kerr (McGraw-Hill, New York, 1951), p. 65.
4. G.A. Korn and T.M. Korn, "Mathematical Handbook for Scientists and Engineers" (McGraw-Hill, New York, 1961) p.735.
5. A.O. Williams, "Some effects of velocity structure on low-frequency propagation in shallow water." J. Acoust. Soc. Am. 32, 363-371 (1960).
6. D.E. Weston, "Horizontal Refraction in a Three-Dimensional medium of variable stratification", Admir. Res. Lab. Rep. 25/L (1960).

STUDIES OF OPTIMUM FREQUENCY OF SOUND PROPAGATION  
IN AUSTRALIAN SHALLOW WATERS

by

F.P. Fessenden\*, D.J. Kewley and L.T. Sin Fai Lam

Weapons Systems Research Laboratory  
Defence Science and Technology Organisation  
Department of Defence  
GPO Box 2151  
ADELAIDE SA 5001

## 1. INTRODUCTION

Recent experimental studies (references 1 and 2) of acoustic propagation in shallow waters of the northern and eastern North Atlantic and the Mediterranean Sea have shown that an optimum frequency of propagation exists. The causes of the optimum frequency are (reference 1) the loss mechanisms of volume attenuation and scattering at high frequencies and the sea bed bottom interaction effects at low frequencies. The actual value of optimum frequency will depend (reference 1) upon the sea bed bottom type, the shape of the sound speed profile (ie the season) and the water depth. The actual cause of the high losses at low frequencies has been investigated by Jensen and Kuperman (reference 1) using normal mode theory and the results indicated the importance of shear waves in the sea bottom sediment. They characterise the ocean bottom types by their physical parameters such as density, compressional and shear wave speeds and their associated attenuations. Their tabulated data have been deduced from literature and using their modelling.

Results (reference 1, figure 7) over a coarse sand bottom showed that to match the experimental data a shear wave speed of 600 m/s was necessary to be included in the SNAP normal-mode model (reference 3). However, Mitchell and Focke (reference 4) have suggested that as the value of 600 m/s is far greater than the 100 to 300 m/s range usually reported then the conclusions of Jensen and Kuperman may have been affected by limitations in the modelling procedures. They show that the possibility of a compressional wave attenuation gradient (held constant by SNAP) without any shear waves can be used to produce an optimum frequency of propagation. This optimum occurs because the modal penetration depth into the sediment increases with decreasing frequency from say 4 to 8 m at 400 Hz to 20 to 30 m at 50 Hz. If the attenuation was higher at greater depths than 8 m then the 50 Hz signal will have more attenuation than the higher frequencies.

\* Visiting US Scientist from Naval Underwater Systems Centre, New London  
1983-84.

They demonstrated this result using a compressional wave speed of 1650 m/s, a density of 2.0 g/cm<sup>3</sup> and attenuations of 0.74 to 1.23 dB/λ in the first 2 m and held constant at 1.23 dB/λ for greater depths.

The reason for the higher than expected shear wave speed (for SNAP) may be due to the large near surface gradients of compressional wave speed found in sand sediments (reference 5). For typical deep ocean sediments Fryer (reference 6) has shown that coupling between compressional and shear waves due to gradients is negligible above a few Hertz. However these gradients are only of the order of 1 S<sup>-1</sup> while the gradients in sand have been found by Hamilton (reference 5) to be 27 S<sup>-1</sup> at a depth of 1 m. Therefore the frequencies where this effect may occur in sand will be high enough to cause the optimum frequency phenomena in sand sediments.

Here data from two sites on the Australian Continental Shelf are compared with predictions using IFD, a finite-difference parabolic equation model (references 7 and 8), and SNAP. The IFD model can include a very complex layering of sediments and rocks but cannot, as yet, consider shear waves. SNAP can include shear wave effects but cannot include any more than two layers of sediment or rock description.

## 2. GEOACOUSTIC MODELS

The data at Site 1 was for a less than constant bathymetry with an isospeed water profile. The receiver was mounted on the bottom. Although both IFD and SNAP can include variable bathymetry, with different approximations, the calculations were made assuming a constant depth bottom of 75 m.

The sediments are classed as fine or very fine sand which are taken to be 75 m thick overlying sedimentary rock. A number of geoacoustic models were developed for IFD with up to 17 separate layers in the sand to follow the rapid changes in compressional wave speed with depth. However, SNAP can only consider two layers.

A simplification of the IFD layers suggested the model given in Table 1 might be adequate except for the high compressional wave gradients. Since neither IFD nor SNAP can account for compressional-to-shear wave conversion the simplification can be made.

The data at Site 2 corresponded to an isospeed water profile with a constant bathymetry of 105 m. The receiver was at 20 m depth.

The sediments were calcareous down to an assumed depth of 20 m overlying bryozal sandstone (shelf carbonates). The simple two layer model is given in Table 2 and was based upon a simplification of the complex geoacoustic model for IFD. A feature of the model was the increasing attenuation with depth.

### 3. COMPARISON OF PREDICTIONS WITH EXPERIMENTAL DATA

The results of IFD and SNAP calculations for a 16 m source at Site 1 that did not include shear effects showed similar losses. When shear is included in sediment layer for SNAP the difference from the no shear case was very clear and they are shown in figure 1 along with the data. The predictions support the 250 Hz optimum frequency observed. These results are consistent with those of Jensen and Kuperman (reference 1). As the shear was required in the sediment layer, as it had no significant effect when used for the sub-bottom layer, the predictions also support the high gradient hypothesis.

The results of IFD and SNAP calculations for a 18.3 m source at Site 2 were similar to each other. They show an optimum frequency of 125 Hz which is shown by the data in figure 2 along with the SNAP results. For this site the compressional attenuation gradient hypothesis appears to be appropriate.

### 4. CONCLUSIONS

Propagation loss calculations at two sites on the Australian Continental Shelf show, when compared to experiments, that different hypotheses on the cause of an optimum frequency of propagation can be supported. The reason for this appears to be due to the different bottom types at these sites.

### 5. ACKNOWLEDGEMENT

The conversion of SNAP to run on the DRCS IBM 3033 was undertaken by P.S. Keays.

### REFERENCES

- (1) Jensen, F. and Kuperman, W.A.; "Optimum frequency of propagation in shallow water environments", J. Acoust. Soc. Am. 73, 813-819 (1983)
- (2) Akal, T. and Jensen, F.B.; "Effects of the sea-bed on acoustic propagation", SACLANTCEN Memorandum SM-167 (ADA137251), SACLANT ASW Centre, La Spezia, Italy, 16 November 1983
- (3) Jensen, F.B. and Ferla, M.C.; "SNAP: The SACLANTCEN Normal-Mode Acoustic Propagation Model", Rep. SM-121, SACLANT ASW Research Centre, La Spezia, Italy (1979)

- (4) Mitchell, S.K. and Focke, K.C.; "The role of sea bottom attenuation profile in shallow water acoustic propagation", J. Acoust. Soc. Am. 73, 465-473 (1983)
- (5) Hamilton, E.L.; "Sound velocity gradients in marine sediments", J. Acoust. Soc. Am. 65, 909-922 (1979)
- (6) Fryer, G.J.; "Compressional-shear wave coupling induced by velocity gradients in marine sediments", J. Acoust. Soc. Am. 69, 647-660 (1981)
- (7) Botseas, G., Lee, D. and Gilbert, K.E.; "IFD: Wide angle capability", NUSC Technical Report 6905, Naval Underwater Systems Center, New London, 28 October 1983
- (8) Lee, D. and Boseas, G.; "IFD: An Implicit Finite-Difference computer model for solving the parabolic equation", NUSC Technical Report 6659, Naval Underwater Systems Centre, New London, 27 May 1982

TABLE 1. GEOACOUSTIC MODEL FOR SITE 1

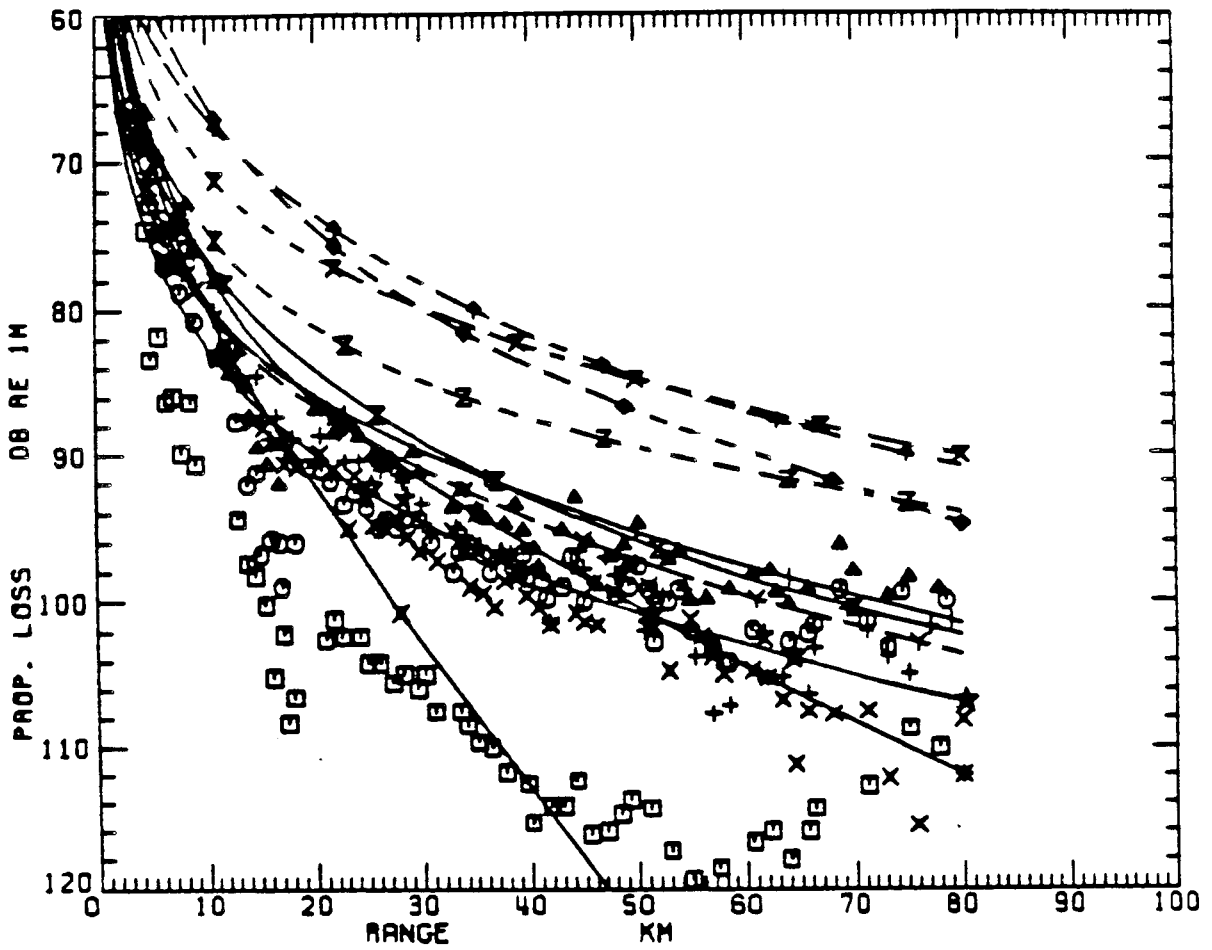
	Density g/cm <sup>3</sup>	Compress. Speed m/s	Shear Speed m/s	Compress. Atten. dB/λ	Shear Atten. dB/λ
Sediment	1.9	1700	600*	0.8	1.5*
Sub-bottom	2.56	3500	-	0.1	-

\* SNAP cases

TABLE 2. GEOACOUSTIC MODEL FOR SITE 2

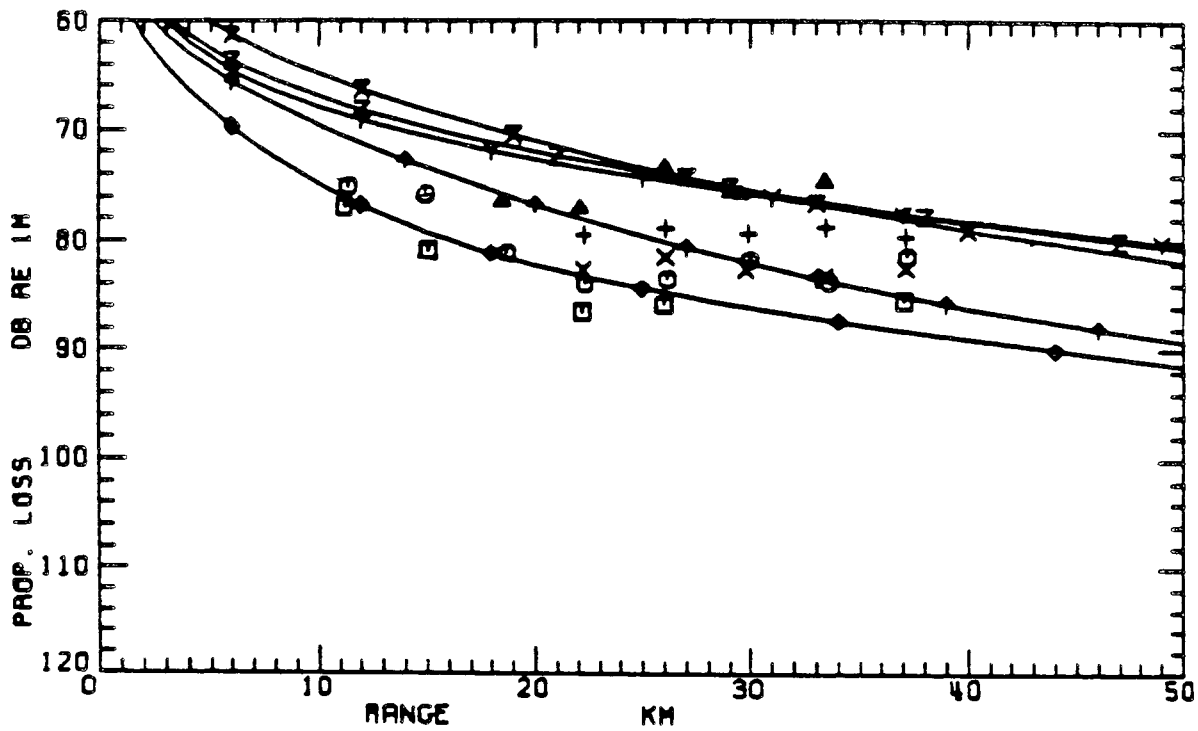
	Density g/cm <sup>3</sup>	Compress. Speed m/s	Shear Speed m/s	Compress. Atten. dB/λ	Shear Atten. dB/λ
Sediment	1.5	1518	150*	0.04	1.5*
Sub-bottom	1.7	1570	-	0.12	-

\* SNAP cases



SNAP		DATA
NO SHEAR	SHEAR	
◆	×	□ FREQUENCY 63.0 HZ
†	✱	○ FREQUENCY 125.0 HZ
×	⊗	▲ FREQUENCY 250.0 HZ
z		+ FREQUENCY 500.0 HZ
y	★	x FREQUENCY 1000.0 HZ

Figure 1. Propagation loss versus range and frequency at Site 1.



SNAP	DATA
◇	□ FREQUENCY 40.0 HZ
⊕	○ FREQUENCY 50.0 HZ
×	△ FREQUENCY 125.0 HZ
+	+ FREQUENCY 315.0 HZ
Y	X FREQUENCY 500.0 HZ

Figure 2. Propagation loss versus range and frequency at Site 2.

Shallow Water Waveguide Characterization  
using the Hankel Transform

George V. Frisk and James F. Lynch  
Woods Hole Oceanographic Institution  
Woods Hole, Massachusetts 02543

A technique for acoustically characterizing shallow water waveguides is described. For a horizontally stratified ocean and bottom, the method consists of measuring the magnitude and phase versus range of the pressure field due to a CW point source and numerically Hankel transforming these data to obtain the depth-dependent Green's function versus horizontal wavenumber. In the context of normal mode theory, the Green's function contains information about the nature of the discrete and continuous modal spectra as well as the plane-wave reflection coefficients of the waveguide boundaries. Inversions are performed using both synthetic data and experimental data obtained in Nantucket Sound, Massachusetts.

The synthetic pressure fields were generated for the cases of an isovelocity water column overlying both hard and fast isovelocity bottoms. The Hankel transform inversions of these fields over reasonable experimental apertures (1-5 km) yield excellent results for the Green's functions, while the subsequently calculated reflection coefficients of the bottom are of somewhat lower quality. The results improve with larger aperture.

The experimental data were obtained at 140 Hz and 220 Hz over an aperture of 1325 m. Modal interference patterns in the pressure fields and modal peaks in the Green's functions are clearly observed at both frequencies. Synthetic pressure fields were also generated and inverted for a Pekeris case using an approximate geoacoustic model based on archival data for the area. The synthetic and experimental data exhibit similar features. The synthetics indicate the dominant influence of two trapped modes at 220 Hz, and one trapped mode and one virtual mode at 140 Hz.

The experimental and synthetic data studies described indicate that the Hankel transform inversion technique has considerable promise as a means of acoustically characterizing shallow water waveguides.

DETERMINING AMBIENT NOISE DUE TO WIND AND WAVES  
USING MEASURED SURFACE SOURCE LEVELS

by

A.S. Burgess and D.J. Kewley

Weapons Systems Research Laboratory  
Defence Science and Technology Organisation  
Department of Defence  
GPO Box 2151  
ADELAIDE SA 5001

## 1. INTRODUCTION

Surface source levels for wind-generated noise were measured in a series of experiments analysed by the authors and reported elsewhere (references 1 and 2). This paper discusses the relationship between the surface source level and the observable omnidirectional ambient noise level. Some of the more important approximations introduced into the earlier analyses are discussed (particularly the hemispheric isotropy) and correction curves, to be applied to omnidirectional noise predictions at several typical Australian ocean areas, are given.

The relationship between the surface source level, as defined here, and the wind source level representations employed by Wilson (references 3 and 4) are explained.

## 2. SURFACE SOURCE LEVEL AND LOCAL NOISE LEVEL

The relationship between the measured surface levels (SL) and local omnidirectional noise level (NL) was given in reference 1 as

$$NL = SL + A + 8.0 \text{ dB re } 1\mu\text{Pa}^2/\text{Hz} \quad (1)$$

where A is an amplification factor resulting from multiple reflections at the bottom and surface (ie, dependent upon bottom loss) and 8.0 (= 10 log (2π)) is a constant resulting from the integration of the sound intensity over a hemisphere. The noise will be hemispherically isotropic only in an isovelocity ocean where the sea bottom grazing angle versus bottom loss relationship balances out the source directivity pattern eg a constant bottom loss at all angles is matched to a dipole source pattern.

Thus equation (1) could be either for a monopole or dipole surface source radiation pattern depending upon the bottom loss relationship with grazing angle. For real oceans refraction effects occur for sound arriving from shallow elevation angles and this also results in significant departures from the assumption of hemispheric isotropy for the sound vertical directionality. The effect of both bottom loss grazing angle dependence and the sensitivity of the results to the prevailing propagation loss conditions are investigated using the RANDI program of Wagstaff (reference 5) to predict the vertical noise directionality and the resulting omni ambient noise level. It is found that the original total omnidirectional noise level predictions are frequently somewhat low, and the effects are more noticeable at sites with good long range propagation and are more significant at lower frequencies.

Therefore equation (1) is generalised to become

$$NL = SL + A + 8 + P \text{ dB re } 1\mu\text{Pa}^2/\text{Hz} \quad (2)$$

with the addition of the profile factor, P, which is a measure of the deviation away from the hemispheric isotropy assumption. Figures 1 and 2 show the values of SL, versus frequency and A that are needed to calculate omnidirectional ambient noise due to wind. Note that the units of SL are dB re  $1\mu\text{Pa}^2/\text{sr-Hz}$  and are equivalent to dB re  $1\mu\text{Pa}^2/\text{Hz-m}^2$  at 1 m. The A factor is derived in reference 1, and based on the normal incidence bottom loss. To extend the model to cases with non-uniform bottom loss (angular dependence) the bottom loss is now specified at 45 degrees. The P-factor can be considered to depend upon whether the bottom loss has variation with angle of incidence, and upon whether the propagation conditions are bottom limited or support RSR paths. Figure 3 shows some values of P versus frequency for typical sites around Australia.

The P-factor is sensitive to the assumed radiation pattern of the surface sources and the original model in the RANDI program is replaced in these predictions with one having a higher frequency transition to a dipole-like pattern. The model now gives predictions with an acceptable fit to the measured omni levels (reference 1) at the higher wind speeds.

### 3. COMPARISON WITH WILSON'S WIND NOISE MODEL

The wind-generated surface source levels published by Wilson (reference 3), and used to predict local (reference 3) and distant (reference 4) storm noise, are related to the local wind noise by

$$\text{LWN} = \text{SW} + 4.97 \text{ dB re } 1\mu\text{Pa}^2/\text{Hz}$$

where SW is Wilson's source level and 4.97 ( $= 10 \log \pi$ ) is the profile factor for a dipole source in a homogenous medium with very high bottom loss. However, to get the absolute level correct Wilson fitted the theory to experiment (see reference 6 equation 4) so the effects of the A factor which will probably be frequency dependent have not been removed. Therefore his absolute values depend upon A being negligible. However figure 2 in reference 4 shows that his predicted levels are a little high.

This result suggests that the appropriate A factor is about 3 dB (ie, the bottom loss at 165 Hz was 5 dB). This value is similar to the values measured in reference 1 for deep ocean sites. Using the typical values of reference 1 and calculating the case of figure 3 in reference 3 excellent agreement with the measured data for his deepest hydrophone was obtained using equation (1). Similarly the predictions for 165 Hz on figure 2 of reference 4 are below the experimental points as desired. These results demonstrate that our source levels are not site dependent, like those of Wilson, and can predict noise at different sites once the A and P factors are known.

#### 4. CONCLUSIONS

It is concluded that the method of measurement of the effective radiated noise level (in radiated intensity per square metre) by means of a directional array of sensors steered toward the surface from below is valid, but that the prediction of the ambient noise level to be expected at an omnidirectional receiver due to this origin is more complicated than could be accounted for in the original simplistic model. For accurate predictions a knowledge of both the bottom reflection loss as a function of angle of incidence and frequency, and the sound velocity variation with depth are needed.

#### REFERENCES

- (1) Burgess, A.S. and Kewley, D.J.; "Wind-generated surface noise levels in deep water east of Australia", J. Acoust. Soc. Am. 73, 201-210 (1983)
- (2) Kewley, D.J. and Burgess, A.S.; "Measurements of Wind-generated noise levels in the Eastern Indian Ocean", J. Acoust. Soc. Am. 74, S123 (1983)
- (3) Wilson, J.H.; "Wind-generated noise modelling", J. Acoust. Soc. Am. 73, 211-216 (1983)

- (4) Wilson, J.H.; "Distant storm noise versus local wind noise at 165 Hz in the north eastern Pacific Ocean", J. Acoust. Soc. Am. 74, 1500-1504 (1983)
- (5) Wagstaff, R.A.; "RANDI: Research Ambient Noise Directionality Model", Naval Ocean Systems Center Report NUC TP 349, April 1983
- (6) Wilson, J.H.; "Low-frequency wind-generated noise produced by the impact of spray with ocean's surface", J. Acoust. Soc. Am. 68, 952-956 (1980)

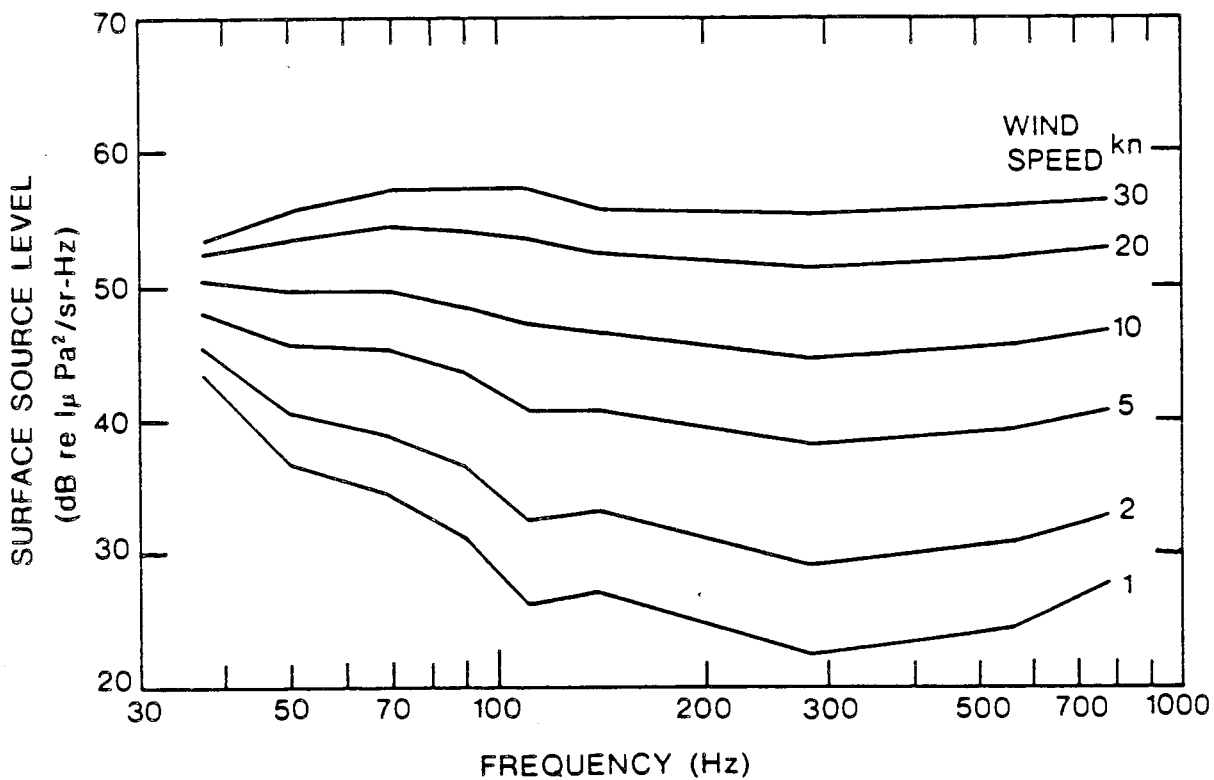


Figure 1. Surface source levels for various wind speeds.

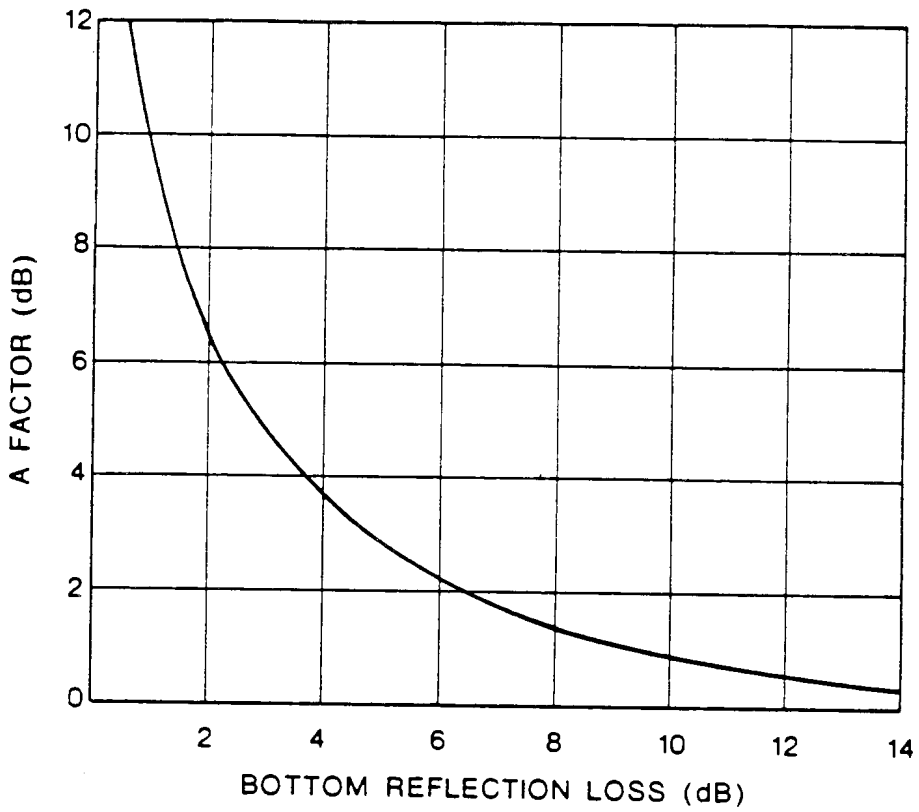


Figure 2. The amplification Factor A used to include the effect of bottom reflection loss on the total omnidirectional noise field.

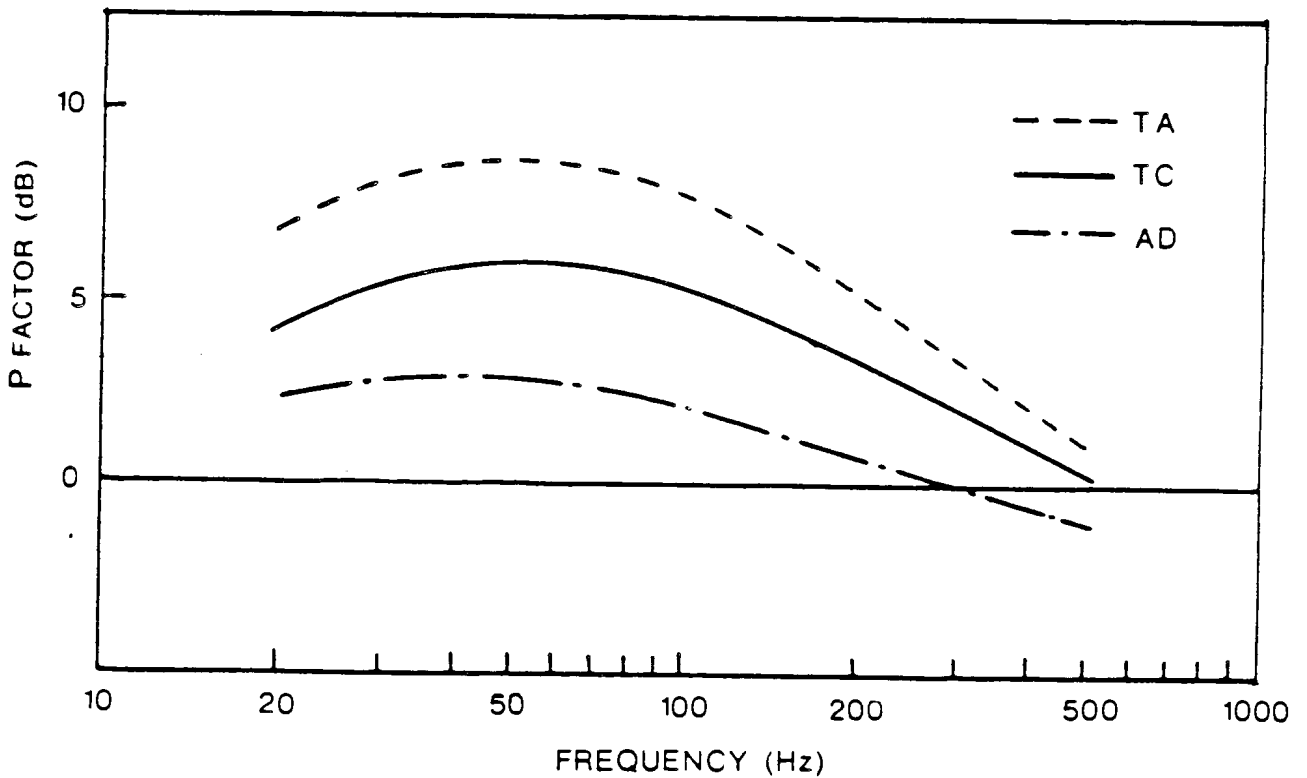


Figure 3. Typical examples for the P-factor frequency dependence in the Australian area.

## INFRASONIC AMBIENT NOISE IN THE OCEAN

by

A.C. Kibblewhite and K.C. Ewans

A B S T R A C T

The underwater acoustic noise field is known to be wind dependent. Several mechanisms have been proposed to explain the transfer of energy from the wind to the acoustic noise field. One of these considers the noise-source to lie in turbulent pressure fluctuations in the atmospheric boundary layer, a second considers the role of non-linear interactions between ocean surface waves, and a third examines the interaction of both surface waves and turbulence.

Because reliable ambient noise data are sparse at frequencies below 10Hz, it has been difficult to assess the agreement between theory and experiment. The difficulties at these frequencies have arisen through problems of self-noise in the monitoring hydrophone system and in deficiencies in the environmental data. While the lack of precise data has not permitted definite identification, there is some evidence to suggest that non-linear wave-wave interactions and/or turbulence are the most likely wind related noise generating mechanisms.

This particular study has examined these mechanisms by looking at that part of the acoustic spectrum which overlaps the frequency range of high frequency seismics. Correlations between the ocean-wave field and the ocean-induced seismic activity detected by a land-based long period seismometer, have been examined. The quality of the data, the long term nature of the observations and a unique property of the recording environment have clarified the role of non-linear wave-wave interactions in ocean-wave and ocean-noise processes. It is concluded that the ocean ambient noise below 5Hz is controlled by non-linear interactions and that above this frequency turbulence becomes dominant. It is shown further that while the noise field is clearly a function of both the wind and wavefields, existing theories account adequately for the effects observed.

NOISE GENERATION AT THE SEA SURFACE: RECENT  
THEORETICAL AND EXPERIMENTAL WORK

Douglas H. Cato  
R.A.N. Research Laboratory  
P.O. Box 706  
Darlinghurst, NSW 2010  
AUSTRALIA

This paper describes the application of a general theory of noise generation at the sea surface by Cato and Jones (1982) to predict noise from surface wave interaction. The results are compared with a carefully controlled experiment in enclosed waters in which the effect of bottom reflections is included. The results show good agreement between theory and measurement.

The theory of sea noise generation of Cato and Jones is a development of the classic work by Lighthill (1952) on sound generation in fluids. The theory is developed from first principles without approximations for an ocean which is statistically homogeneous in the horizontal plane and results in a general relationship between the received sound pressure spectrums  $P(\omega, z)$ , at frequency  $\omega/2\pi$  and depth  $z$ , and the frequency wave number spectrum  $\phi_{ijklm}(\omega, \underline{k})$  of the fluid properties inherent in noise generation: mass flux  $\rho u_i$ , momentum flux  $\rho u_i u_j$  and stress  $p_{ij}$ . Here  $i, j, l, m$  are tensor subscripts,  $\rho$  is density and  $u_i$  velocity. The expression is of the form

$$P(\omega, z) = \int_{-\infty}^{\infty} \phi_{ijklm}(\omega, \underline{k}) H_{ij}(\omega, \underline{k}, z) H_{lm}^*(\omega, \underline{k}, z) dk / (2\pi)^2 \quad (1)$$

$H_{ij}(\omega, \underline{k}, z)$  is a "coupling factor" which determines how well the source spectral components couple to the receiver and contains the effects of propagation, source directivity and phasing (retarded time).  $H_{ij}$  may be interpreted as integrals over the ocean surface of the "wave" part of the source spectral components. Analytical expressions for  $H_{ij}$  have been obtained and, although fairly complicated, simplifications can be made applying to a wide range of conditions of interest. For a dipole

distribution where the axis of maximum radiation is vertical, and for ocean of dimensions large compared to the acoustic wavelength and receiver depth (conditions normally applying) equn. (1) can be reduced to,

$$P(\omega, z) \approx \frac{1}{16\pi^2} \int_{|k|=0}^{\omega/c} \phi_{ijlm}(\omega, \underline{k}) d\underline{k} \quad (2)$$

where  $c$  is the speed of sound. This result may be applied to any mechanism of noise generation. The difficulty, as with any theory of noise generation at the sea surface, is in modelling or measuring  $\phi_{ijlm}(\omega, \underline{k})$ , owing to our limited understanding of the dynamics of the sea surface.

So far, we have applied this result to determine noise from non linear effects in surface wave orbital motion in which the source term  $\rho u_i u_j$  is appropriate. This is effectively the same mechanism as non linear wave interaction addressed by Brekhovskikh (1966), Hughes (1976) and Lloyd (1981) but they used a different theoretical approach with approximations not used in our theory. Also, whereas we show that significant noise is generated by dipoles with both vertical and horizontal axes, these authors treated noise from dipoles with vertical axes only. As these authors show, acoustic waves are generated by surface wave interaction only when waves of almost equal wave length, and travelling in almost opposite directions meet. Although ocean swell appears to be almost unidirectional, the smaller scale waves generated directly by wind action have energy spread over a broad range of directions so that there is significant energy in waves travelling in opposite directions.

Determination of  $\phi_{ijlm}(\omega, \underline{k})$  for this mechanism is a long and involved process which includes the following steps:-

- (a) relating the frequency spectrum of surface wave height to that of orbital velocity  $u_i$

- (b) relating the frequency spectrum of  $u_i$  to its frequency wave number spectrum using the measured directional spectrum of surface wave energy and using the fact that the frequency and wave number of surface waves are uniquely related
- (c) relating the frequency wave number spectrum of  $u_i$  to that of  $\rho u_i u_j$ .

The final result gives noise as a function of the wave height spectrum at half the acoustic frequency.

Some measurements have been made in Woronora Dam, near Sydney, which is about 1 km across. The hydrophone with preamplifier were on the bottom, water depth 35 m, near the centre of the dam and connected by cable to a pontoon about 100 m away where wave height and wind speed were measured. This site allowed much more experimental control than at sea, and the absence of man made noise avoided the problem of shipping noise inherent in measurements at sea. Considerable care was taken to minimise the possibility of system flow noise by use of fairings and ensuring the cable from the hydrophone was on the bottom for some distance before it rose under the pontoon. The system response was 3 dB down at 0.3 Hz and 24 kHz. The wave height was measured by detecting the change in capacitance of an insulated wire, 6 Hz being the -3 dB point in the upper limit of the response.

A comparison between measurements from this experiment and theoretical predictions was presented at the 11 International Congress on Acoustics (Cato, 1983). The theory and measurements showed a spectral peak at 2 Hz, twice the frequency of the peak in the wave height spectrum. The noise spectrum from this mechanism falls rapidly with frequency and was found to be insignificant compared to other noise at frequencies above 4 Hz. Although there was good agreement between theory and measurement, no allowance was made for bottom reflections in the theory, i.e. the bottom was assumed to be perfectly absorbing. Since then the contribution from bottom reflections has been modelled.

The bottom of Woronora Dam consists of sandstone overlain by sediment. However, since the thickness of the sediment was very much less than an acoustic wavelength the sediment was assumed to have a negligible effect on the bottom reflectivity. The reflectivity and phase change on reflection from the bottom was determined by the conventional method of matching stresses and displacements at the boundary, (Brekhovskikh, 1980). Bottom loss was calculated to be about 4 dB with no phase change for grazing angles above the critical angle. At lower grazing angles, losses were up to 8 dB decreasing to zero at grazing incidence with phase change increasing with decreasing angle to a maximum at  $180^{\circ}$ . The effect of bottom reflections on the received noise was determined by summing coherently the contribution of as many bottom reflected paths as contributed significantly, making allowance for the directivity of the source. The result was then compared with that of the direct path only, which is equivalent to the theoretical prediction for a perfectly absorbing bottom.

The results are complicated by the interference between the incident and reflected fields for any path. At low grazing angles this interference becomes destructive because of the large phase change on reflection. In the case of the dipoles with horizontal axes (of maximum radiation), paths with up to 8 bottom reflections needed to be included in the calculation. The effect of bottom reflections was to cause an enhancement of about 2 dB in received noise from sources close to the receiver and a reduction of about 5 dB for distant sources. The total effect is that noise from the dipoles with horizontal axis is about 2.5 dB lower when bottom reflections are included than for the direct path only.

In the case of the dipoles with vertical axes, paths with up to 14 reflections must be included. This is because the steeper rays with larger numbers of bottom reflections leave the source at angles of greater radiation efficiency than the low angle rays, and this to some extent compensates for the higher bottom loss from the multiple reflections. The result is a complicated variation, with source range, of the effect of bottom reflections from about 2 dB enhancement to 4 dB reduction. The

total effect is less than  $\frac{1}{2}$  dB reduction in the received noise from these dipoles when bottom reflections are included. Since these dipoles contribute more to the received noise than those with horizontal axes, we expect this result to dominate.

When the contributions from all sources are included we find that the effect of bottom reflections is to reduce the received noise by slightly less than 1 dB. Thus we maintain a good agreement between the theory and measurement. The complicated way in which the many paths and their incident and reflected fields interaction indicate the inadequacy of simple models of bottom reflected effects. The contribution from each path depends on correctly allowing not only for the loss and phase change on reflection for the various ray paths but also for the way in which the radiation efficiency of the source varies with ray angle.

#### REFERENCES

- L.M. Brekhovskikh (1980) *Waves in Layered Media*, Academic, New York, 2nd ed.
- L.M. Brekhovskikh (1966) *Izv. Atmos. Ocean Phys.*, 2, 582.
- D.H. Cato and I.S.F. Jones (1982) Marine Studies Centre Technical Report 2/82, University of Sydney.
- D.H. Cato (1983) *Proc. 11 International Congress on Acoustics*, Paris, July 1983, Vol. 2, 449-452.
- G. Hughes (1976) *J. Acoust. Soc. Am.*, 60, 1032.
- M.J. Lighthill (1952) On sound generated aerodynamically: I. General theory. *Proc. Roy. Soc. (Lon.) Series A*, 211, 564.
- S.P. Lloyd (1981) *J. Acoust. Soc. Am.*, 62, 425.

THE PROBLEMS IN PREDICTING SEA SURFACE NOISE IN THE  
FREQUENCY BAND 10 Hz to 200 Hz

Douglas H. Cato  
R.A.N. Research Laboratory  
P.O. Box 706, Darlinghurst  
N.S.W. 2010, Australia

This paper discusses the uncertainty in predicting sea surface generated noise in the frequency range 10 Hz to 200 Hz. Empirical methods are fairly ineffective because of the limited amount of data, the widespread of data at a particular wind speed, and the difficulty in removing the contribution from other sources such as flow noise. Theoretical methods are also unreliable because of the uncertainties in the models due to our lack of knowledge of sea surface dynamics. In addition some errors and misleading manipulations in published theoretical work have confused the issue.

Noise generated at the sea surface extends over a frequency range from a fraction of one Hertz to at least tens of kiloHertz. There appear to be a number of mechanisms of noise generation and it is convenient to consider three frequency regimes where different mechanisms are dominant: (a) below 5 Hz (b) 5 Hz to 200 Hz (c) above 200 Hz. The regime above 200 Hz is the best known and there is a large amount of data available. There have been prediction methods for this frequency range since Knudsen, Alford & Emling (1944), the best known probably being those of Wenz (1962). Although it is generally accepted that the mechanisms of noise generation are related to the breaking of waves, the impact of droplets and the bursting of bubbles there appears to be no theoretical model of noise generation. However measurements of the noise on impact of water drops in controlled experiments (Franz, 1959) have been found to be spectrally similar to the sea surface noise above 200 Hz.

In the regime below 5 Hz there have been few measurements but some theoretical work. Perhaps it would be more accurate to say that most of the theoretical work on noise generation at the sea surface has turned out to apply to the mechanism that is dominant below 5 Hz. Brekhovskikh (1966) was first to apply to underwater noise the theory of non linear wave interaction, and this was later developed further by Hughes (1976) and Lloyd(1981). Although the agreement with measurement was not particularly good, a different theoretical approach by Cato & Jones (1982) applied to the same mechanism (Cato, 1983; and paper this conference) has resulted in good agreement between theory and measurement. These results clearly show that noise by this mechanism falls rapidly with increasing frequency and would not be significant compared with other measured noise above about 5 Hz.

Much less is known about the sea surface generated noise in the region 5 Hz to 200 Hz and our ability to predict the noise in this frequency range is poor. There are two problems in obtaining reliable measurements of this noise component. These are (a) separating out the wind dependent noise from traffic noise (the noise of distant shipping) (b) avoiding contamination from "flow noise". Both traffic noise and flow noise appear to be spectrally similar to the surface generated noise. "Flow noise" results from non acoustic pressure fluctuations due to relative motion of the hydrophone and the surrounding water. Even a bottom mounted system is not immune to flow noise as loose loops of cable or protruberances can cause vortices to be shed in the current, as we have found. Empirical estimates of wind dependent noise are usually obtained by plotting noise in decibels as a function of the logarithm of the wind speed thus separating out the wind dependent and non wind dependent components. This method does not necessarily work for flow noise as the relative hydrophone motion may increase as sea state increases. So many measurements have been obtained in areas of high traffic noise that the amount of data relatively free of traffic noise and flow noise is fairly small. This paper makes a comparison of available measurements of wind dependent noise at 10 Hz in which data obtained on systems which are likely to have induced flow noise have been excluded. Data points have been plotted as a function of wind

speed. In the data points of any set of measurements there is a clear trend of increasing noise with increasing wind speed at the higher wind speeds. When a comparison is made of wind dependent data from all sets of measurements there is a spread of about 20 dB at any wind speed. Thus there is considerable uncertainty in predicting noise empirically. Presumably, some of the variation is due to varying propagation conditions. There may be other parameters which affect noise generation such as the roughness at the sea surface.

A number of theories have addressed sea surface noise at low frequencies. As discussed above, the latest work on non linear wave interaction indicates that it would not be significant above about 5 Hz, so we look to other mechanisms for the frequency range 10 Hz to 200 Hz. There is some evidence to suggest that the mechanism addressed by Isakovich and Kuryanov (1970) is the most likely source of noise in this frequency range. They examined noise from pressure fluctuations induced by wind turbulence over the ocean surface. Prediction of noise requires a knowledge of the frequency wave number spectrum of the turbulent pressure fluctuations. There are considerable difficulties in either measuring or modelling this spectrum. Isakovich and Kuryanov developed a rather ingenious model for this, but it contains some limitations and uncertainties forced on them by the limitations in our knowledge of sea surface dynamics. As a result, there would be some uncertainty in using this theory to predict noise, but no better model of the turbulent pressure fluctuations is available. The wide spread in measured noise means that theories cannot be reliably tested by existing data.

The situation has become rather confused by later work by Wilson (1979) who claimed to have corrected errors in, and improved on, Isakovich and Kuryanov's theory. In fact Wilson used the same model but with more recent estimates of surface wave height spectrum and wave attenuation, and a different evaluation of an integral using less approximations than Isakovich and Kuryanov. Unfortunately, Wilson made errors in this evaluation which resulted in an error of about 20 dB in

the final noise levels (Cato, 1981), his predictions being 20 dB lower than they should have been. The errors in Isakovich and Kuryanov's approximate evaluation varied with frequency from about 3 to 8 dB. When Wilson was advised of the errors in his evaluation he changed the value of a parameter, the coefficient of wave attenuation  $\alpha_0$ , by an amount which compensated for the error in the evaluation, and thus claimed that his noise predictions remained unchanged (Wilson, 1981). There is no physical justification for his change (a reduction) in the value of  $\alpha_0$  and in fact his new value is physically impossible since it is less than the lowest possible value: that due to purely molecular viscosity. In Isakovich and Kuryanov's theory, the received noise pressure spectrum is directly proportional to  $\alpha_0$ , hence one can vary the noise predictions at will by varying  $\alpha_0$ . However,  $\alpha_0$  is not an arbitrarily chosen constant but a known physical quantity, the coefficient of wave attenuation, and must be chosen from the best theoretical or empirical data. Thus Wilson's noise predictions are about 20 dB lower than they should be, if Isakovich and Kuryanov's theory is used correctly and the correct values of input parameters are used.

Yen and Perrone (1979) have also examined theoretically the noise from turbulent pressure fluctuations over the sea surface but were also limited by lack of information on the structure of the turbulence.

When a comparison of the sea surface noise predictions obtained from available theories is made there is a spread of about 20 dB in the noise prediction at any wind speed. Some of this variation is due to the inclusion of estimates of wave-wave interaction which at the time were considered applicable in this frequency range but, as previously discussed, appear not to be the dominant component at this frequency. Even so, considering the uncertainty in the models due to our lack of understanding of sea surface dynamics, there must be considerable uncertainty in predicting the noise theoretically.

Thus there are considerable uncertainties in predicting noise at 10 Hz either theoretically or empirically. We will improve this situation only by improved theory and experiment. We need to

obtain reliable measurements over a wide range of wind speeds in areas of low traffic noise and using systems in which every effort has been made to minimise flow noise. In addition, other parameters likely to effect noise generation should be measured. Just what are the most appropriate parameters can only be obtained by improved understanding of noise generation mechanisms. Presumably, the wave height spectrum is a likely contender. In addition, of course, we need to know how propagation conditions at the site affect the received noise levels. Improvements in theory require a better understanding of sea surface dynamics including air sea interaction. Tests of a theory require more than simply a comparison of theory and measurement at a particular wind speed, since there is a spread of about 20 dB in available data. The theory also needs to predict the observed, non wind dependent, variation evident at a particular wind speed.

#### REFERENCES

- L.M. Brekhovskikh (1966) Underwater sound waves generated by surface waves in the ocean. *Izv. Atmos. Ocean Phys.*, 2, 582.
- D.H. Cato and I.S.F. Jones (1982) The sound field generated by fluid motion in a horizontally homogeneous ocean. Marine Studies Centre Technical Report 2/82, University of Sydney.
- D.H. Cato (1981) Comments on "Very low frequency (VLF) wind-generated noise produced by turbulent pressure fluctuations in the atmosphere near the ocean surface". *J. Acoust. Soc. Am.*, 70, 1783.
- G.J. Franz (1959) Splashes as sources of sound in liquids. *J. Acoust. Soc. Am.*, 31, 1080.
- G. Hughes (1976) Estimates of underwater sound (and infrasound) produced by non linearly interacting ocean waves. *J. Acoust. Soc. Am.*, 60, 1032.
- M.A. Isakovich and B.F. Kuryanov (1970) Theory of low frequency noise in the ocean. *Soviet Physics - Acoustics*, 16, 49.
- V.O. Knudsen, R.S. Alford and J.W. Emling (1944) *Survey of underwater sound*, Report No.3, ambient noise, OSRD Report No.4333 (Publication Board, Dept. Commerce, Washington D.C.).

- S.P. Lloyd (1981) Underwater sound from surface waves according to the Lighthill-Ribner Theory. *J. Acoust. Soc. Am.*, 62, 425.
- G.M. Wenz (1962) Acoustic ambient noise in the ocean: spectra and sources. *J. Acoust. Soc. Am.*, 34, 1936.
- J.H. Wilson (1979) Very low frequency (VLF) wind-generated noise produced by turbulent pressure fluctuations in the atmosphere near the ocean surface. *J. Acoust. Soc. Am.*, 66, 1499.
- J.H. Wilson (1981) Erratum to Wilson (1979). *J. Acoust. Soc. Am.*, 69, 1517.
- N.C. Yen and A.J. Perrone (1979) *Mechanisms and modelling of wind induced low frequency ambient sea noise*. NUSC Tech. Report 5833, U.S. Naval Underwater Systems Center, New London, Connecticut.

DETERMINING THE HORIZONTAL DIRECTIVITY OF AMBIENT NOISE  
USING A TOWED ARRAY

by

R Marrett  
Defence Scientific Establishment  
Auckland, New Zealand

Introduction

1 For a number of years the mainstay of the passive acoustics programme at DSE has been a towed array, now incorporated into DSE's towed array data acquisition system. The towed array is a versatile instrument, easily deployed, and highly mobile. It is currently used for a variety of experiments whose overall aim is the assessment of the effect of environmental factors on the performance of present and future sonars in the New Zealand area.

2 One of these factors which is of considerable importance, particularly for the performance prediction of directional passive sonars, is the horizontal directionality of the ambient noise field. Since major shipping lanes are not a feature of the New Zealand environment, it is of interest to determine whether other sources of noise, such as distant storms, produce significant effects at various sites.

3 Since the towed array is a horizontal line array, noise field estimates from a single array orientation (heading) are symmetric. To obtain a non-ambiguous estimate, measurements must be utilised from two or more array headings derived from separate "legs" of a polygonal track.

4 The direct utilisation of "primary" data (hydrophone measurements) to estimate the ambient noise field can be expected to provide the best results. However, owing to the amount of data which is involved, some form of preliminary data reduction is invariably employed. This discussion will focus on the estimation of the ambient noise field from "beam data", that is spectral data from the output of a beamformer with known, or assumed, characteristics, at a particular frequency of interest.

5 Several techniques have been published which attempt to utilise beam data for the estimation of the ambient noise field. This paper presents a new approach which utilises Jaynes' principle, also known as the maximum entropy criterion, to arrive at an ambient noise field estimate.

The maximum entropy approach

6 The general approach for utilising the maximum entropy principle is to formulate the quantities being estimated as proportions or probabilities  $p_i$ ,  $i = 1, \dots, r$ , with  $\sum p_i = 1$ , and then maximise the entropy function

$$e(p) = - \sum_{i=1}^r p_i \log(p_i)$$

subject to any constraints imposed on the  $p_i$  by the data or available information. In this context, the entropy function can be thought of as measuring the lack of "structure" in the set  $\{p_i\}$ . A low value implies considerable structure is incorporated in  $\{p_i\}$ , with the minimum ( $e = 0$ ) being achieved when  $p_j = 1$  for some  $j$ , and  $p_i = 0$  for  $i \neq j$ . Thus Jaynes' principle in effect says that the best estimate of the set of  $p_i$  is obtained by incorporating the minimum structure necessary to satisfy known constraints.

7 The horizontal directivity problem may be formulated as follows.

Let  $n_{kl}$  be the "measured" beam level for beam  $k$  on leg  $l$ , and  $b_{kl}$  be the (unknown) component due to the ambient noise  $a(\theta)$ . Then

$$n_{kl} = b_{kl} + r_{kl} \tag{1}$$

where  $k = 1, \dots, K$ ,  $l = 1, \dots, L$  and  $r_{kl}$  is the (unknown) residual. Without loss of generality it can be assumed that  $\sum n_{kl} = 1$ . Jaynes' principle then suggests estimation of  $b_{kl}$  and  $r_{kl}$  by maximising

$$e = - \sum \sum b_{kl} \log b_{kl} - \sum \sum r_{kl} \log r_{kl}$$

or in vector notation,

$$e = -b^t \log b - r^t \log r, \tag{2}$$

subject to any constraints imposed by measured data or known information. From (1) we can immediately write

$$e = -b^t \log b - (n-b)^t \log (n-b) \tag{3}$$

8  $b_{k1}$  is related to the ambient noise field  $a(\theta)$  via the beam response function  $f_k$  as follows

$$b_{k1} = \int_0^{2\pi} f_k(\theta - \phi_1) a(\theta) d(\theta)$$

where  $\phi_1$  is the array heading for leg 1. This can be written in discrete form for all beams of leg 1 as

$$b_1 = B H_1 a^1 \quad (4)$$

where  $B$  is the beam response matrix for an array heading of  $0$  degrees,  $H_1$  is a permutation matrix which rotates the beams according to the array heading on leg 1, and  $a^1$  is the ambient noise field  $a(\theta)$  discretised to an appropriate resolution. For 1 degree resolution,  $a^1 \in \mathbb{R}^{360}$ .

9 While a resolution of 1 degree is necessary for adequate representation of the beam response function, it is not realistic to expect this in the final noise field estimate. Consequently, it is convenient to allow a lower resolution in the final result by writing

$$a^1 = P a$$

where  $P$  is an interpolation matrix, and  $a \in \mathbb{R}^r$  is the representation of the ambient noise field to a resolution  $r < 360$ . Equation (4) may then be written as

$$b_1 = B H_1 P a$$

or, for all legs  $l = 1, \dots, L$ , as

$$b = B^l a \quad (5)$$

where  $B^l = \begin{bmatrix} B & H_1 \\ \vdots & \\ B & H_L \end{bmatrix} P$

10 Equation (5) may now be substituted into (3) to give the entropy in terms of  $a$  as

$$e = - (B^l a)^t \log (B^l a) - (n - B^l a)^t \log (n - B^l a)$$

This function now includes all information except for the non-negativity constraints  $B^1a \geq 0$  and  $(n-B^1a) \geq 0$ . It may therefore be maximised using unconstrained maximisation techniques such as the method of steepest ascent, where the partial derivatives are given by

$$\frac{\partial e}{\partial a} = (B^1)^t (\log (n-B^1a) - \log (B^1a))$$

### Conclusion

11 A series of tests using simulated data has shown that the method described works well in non-ideal situations. The minimisation of spurious structure in the final estimate is characteristic of the maximum entropy approach and renders the method well suited for use in this application, where contamination of data can be considerable.

IS THERE A SUBMARINE VOLCANO IN THE TASMAN SEA?

by

L H Hall  
Defence Scientific Establishment  
Auckland, New Zealand

During the 27-30 June 1981 deployment of the DSE towed array sonar system in the vicinity of  $46^{\circ}\text{S}$ ,  $164^{\circ}\text{E}$ , numerous large amplitude transients were detected from a fixed bearing roughly to the north of the deployment area.

The paper begins by outlining the system used to detect these transients. The general features of the transients are then described and it is shown that the transients were water-borne and were neither instrumental in origin, array generated nor travelling through the sea floor near the array as would locally generated seismic waves.

An estimate of the bearing line of the transients is then made. Propagation loss has been measured on the north trending portion of the Lord Howe Rise along which this bearing line passes but the estimated propagation losses from a source on this line to the receiving array are too low to permit a bounding of the range, given the possible source levels. Bathymetric blocking from the rather sparsely surveyed northern part of the Lord Howe Rise would probably preclude transmission paths extending to the Solomon Islands.

It is considered that the most likely source of the transients is underwater volcanism. The Lord Howe Rise has a Mohorovicic discontinuity at about 26 km, a depth typical of continental crust. It is generally considered that the Lord Howe Rise was once adjacent to the eastern margin of the Australian continent and that when the Tasman Basin opened up it was moved to its present position, relative movement ending about 60 million years ago. Episodes of explosive volcanicity in the Tasman Rise since that time are evident as ash layers in cores obtained by the Deep Sea Drilling Programme. Bentz<sup>1</sup> has reported evidence of a large number of volcanic peaks on the southern Lord Howe Rise. Many of these peaks are surrounded by features which he interprets as the sub-aqueous equivalents of tuff rings. Consequently, the eruptions are taken by him as being explosive in nature, and because the tuff rings have not been smoothed out or

covered by sediment, he concludes they are of recent origin. He writes of "recurrent and still active submarine volcanism".

If it accepted that the transients could be produced by a submarine volcano, then there are a number of possible noise producing mechanisms including explosions caused by the exsolution of dissolved water from magma, by thermally induced hydraulic fracturing, or by the rupture of a solidified lava skin and the ejection of molten lava or very hot rock into the surrounding water or by implosions caused by the collapse of pillow lava.

The towed array has been deployed in the Tasman a number of times and only once have these transients been detected. A second detection of similar transients but with a quite different bearing is required if further investigation into their origin is to be possible.

- 
- 1 Bentz F P 1974. Marine Geology of The Southern Lord Howe Rise, Southwest Pacific, in The Geology of Continental Margins edited by Burk C A and Drake C L Springe - Verlag.

## A Brief Review of Fisheries Acoustics

## Part 1: Acoustic Assessment of Fish Stocks

R. B. Mitson  
Ministry of Agriculture, Fisheries and Food  
Directorate of Fisheries Research  
Fisheries Laboratory  
Lowestoft, Suffolk NR33 OHT

## Foreword

The first report of fish detection, by an acoustic method, was in 1929 when Kimura used a sine wave modulated 200 kHz continuous wave transmission in a pond containing 25 fish of about 45 cm length and about 50 000 fry of 4cm. A few years later the first survey of marine fish started (Sund, 1935) and the application of acoustic systems to fishing (Cushing, 1963) (Mitson, 1983) and research have steadily increased. Fishermen have made good use of echo-sounders, from the simple systems (Balls, 1946) to complex devices in more recent years (Drever and Ellis, 1969) for the detection and capture of fish, often being able to deduce more from these than can be proved scientifically.

It is the purpose of this paper to review briefly the application of acoustics to the assessment of fish stocks. This process can be used to provide, either a relative index, or a quantitative measure of fish abundance.

## 1. Introduction

The primary tool for this work is a system comprising an echo-sounder and generally an echo-integrator, both of high precision. Echo-sounders produce information on the amplitude of signals and the time ( $t$ ) at which they occur. The latter is converted to range  $R$  if the speed of propagation ( $c$ ) of the acoustic waves is known,  $R = ct/2$ .

To describe fish targets from this information it is necessary to take account of the spreading of energy with range, the absorption loss due to chemical effects in the water and also the position of the target with respect to the beam axis if individual fish target strength is to be measured.

## 2. Accuracy and calibration

There are two functions normally required of the fisheries echo-sounder, the ability to measure the target strength of individual fish and

the measurement of volume reverberation from aggregations of fish. Knowledge of fish TS is essential if the latter is to be quantitative. Assuming that most surveys are quantitative, it is instructive to examine the level of accuracy possible and to compare this to what is necessary. The electronic equipment must be well calibrated and the terms of the relevant acoustic equation satisfied, i.e. the acoustic calibration factor, the fish target strength and knowledge of the propagation path. The accuracy to which these factors must be determined depends upon the overall accuracy required for a given survey, including the sampling statistics of the survey design.

Pope (1982) discussed the matter of accuracy in relation to certain management goals. In summary he showed that the overall accuracy of a survey to 95% confidence limits must be  $\pm 3$  dB for an exploratory survey;  $\pm 2$  dB for a time series of surveys calibrated against the Virtual Population Analysis (VPA) method (Jacobsson, 1982) and  $\pm 1$  dB when used as the only basis for setting the Total Allowable Catch (TAC) from an exploited fishery. Survey design is outside the scope of this paper.

System calibration can be considered in two parts, electronic and acoustic. The first comprises the transmitter and receiver of the echo-sounder and the echo-integrator. From the echo-sounder the important factors are the duration of the transmitted pulse and its repetition rate, and the accuracy and gain of the receiving Time Varied Gain amplifier, which corrects for the spreading and absorption losses. There is also the accuracy and gain of the echo-integrator to be taken into account. Electronic circuits employed in the echo-sounders and echo-integrators have a high degree of stability and can be calibrated to an accuracy of better than  $\pm 0.5$  dB.

Acoustic calibration usually includes the lumped parameter (SL + SRT) i.e. source level (SL) and transducer receiving sensitivity (SRT), but it must also take into account the equivalent beam width ( $\Psi$ ) of the transducer. The acoustic absorption coefficient has been investigated in recent years (Fisher and Simmonds, 1977) but it is not known to better than  $\pm 10^{-3}$  dB/m at 38 kHz the most commonly used survey frequency, nor to better than  $\pm 4 \times 10^{-3}$  dB/m at 120 kHz, Robinson (1984). This factor sets a fundamental limit to the calibration accuracy possible; at 100 m range it cannot be better than  $\pm 0.2$  dB or  $\pm 1$  dB respectively.

Acoustic calibration in fisheries has been regarded as a particularly difficult problem, partly because of the practical difficulties of far-field measurements at sea, but also due to the variability of hydrophones

or, until recently, the inadequate characterisation of so-called standard targets (Robinson, 1984).

The theory of scattering from solid elastic spheres was derived by Anderson (1950) and extended by Foote and MacLennan (1982) to allow for the effects of finite receiver bandwidths. These authors recommend the use of spherical standard targets manufactured either from electrical grade copper, or from tungsten carbide. Foote (1982) concluded that the compressional and shear wave speeds in copper spheres could be quantified to better than 0.1% thus reducing errors in their target strength to no more than 0.02 dB. Currently available designs maintain target strength to  $\pm 0.1$  dB over a temperature range of 0-30°C.

Practical measurement techniques have also been developed by Foote et al (1982). The full acoustic system can be calibrated at a selected range and signal level by locating a copper sphere, suspended on thin monofilament lines beneath a transducer. If the calibration is for a hull-mounted transducer careful control of the 3 point suspension for the target is necessary, especially at a range of 20 m or more. Calm sheltered water with a well anchored ship is essential if adequate calibration is to be achieved. A recommended method, once the sphere is located on the acoustic axis, is to integrate its echo signal over a period of time thus including the whole system in the calibration.

Towed bodies have many advantages and are frequently employed for acoustic survey but the calibration procedure described above is difficult to implement with these. A reciprocity method can be used with a similar order of precision, Robinson and Hood (1983). Johannesson (1977) used caged fish captured from the population he was to survey to calibrate the complete acoustic system.

### 3. Target strength

Fish target strength has been the subject of much research which continues. At first measurements were made using single dead fish, Middtun and Hoff (1962) Cushing et al. (1963), Shibata (1970). At the same time studies were made on the bodies of fish in an attempt to determine the relationship between the echo and the size, shape, density and internal structure of haddock and whiting (Haslett, 1962). He showed that the fish bone has an acoustic impedance of about  $2.5 \times 10^6$  Rayls whilst flesh is  $1.6 \times 10^6$  Rayls, rather close to that of seawater,  $1.54 \times 10^6$  Rayls. There is difficulty in applying such results to realistic models of free-swimming fish even for simple body shapes, or where one

organ is the dominant factor, e.g. the swimbladder. Investigations by Harden Jones and Pearce (1958) showed that it accounted for more than 50% of the energy reflected from the freshwater fish they studied (Perca fluviatilis L. Love (1978) provided a new basis for modelling swimbladder fish which improves the predictions of their resonant frequency and acoustic cross-section,  $\sigma$ .

Acoustic scattering from fish is considered to fall into the following regions.

- (i) Rayleigh scattering, when the length of the fish is small compared to  $\lambda$ .  $\sigma$  is proportional to the fish volume squared and to  $\lambda^{-4}$ .
- (ii) Resonance, which causes the swimbladder to vibrate at the frequency of the incident wave, thus absorbing and re-radiating more energy than predicted by the Rayleigh approximation.
- (iii) The transition region where  $\sigma$  is proportional to the fish length squared and largely independent of  $\lambda$ .
- (iv) Geometric scattering when the fish length is much greater than  $\lambda$ .

The limitations of measurements on dead fish and the difficulties of modelling fish for acoustic purposes were recognised, leading to studies on single live fish, anaesthetised and tethered (Love 1969, 1971). Four species of free-swimming but caged fish were used in experiments by (Goddard and Welsby, 1975). In this work the mean amplitude of echoes from 1000 transmissions on each fish were converted into TS by reference to the system calibration. A further analysis of these results by Forbes (1975) used mean squared echo amplitude to convert to mean echo intensity as required for echo-integration purposes.

In-situ methods of obtaining fish TS are preferred, but then capture for positive identification and measurement of size is necessary. The fish must also be mono-specific and preferably be contained within a limited size distribution and at a density low enough for the discrimination of echoes from single fish. Craig and Forbes (1969) made indirect measurements of TS, removing the effects of the transducer beam pattern by solution of a matrix to correct the echo strength distribution to a TS distribution. For small samples and when fish are not uniformly distributed within the sampled volume this technique gives a biased result. A development of the indirect technique was reported by Robinson (1982). This relies on the premise that if a sufficient number of fish are taken into account, the probability that all positions in the beam will be occupied at some time can be described statistically. The directivity pattern of the transducer must be known and the assumption about the

likely distribution of the fish must be valid. From these two factors a beam pattern density distribution results which when convolved with the fish target strength distribution produces an intensity distribution of received echoes. The fish target strength distribution has to be recovered from the other two.

A direct method of measuring fish TS in situ on survey was first proposed by Ehrenberg (1972) when discussing various existing methods, he later described this important advance in detail (1974). Design of the transducer is such that dual concentric beams can be formed, one wide, the other narrow. The main lobe of the narrow beam covers the same volume as the region of unity response in the centre of the wide beam, thus the ratio of received echo intensity for targets in the two beams is

$$I_n / I_w = k_n / k_w (b_n(\theta, \phi)) \dots\dots\dots(1)$$

$I_n$  = intensity in the narrow beam;  $k_n$  = constant for the narrow beam

$I_w$  = intensity in the wide beam;  $k_w$  = constant for the wide beam

$b_n(\theta, \phi)$  = directivity function for the narrow beam, which is defined as the distribution of acoustic power transmitted in different directions  $(\theta, \phi)$  relative to the acoustic axis of the transducer.  $b_n$  is a quantity between 0 and 1. Signals are processed via amplifiers with  $40 \log R + 2 \alpha R$  characteristics for fish TS analysis, but simultaneously in another channel with  $20 \log R + 2 \alpha R$  for total biomass estimation.

Other approaches to obtaining fish TS measurements include an investigation (Ehrenberg (1979) (1980) and Foote (1979) of the use of a specific electronic sector scanning sonar (Voglis, 1970) (Mitson and Cook, 1971) where an extremely narrow beam ( $0.33^\circ$ ) is swept across a  $30^\circ$  sector at a rate of 10 kHz. Practical use of such a system as described together with several methods for presenting the results, by Cook and Rushworth (1978).

#### 4. Acoustic properties of fish shoals

Acoustic surveys of fish are based on the assumption that the total echo intensity from schools is equal to the arithmetic sum of echo contributions from individual fish, justified only if the echoes are uncorrelated. For a doubling of the number of fish in a uniform sized population, the echo power should be doubled, i.e. increased by 3 dB, but Goddard and Welsby (1975) produced some evidence that a small but significantly greater increase occurred in their experiments. Smith and Welsby (1979) examined these results noting that for 32 fish there was an excess of 1.5 dB, i.e., about 40% in echo intensity. It seemed unlikely that this apparent increase could be accounted for by coherence of the

echoes from adjacent fish for the fish were of 300 mm mean length and  $\lambda$  was equal to 15 mm.

Multiple scatter theory was examined to see if this could account for the excess. When the incident intensity intercepted by one fish is re-radiated in all directions and a portion is in turn intercepted by a second fish it also re-radiates its portion in all directions, some of which reaches the transducer. This is known as multiple scattering. If the second fish had not been in position this fraction of the energy would not have reached the transducer. Experimental data from a large herring school have been analysed and compared to a theoretical multiple scatter model which is shown to adequately described the school echo characteristics, (Ertugral and Smith, 1982). They conclude that fish abundance measurements which employ echo-integration techniques could underestimate the numbers of fish if the school is large and fish density is high. Acoustic shadowing is another effect to be noted. It has been examined by Lytle and Maxwell (1982) and Foote (1983).

Despite possible problems due to multiple scattering and shadowing effects, a study of the linearity of fisheries acoustics by Foote (1983) showed no deviation from a straight line relationship between fish numbers and received echo energy. Four different acoustic frequencies were used, 38, 50, 70 and 120 kHz, directed at up to 40 herring of about 27 cm length, contained within a volume of 0.7 m<sup>3</sup>. Foote concludes that the acoustic scattering from fish under survey conditions is strictly linear and the echo integration method of determining fish density is valid. He points to the need for further work on the effects of depth change and depth adaptation to supplement that reported by Harden Jones and Scholes (1979), (Olsen, 1976) (Hawkins, 1977).

##### 5. Estimation near boundaries

Acoustic survey is confined mainly to pelagic fish stocks although there are some notable exceptions (Nakken and Ulltang, 1983) (Dickie et al., 1983). When a pelagic survey must extend to the surface because a proportion of a pelagic school is close to this boundary, acoustic conditions are often poor. An upward looking transducer is needed, but the surface reflection is usually unstable and variable, rendering normal methods of signal-locked reference unusable. Propagation in this region can also lead to inaccuracies through the presence of a high density bubble population. Some pelagic fish spend a significant part of the day close to the sea bed.

Problems of a different type become evident when near-seabed fish are surveyed because of the physical limitations of acoustic systems in relation to the seabed boundary (Mitson, 1983). Survey transducers have limited bandwidth and moderately wide beam angles ( $5^{\circ}$ - $15^{\circ}$ ), the bandwidth in most cases restricts the pulse duration to 0.3 to 1 ms giving a length of pulse in the water  $c\tau$  of 0.45 m to 1.5 m. The best possible resolution is  $(c\tau)^{-2}$  thus creating a definite dead zone of 0.225 m to 0.75 immediately above the sea bed where no fish can be detected. Given a fish density of 50 per  $m^3$  this could result in the survey missing between  $1 \times 10^7$  and  $3.7 \times 10^7$  fish per  $km^2$ . There is a need for development of wider band transducers so that shorter pulses may be used to reduce the sampling difficulties in such circumstances.

#### 6. Acoustic noise

Noise is any unwanted input to the receiver amplifier regardless of the source. In the context of fish stock assessment a significant generator of noise is the propeller of the survey vessel. In many cases the speed related noise from this source prevents the vessel from achieving a speed near its maximum, thereby either reducing effective coverage of the area, or extending the duration of the survey. Particular attention is given to the reduction of underwater radiated noise in modern research vessels. The aim in several recently built vessels has been to achieve a fall of in the spectrum level of noise of about 15 dB per decade of frequency from a level of about 135 dB// $\mu Pa$ //1Hz ref 1 metre at 10 Hz. Propellers dominate the noise spectrum at frequencies above 5 kHz and it seems difficult to predict their noise performance even for a given propeller/hull design, to better than  $\pm 15$  dB.

#### 7. Fish sizing

If it is possible to obtain fish target strength distributions, why not size distributions? In principle this can be done if the relationship between target strength and length is known, but TS varies seasonally for a particular species at a given length. This is due to changes in weight hence acoustic cross-section and changes in density due to different levels of fat and oil content in the body.

Swimbladder resonance was investigated by McCartney and Stubbs (1971) who placed a fish inside a ring hydrophone and by use of a wideband acoustic source measured the frequency response and the Q of the swimbladder. A figure of about 2.5 was obtained for Q from an adult

saithe. Holliday (1972) investigated the resonance structure of echoes from schools of pelagic fish containing swimbladders were examined. Later, Holliday (1978) carried out measurements to determine the fish size distribution within schools of anchovy. The broadband equipment had a frequency range of 80 kHz. Analysis of the received signals gave an estimate of the relative population abundance in each of 30 swimbladder size classes from 0.01 to 4.7 cm equivalent spherical radius. This includes fish sizes from 10 mm anchovy larvae to jack mackerel of 35 cm length.

#### 8. Plankton assessment

Since the discovery of the deep scattering layer by Hersey et al. (1952) and investigation by Andreeva (1964) there has been interest in the detection of mixtures of small fish and of small organisms which comprise the plankton population.

In the latter case the organisms may contain inclusions of gas, and are therefore likely to resonate, but some are without gas, including phytoplankton, zooplankton and some small fishes. For the non-resonant types the relative density and elasticity compared with sea water must be determined in order to ascertain their scattering properties. Greenlaw and Johnson (1982) measured samples of zooplankton giving an average acoustic speed ratio of  $1.01 \pm 0.005$  and density ratio of  $1.04 \pm 0.008$ , commenting that for densities and speed ratios near unity the scattering strengths predicted by fluid sphere models are sensitive to the precise value of the contrasts.

Measured volume scattering strengths and values calculated from a truncated fluid sphere model (Holliday and Pieper, 1980) show the best correlation (0.843) at the highest frequency (3.08 MHz) and the lowest 0.664, at 0.54 MHz.

The use of such high frequencies poses problems in the range at which detection is possible, tens of metres or less, and in the development of methods for calibration.

#### Conclusion

Progress in the quantitative use of acoustic methods for fish stock assessment has been relatively slow by some standards. Much effort has been concentrated on improvements to equipment in order to achieve the level of precision now possible so that with the present-day electronic

circuits and the latest standard target method of calibration the acoustic survey systems are more than adequate in their performance.

What remains to be done is to obtain a better understanding of the relation between fish and their target strength. To seek methods of discrimination between different species and to extract size distributions of the fish being surveyed.

#### References

- KIMURA, K. (1929). On the detection fish-groups by an acoustic method. *J. Imp. Fish. Inst.*, Tokyo 24 (2): 41-5.
- SUND, O. (1935). Echo sounding in fishery research. *Nature* 135, 953.
- CUSHING, D. H. (1963). The uses of echo-sounding for fishermen. London HMSO, 26 p.
- MITSON, R. B. (1983). Fisheries sonar. Fishing News Books Ltd., Farnham, Surrey, 280 p.
- BALLS, R. (1946). Fish on the spot line. Marconi Int. Mar. Comm. Co. Ltd., London, 37 pp.
- DREVER, C. and ELLIS, G. (1969). Deep sea trawling and echo sounding techniques. *World Fishing Reprint*, 29 p.
- POPE, J. G. (1982). User requirements for the precision and accuracy of acoustic surveys. *Symp. Fish. Acoustics.*, Bergen, No. 84.
- JAKOBSSON, J. (1982). Echo surveying of the Icelandic summer spawning herring 1973-1982 *Symp. Fish. Acoustics*, Bergen, No. 22.
- FISHER, F. H. and SIMMONS, V. P. (1977) Sound absorption in sea water. *J. Acoust. Soc. Am.* 62: 558-64.
- ROBINSON, B. J. (1984). Calibration of equipment, Subject group C. *Rapp. P.-v. Réun. Cons. int. Explor. Mer*, 184.
- ANDERSON, V. C. (1950). Sound scattering from a fluid sphere. *J. Acoust. Soc. Am.* 22: 426-431.
- FOOTE, K. G. and MACLENNAN, D. N. (1982). Use of elastic spheres as calibration targets. *Symp. Fish. Acoustics*, Bergen, *FAO Fish Rep.* (300) 331 p, 52-58.
- FOOTE, K. G. (1982). Linearity of fisheries acoustics, with addition theorems. *J. Acoust. Soc. Am.*, Vol. 73 (6).
- FOOTE, K. G., KNUDSEN, H. P. and VESTNES, G. (1982). Standard calibration of echo sounders and integrators with optimal copper spheres. *Symp. Fish. Acoustic*, Bergen, No. 40.

- ROBINSON, B. J. and HOOD, C. R. (1983). A procedure for calibrating acoustic survey systems, with estimates of obtainable precision and accuracy. FAO Fish Rep. (300) 331 p, 59-62.
- JOHANNESSON, K. A. and LOSSE, G. F. (1977). Methodology of acoustic estimates of fish abundance in some UNDP/FAO resource survey projects. Rapp. P.-v. Réun. Cons. int. Explor. Mer, 170, 296-318.
- MIDTTUN, L. and HOFF, I. (1962). Measurements of the reflection of sound by fish. Rpts. Norwg. Fish. Mar. Invest., Vol. 13, No. 3.
- CUSHING, D. H., HARDEN JONES, F. R., MITSON, R. B., PEARCE, G. and ELLIS, G. (1963). Measurements of the target strength of fish. J. Brit. I.R.E., 25 (4): 299-303.
- SHIBATA, K. (1970). Experimental measurement of target strength of fish. FAO Tech. Conf. Fish Finding Purse Seining and aimed trawling, Reykjavik, Iceland. FII: FF/70/42.
- HASLETT, R. W. G. (1962). Measurement of dimensions of fish to facilitate calculations of echo-strength in acoustic fish detection. J. Cons. Int. Exp. Mer, 27: 3, 261-26.
- HARDEN JONES, F. R. and PEARCE, G. (1959). Acoustic reflexion experiments with perch to determine the proportion of the echo returned by the swimbladder. J. Exp. Biol., 35: 2437.
- LOVE, R. H. (1969). Maximum side-aspect target strength of an individual fish. J. Acoust. Soc. Am., 46 (3) 746-52.
- LOVE, R. H. (1971). Dorsal-aspect target strength of an individual fish. J. Acoust. Soc. Am., 49 (3) 816-23.
- LOVE, R. H. (1977). Target strength of an individual fish at any aspect. J. Acoust. Soc. Am., 62, (6) 1397-1403.
- GODDARD, G. C. and WELSBY, V. G. (1975). Statistical measurements of the acoustic target strength of live fish. Uni. of Birmingham, Dept. of Electronic and Electrical Eng. Memo No. 456, Jan. 1975.
- FORBES, S. T. (1975). An extended analysis of the Goddard and Welsby results. Acoustic Surveying of Fish Populations, Lowestoft, Paper 2, 15-20, Institute of Acoustics, Underwater Acoustics Group, Edinburgh.
- CRAIG, R. E. and FORBES, S. T. (1969). Design of a sonar for fish counting. Fiskdir. Skr. Ser, Havunders., Vol. 15, 210-219.
- ROBINSON, B. J. (1982). An in situ technique to determine fish target strength with results for blue whiting (micromesistius poutassou (Risso)). J. Cons. int. Exp Mer. 40 (2): 153-60.

- EHRENBERG, J. E. (1972). A method for extracting the fish target strength distribution from acoustic echoes. Proc. 1972, IEEE Conf., Engn Ocean Environ., 1: 61-4.
- EHRENBERG, J. E. (1974). Two applications for a dual-beam transducer in hydroacoustic fish assessment systems. Proc. 1974, IEEE Conf. Engn. Ocean Environ., 1: 152-5.
- EHRENBERG, J. E. (1979). The potential of the sector-scanning sonar for in situ measurement of fish target strengths. Lowestoft, Dec. 1979, pp. 53-63, Institute of Acoustics, Underwater Acoustics Group, Edinburgh.
- EHRENBERG, J. E. (1980). Echo-counting and echo-integration with sector scanning sonar. J. Sound Vib. 73 (3) 321-32.
- FOOTE, K. G. (1979). Biasing of fish abundance estimates derived from use of sector scanning sonar in the vertical plane. Proc Conf. on Progress in Sector Scanning Sonar, Lowestoft, Dec 1979, pp 42-52. Institute of Acoustics, Underwater Acoustics Group, Edinburgh.
- VOGLIS, G. M. (1971). A general treatment of modulation scanning as applied to acoustic linear arrays - Parts 1 and 2 Ultrasonics, 9, pp 142-153 and 215-223.
- VOGLIS, G. M. (1972). Design features of advanced scanning sonars based on modulation scanning - Parts 1 and 2 Ultrasonics 10, pp 16-25 and 103-113.
- MITSON, R. B. and COOK, J. C. (1971). Shipboard installation and trials of an electronic sector scanning sonar. Radio and Electron. Eng. 1971, 41 pp. 339-350.
- COOK, J. C. and RUSHWORTH, A. (1979). Measuring fish target strength and shoaling density using a high resolution scanning sonar. Proc. Con. Acoustics in fisheries, Institute of Acoustics, Underwater Acoustics Group, Edinburgh.
- SMITH, B. V. and WELSBY, V. G. (1979) Sonar Echoes from groups of fish. Acoustics in Fisheries, Hull, Sept 1978, Paper 1. Institute of Acoustics., Underwater Acoustics Group, Edinburgh.
- ERTUGRUL, M. G. and SMITH, B. V. (1982). Multiple scattering effects in fish abundance estimation. Dept. Electronic and Electrical Eng., Univ. Birm., Memo 492.
- LYTLE, D. W. and MAXWELL, D. R. (1983). Hydroacoustic assessment in high density fish schools. FAO Fish. Rep. (300): 157-71.
- FOOTE, K. G. (1983). Linearity of fisheries acoustics, with addition theorems. J. Acoust. Soc. Am., 73 (6): 1932-1940.

- HARDEN JONES, F. R. and SCHOLLES, P. (1979). The swimbladder, vertical movements, and the target strength of fish. Meeting on Hydroacoustical Methods for the Estimation of Marine Fish Populations, 25-29 June 1979. Vol 2 part a. ed. J. B. Suonsala, Cambridge. Mass. Charles Stark Draper Lab Inc, pp 167-82.
- OLSEN, K. (1976). Some experiments on the effect on target strength of fish undertaking vertical migrations. ICES CM 1976/B:42 mimeo.
- HAWKINS, A. D. (1977). Fish sizing by means of swimbladder resonance. Rapp. P.-v.Reun. CIEM 170: 122-129.
- NAKKEN, O. and ULLTANG, O. (1982). Comparison of reliability of acoustic estimation of fish stock abundance and estimation by other assessments in N E Atlantic. Symp. Fish. Acoustics., Bergen, No. 38.
- DICKIE, L. M., DOWD, R. G. and BOUDREAU, P. R. (1983). An echo counting and logging system (ECOLOG) for demersal fish size distributions and densities. Can. J. Fish. Aquat. Sci. 40: 487-498.
- MITSON, R. B. (1983). Acoustic detection and estimation of fish near the sea-bed and surface. FAO Fish. Rep. (300), 309 pp. 27-34.
- McCARTNEY, B. S., STUBBS, A. R. (1971). Measurements of the acoustic target strengths of fish in dorsal aspect, including swimbladder resonance. J. Sound Vib., 15 (3): 397-420.
- HOLLIDAY, D. V. (1972). Resonance structure in echoes from schooled pelagic fish. J. Acoust. Soc. Am., 51 (4) Pt 2: 1322-1332.
- HOLLIDAY, D. V. (1977). The use of swimbladder resonance in the sizing of schooled pelagic fish. Rapp. P.-v. Réun. CIEM, 170: 130-5.
- HERSEY, J. B., JOHNSON, H. R. and Davis, L. C. (1952). Recent findings about the deep scattering layer, J. Mar. Res., 11:1-9.
- ANDREEVA, I. B. (1964). Scattering of sound by air bladders of fish in deep sound-scattering ocean layers. Akust. Zh. 10:10-24 (in Russian, English translation in Soviet Physics) - Acoustics 10: 17-20.
- GREENLAW, C. F. and JOHNSON, R. K. (1982). Physical and acoustical properties of zooplankton. J. Acoust. Soc. Am., 72 (6): 1706-10.
- HOLLIDAY, D. V. and PIEPER, R. E. (1980). Volume scattering strengths and zooplankton distributions at acoustic frequencies between 0.5 and 3MHz. J. Acoust. Soc. Am., 67 (1): 135-46.

## A Brief Review of Fisheries Acoustics

## Part II: Acoustic Telemetry for the Study of Fish Behaviour

R. B. Mitson  
Ministry of Agriculture, Fisheries and Food  
Directorate of Fisheries Research  
Fisheries Laboratory  
Lowestoft, Suffolk NR33 OHT

## 1. Introduction

The study of fish behaviour is difficult because continuous observation is rarely possible and progress was slow, until acoustic methods became practicable with the advent of the transistor and its associated miniature components. In 1956 the first report occurred of fish tracking by sonar detection of an acoustic tag attached to a fish (Trefethen, 1956). Johnson (1960) followed acoustically tagged chinook salmon as they migrated up the Columbia River. A telemetry system consists essentially of a transmitter (the telemeter) usually called a fish tag in this application, a transmission channel, (water) and a receiver. A suitably modulated carrier signal is sent via the transmission channel to the receiver where it is decoded to yield the information it contains. A fish tag must be small enough to be carried by a fish without significantly affecting its behaviour.

Studies in rivers, lakes and seas, necessary for the examination of fish migration and behaviour include location and orientation which may require the monitoring of physiological and environmental variables, the latter preferably from sensors on the body of the fish. This is particularly important in estuarine conditions. A telemeter must relay information on widely different timescales, from momentary to monthly patterns.

## 2. Propagation and range

Most fisheries telemetry links work at ranges less than 1 km but are vulnerable to effects which interfere with and limit the propagation of signals. Thermal layering of the water can cause speed gradients with the result that acoustic waves are refracted and this may cause the failure of a link for certain periods of time. Entrapped air bubbles due to turbulence in the upper layers of the sea, or fast-running water over the rough bottoms of streams, can cause severe attenuation.

Noise may arise from various sources including sea-state and precipitation (McCartney, 1971) at frequencies below about 70 kHz whilst thermal noise (Mellen, 1952) predominates at higher frequencies. Certain areas in

the sea produce high levels of wideband time-varying noise by the tidal movement of water across ridges, (Harden Jones and Mitson, 1982). Biological noise can also be significant (Tavoiga, 1967).

Range is dependent on the source level, the noise background and the propagation losses due to spreading and absorption, the latter becoming more important as frequency increases (Fisher and Simmons, 1977).

Source level is limited by the power available and this related to the size of battery that the fish can carry.

$$SL = 170.8 + 10 \log \eta W \text{ dB re } 1 \mu\text{Pa } 1\text{m}^{-1} \quad (1)$$

where  $\eta$  = transducer efficiency

$W$  = peak current times battery voltage

A critical factor is the capacity of the battery on which depends the operating life of the fish tag.

$$\text{Number of days life} = \text{mAh} (24I_p)^{-1} \times 10^3 (\text{PRF} \times \tau)^{-1} - 24I_o(\text{mAh})^{-1} \quad (2)$$

where mAh = cell capacity

$I_p$  = current drawn during pulse

$I_o$  = current when circuit is quiescent

PRF = number of pulses per second

$\tau$  = duration of pulse in milliseconds

Eqn. 2 shows there is wide scope for adjusting the active life of a tag by the selection of  $\tau$  and PRF. Pulse duration is related to detectability of the signal. Variation of PRF is often used to convey information.

### 3. Frequency

Choice of frequency is a compromise based on the need for long range but small transducers. Efficient use of power means resonant transducers, and electrostrictive rings are well-suited for near omni-directional radiation and fitting into a cylindrical assembly. A frequency between 50 to 350 kHz is usually selected but for fish below 0.5 m length 70 kHz or above is preferred (transducer diameter about 13 mm). At 300 kHz a resonant ring is 3 mm diameter and can be made only 1.5 mm long.

### 4. Systems and Information

The level of effort involved in obtaining information from fish fitted with acoustic tags varies, from one man with a hand-held hydrophone (Henderson et al., 1966) to a sophisticated sea-going research vessel having an advanced sonar and carrying a number of research staff and many crew members (Harden Jones and Arnold, 1982).

The majority of fish species studied by means of acoustic telemetry are less than 0.5 m in length (Mitson and Young, 1975) and it is important that a tag does not affect fish behaviour. Few studies have taken place to determine the effects of internal or external tagging. Arnold and Holford (1978) measured the effects of tag externally attached to a flatfish and a roundfish finding that it increased the drag of the fish when swimming by about 5%.

In reported studies, the information sought has permitted simple modulation methods to be used (Stasko and Pincock, 1977) (Nelson, 1978) (Ireland and Kanwisher, 1978). Frequency modulated CW, pulse recurrence frequency, pulse position and constant rate pulse; all but the latter permit telemetry of variables.

The simplest form of information from a telemetry link is an indication of the actual position of the fish. A useful system where the movements of fish are restricted by land boundaries and shallow water is a telemeter emitting a train of pulses typically at a rate of 1 every 2 seconds, and detected by a directional hand-steered hydrophone. Range between the telemeter and receiver can only be estimated crudely from signal strength, so the signals could originate almost anywhere within the volume swept out by dimensions of the hydrophone beam. An improvement is possible if the transmission can be received simultaneously at well-spaced distant points, the positional uncertainty being reduced to a volume determined from the dimensions of the beams at their intersection. Where fish are free to move over long distances a simple system such as that described above may be too difficult to operate.

When a fish is unlikely to move very far during the course of a telemetry experiment its position may be fixed by means of an underwater adaptation (Hawkins et al., 1973) of the hyperbolic navigation system used by ships and aircraft. Omni-directional hydrophones are laid on the sea bed or are suspended in the water separated by accurately measured distances. This measurement is achieved by placing a pinger by each hydrophone in turn and noting the arrival time of its transmitted pulse at each receiving point. The difference in these times, multiplied by the acoustic wave speed, define hyperbolic which intersect at the pinger position. Positional errors in such a system are due mainly to local changes in acoustic wave speed but a theoretical accuracy of about  $\pm 1$  m is possible in the horizontal plane. The formula currently used in fisheries for the calculation of acoustic wave speed is that due to Mackenzie (1981).

Tracking of tuna in the open sea was reported by Yuen (1970) who used a 50 kHz pinger tag inserted into the stomach of the fish. The signals were received by using the listening mode of a continuous-transmission, frequency-modulated sonar. The hydrophone was 4 m below the water surface and had a beam of 6° horizontal and 15° vertical. A maximum range of 2.3 km was possible. Range had to be estimated from signal strength and this caused some difficulty in maintaining the preferred distance of 1 km from the fish.

At a cost of greater complexity in the fish tag the transponding principle allows precise measurement of range. It also offers an advantage in control of the interrogation rate, which can be high to correspond with a high information rate when required, or low to conserve power.

Meares and McDearman (1975) designed a transponder for use at 75 kHz, intended for fish studies. An operating life of 6000 h was expected with an interrogation rate of 100 per hour. For an electrical power of 400 m the range was expected to be 800 m.

Another transponding tag (Mitson and Storeton-West, 1971) was designed to work at 300 kHz with an electronic sector scanning sonar (Voglis, 1971, 1972) (Mitson and Cook, 1971) (Mitson, 1984). This system has subsequently been used in a variety of studies (Harden Jones and Arnold, 1982) including the measurement of trawl efficiency by observation of a tagged fish in its path; the investigation of selective tidal transport and, by means of a compass included with the transponder (Mitson *et al.*, 1983), on-line information of the heading of fish. Pulse position modulation was used to convey the compass information.

Design and construction of sensors for attachment to fish poses many problems mainly because of the small size. The swimming speed of fish has been monitored by means of a free-wheeling propeller which interrupts a light beam twice for each rotation (Voegeli and Pincock, 1980).

Temperature measurement on a fish presents little difficulty. Salinity is important in estuaries where salmon are leaving the sea and entering freshwater. A membrane type of salinometer has been designed and used for this type of investigation, (Priede, 1982).

## 5. Discussion

Much of the work reported to date has included the observation of fish movements without the means to establish why these took place. Because of the need in fish behaviour studies for a more fundamental

understanding of the relationship between the physical and biological features of the environment there is likely to be a requirement for greater complexity in the design of acoustic tags. If simultaneous measurements of variables are needed, problems of sensor design and information coding and transmission will arise.

#### References

- Trefethen, P. S. (1956). Spec. Sci. Rep., Fish Wildlife Ser., US, 179, 11 pp.
- Johnson, J. H. (1960). Sonic tracking of adult salmon at Bonneville Dam in 1957. U.S. Fish Wildl. Serv. Fish. Bull. 60: 471-485.
- McCartney, B. S. (1971). Ambient Noise in the Sea. Encyclopaedic Dictionary of Physics, Supp. Vol. 4. Pergamon Press, Oxford and New York.
- Mellen, R. H. (1952). The thermal-noise limit in the detection of underwater acoustic signals. J. Acoust. Soc. Am. 24: 478-480.
- Harden Jones, F. R. and Mitson, R. B. (1982). The movement of noisy sandwaves in the Strait of Dover. J. Cons. int Explor. Mer, 40(i) 53-61.
- Arnold, G. P. and Holford, B. H. (1978). The physical effects of an acoustic tag on the swimming performance of plaice and cod. J. Cons. int Explor. Mer. 38: 189-200.
- Tavolga, W. N. (1967). Underwater sounds in marine biology. In W. M. Albers (ed), Underwater acoustics, Plenum Press. N.Y., 2: 416 p, 35-41.
- Mitson, R. B. and Young, A. H. (1975). A survey of the engineering problems of developing small acoustic fish tags. Proc. IERE Conf. Instrum. Oceanogr. Bangor, Wales. p 163-174.
- Fisher, F. H., and Simmons, V. P. (1977). Sound absorption in seawater. J. Acoust. Soc. Am. 62: 558-564.
- Henderson, H. F., Hasler, A. D. and Chipman, G. G. (1966). An ultrasonic transmitter for use in studies of movements of fishes. Trans. Am. Fish. Soc. 95: 350-356.
- Harden Jones, F. R. and Arnold, G. P. (1982). Acoustic Telemetry and the Marine Fisheries. Symp. Zool. Soc. Lond. 49: 75-93.
- Stasko, A. B. and Pincock, D. G. (1977). Review of Underwater Biotelemetry, with Emphasis on Ultrasonic Techniques. J. Fish. Res. Bd. Can. 34: 9, 1261-1285.

- Nelson, D. R. (1978). Telemetry techniques for the study of free-ranging sharks. In Sensory biology of sharks, skates and rays. E. S. Hodgson and R. F. Mathewson (eds) Arlington, Va, US Office of Naval Research, 419-482.
- Ireland, L. C. and Kanwisher, J. W. (1978). Underwater acoustic biotelemetry: procedures for obtaining information on the behaviour and physiology of free-swimming aquatic animals in their natural environments. In The behaviour of fish and other aquatic animals. D. I. Mostofsky (ed) London and New York, Academic Press, 341-379.
- Yuen, H. S. H. (1970). Behavior of skipjack tuna. Katsuwonus pelamis, as determined by tracking with ultrasonic devices. J. Fish. Res. Bd. Can., 27: 2071-2079.
- Meares, G. T. and McDearman, J. R., (1975). Ultrasonic Fish Tagging System Development, Tennessee Wildlife Resources Agency, Nashville, TN.
- Hawkins, A. D., MacLennan, D. N., Urquhart, G. G. and Robb, C., (1974). J. Fish Biol., 6, 225-236.
- Mackenzie, K. V. (1981). Nine-term equation for sound speed in the oceans. J. Acoust. Soc. Am. 70: 3, 807-812.
- Mitson, R. B. and Storeton-West, T. J. (1972). A transponding acoustic fish tag. Radio and Electron. Eng., 41: 483-489.
- Voglis, G. M. (1971). A general treatment of modulation scanning as applied to acoustic linear arrays - Parts 1 and 2, Ultrasonics 9, pp 142-153 and 215-223.
- Voglis, G. M. (1972). Design features of advanced scanning sonars based on modulation scanning - Parts 1 and 2, Ultrasonics 10, pp 16-25 and 103-113.
- Mitson R. B. and Cook, J. C. (1971). Shipboard installation and trials of an electronic sector scanning sonar. Radio and Electron. Eng. 41: 339-350.
- Mitson, R. B. (1984). Review of high-speed sector-scanning sonar and its application to fisheries research. Proc. IEE. 131: Part F, 3: 357-269.
- Mitson, R. B., Storeton-West, T. J. and Pearson, N. D. (1982). Trials of an acoustic transponding fish tag compass. Biotelem. and Patient Monit. 9: 69-79.
- Voegeli, F. A. and Pincock, D. G. (1980). Determination of fish swimming speed by Ultrasonic Telemetry. Biotelem. and Patient Monit. 7: 215-220.

Priede, I. G. (1982). An Ultrasonic Salinity Telemetry Transmitter for use on Fish in Estuaries. *Biotelemetry* 9: 1, 68 p, 1-9.

SCATTERING FROM FISH SHOALS AND THE DETERMINATION OF FISH DENSITY FROM A STATISTICAL ANALYSIS OF ECHO WAVEFORMS.

P.N. Denbigh

Central Acoustics Laboratory, University of Cape Town.

1. Introduction.

If, at any instant, the average number of scatterers contributing to a backscattered acoustic signal is large, the Central Limit theorem suggests that the statistics of the instantaneous amplitude are Gaussian, and that the envelope therefore has Rayleigh statistics. As the number of overlapping echoes decreases, the statistics change and a measure of the statistical properties of the return signal envelope can be used to deduce the average number of scatterers contributing to the signal. This is the basis of a technique proposed by Wilhelmij and Denbigh (1), (2) as an alternative to echo counting and echo integration as a means of assessing the number density of fish. The technique is believed to provide a useful extension to the echo counter because it operates with overlapping echoes and can accept therefore an order of magnitude more scatterers in the resolution cell. Like the echo-counter and in contrast to the echo integrator, it does not require a knowledge of the mean value of the single fish target strength. The method was demonstrated experimentally using a randomized volume array of polystyrene spheres in a small tank. A promising degree of agreement was obtained between the estimates of scatterer number density and the true number density. The theory used was based upon two assumptions - firstly that the scatterers were Poisson distributed in volume - and secondly that the scatterers produced independent but identical echoes. The model of polystyrene spheres conformed reasonably well to these assumptions. It is believed, however, that the assumption of identical echoes is invalid for fish and the purpose of this paper is to show how a modified theory can cover the case of real fish shoals.

## 2. The PDF of echo envelopes from individual fish.

Considering an individual fish as a flexible line array of many small scattering points, its echo is determined by the sum of contributions from each scattering point. The result of interference between these point scatterers will vary with time and will be different for each fish; if the contributions are of similar amplitude but random phase, the Central Limit theorem may be applied once again to suggest that the echo envelope will vary from fish to fish in accordance with a Rayleigh distribution. A recent paper by Clay and Heist (3) gives evidence that the Rician PDF is a more accurate description of acoustic scattering by individual live fish. The physical explanation is that the backscattered signal may have two components, one of constant amplitude and one noiselike. The resultant envelope can be thought of as arising from the envelope of a sine wave plus noise, thus leading to the classical Rician distribution. The constant amplitude component arises from the swim bladder when it is small enough in wavelengths to produce constant conditions for interference, irrespective of flexing by the fish. The noiselike component arises from distributed scattering points along the remainder of the fish.

It is proposed that the sonar used for the assessment of fish number density by the statistical technique would have a narrow beam and a good range resolution in order to achieve a small average number of scatterers in the resolution cell. It follows that high operating frequencies are needed, and that the swim bladder is likely therefore to have an appreciable dimension in wavelengths. In these circumstances, and in accordance with the findings of Ref. 3 for fish more than  $25 \lambda$  long, the constant amplitude component will be small and a close approximation to a Rayleigh PDF may be expected. This Rayleigh distribution of echo amplitudes is the case considered in the following analysis.

## 3. Theory.

The measures of envelope statistics used in the technique are the first and second moments of intensity, where the intensity is the square of the envelope. Consider initially that there are a fixed number of fish  $N$  contributing to the return signal at

any instant. As an example let  $N = 4$  so that there are four overlapping echoes  $a \cos (\omega t + \alpha)$ ,  $b \cos (\omega t + \beta)$ ,  $c \cos (\omega t + \gamma)$  and  $d \cos (\omega t + \delta)$  where the amplitudes  $a$ ,  $b$ ,  $c$  and  $d$  may be considered random variables with a Rayleigh PDF, and where the phases  $\alpha$ ,  $\beta$ ,  $\gamma$  and  $\delta$  may be considered random variables with a uniform distribution between 0 and  $2\pi$ . The resultant intensity, which is the square of the envelope, will be termed  $I_4$ , where the subscript 4 denotes that it results from the sum of 4 echoes. By adding the in-phase components of the four terms, and then the quadrature components, it follows that

$$I_4 = (a \cos \alpha + b \cos \beta + c \cos \gamma + d \cos \delta)^2 + (a \sin \alpha + b \sin \beta + c \sin \gamma + d \sin \delta)^2$$

Making use of the relationships  $\cos^2 x + \sin^2 x = 1$ , and  $\cos x \cdot \cos y + \sin x \cdot \sin y = \cos (x-y)$ , this can be expanded to become

$$I_4 = a^2 + b^2 + c^2 + d^2 + 2ab \cos (\alpha-\beta) + 2ac \cos (\alpha-\gamma) + 2ad \cos (\alpha-\delta) + 2bc \cos (\beta-\gamma) + 2bd \cos (\beta-\delta) + 2cd \cos (\gamma-\delta)$$

$\therefore \langle I_4 \rangle = \langle a^2 \rangle + \langle b^2 \rangle + \langle c^2 \rangle + \langle d^2 \rangle = 4\langle a^2 \rangle$  assuming that each amplitude has the same mean value.

Squaring the expression for  $I_4$  and making use of the fact that all cross product terms such as  $2ab \cos (\alpha-\beta)$ ,  $2ac \cos (\alpha-\gamma)$  have zero mean, we obtain

$$\langle I_4^2 \rangle = \langle a^4 \rangle + \langle b^4 \rangle + \langle c^4 \rangle + \langle d^4 \rangle + \langle 4a^2 b^2 \rangle + \langle 4b^2 c^2 \rangle + \langle 4c^2 d^2 \rangle + \langle 4b^2 c^2 \rangle + \langle 4b^2 d^2 \rangle + \langle 4c^2 d^2 \rangle$$

The format of this expression is chosen to show how the terms originate and to enable a generalized prediction of  $\langle I_N^2 \rangle$  for values of  $N$  other than 4.

In the above example and noting that  $\langle a^2 b^2 \rangle = \langle a^2 \rangle^2$  if the amplitudes are independent random variables, we obtain

$$\langle I^2 \rangle = 4 \langle a^4 \rangle + 4(3+2+1) \langle a^2 \rangle^2 .$$

A similar derivation for  $N$  overlapping echoes gives

$$\langle I_N \rangle = N \langle a^2 \rangle \tag{1}$$

$$\langle I_N^2 \rangle = N \langle a^4 \rangle + 2N(N-1) \langle a^2 \rangle^2 \tag{2}$$

which makes use of the simplification that  $[(N-1)+(N-2)+(N-3) + \dots + 1]$

equals  $N(N-1)/2$  .

For the Rayleigh distribution  $p(a) = \frac{a}{\sigma^2} e^{-a^2/2\sigma^2}$ , it is readily shown that  $\langle a^2 \rangle = 2\sigma^2$  and  $\langle a^4 \rangle = 8\sigma^4$  . Arbitrarily putting  $\sigma = 1/\sqrt{2}$  it follows that

$$\langle I_N \rangle = N \tag{3}$$

$$\langle I_N^2 \rangle = 2N + 2N(N-1) \tag{4}$$

The next step is to proceed from the situation where the number of fish in each resolution cell is fixed at  $N$ , and to consider instead fish which are Poisson distributed in volume. The Poisson distribution predicts that the probability that there are  $N$  fish in a resolution cell is given by

$$P_{\langle N \rangle}(N) = \frac{\langle N \rangle^N e^{-\langle N \rangle}}{N!}$$

where  $\langle N \rangle$  is the average number of fish in the resolution cell. We can now take the moments  $\langle I_N \rangle$  and  $\langle I_N^2 \rangle$  corresponding to a fixed number of fish  $N$  in the resolution cell, and multiply them by the probability  $P_{\langle N \rangle}(N)$  that there are  $N$  fish in the resolution cell. We do this for every value of  $N$  for which  $P_{\langle N \rangle}(N)$  is significant and then perform a summation of these weighted first moments and of these weighted second moments. This gives us averaged intensity moments  $\langle I \rangle$  and  $\langle I^2 \rangle$  which are appropriate to fish which have a Poisson distribution in volume and have a Rayleigh distribution of amplitudes.

Using the expression for  $\langle I_N \rangle$  given in Eq. 3 we obtain

$$\begin{aligned} \langle I \rangle &= \sum_{N=1}^{\infty} \langle I_N \rangle P_{\langle N \rangle}(N) = \sum_{N=1}^{\infty} N P_{\langle N \rangle}(N) \\ &= \langle N \rangle, \text{ by the definition of a mean value.} \end{aligned}$$

Doing the same operation for the value of  $\langle I_N^2 \rangle$  given in Eq. 4 we obtain

$$\begin{aligned} \langle I^2 \rangle &= \sum_{N=1}^{\infty} \langle I_N^2 \rangle P_{\langle N \rangle}(N) \\ &= \sum_{N=1}^{\infty} 2N P_{\langle N \rangle}(N) + \sum_{N=1}^{\infty} 2N(N-1) \cdot \frac{\langle N \rangle^N e^{-\langle N \rangle}}{N!} \\ &= 2\langle N \rangle + 2e^{-\langle N \rangle} \sum_{N=2}^{\infty} \frac{\langle N \rangle^N}{(N-2)!} \\ &= 2\langle N \rangle + 2e^{-\langle N \rangle} \left[ \frac{\langle N \rangle^2}{0!} + \frac{\langle N \rangle^3}{1!} + \frac{\langle N \rangle^4}{2!} + \dots \right] \end{aligned}$$

Making use of the expansion  $e^x = 1 + x + \frac{x^2}{2!} + \frac{x^3}{3!} + \dots$  this simplifies to

$$\langle I^2 \rangle = 2\langle N \rangle + 2\langle N \rangle^2$$

$$\therefore \langle I^2 \rangle / \langle I \rangle^2 = 2 / \langle N \rangle + 2$$

$$\text{or } \langle N \rangle = \frac{2}{\langle I^2 \rangle / \langle I \rangle^2 - 2} \quad (3)$$

The equation previously used in Refs. 1 and 2 originated from a paper on light scattering by Pusey, Schaefer and Koppel (4) and was

$$\langle N \rangle = \frac{1}{\langle I^2 \rangle / \langle I \rangle^2 - 2} \quad (4)$$

This assumes scatterers which are Poisson distributed in volume but which have identical backscattering cross-sections. Experimental estimates of the density of a randomized volume by polystyrene spheres were obtained using this formula and have shown good agreement with the true densities (1), (2). The new equation gives number densities which are exactly twice as great. It is believed that the Rayleigh distribution of echo amplitudes assumed in this new equation is likely to be more appropriate to fish in a shoal. This applies even if the fish do not vary in size.

When the fish length drops below 25 wavelengths, it is expected that the amplitude statistics will become non-Rayleigh and that the correct constant in the numerator of Eq. 3 will now lie between one and two. An extension to the preceding analysis can determine this constant if the amplitude statistics of the individual fish are known.

### Conclusions

It is believed, subject to experimental verification with real fish shoals, that measured normalized second moments of intensity may, in conjunction with Eq. 3, be useful in predicting the number densities of fish in conditions where the densities are up to an order of magnitude greater than is suitable for an echo-counter. It is seen that, depending upon the assumptions made about the probability distribution of echo amplitudes, there can be an error, never exceeding two, in the estimates of number density.

### References.

1. G.P. Wilhelmij, P.N. Denbigh, "Random Scatterer Density Determination using a Simple Statistical Analysis of Back-scattered Pulses". 11th ICA Paris, 385-388 (1983). (Please note an error in the scaling of the vertical axis of Fig. 1).
2. G.P. Wilhelmij, P.N. Denbigh, "A Statistical Approach to Determining the Number Density of Random Scatterers from Back-scattered Pulse". J. Acoust. Soc. Am., - to appear shortly.
3. C.S. Clay, B.G. Heist, "Acoustic Scattering by Fish - Acoustic Models and a Two-Parameter Fit". J. Acoust. Soc. Am., 75(4) 1077 - 1083 (1984).
4. P.N. Pusey, D.W. Schaefer, D.E. Koppel, "Single-interval Statistics of Light Scattered by Identical Independent Scatterers". J. Phys. A. Math. Nucl. Gen. Vol. 7 No. 4, 530 - 540 (1974).

## HIGH FREQUENCY MID-WATER ECHO SOUNDING

J.G.H. Maxwell, Marine Studies Centre, University of Sydney  
Ian S.F. Jones, RAN Research Laboratory  
Richard Coleman, Ocean Sciences Institute, University of Sydney.

Since the early days of ASDIC, sonar operators have known that the marine environment was noisy and contained layers of acoustic scatterers. To the biologist it is the infinite variety of different events that can be detected acoustically, their identification and the development of an understanding of the parameters that influence their occurrence spatially and temporally, that presents the challenge. To the physical oceanographer it is the water motions and the nature of the changes in acoustic impedance which can be detected acoustically that provides the interest. This means that an understanding is required of the role of biological and suspended particle distributions in scattering to allow remote sensing by acoustics to be a valuable tool in marine studies.

In the ocean many factors affect the total biological activity and hence the biomass per cubic metre in the water column. Acoustic measurements will contain signatures from these potential scatterers as well as from other scattering mechanisms such as turbulence fluctuations, bubbles, suspended particles or reflection from layers of different mean density. During the BASS '84 experiment a number of measurements were taken using both 50 kHz and 200 kHz sounders and our ability to detect the base of the mixed layer varied markedly. The Bass Strait region is, biologically speaking, one of contrasts. In terms of overall productivity it is, in keeping with much of the waters surrounding the Australian continent, low in productivity. Previous acoustic studies in Bass Strait have shown that there can be on certain occasions extensive schools of sardine (*Sardinops neopilchardus*). Figure 1 shows a typical echogram from a 50 kHz sounder of sardine schools extending along the 90 mile beach area.

During a Kimbla cruise in early February, 1984 a period of calm weather was experienced which resulted in a warming of the surface waters and a small scale localised 'bloom' of phytoplankton was noted at one location near the Barracouta oil platform. This small scale and presumably shortlived local event highlights just how difficult it is to place a generalisation of the biological activity in the region into a physical setting.

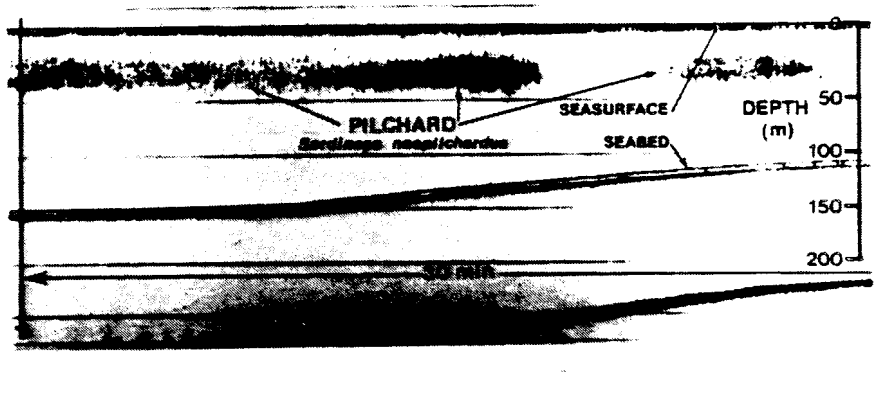


Fig. 1. Echogram of sardine shoales near 90 Mile Beach, Victoria. Acoustic frequency 50 kHz.

Of interest to physical oceanographers is the internal wave motion seen in the Bass Strait region at the shelf break and in the Strait itself. An example of this physical feature is indicated in Figure 2 where the signature of the sharp thermal interface of the thermocline is visible with the long period internal wave propagating shorewards. Fish and associated biological activity can demonstrate a high degree of thermal specificity and so can often 'mark' the thermocline boundary. Are we seeing a biological tracer or reflections from the base of the well mixed layer?

Let us look at temperature gradients. Acoustic reflections using sound of wave lengths,  $\lambda$ , in the range 5 cm to 0.5 m are strongest for microstructure with temperature gradients having vertical extents less than an acoustic wave length. We imagine horizontal sheets of microstructure with a temperature gradient  $G$  of vertical extent  $\ell$ . If the speed of sound depends on the temperature  $T$  as

$$c \frac{\partial}{\partial T} \frac{1}{c} = \alpha T$$

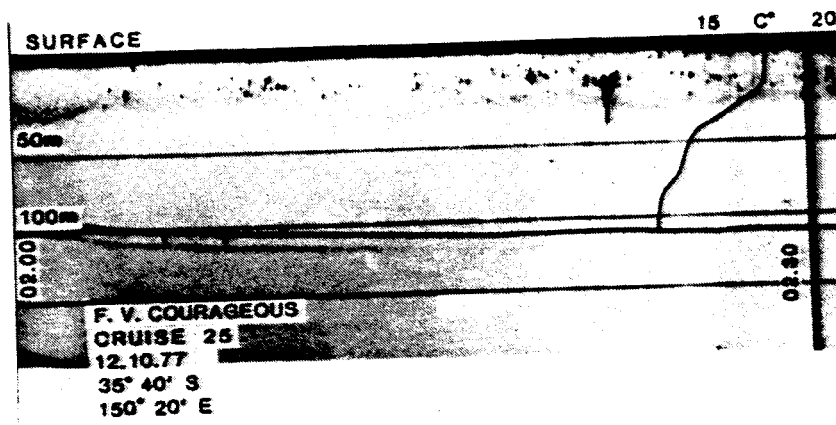


Fig. 2. Echogram detailing the thermal interface on which a long period internal wave is visible.

Brekhovskikh (1980) presents an expression [20.44] for the reflection coefficient which can, for small gradients and normal incidence, be approximated as

$$\rho \approx \frac{5.6 \left(\frac{\ell}{\lambda}\right) \alpha G}{\sinh \left(\frac{11.2\ell}{\lambda}\right)}$$

for a particular form of temperature profile. We have presented  $20 \log \rho$  in Fig. 3 as a function of  $\ell/\lambda$ . Note that for layers of given temperature

gradient but very thin or thick compared with the acoustic wave length, the reflection coefficient decreases rapidly. For a layer with fixed gradient but vanishing thickness  $\lambda$ , the change in acoustic impedance becomes zero and so there is no reflection. Gregg (1976) has shown that the largest temperature gradients have scales of order  $\lambda$  in the upper ocean and as Fig. 3 indicates these gradients have reflection coefficients in dB of order  $-20 \log (G\alpha\lambda) - 70$ . A typical value of  $\alpha$  is  $10^{-3} \text{ } ^\circ\text{C}$  while  $\lambda$  is order 1 cm. For temperature gradients of  $0.1 \text{ } ^\circ\text{C}/\text{cm}$  (a very large value compared with the results of Gregg (1976)) the reflection coefficient is  $-135 \text{ dB}$ .

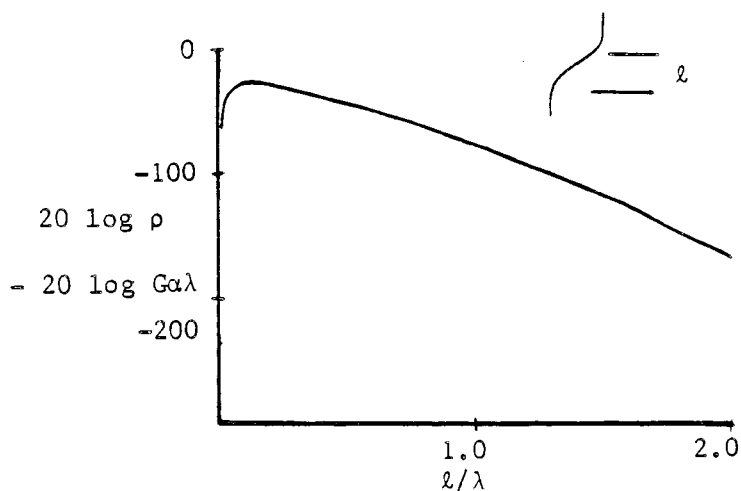


Fig. 3. Reflection coefficient for a sheet of microstructure with temperature gradient  $G$ .

Whether this level of reflection (from a single microstructure layer) can be detected depends upon the sonar design. However we can compare this reflection coefficient with a coefficient for zooplankton scattering. Hall (1981) examined backscattering in waters around Australia and his data for the Great Australian Bight area, a region expected to have

intermediate backscattering strengths, allows an approximate calculation of the reflection from typical concentrations of zooplankton. These data are quite successful in predicting backscattering at 20 kHz frequencies. Using Hall's predicted backscatter reflection coefficient for a 1 meter portion of the water column one estimates a backscatter strength in dB per cubic meter referenced to 1 m of about  $-100 \text{ dB} - 10 \log (\lambda/7.5)^4$  where  $\lambda$  is in cm. (for our restricted range of  $\lambda$ ). We have used only the copepoda scatters to ensure a conservatively low estimate of backscatter.

Thus for a layer of depth  $\lambda$  the expected backscatter from zooplankton is  $-114 \text{ dB} - 30 \log (\lambda/7.5)$ . While the concentration of zooplankton will be a particularly variable quantity, the above calculation makes it clear that biological scatters were more likely responsible for the scattering level seen in our records.

This may provide an explanation for the fact that the thermocline was seen only occasionally in the record since we believe microstructure is very common on the Bass Strait thermocline, e.g. Jones & Bruzzone (1981). Biological scattering is dominating the sonar returns and only when the zooplankton concentrates at the thermocline are oceanographic features visible.

We have to contend with the problem of animal behaviour when interpreting the distribution of sonic scattering layers. The vertical migrations undertaken by both large and small organisms is well documented and is in the main influenced by ambient light levels (Boden & Kampa, 1967). While it may be possible to broadly classify some of the major ocean basins in terms of their sonic scattering layers, the Bass Strait and western Tasman Sea regions appear to be highly variable acoustic environments (Hall, 1973; Hall & Quill, 1983). Future work will attempt to test some of the above assumptions directly.

#### REFERENCES

Boden, P.B. and E.M. Kampa (1967) The influence of natural light on the vertical migrations of an animal community in the sea. Symp. Zoo. Soc. Lond. 19:15-26.

- Brekhovskikh, L.M. (1980) Waves in Layered Media. Academic Press, N.Y. pp. 503.
- Gregg, M.C. (1976) Finestructure and Microstructure Observations During the Passage of a Mild Storm. J. Phys. Oceanogr., 6, p.528.
- Hall, M. (1973) Volume backscattering in the Tasman Sea, the Coral Sea and the Indian Ocean. J. Acoust. Soc. Am. 54:473-477.
- Hall, M. (1981) Measurements of Acoustic Volume Backscattering in the Indian and Southern Ocean. A. J. Mar. Freshwater Res., 32, p.855.
- Hall, M. and A.F. Quill (1983) Biological sound scattering in an ocean eddy. Aust. J. Mar. Freshw. Res., 34:563-72.
- Jones, Ian S.F. and F. Bruzzone (1981) An oceanographic Richardson number probe, Deep Sea Res., 28, p.507.

An Assessment of Second-Order Perturbation Theory for Scattering of Sound  
by a Surface Roughened by Hard, Spherical, Randomly Distributed Bosses

A. Tolstoy, D. Berman, O. Diachok  
Naval Research Laboratory, Washington, D.C. 20375

I. Tolstoy  
Knockvennie, Castle Douglas, S.W. Scotland

ABSTRACT

Perturbation theory and boss models for rough surface scattering are compared for the case of a surface consisting of identical, hard, spherical bosses sparsely and independently distributed on a hard plane by means of a uniform probability law. Calculations of the magnitude of the reflection coefficient  $|R|$  are presented showing that for low frequencies the discrepancies relative to known near-exact solutions are effectively zero ( $\ll 0.004$  dB) and in general decrease as grazing angle increases. Thus, at low frequencies perturbation theory is shown to give good results for  $|R|$  despite the discontinuous and infinite slope in the surface where the bosses meet the base plane. We also examine the effects of increasing frequency for bosses of 1 m height and find errors less than 3 dB for frequencies less than 190 Hz.

## INTRODUCTION

One potential application of the theory of reflectivity from bossed surfaces occurs in underwater sound propagation over a rough bottom. Second-order perturbation theory [1,2] is one of the few theories presently capable of describing the scattering of low-frequency (L.F.) acoustic waves by statistically rough surfaces. It requires, at least for computing the reflection coefficient  $R$ , only a rather simple description of surface roughness, i.e. the spectrum of surface heights. This simplicity makes it very attractive to use, but at the same time limits its domain of applicability. Although it is known that this domain is characterized by small surface heights compared to an acoustic wavelength, and by small surface slopes [3], it is important to have quantitative limits of applicability.

In order to determine just when one can use perturbation theory, we will compare perturbation theoretic results for  $|R_{\text{per}}|$  with available results for  $|R_{\text{n.ex}}|$  obtained from the scattering amplitudes of the individual bosses where such results are nearly exact in the limit of sparse bosses. Another reason for examining perturbation results in the case of a bossed surface is that such a surface exhibits large slopes where the bosses meet the base plane. It might be thought that perturbation theory would fail as a result. In fact, perturbation theory does quite well, as will be shown below.

We will consider surfaces which consist of identical, hard, spherical bosses sparsely and independently distributed on a hard plane by means

of a uniform probability law [4] (see Fig. 1). In order to apply perturbation theory to such a surface we computed its surface height covariance function and calculated various integrals of the covariance function to obtain the effective surface admittance. The computation of the scattering amplitudes required a series evaluation of Legendre polynomials with coefficients in terms of the derivatives of spherical Bessel functions [5]. Subsequently, calculations of  $|R|$  will be presented using both approaches for various frequencies.

## I. COMPUTATIONS

For the results presented here we shall assume a boss height  $a$  of 1 m and a density of 1 boss per  $m^2$ . First, we computed  $|R|$  as a function of grazing angle  $\theta$  for wavenumber  $k = 0.1 \text{ m}^{-1}$  (frequency = 25 Hz). We found that  $|R_{\text{per}}| > |R_{\text{n.ex}}|$  for all  $\theta$ . The disagreement was greatest at low values of  $\theta$  and improved as  $\theta$  increased (Fig. 2). Quantitatively this discrepancy is most easily seen by examining the different reflection losses, i.e., by computing RATIO where  $\text{RATIO} = \text{Loss}_{\text{per}}/\text{Loss}_{\text{n.ex}}$  with  $\text{Loss} = 1 - |R|$ . We find that the loss to  $|R|$  predicted by perturbation theory is  $\sim 70\%$  too low at  $\theta$  small (see Fig. 3). However, we note that  $|R| > 0.9988$  for both approaches. Hence, the difference between the approaches will not actually be observable, i.e.,  $10[\log(0.9996) - \log(0.9988)] \approx .004 \text{ dB}$ .

In an effort to quantify when perturbation theory predictions will have observably large errors (for a single surface interaction), we have also examined the effects of increasing frequency given a surface of

spherical bosses. In Fig. 4 we see that perturbation theory will show errors less than 3 dB at  $\theta < 50^\circ$  for  $k < 0.8 \text{ m}^{-1}$  (190 Hz). The corresponding  $|R|$  plots are shown in Fig. 5, and we note that for  $ka = 1$  we have high scattering losses. That is,  $|R| \ll 1$  for both approaches. At shallow grazing angles ( $\theta < 50^\circ$ ) perturbation theory underestimates these losses. This behavior is consistent with what we observed at low frequencies (Fig. 2). However, at the higher frequencies we no longer have consistently improved agreement as  $\theta$  increases.

## II. CONCLUSIONS

For the statistical boss surface considered we have concluded that second-order perturbation theory predicts well the low frequency scattering behavior even though the small slope requirement is violated (over a small region). It is often stated that perturbation theory is applicable only to surfaces with small slopes [6]. Nevertheless, perturbation results will be good at low frequencies. The reason for this is that the "small slope" requirement is really only a requirement that the characteristic vertical scale,  $a$ , of the rough surface be smaller than the characteristic horizontal scale of the surface roughness,  $b$ . The calculations presented here show explicitly that even in the case of spherical bosses ( $a=b$ ), perturbation theory works well for low frequencies even when there are large slopes.

This perturbation approach can be further generalized (by means of its covariance function) to consider a surface where the bosses do not overlap, i.e., are not independently distributed, or where the bosses are not identical. It can also be applied to surfaces of small-sloped bosses like caps [7] or to those not characterized by boss-like structures at

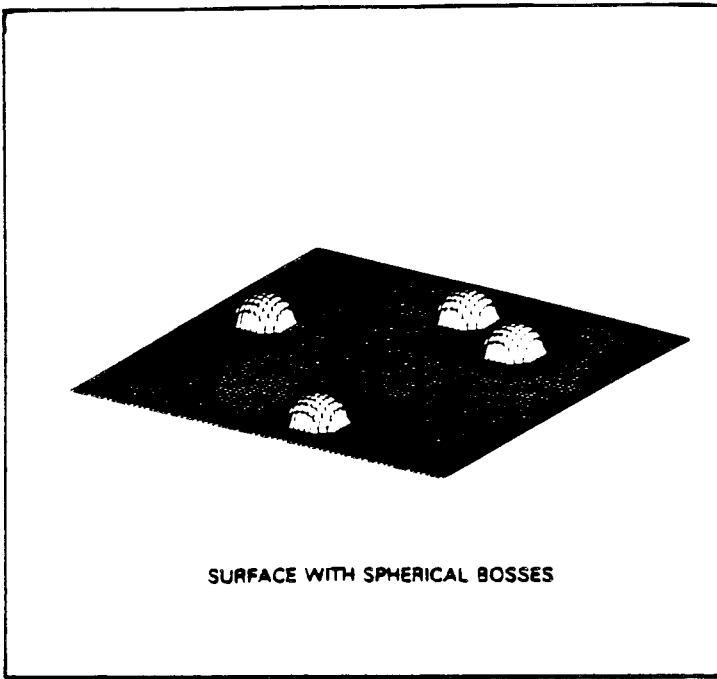
all. In the above calculations we also required that the acoustic wavelength  $\lambda$  ( $\lambda \simeq 6.28 \text{ m}$  for  $k = 1 \text{ m}^{-1}$ ) was much greater than the correlation length  $L$  ( $L = a$ ). However, Wenzel [1] shows how to treat the case  $a \ll \lambda \ll L$ .

#### Acknowledgements

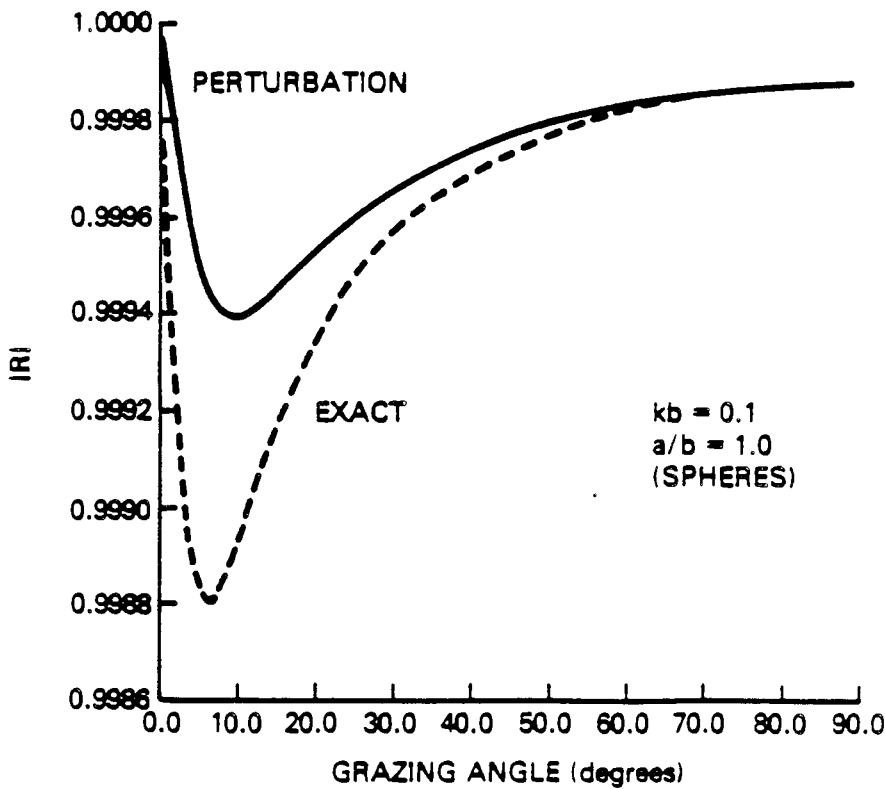
This work was supported by ONR and NRL.

## REFERENCES

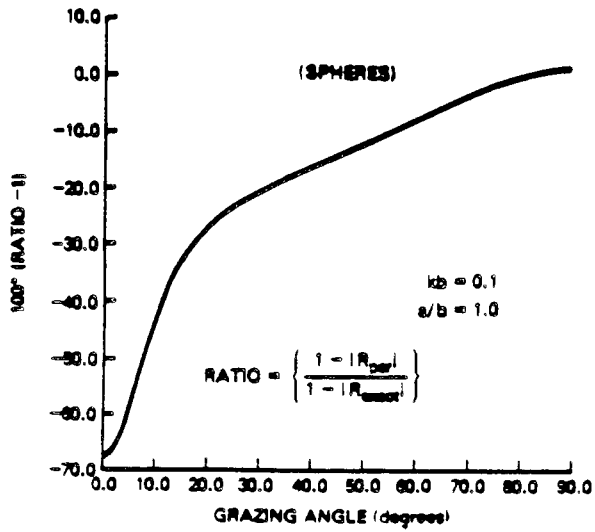
1. A.R. Wenzel, "Smoothed boundary conditions for randomly rough surfaces," *J. Math. Phys.* 15, 317 - 323 (1974).
2. F.G. Bass and I.M. Fuks, *Wave Scattering from Statistically Rough Surfaces* (Pergamon Press, Oxford, 1979). Trans. C.B. Vesecky and J.F. Vesecky.
3. F.M. Labianca and E.Y. Harper, "Connection between various small wave-height solutions of the problem of scattering from the ocean surface," *J. Acoust. Soc. Am.* 62, 1144 - 1157 (1977).
4. V. Twersky, "On scattering and reflection of sound by rough surfaces," *J. Acoust. Soc. Am.* 29, 209 - 225 (1957).
5. A. Tolstoy, D. Berman, O. Diachok, and I. Tolstoy, "An Assessment of Second-Order Perturbation Theory For the Scattering of Sound by a Statistically Rough Surface" submitted to *J. Acoust. Soc. Am.*
6. J.G. Watson and J.B. Keller, "Reflection, scattering, and absorption of acoustic waves by rough surfaces," *J. Acoust. Soc. Am.* 74, 1887 - 1894 (1983).
7. I. Tolstoy, "Smoothed Boundary Conditions, Coherent Low-Frequency Scatter, and Boundary Modes," *J. Acoust. Soc. Am.* 75, 1 - 22 (1984).



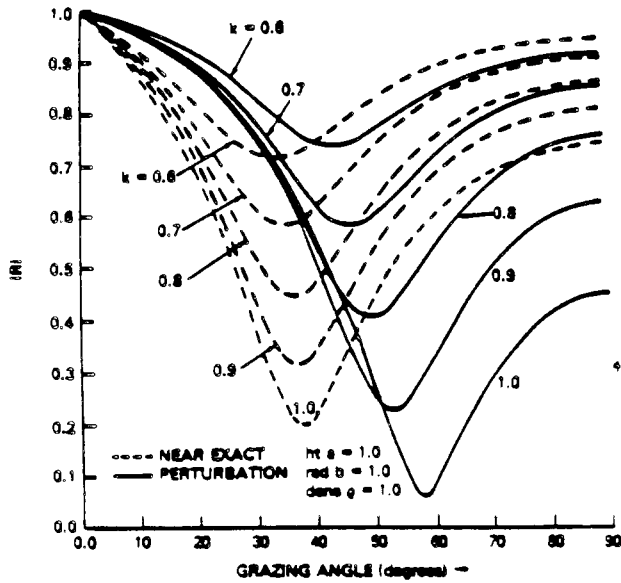
1. A surface of spherical bosses which have been distributed on a plane by means of a uniform probability law.



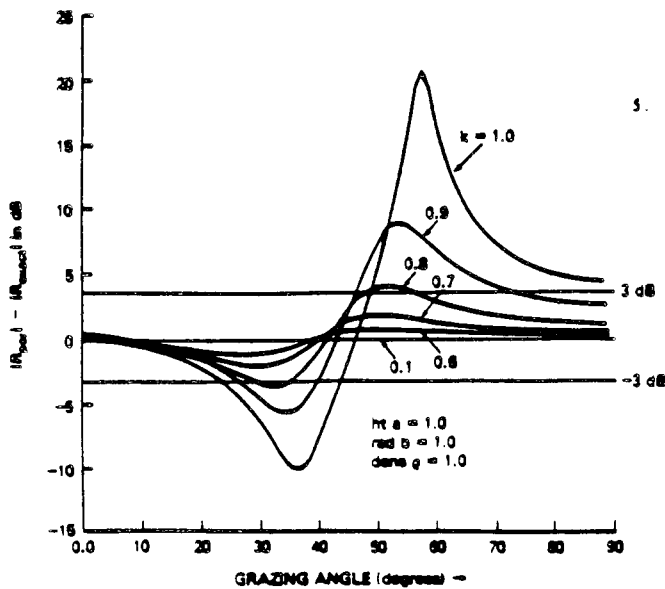
2. The magnitude of the reflection coefficient  $|R|$  as a function of grazing angle. The incident plane wave has wavenumber  $k = 0.1 \text{ m}^{-1}$  (frequency 25 Hz), boss height  $a =$  boss radius  $b = 1 \text{ m}$ , distribution density of 1 boss per  $\text{m}^2$ . The solid curve corresponds to the perturbation theory prediction while the dashed curve computes the near-exact value as predicted by Twersky. Note that the vertical axis begins at 0.9986 indicating that very little scattering is occurring.



3. Relative losses to  $|R|$  as a function of grazing angle. We note here that perturbation theory underestimates the loss to  $|R|$  by as much as 70% at shallow grazing angles on the order of  $1^\circ$ .



4. The difference in dB between  $|R|$  as computed by perturbation theory and by the near-exact theory as a function of grazing angle and as a function of wavenumber  $k$  ( $m^{-1}$ ). We note that increasing  $k$  results in increased error for perturbation theory, and we see that at grazing angles less than  $50^\circ$  perturbation theory results in less than 3 dB error for  $k < 0.8\ m^{-1}$ .



5. Same as Fig. 2 except that wavenumber  $k$  varies from  $0.6\ m^{-1}$  to  $1.0\ m^{-1}$ . We note that perturbation theory continues to underestimate the losses to  $|R|$  at grazing angles less than  $40^\circ$ .

## ECHO STRENGTH OF SPHERICAL OBJECT IN THE PRESENCE OF NEARBY BOUNDARIES

Xiao-ling Bao    Bo-snen Liu    Fei-hu Li

Department of Underwater Acoustic Engineering  
Harbin Shipbuilding Engineering Institute  
HARBIN, CHINA

## 1. INTRODUCTION

It is of interest to study the frequency response and directional characteristics of echo strength for an object in the presence of nearby boundaries. In recent years, the T-matrix method was used to solve this kind of problems.<sup>[1,2]</sup> In this paper, the Rayleigh image method<sup>[3]</sup> is extended to solve echo strength of object near a rigid boundary, and the dual-sphere model is used to estimate the effects of multiple reflections on the echo strength of the object, lying under the liquid-liquid interface.

The results of numerical calculation show that, for the case of an object near a rigid boundary, the echo strength is changed by interference between the direct echo of the object and the echo of the object, reflected by the interface. In the case of an object under the fluid-fluid interface, the decrease of echo strength principally comes from the deflection of the wave transmitting through the interface, and the effects of multiple reflecting on the total echo strength generally are small enough and can be ignored.

## 2. ECHO STRENGTH OF THE SPHERICAL OBJECT ABOVE THE BOUNDARY

According to the image method of Rayleigh,<sup>[3]</sup> the scattered field of a semi-sphere protruding from a rigid plane for an incident plane wave equals the scattered field of a sphere in the free space illuminated by two incident waves: the originally incident wave and its image with respect to the plane. This result may be generalized to the case of elastic hemisphere on a rigid boundary or an elastic sphere above a rigid boundary. The symmetry of the sources and objects with respect to the plane  $z=0$ , ensures the rigid boundary condition at the plane  $z=0$  will be satisfied.

As well known, when plane acoustic wave incident on an elastic sphere of radius  $a$  in the fluid, the scattered field can be written as follows:

$$p_{sc} = p_0 \sum_{n=0}^{\infty} (2n+1) i^n R_n(x) h_n'''(kr) F_n(\cos\theta) \quad (1a)$$

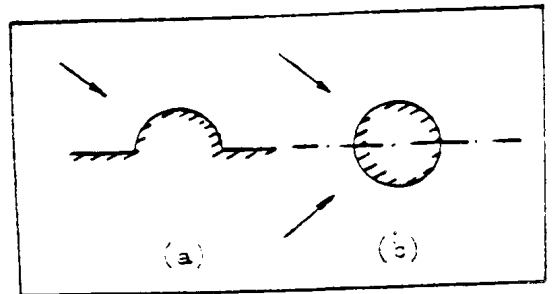


Fig.1. Rayleigh image method

where

$$R_n(x) = - \frac{j_n(x)Y_n - xj_n'(x)}{Y_n'(x)Y_n - xY_n''(x)} \quad (1b)$$

The  $j_n$  and  $h_n^{(1)}$  in Eq.(1) are the Spherical Bessel functions and the Spherical Hankel functions of the first kind, respectively. The expressions of the quantities  $F_n$  can be found in reference.<sup>[4]</sup> The argument  $x$  is  $x = ka = \omega a/c$ , where  $c$  is the speed of sound in fluid.

In the far field,  $h_n^{(1)}(kr)$  may be written in its asymptotic form, then the scattered pressure can be rewritten as:

$$f_\infty(\theta) = - \frac{2}{ka} \sum_{n=0}^{\infty} i(2n+1)R_n(x)P_n(\cos\theta) \quad (2)$$

where  $f_\infty(\theta) = (2r/a)(p_{sc}/p_0)e^{i\theta}$  (3)

is called the far-field form function.

According to image method of Rayleigh, the final expression for the echo field from the elastic semisphere on rigid plane is

$$f_\infty(\alpha) = \frac{2}{ka} \sum_{n=0}^{\infty} i(2n+1)(-1)^{n+1}R_n(x)[1+P_n(\cos 2\alpha)] \quad (4)$$

And for the case of elastic sphere, ignoring the multiple scattering, the echo field is

$$f_\infty(\alpha) = \frac{4}{ka} \sum_{n=0}^{\infty} i(2n+1)(-1)^{n+1}R_n(x)[\cos(2hk \sin\alpha) + P_n(\cos 2\alpha)] \quad (5)$$

where the argument  $\alpha$  represents the grazing angle of incident wave.

The results of numerical calculation show that, in the case of a sphere or semisphere above rigid boundary, there is a fluctuating component added to the curves of frequency response of echo signal, compared with the frequency response of echo signal of single sphere in free space. For wave incident at small grazing angle or for case of semisphere, the fluctuating period of additional frequency response is longer and it decreases with the increase in grazing angle and the distance between the sphere and boundary. The frequency response of echo signal from semisphere is plotted in Fig.2, where the dashed line represents additional fluctuation obtained by geometrical acoustic method.

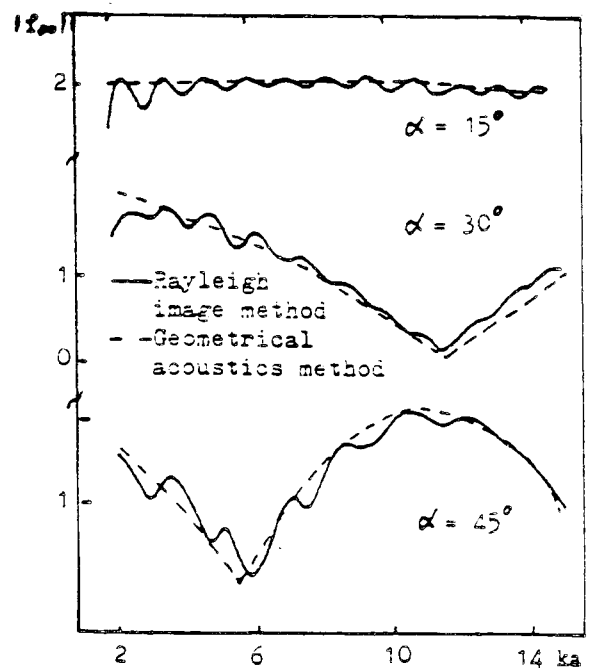


Fig.2. The frequency response of the rigid semisphere on rigid boundary



the sphere and the interface will be equivalent to the multiple scattering between the dual-sphere as shown in Fig. 4. Therefore  $\Phi_{mi} = V \Phi_{s2}$ , where  $\Phi_{s2}$  is the scattering field from the image sphere. The total field on the two spherical surfaces will be

$$\left. \begin{aligned} \Phi_1 &= \Phi_{i1} + \Phi_{s1} + V \Phi_{s2} \\ \Phi_2 &= \Phi_{i2} + \Phi_{s2} + V \Phi_{s1} \end{aligned} \right\} \quad (6)$$

and  $\Phi_{s1}$ ,  $\Phi_{s2}$  can be written as

$$\left. \begin{aligned} \Phi_{s1} &= \sum_{n=0}^{\infty} \sum_{m=-n}^n A_{1mn} h_n^{(u)}(kr_1) P_n^m(\cos \theta_1) e^{im\varphi_1} \\ \Phi_{s2} &= \sum_{n=0}^{\infty} \sum_{m=-n}^n A_{2mn} h_n^{(u)}(kr_2) P_n^m(\cos \theta_2) e^{im\varphi_2} \end{aligned} \right\} \quad (7)$$

where  $(r_1, \theta_1, \varphi_1)$  and  $(r_2, \theta_2, \varphi_2)$  are spherical coordinates of the receiver in relation to origins  $o_1$  and  $o_2$ , respectively.

Following the methods of Twersky<sup>[6]</sup> which is used to solve the scattering field from the dual-cylinders, we can use the Addition Formula of Legendre function to transform the coordinate from one origin to another. After using the boundary conditions on the spherical surface, we find the following relationships between the coefficients  $A_{1mn}$  and  $A_{2mn}$  for the rigid object.

$$A_{1mn} = ik(-1)^{m+n} (2n+1) R_n(ka) h_n^{(u)}(kr_1) P_n^m(\cos \theta_{01}) - VR_n(ka) \sum_{n'=0}^{\infty} \sum_{m'=-n'}^n A_{2m'n'} \sum_{r=|n'-n|}^{n'+n} a(n, r, n', m, m') h_r(kr_{12}) P_r^{m'-m}(\cos \theta_{21}) \quad (8a)$$

$$A_{2mn} = ik(-1)^{m+n} (2n-1) R_n(ka) h_n^{(u)}(kr_2) P_n^m(\cos \theta_{02}) - VR_n(ka) \sum_{n'=0}^{\infty} \sum_{m'=-n'}^n A_{1m'n'} \sum_{r=|n'-n|}^{n'+n} a(n, r, n', m, m') h_r(kr_{12}) P_r^{m'-m}(\cos \theta_{12}) \quad (8b)$$

$$R_n(ka) = -j_n'(ka) / h_n^{(u)}(ka) \quad (8c)$$

Repeatedly use expressions (8a) and (8b) we can approach the value of  $A_{1mn}$ . If using the matrix notation, the Eq (8) can be rewritten as follows

$$A_1 = (I - M)^{-1} A_{i1} \quad (9a)$$

where

$$A_{i1mn} = ik(-1)^{m+n} (2n+1) R_n(ka) h_n^{(u)}(kr) P_n^m(\cos \theta_{01}) \quad (9b)$$

$$M_{mnm'n'} = (-1)^{n'} R_n(ka) \sum_{r=|n'-n|}^{n'+n} a(n, r, n', m, m') h_r(kr_{12}) P_r^{m'-m}(\cos \theta_{21}) \quad (9c)$$

are the elements of the matrix  $A_{i1}$  and  $M$ , the elements of matrix  $A$ , are  $A_{1mn}$  and  $I$  represents unit matrix. For the convenience of comparison, the notation  $TS_1$  and  $TS_0$  are used to express the target strength.

$$TS_1 = 20 \log [r \Phi_{s1}(kr)] \quad (10a)$$

$$TS_0 = 20 \log [r \Phi_{s1}^0(kr)] \quad (10b)$$

where  $\Phi_{s1}$  and  $\Phi_{s1}^0$  are far scattering fields in the orientation of echo, each corresponds to the case of including multiple scattering or not, respectively. Then the effects of the multiple scattering can be measured by the deviation  $\Delta TS$ .

$$\Delta TS = TS_1 - TS_0$$

(11)

The numerical calculation have been done by using of Eq.8 and Eq.9. Both results are consistant with each other. In Fig.6, the target strength  $TS_1$  and  $TS_0$  is plotted as a function of  $ka$ . The solid line and the dashed line represent the  $TS_0$  and  $TS_1$  of the rigid sphere, respectively, where  $\alpha$  is the grazing angle of deflected wave and the sphere submerged at the depth of  $h/a = 1.5$ . In the Fig.7, the deviation  $\Delta TS$  is plotted as a function of  $ka$  for different  $h/a$ . From these curves, we find that the deviation  $\Delta TS$  is smaller than 0.5dB for the case considered. It is concluded that for oblique incidence, for  $h/a \geq 1.5$ , the effects of the multiple scattering on the total echo strength are small enough and can be ignored. These results are similar to the results obtained in reference [2], in which the authors used T-matrix method to solve the problem of the wave scattering by a subsurface flaw in joined fluid-solid half spaces.

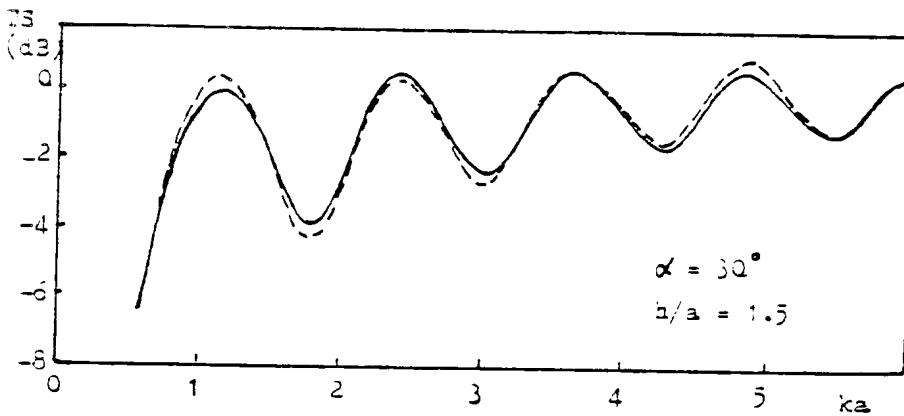


Fig.6. Target Strength of  $TS_1$  and  $TS_0$ .  
 $TS_0$  (—)  $TS_1$  (---)

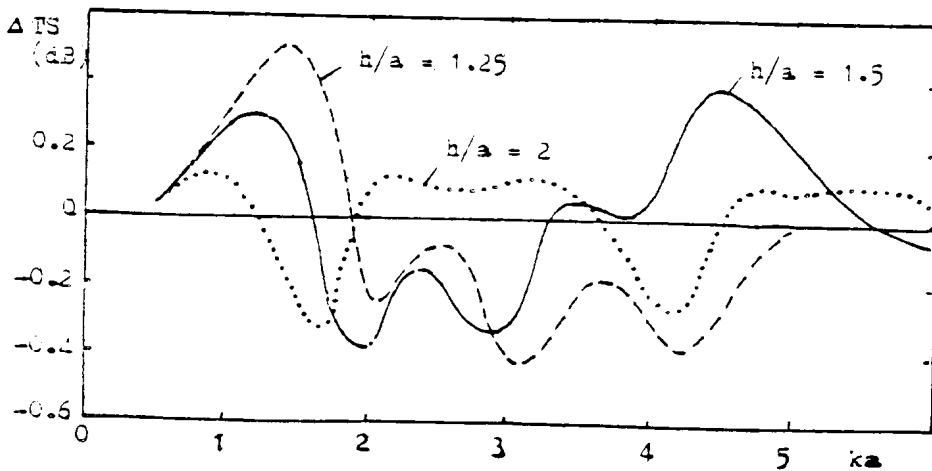


Fig.7. The Curves of  $\Delta TS$

## References

- [1] G.Kristensson and S.Ström, "Scattering from buried inhomogeneities— a general three - dimensional formalism" J.Acoust.Soc.Am., Vol. 54, 917-936 (1978)
- [2] V.V.Varadan, T.A.K.Pillai and V.K.Varadan, "Ultrasonic wave scattering by a subsurface flaw in joined fluid -solid half spaces" J.Applied Mechanics, Vol.105, 802-806 (1983)
- [3] L.Rayleigh, Phil. Mag. 14, 350-359 (1907)
- [4] R.Hickling, J. Acoust. Soc. Am., Vol. 34, 1582-1592 (1962)
- [5] L.M.Brekhovskikh, "Waves in layered media" Academic Press Inc., New York, (1960)
- [6] V.Twersky, J. Acoust. Soc. Am., Vol. 24, 42-46 (1952)
- [7] R.New and T.J.Eisler, J. Sound Vib., Vol. 22, 1- (1972)

## ECHO INTEGRATION APPLIED IN FISHERIES

by REINHOLD WAWROWSKI

AUSTRALIAN MARITIME COLLEGE, LAUNCESTON, TASMANIA

for INTERNATIONAL CONFERENCE

DEVELOPMENT IN MARINE HYDROACOUSTIC - 4-6 DECEMBER, 1984. SYDNEY

### INTRODUCTION

The subject hydroacoustic as science was an object of interest predominantly by persons whose background was physics. Thus, the propagation of sound in water, the energy and the formation of waves was observed and examined.

The equipment which produces the waves is well known as SONAR. This device was successfully applied in the second world war detecting submerged objects. Since then this equipment found application in commercial and fisheries science surveying life objects like fish as well for the evaluation of sea bottom conditions. Thus, the high mathematically subject become used by fishermen, marine biologists and other persons dealing with marine.

The contribution of this paper is not going to consider and analyse the technical performance of the equipment which converts the electrical energy to acoustic waves and vice versa, but will explain the range of application in the fisheries aimed in fish stock assessment.

### SONAR IN FISHING TECHNOLOGY

As mentioned above SONAR of any type whether for horizontal or vertical sound transmission is now a tool for commercial and scientific use in the marine environment. As far as the fishing technology is concerned, hydroacoustic systems are applied in order to detect fish, for examination of the fishing gear performance and for the estimation of fish abundance.

Fig.1 shows Fishing methods where hydroacoustic devices might be applied. Generally the fishing gear is classified in 16 methods depicted symbolically as the following:-

1. Without gear
2. Wounding gear

3. Stupefying methods
4. Lines
5. Traps
6. Aerial traps
7. Bag nets with fixed mouth
8. Dragged gear
9. Seine nets
10. Surrounding nets
11. Drive in nets
12. Lift nets
13. Falling nets
14. Gill nets
15. Tangle nets
16. Harvesting machines

For most or all of these methods a hydroacoustic arrangement can be applied and the technical performance of each gear can be empirically examined.

The fishing gear ranging from hooks and line systems to towed nets causing drag is analysed by a Fishing Gear Technologist at least in 3 aspects:-

1. The construction as a solid and flexible arrangement when working in water. This is an engineering aspect of fishing gear. Fig.2 indicates instrumentation of drag gear in order to measure the geometry of the trawl. The hydroacoustic instrumentation is widely applied.
2. In terms of the impact to the environment - fish behaviour aspect. Fig.3 shows a typical hydroacoustic system for fish detection and the observation of its reaction towards the gear.
3. The catch efficiency of a particular catching method - the aspect of fish availability and selectivity of the gear. Fig.4 suggests the use of an echo integrator for this aspect, which will be explained separately.

The information about the described aspects are obtainable if a hydroacoustic arrangement is applied. From the different sensors (transducers) the signal can be integrated and in a process of time printed or displayed on screen. Such project was already considered and described in a study under the name Integrated Fishing System in Europe, 1970's, conducted by Prof. V. Brandt.

#### ECHO INTEGRATOR BACKGROUND

Apart from the technical aspects of a fishing gear the efficiency of a catching method depends upon fish availability on a particular fishing ground. Thus the fisheries manager, the fishing gear technologist and the fishermen are interested to

know how large the fish resources are and where they are dwelling daily and seasonally.

In order to estimate the Fish Population Abundance, the biologists has a very labor and time consuming method. The method is based on statistical estimations from fishermen's returns and includes measured parameters of:- Age of fish, Live weight, Gonad maturity and variety of species composition.

To assess the fish availability in faster time the FAO has issued a lot of proposals and reports as well as organized a number of conferences promoting the use of an echosounder system for the estimation of fish abundance. At the end of the 1950's marine and aquatic scientists recognized the potential of acoustic techniques for the fish abundance estimation and the management of fish resources. The British, U.S.A., Canadian, Norwegian and other countries researchers and engineers started to work on this problem applying SONAR equipment for the estimation of fish quantity.

## COUNTERS

The first development refers to estimation and was based on counting echoes from fish. This can be seen in the diagram fig.5, which indicates the signal processing.

The counting method was developed by Mr. R. Dowd from the Fisheries Research Board in Canada. Dowd had used a commercial echo sounder of 38kHz connected to a signal processing circuit eliminating echoes from the bottom and counting via a computer echo from individual fish.

The method developed in the Marine Laboratory of Aberdeen by Dr. Craig was based on a special constructed echo sounder of 400kHz and very short 0.1ms pulses and furnished with a variable gain control. The range was divided into 20 phase ranges. Each of the phased range of 7.5m high had the possibility to differentiate 20 levels of voltages received from echoes (80mv to 1.68 volt).

The system was able to count single fish and the amount finally calculated by a computer.

The method developed in Fisheries Laboratory of Lowestoft by Dr. Crushing was based on counting echo traces from a Kelvin Hughes echo sounder and from an oscilloscope, the amplitude. Comparing the two and using a correlation curve it was possible to appraise the length of the fish.

Mr. Minton of the Lowestoft laboratory, who is presently on this conference is continuing the tradition of this development.

The system based on echo counting using commercial echo sounder

does not find application in the fisheries because of the difficulty in the signal processing of the HF amplifier when groups or larger shoals of fish occur.

## INTEGRATORS

The next step in the development in the method of signal processing from echoes is the summation technique of received energy from echoes over a selected time interval.

A Norwegian scientist, Mr. S. Olsen has introduced integration techniques for the estimation of fish using the received energy from an echo producer. As the transmission is determined by time the energy can be calculated by the equation:

$$E_t = k \int_{t_1}^{t_2} U^2 dt$$

Where by  $E_t$  = the energy of an impulse equal to echo signal  
 $k$  = a proportionality coefficient  
 $U$  = the voltage of the impulse in time  
 $t_1$  &  $t_2$  = start and end of the pulse

As the vessel is moved over a number of fish the energy from the transmission of one fish can be expressed in the equation

$$E_e = \sum_{i=1}^n E_i$$

$E$  = the total energy from echoes of one fish  
 $n$  = the number of echoes received from one fish

As in the fish occurs in density and the echoes from two or more fish will overlap, the echo will then be recorded as one trace but of longer duration and larger amplitude.

The value of the energy will be squared and summarized as follows:-

$$E_{n_i} = \sum_{c=1}^N E_e$$

Where  $E$  = the energy impulse from fish  
 $N$  = number of single fish

In the practice the fish is distributed at different distances from the beam with a transducer. Therefore, the integration technique is determined by referral factors. In order to overcome the factors influencing the amplitude a calibration of the echo sounder system as well as the target is essential.

The factors influencing the integration results can be in an

abbreviated form expressed as follows:-

Factors associated with the apparatus  
Factors associated with the fish  
Factors associated with the sound propagation

It has to be mentioned that the processing of the integrated voltage were possible at the moment the transistor and micro processing technology to store the echoes in a capacity of  $16^2$  bits becomes available commercially.

Electronics companies like Simrad of Norway and BioSonics of Seattle, USA overcame the major difficulties of the hard and software by applying the theory of sound propagation and echoes processing very successfully offering to the fisheries for a reasonable price a computerized integrator system for fish abundance calculations.

Fig.6 shows the acoustic signal processing system used for stock assessment.

#### BIOSONICS DIGITAL ECHO INTEGRATOR

The system I have recently worked with and contributed to fish survey in South Dakota, USA was a BioSonics, Seattle development.

Fig.7 shows the complete arrangement for the survey and Fig.8 the model used.

The echo integrator hydroacoustic system consists of the following equipment:-

1. Echo sounder - transmitter and receiver for cresting and receiving electronic signals. The frequency produced and applied for the integration might be between 20-400 kHz.
2. Transducer, oscillator converting the electrical pulse energy into sound pressure waves and vice versa if an echo is crested.
3. Display units - Oscilloscope for the purpose of calibration and signal observation. Paper or colour recorder for the interpretation of fish echo traces and the bottom conditions.
4. Magnetic type recorder for the storing of the survey development and traces.
5. Computer for data recording and processing to biomass calculation using BioSonic software; CRUNCH or ASCOM

The Digital Echo Integrator, Model DEI 121 is designed for field work on board salt and fresh water vessels or for laboratory use. Fig.8.

The front panel of the integrator has special features which allows the operator programming the survey, entering parameters for the integration mode. The parameter programmed is itemized in Fig.9.

After parameters are chosen and entered via data entry key pad, they can be checked using the Mode Selection Switch.

Fig. 10 shows an example of Parameter check printed out.

Surveying a programmed area of water the situation beneath the transducer can be controlled on an oscilloscope or chart recorder. Fig.11 and 12 shows monitored signals on an oscilloscope and the echo traces sampled for integration.

The results of the integrated echoes are printed as raw values for each depth stratum and the portion of the sampled volume. This is shown in Fig.12 and 13.

The data printed on a label after each sequence includes also the acoustic target density.

After the survey is completed the data is compared with the chart records and corrections to each sequence might be discussed alternatively and the data edited through the computer WORD STAR programme.

Consequently all data will be processed in a programme that reads files and coefficients calculating the total biomass in number of fish density per unit area ( $m^3$ ) or fish quantity in kilograms. The computer printout of the final calculation is shown in Fig.14.

## CONCLUSION

1. An acoustic survey system is able to assess the total Biomass and the distribution of fish in open seas as well as in lakes.
2. The system applied in fishing gear technology is able to optimize the catch efficiency of the gear as well as judge the best fishing technique to catch the resources.
3. The evaluation of echo integration data by using precise calibration and dual beam transducer will determine the size of fish available in the fishing area.
4. The anticipated sustainable yield can be forecasted.

## THE EFFECT OF WEIGHT VECTOR ERRORS ON THE PERFORMANCE OF AN ANTENNA ARRAY

Lal C. Godara

Department of Systems Engineering, Research School of Physical Sciences,  
Australian National University, GPO Box 4, Canberra ACT 2601, Australia

INTRODUCTION

The optimal weights of an adaptive antenna array which maximises the output signal to noise ratio can be computed [1-3] using the array correlation matrix of noise and the steering vector in the direction of arrival of the desired narrowband signal, the look direction. In practice the estimated optimal weights are corrupted by random errors which arise due to imperfect knowledge of the array correlation matrix, the errors in steering vector estimation caused by the imperfect knowledge of the element positions and the direction of arrival of desired signal, the error due to the finite word length arithmetic used and so on.

The effect of random errors in the steering vector, which is used in computing the optimal weight vector, is examined in [4]. Results are presented by computer studies to demonstrate the sensitivity of the performance of the array in the presence of steering vector errors to the input signal to noise ratio (SNR). The computer studies show that the output SNR drops faster at high input SNR than at low input SNR as the variance of random errors increases.

In this paper the effect of additive random errors in the estimated weights of an optimal array processor on its performance is studied by deriving the analytic expression for the output SNR and array gain. The aspect of steering vector error is further considered for a general array configuration and analytical expressions for the output SNR and array gain are derived as a

function of the variance of random errors. The cause of the signal sensitivity of the array performance is pointed out and a cure is presented.

## 2. OPTIMAL PROCESSOR

It is assumed that an L element array is located in the far field of a point source. Let  $R_S$  be the array correlation matrix for the signal and  $R_N$  be the array correlation matrix of the noise alone. For a narrowband directional source of power  $p_s$  an expression for  $R_S$  is given by

$$R_S = p_s \underline{S}_0 \underline{S}_0^H \quad (1)$$

where  $\underline{S}_0$  is the steering vector in the look direction.

Let an L dimensional complex vector  $\hat{\underline{W}}$  represent the L optimal weights of the array processor which maximises the output signal to noise ratio. For an array which is not presteered an expression for  $\hat{\underline{W}}$  is given by [1-3].

$$\hat{\underline{W}} = \mu R_N^{-1} \underline{S}_0 \quad (2)$$

where  $\mu$  is a constant. If the array is constrained to have a unit response in the look direction then

$$\mu = \frac{1}{\underline{S}_0^H R_N^{-1} \underline{S}_0} \quad (3)$$

The output signal power  $\hat{P}_S$  and the output noise power  $\hat{P}_N$  of the optimal processor with the unit response in the signal direction are given by

$$\hat{P}_S = p_s \quad (4)$$

and

$$\hat{P}_N = \frac{1}{\underline{S}_0^H R_N^{-1} \underline{S}_0} \quad (5)$$

Let  $\alpha$  denote the output signal to noise ratio of the optimal processor with the unit response in the signal direction, then

$$\alpha \triangleq \frac{\hat{P}_S}{\hat{P}_N} = p_s \underline{S}_0^H R_N^{-1} \underline{S}_0 \quad (6)$$

Array Gain The array gain is defined as the ratio of the output SNR to the input SNR. Let  $\hat{G}$  denote the array gain of the optimal processor, then

$$\hat{G} = \frac{\text{Output SNR}}{\text{Input SNR}} = p_N \underline{S}_0^H R_N^{-1} \underline{S}_0 = \frac{p_N}{\hat{P}_N} \quad (7)$$

where  $p_N$  is the total input noise power. Note that  $\hat{G} > 1$ .

In the next section the effect of random errors in the estimated weights of the optimal processor on its performance is examined.

### 3. WEIGHT VECTOR ERRORS

Let an L dimensional complex vector  $\bar{W}$  represent the estimated weights of the optimal processor. It is assumed that these weights are different from the optimal weights by an additive noise component, that is

$$\bar{W} = \hat{W} + \Gamma = \mu R_N^{-1} S_0 + \Gamma \quad (8)$$

where

$$E[\Gamma_i] = 0 \quad i = 1, 2, \dots, L \quad (9)$$

$$E[\Gamma_i \Gamma_j^*] = \begin{cases} \sigma^2 & \text{if } i = j \\ 0 & \text{otherwise} \end{cases} \quad i, j = 1, 2, \dots, L \quad (10)$$

The output signal power of the processor with estimated weights is given by

$$\begin{aligned} P_S(\bar{W}) &= \bar{W}^H R_S \bar{W} \\ &= p_S (\mu R_N^{-1} S_0 + \Gamma)^H S_0 S_0^H (\mu R_N^{-1} S_0 + \Gamma) \end{aligned} \quad (11)$$

Taking the expected value on both sides and using (3), (9) and (10)

one obtains

$$P_S = p_S (1 + \sigma^2 L) \quad (12)$$

Thus the output signal power increases due to the random errors in the weight vector. Now consider the output noise power.

The output noise power of the processor with estimated weights is given by

$$\begin{aligned} P_N(\bar{W}) &= \bar{W}^H R_N \bar{W} \\ &= (\mu R_N^{-1} S_0 + \Gamma)^H R_N (\mu R_N^{-1} S_0 + \Gamma) \end{aligned} \quad (13)$$

Taking the expected value on both sides and using (3), (9) and (10) one

obtains after manipulation

$$P_N = \hat{P}_N + p_N \sigma^2 L \quad (14)$$

Where  $p_N$  is the total input noise power including directional interferences as well as white noise. Thus the output noise power increases due to the presence of random errors in the weights of the processor. The increase is proportional to the variance of the error, number of elements in the array and the total input noise power of the processor.

Array Gain The following result on the array gain can be established.

The array gain  $G_w$  of the processor with the random additive errors in the weights is a monotonically decreasing function of the variance of the random errors. An expression for  $G_w$  is given by

$$G_w = \hat{G} \frac{1 + \sigma^2 L}{1 + \sigma^2 L \hat{G}} \quad (15)$$

It is evident from (15) that as  $\sigma^2$  grows very high  $G_w$  approaches unity. In the absence of errors in the weights  $G_w$  is equal to  $\hat{G}$ , the array gain of the optimal processor.

#### 4. STEERING VECTOR ERRORS

In this section the steering vector error is considered. It is assumed that each component of the estimated steering vector  $\tilde{\underline{S}}$  is different from  $\underline{S}_0$  by an additive error component, that is,

$$\tilde{\underline{S}} = \underline{S}_0 + \underline{\Gamma}_s \quad (16)$$

where

$$E[\Gamma_{si}] = 0 \quad i = 1, 2, \dots, L \quad (17)$$

and

$$E[\Gamma_{si} \Gamma_{sj}^*] = \begin{cases} \sigma_s^2 & \text{if } i = j \\ 0 & \text{otherwise} \end{cases} \quad i, j = 1, 2, \dots, L \quad (18)$$

Let an  $L$  dimensional vector  $\tilde{\underline{W}}$  represent the estimated weights of the processor when  $\tilde{\underline{S}}_0$  rather than  $\underline{S}_0$  is used in estimating the optimal weights.

The expression for the estimated optimal weights of the processor in this case becomes

$$\tilde{\underline{W}} = \tilde{\mu} R_N^{-1} [\underline{S}_0 + \underline{\Gamma}_s] \quad (19)$$

where  $\tilde{\mu}$  is a constant.

The output signal power of the processor with weight vector  $\tilde{\underline{W}}$  is given by

$$P_s(\tilde{\underline{W}}) = \tilde{\underline{W}}^H R_s \tilde{\underline{W}} \quad (20)$$

Substituting for  $\tilde{\underline{W}}$  and taking the expected value on both sides one obtains after rearrangement and manipulation

$$P_s = p_s [1 + \beta \sigma_s^2] \frac{\tilde{\mu}^2}{\hat{P}_N^2} \quad (21)$$

where

$$\beta = \frac{S_0^H R_N^{-1} R_N^{-1} S_0}{(S_0^H R_N^{-1} S_0)^2} \quad (22)$$

The output noise power of the processor with weight vector  $\tilde{W}$  is given by

$$P_N(\tilde{W}) = \tilde{W}^H R_N \tilde{W} \quad (23)$$

Substituting for  $\tilde{W}$  and taking the expected value on both sides one obtains after rearrangement and manipulation

$$P_N = \frac{\mu^2 [1 + \sigma_s^2 \gamma]}{\Delta} \quad (24)$$

where

$$\gamma \triangleq \frac{\text{Tr } R_N^{-1}}{S_0^H R_N^{-1} S_0} \geq 1 \quad (25)$$

It follows from (24) that the output noise power increases in proportion to the variance of the random errors in the steering vector.

Array Gain Now the result on the array gain of the processor with the random errors in the steering vector is established.

The array gain,  $G_s$ , of the processor with the random errors in the steering vector is a monotonically decreasing function of the variance of the errors.

An expression for  $G_s$  is given by

$$G_s = \frac{1 + \sigma_s^2 \beta}{1 + \sigma_s^2 \gamma} \Delta G \quad (26)$$

Comparison with Previous Study Consider the case of the noise environment when only white noise is present. Let the white noise power on each element is  $p_{WN}$ . A simple calculation yields

$$G_s = \frac{L + \sigma_s^2}{1 + \sigma_s^2} \quad (27)$$

One observes from (27) that for a given error level and input SNR the output SNR of the processor increases as  $L$  increases whereas it is reported in [4] that for a given error level the behaviour of the output SNR depends on the input signal power. Thus there exists a discrepancy between the results presented in this paper and those presented in [4]. The discrepancy is due to

the fact that in estimating the optimal weights in [4] the total array correlation matrix has been used instead of the noise only array correlation matrix as in this paper. The presence of the signal component in the expression for optimal weight has resulted in the strong dependency of the behaviour of the output SNR on the input signal power. This is now proved.

### Signal Sensitivity of Array Performance

Let  $\underline{W}^V$  denote the optimal weights calculated using the total array correlation matrix. In the presence of steering vector errors the expression for  $\underline{W}^V$  becomes

$$\underline{W}^V = \tilde{\mu} R^{-1} [S_0 + \Gamma_S] \quad (28)$$

where

$$R = R_S + R_N \quad (29)$$

Substituting for  $R_S$  from (1) and using the matrix inversion lemma one obtains after manipulation

$$\underline{W}^V = \tilde{\mu} R_N^{-1} (S_0 + \Gamma_S) - \frac{\tilde{\mu} p_S R_N^{-1} S_0 S_0^H R_N^{-1} (S_0 + \Gamma_S)}{1 + p_S S_0^H R_N^{-1} S_0} \quad (30)$$

Comparing (30) with (19) one notes the second term in (30) is due to the presence of the signal component in the array correlation matrix which is used in estimating the optimal weight.

In this case the expression for the output signal power is given by

$$P_S = \frac{\tilde{\mu}^2 p_S (S_0^H R_N^{-1} S_0)^2}{(1 + p_S S_0^H R_N^{-1} S_0)^2} [1 + \sigma_S^2 \beta] \quad (31)$$

and the expression for the output noise power is given by

$$P_N = \frac{\tilde{\mu}^2 (S_0^H R_N^{-1} S_0)^2}{(1 + p_S S_0^H R_N^{-1} S_0)^2} \hat{P}_N [1 + \sigma_S^2 [\gamma + (\alpha^2 + 2\alpha)(\gamma - \beta)]] \quad (32)$$

and  $\gamma \geq \beta$

Thus the output noise power of the processor increases with the increase in the variance  $\sigma_S^2$ , of the random error and the increase is enhanced by the input signal power due to the presence of product terms  $\sigma_S^2 \alpha^2$  and  $\sigma_S^2 \alpha$ .

The out signal to noise ratio is now examined.

Let  $\overset{V}{\text{SNR}}$  denote the output signal to noise ratio of the optimal processor when the total array correlation matrix is used in calculating the optimal weights, then

$$\overset{V}{\text{SNR}} = \frac{\alpha (1 + \sigma_S^2 \beta)}{1 + \sigma_S^2 [\gamma + (\alpha^2 + 2\alpha)(\gamma - \beta)]} \quad (33)$$

Consider a special case when the noise environment consists of white noise only. In this case

$$\overset{V}{\text{SNR}} = \frac{P_S}{P_{Wn}} \frac{L + \sigma_S^2}{1 + \sigma_S^2 [1 + (\frac{P_S}{P_{Wn}})^2 L(L-1) + 2 \frac{P_S}{P_{Wn}} (L-1)]} \quad (34)$$

It is clear from (34) that in the presence of errors the behaviour of output SNR is sensitive to the input SNR. For example, for a given L the  $\overset{V}{\text{SNR}}$  drops faster at higher input SNR than at lower input SNR, as reported in [4]. The details of the results presented here can be found in [5].

ACKNOWLEDGEMENT The work is supported by the Department of Defence, Australia.

#### REFERENCES

1. Applebaum, S.P., "Adaptive arrays", IEEE Trans. Antenna Propagat., Vol. AP-24, No. 5, September 1976, pp. 585-598.
2. Vural, A.M., "An overview of adaptive array processing for sonar applications", EASCON 75, pp. 34-A - 24-M.
3. Reed, I.S., Mallet, J.P. and Brennan, L.E., "Rapid convergence rate in adaptive arrays", IEEE Trans. Aerospace Electronic Syst., Vol. AES-10, No. 6, November 1974, pp. 853-863.
4. Compton, JR, R.T., "The effect of random steering vector errors in the Applebaum adaptive array", IEEE Trans. Aerospace Electronic Syst., Vol. AES-18, No. 5, September 1982, pp. 392-400.
5. Godara, L.C., 'The effect of weight vector errors on the performance of an antenna array', to be published.

## A COMPARISON OF VARIOUS FREQUENCY ESTIMATORS

R.F. Barrett and D.R.A. McMahon

Weapons Systems Research Laboratory  
Defence Research Centre, Salisbury  
ADELAIDE, South Australia

Optimal frequency estimation from a discrete time series of acoustic signals in noise is essential to the passive sonar classification of acoustic sources. At DRCS an evaluation of various autoregressive and non-autoregressive techniques of frequency estimation has been carried out for a discrete time series constructed from sinusoids embedded in white gaussian noise.

Among the autoregressive techniques investigated are the standard Pisarenko algorithm (references 1 and 2), the extended Prony method of Marple (references 1 and 3) and a diagonalisation Prony method developed by the authors (reference 4). The autoregressive techniques have the attractive feature of removing side lobes associated with the standard Fast Fourier Transform (FFT) periodogram, thus enabling the resolution of two or more closely spaced sinusoids without sacrificing details of the short-period frequency-time history.

The non-autoregressive methods considered here are the maximum likelihood technique (references 5 and 6) and a phase interpolation estimator (PIE) developed by the authors (reference 4). The former method requires the accurate location of the frequency corresponding to the maximum power in the power spectrum. A conventional FFT is first used to obtain a rough first approximation to the signal frequency. A refinement of this estimate is then obtained by a least squares quadratic fit to the spectrum at several closely spaced frequencies to find the frequency corresponding to maximum power. Either ordinary Fourier transforms or zero padded FFT's can be used to obtain the spectral power at frequencies closer than the nominal FFT bin separation,  $T^{-1}$ , where  $T$  is the time interval of the data samples used for the frequency estimation.

The phase interpolation method makes use of the phase information normally discarded from the Fourier transform when calculating the spectral power. The amplitude  $A(f)$  and phase  $\phi(f)$  of the Fourier transform at frequency  $f$  of the time series  $y(t)$  are defined by:

$$A(f) e^{-i\vartheta(f)} = \frac{1}{\sqrt{T}} \int_0^T y(t) e^{-2\pi i f t} dt.$$

It can be shown that for a sinusoid  $y(t) = \cos(2\pi f_s t - \varphi)$  in the absence of noise the fourier transform phase  $\vartheta(f)$  is to a good approximation linearly related to the phase  $\varphi$  of the sinusoid by an expression of the form

$$\vartheta(f) = \varphi + \Phi(f_s, f, T) .$$

Consider two intervals  $(0, T)$  and  $(T', T + T')$  which have corresponding sinusoids  $\cos(2\pi f_s t - \varphi)$  and  $\cos(2\pi f_s t' - (\varphi - 2\pi f_s T'))$ . The function  $\Phi(f_s, f, T)$  is the same for both time intervals so that the difference between the phases of the two fourier transforms is related to the signal frequency  $f_s$  by

$$\vartheta'(f) - \vartheta(f) = -2\pi f_s T' .$$

Explicitly allowing for the fact that  $\vartheta'(f) - \vartheta(f)$  is uncertain to some multiple of  $2\pi$ , the frequency estimation is given by

$$f_s^{(L)} = \frac{L}{T'} - \frac{\Delta\vartheta}{2\pi T'}$$

where  $L$  is a positive integer, and  $\Delta\vartheta$  is uniquely determined in the range  $(-\pi, \pi)$ . The term  $L/T'$  is a "bin" frequency which lies within  $\pm(2T')^{-1}$  of the sinusoid's frequency.

The removal of ambiguity in the frequency estimate  $f_s^{(L)}$  due to the unknown value of  $L$  is best accomplished by repeating the estimation using a different value for the time  $T'$ . From the two sets of frequency estimates thus obtained, the frequency common to both sets is selected as the time estimate.

A comparison of the various frequency estimators for simulated data consisting of a single 49.8 Hz sinusoid embedded in white gaussian noise is presented in Figure 1. The simulation assumes a sampling rate of 256 Hz and a one second integration time. The Cramer-Rao bound (reference 6) is also presented for this data.

From figure 1, it is clear that only for signal-to-noise ratios (SNR) greater than about 3 dB are the autoregressive techniques more accurate than the conventional FFT, for which the accuracy is 1 Hz for these data. On the other hand, both the maximum likelihood and phase interpolation methods provide accurate estimates and should be of use for frequency estimation with passive sonar data for which the SNR is usually considerably less than 0 dB.

An example of the application of the phase interpolation method to the frequency estimation of the signal from a nominally 45 Hz acoustic projector (SNR ~ 0 dB) is shown in Figure 2. Accuracies considerably greater than the conventional FFT resolution are obtained. The downward trend in the projector frequency is a result of the Doppler effect due to relative motion of the projector and receiving hydrophone. Correlations between frequencies of the projector fundamental and 3rd harmonic are clearly visible.

Further applications of the frequency estimation techniques described here are being pursued with real acoustic data.

#### REFERENCES

- (1) Kay, S.M. and Marple, S.L., Jr; "Spectral Analysis: A Modern Perspective", Proc. IEEE 69, pp 1380-1419, 1981
- (2) Pisarenko, V.F.; "The Retrieval of Harmonics from a Covariance Function", Geophysics J.R. Astron Soc. 33, pp 247-266, 1973
- (3) Marple, S.L., Jr; "Spectral Line Analysis Via a Fast Prony Algorithm", In Proc. 1982 ICASSP, pp 1375-1378, 1982
- (4) Barrett, R.F. and McMahon, D.R.A.; Paper in preparation
- (5) Tufts, D.W. and Kumaresan, R.; "Improved Spectral Resolution II", In Proc. 1980 ICASSP, pp 592-597, 1980
- (6) Rife, D.C. and Boorstyn, R.R.; "Single-Tone Parameter Estimation from Discrete-Time Observations", IEEE Trans Information Theory, Vol. IT-20, pp 591-598, 1974

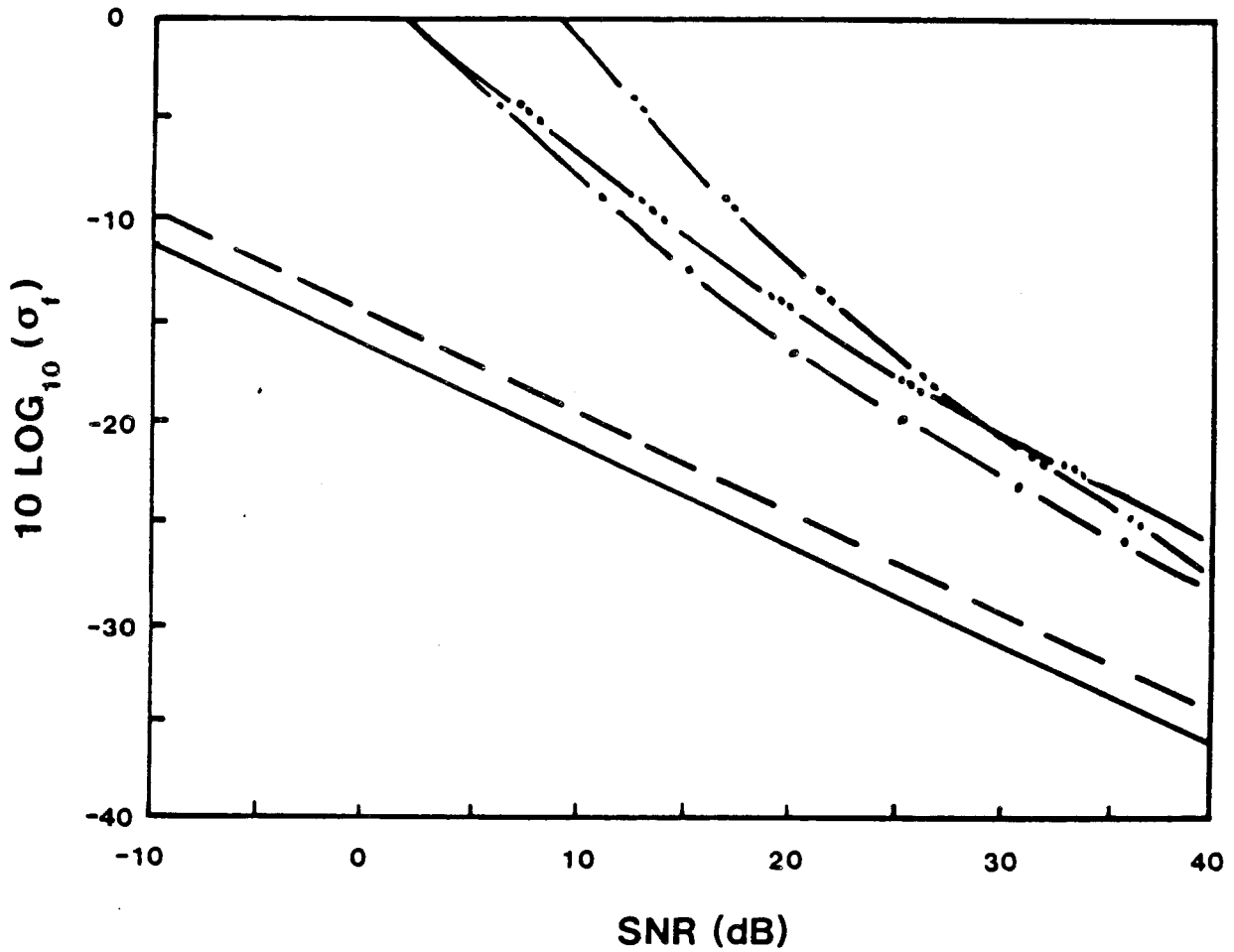


Figure 1

Standard deviation  $\sigma_f$  of various frequency estimators as a function of SNR for 256 sample points.

- Cramer-Rao bound
- - - - - Maximum likelihood and phase interpolation methods
- · - · - Diagonalization technique for Prony method
- · · - · · Extended Prony method of Marple
- · · · - · · · Standard Pisarenko method

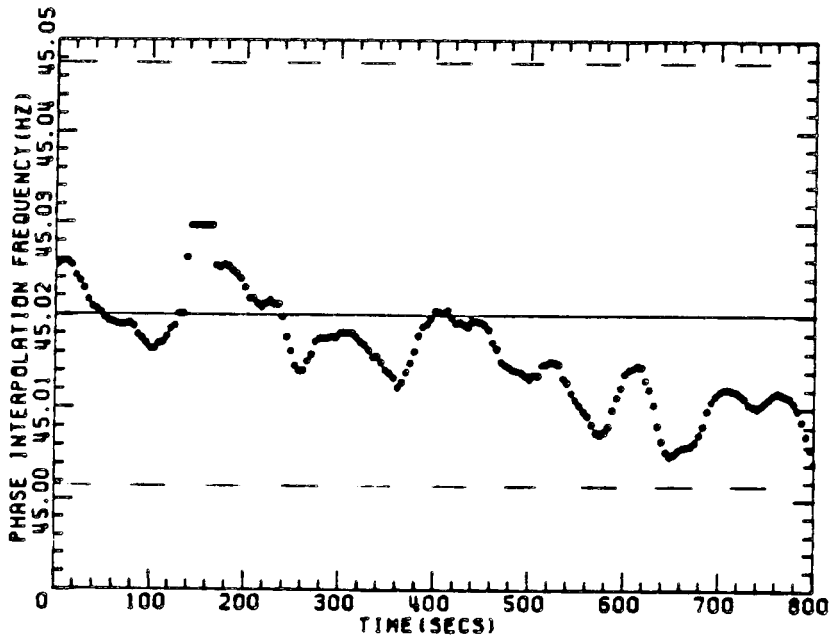


Figure (2.a)

Application of long integration times with the PIE to track the fundamental of a projector. All phases are calculated at the one frequency shown by the solid line. The location of the FFT bins for the same sample size (10,240) is shown by dashed lines.

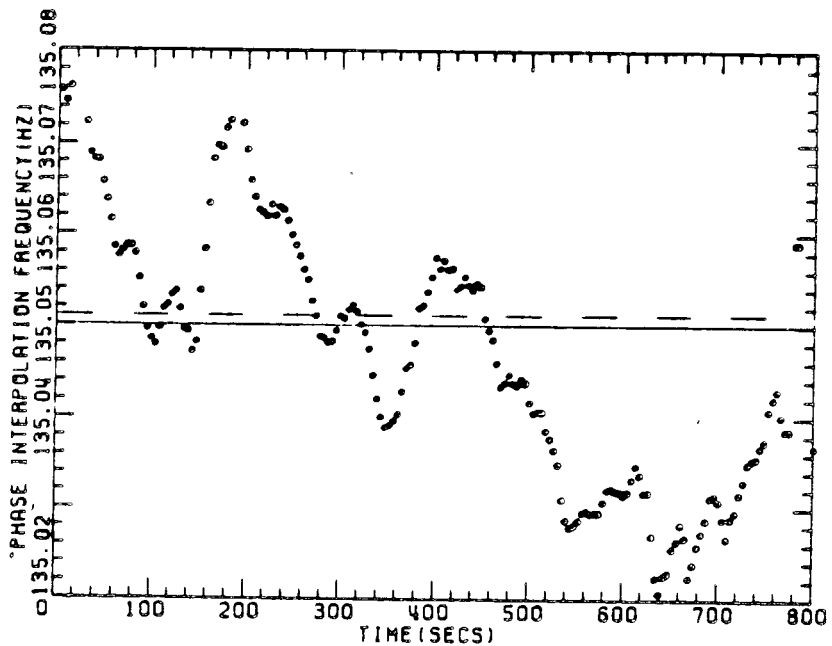


Figure (2.b)

Tracking of the third harmonic of the projector using the PIE with a sample size of 10,240 for each phase determination. The SNR is 15 dB below that for the fundamental.

MEASUREMENTS ON THE OUTPUT STATISTICS OF CONVENTIONALLY AND  
ADAPTIVELY BEAMFORMED UNDERWATER ACOUSTIC DATA

D.A. Gray

Weapons System Research Laboratory  
Defence Science and Technical Organisation  
Department of Defence  
GPO Box 2151 ADELAIDE South Australia 5001

INTRODUCTION

The detection of stable narrowband signals in noise using spectral techniques depends on both the mean and variance of the spectral estimates of the noise power. Conventional beamforming, by virtue of enhancing signals from a desired direction and rejecting, often only partially, noise from unwanted directions can improve the detection performance over that of a single receiver. Adaptive beamforming attempts to steer nulls at strong interferences and by doing so can often markedly reduce the level of noise in beams steered away from the interferences below that of the conventional beamformer. However this improvement in detection performance may be reduced due to an increased variability of the beam noise power spectral estimates relative to those of the conventional processor. The distributions of the outputs of conventional and adaptive frequency domain processors have been extensively discussed in [1] where it is shown, based upon the assumption of Gaussian input data, that they are both central Chi-square distributions but with differing numbers of degrees of freedom. In view of the importance of the second order statistics of the beam powers in statistical detection theory some results of Goodman's work are compared with experimental underwater acoustic data where the time series may no longer be Gaussian. Periods of data characterized by the presence of a strong broadband interference, together with some weaker narrowband and broadband targets at different azimuths were analysed.

It is not the value of the standard deviation of the beam noise estimates that is of interest but rather the ratio of it to the mean of these estimates. The inverse of this quantity squared, known as the equivalent number of degrees of freedom, is commonly used in statistical detection theory to quantify the detection performance. After some discussion of the statistical properties of various estimators of the number of degrees of freedom, the results of applying such estimators to conventional and adaptive beams are presented and discussed. For Gaussian inputs  $R$  has a complex Wishart distribution and from [1] the probability density functions of  $p_c$  and  $p_o$  are both central Chi-square distributions with  $2N$  and  $2(N-K+1)$  degrees of freedom respectively. Note that for conventional beamforming the number of degrees of freedom is independent of the number of receivers used whilst for adaptive beamforming it is directly proportional to the number used. Furthermore for a central Chi-square distribution the ratio of twice the mean squared to the variance is equal to the number of degrees of freedom.

METHOD

Underwater acoustic data from experimental arrays of 25 hydrophones were Fourier transformed and the crosspower spectral matrix at each frequency bin

was estimated by averaging over 50 integrations. The conventional and adaptive beam spectra were estimated at each frequency bin in the bandwidth analysed.

To estimate the number of degrees of freedom at a given frequency, the mean and variance of the spectral estimates at each frequency were first calculated. This is usually done by averaging over independent realisations of the random process and for ergodic processes contiguous blocks of time history can be used. However in this case the total length of data was limited and furthermore the data was not guaranteed to have been sufficiently stationary over the total time period. The following procedure was thus used. At a given frequency the mean and variance of the spectral estimate was estimated by using the nearest 32 spectral estimates. This was repeated for each frequency bin although it should be realised that only estimates separated by 32 bins can be considered independent. At any frequency  $f$  an estimate of the number of degrees of freedom is given by

$$n_{\text{dof}} = \frac{2 M_p^2(f)}{MS_p(f) - M_p^2(f)}$$

where  $M_p(f)$  is the mean of the windowed beam power estimates and  $MS_p(f)$  is the mean of the square of the values in the window.

Assuming Gaussian data, then the resulting distribution of beam powers from conventional processing using a covariance matrix averaged over 50 realisations is Chi-square with 100 degrees of freedom. However experimental simulations indicated that the above estimator is positively biased, this bias decreases as the window size increases. Allowing for this bias the mean result for the estimated number of degrees of freedom would be 113. For adaptive processing with 25 receivers, the corresponding beam power spectral estimates are Chi-square distributed with 52 degrees of freedom which allowing for the bias would result in an estimated mean of 59.

Two examples of the results used as a basis for the conclusions drawn in this paper are shown in figures 1 & 2. The beam power spectrum are plotted above the number of degrees of freedom estimated from it. A running mean also was used to smooth the estimated number of degrees of freedom. The conventional results of figure 1 can be directly compared with the corresponding adaptive results of figure 2.

#### RESULTS FOR DIFFERENT DIRECTIONS

It was found that the results could be classified in terms of the beam spectra which fell into 3 main categories:

- (i) steering at the dominant broadband interferences
- (ii) steering at weaker broadband and line interferences
- (iii) steering in directions apparently void of any signals.

#### (i) Dominant broadband interferences

The beam spectra of broadband interferences were all dominated by numerous spectral lines in the region 10-300 Hz. Above 300 Hz for some interferences the spectrum was reasonably flat whilst for others it rolled off at the rate of about 6-9 dB per octave.

The conventional and adaptive spectra were almost identical and consequently

the estimated number of degrees of freedom were very similar. In the cases analysed the results were approximately independent of the shape of the spectra with an estimated number of degrees of freedom of 3-4 below 300 Hz and of the order of 30-40 in the region 300-600 Hz. For both processors these results are well short of theoretical predictions based on Gaussian assumptions and furthermore do not show anything like the expected differences between conventional and adaptive beamforming predicted by theory.

(ii) Weaker broadband and narrowband interferences

For periods during which an additional source consisting of both broadband and narrow band signals was present the estimated number of degrees of freedom for both processors still fell well below theoretical predictions. This was in part due to a number of sinusoidal components in the spectra whose effect could not be removed by the iterative refinement process and results from periods where the number of lines were lower showed an increased number of degrees of freedom. Above 300 Hz typical values were 8-15 for adaptive beamforming and 15-25 for conventional beamforming.

One important difference between the adaptive and conventional results is that the adaptive results show less variation with frequency and in fact below 300 Hz were often greater than the corresponding conventional ones. This can be understood by reference to the corresponding beam spectra; at all frequencies but particularly below 300 Hz the adaptive beamformer by virtue of its null steering capability is able to reject more of the dominant broadband interference than the conventional processor. It is the rejection of the high variance and spectral lines of this interference that results in the adaptive spectra showing a greater number of degrees of freedom ( typically 5-10 ) than the conventional ones ( typically 3-4 ).

(iii) Directions void of targets

As would be expected the estimated number of degrees of freedom of beams steered in these directions gave the closest agreement with theoretical results. Above 300 Hz the conventional results ranged from 45-90 and the adaptive ones from 35-60 , on some occasions and at some frequencies the adaptive ones being equal to the conventional. The agreement with theory is better for adaptive than conventional beamforming and their differences are much less than predicted by theory. Below 300 Hz both beamformers gave values around 5-10 with the adaptive results, in general, being greater than the corresponding conventional ones.

In almost all cases considered the improvement of the adaptive results relative to conventional occurred when the adaptive beamformer more effectively nulled out the broadband interference than did the conventional beamformer.

#### RESULTS FOR DIFFERENT NUMBERS OF RECEIVERS AND INTEGRATIONS

The expression for the number of degrees of freedom is, for conventional beamforming independent of the number of receivers whilst, for adaptive beamforming it is directly proportional to the number of receivers used. These predictions were tested by comparing the results for beams formed from the full 25 hydrophones with those for beams formed using only 10 hydrophones.

In beams steered at the dominant interferences and in directions void of targets the conventional results were, to within the accuracy of the measurements, independent of the number of receivers used. When steered at weaker broadband interferences the results implied that the subarray conventional beams had a slightly greater number of degrees of freedom than the beams formed using the full array.

The adaptive results were, for 50 integrations, better for the subarray beams than for the full array ones and in many cases the ratio of the estimated number of degrees of freedom was what would be expected theoretically, particularly in the directions of the dominant interference. In directions of weaker broadband interferences the ratio was slightly greater than predicted whilst in directions void of targets it was slightly lower. When a larger number of integrations was used the results, somewhat surprisingly indicated a slight advantage to the use of the full array.

#### SUMMARY AND CONCLUSIONS

The number of degrees of freedom are an important ingredient in assessing the detection performance of any type of processing algorithm and theoretical predictions imply that these values will be less for adaptive than for conventional beamforming. In noise fields consisting of a dominant non-Gaussian broadband interference the absolute agreement with theory was in general poor, although the results for both beamformers, in most cases, varied in approximately the correct manner when either the number of receivers or integrations were altered.

Below 200-300 Hz the adaptive results were consistently superior to the conventional ones although both were way below theory. However as the number of integrations was increased the adaptive results showed a marked improvement in this region of the spectra. This shortfall was interpreted as being due to the numerous discrete shipping lines in this region of the spectra. In the 300-600 Hz region the results for both conventional and adaptive beamforming were strongly angular dependant i.e. ;

In directions pointing at either strong broadband interferences, the conventional and adaptive results were almost identical both falling well below theoretical predictions probably as a result of the non-Gaussian nature these sources.

When conventional beams steered in directions void of targets allowed leakage from such interferences it is not just the mean noise level that increases but also the variability of that level. In a sense the variance of the broadband interference leaks through and since this variance is significantly higher than for Gaussian noise then the detection performance will be reduced. Adaptive beamforming, by virtue of its null steering capabilities reduces more effectively not only the mean noise power but also its variability. In these directions this reduced leakage of variance in adaptive beamformers offsets their natural greater statistical variability and the results to date imply that the relative detection performance of adaptive beamformers, with respect to conventional beamformers, will be better than theoretical predictions of their relative detection performance based upon Gaussian assumptions.

It is worth commenting that these results extend to the use of adaptive beamforming in any environment where the dominant interfering noise is non-Gaussian.

#### REFERENCES

- (1) Capon, J. and Goodman, N.R. "Probability Distribution for Estimates of the Frequency-Wavenumber Spectrum." Proc IEEE, Oct 1977 pp1785-1786.

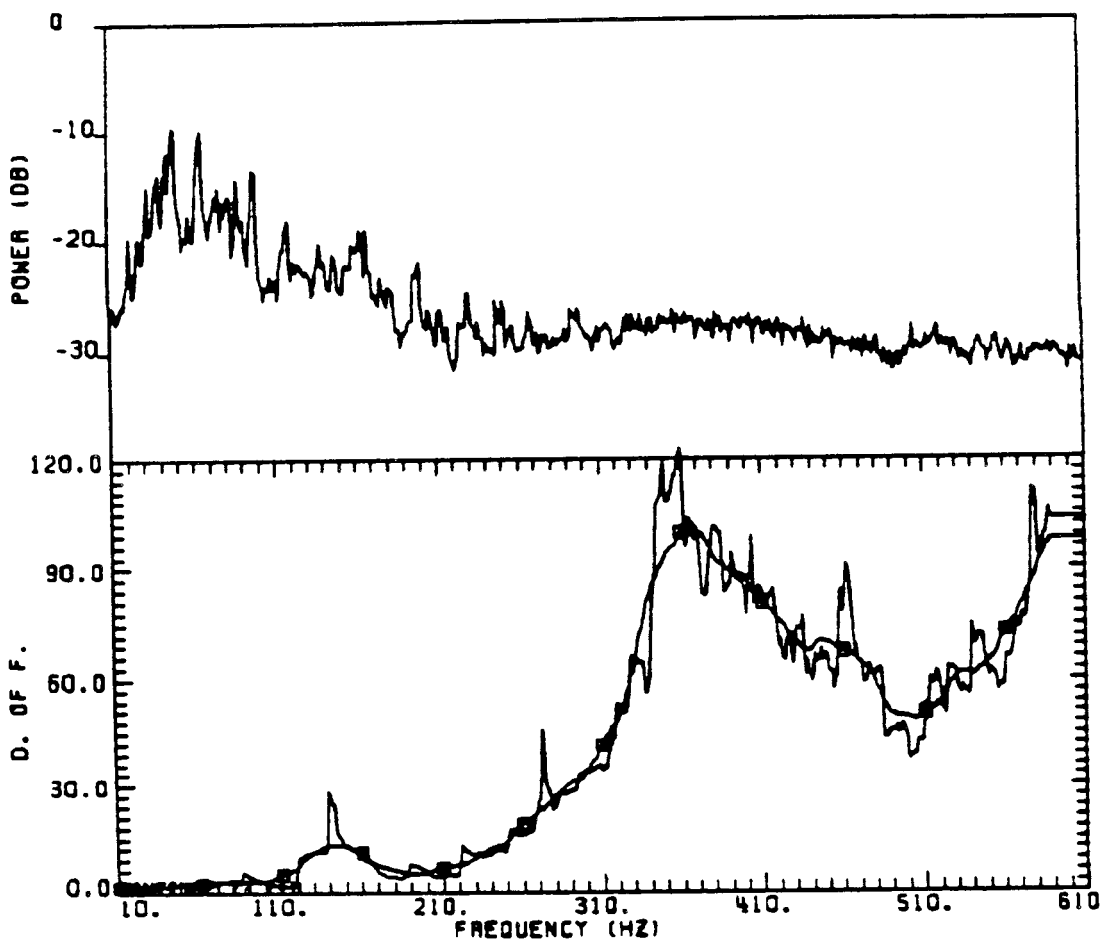


Figure 1 : Spectra and estimated number of degrees of freedom - conventional beamforming.

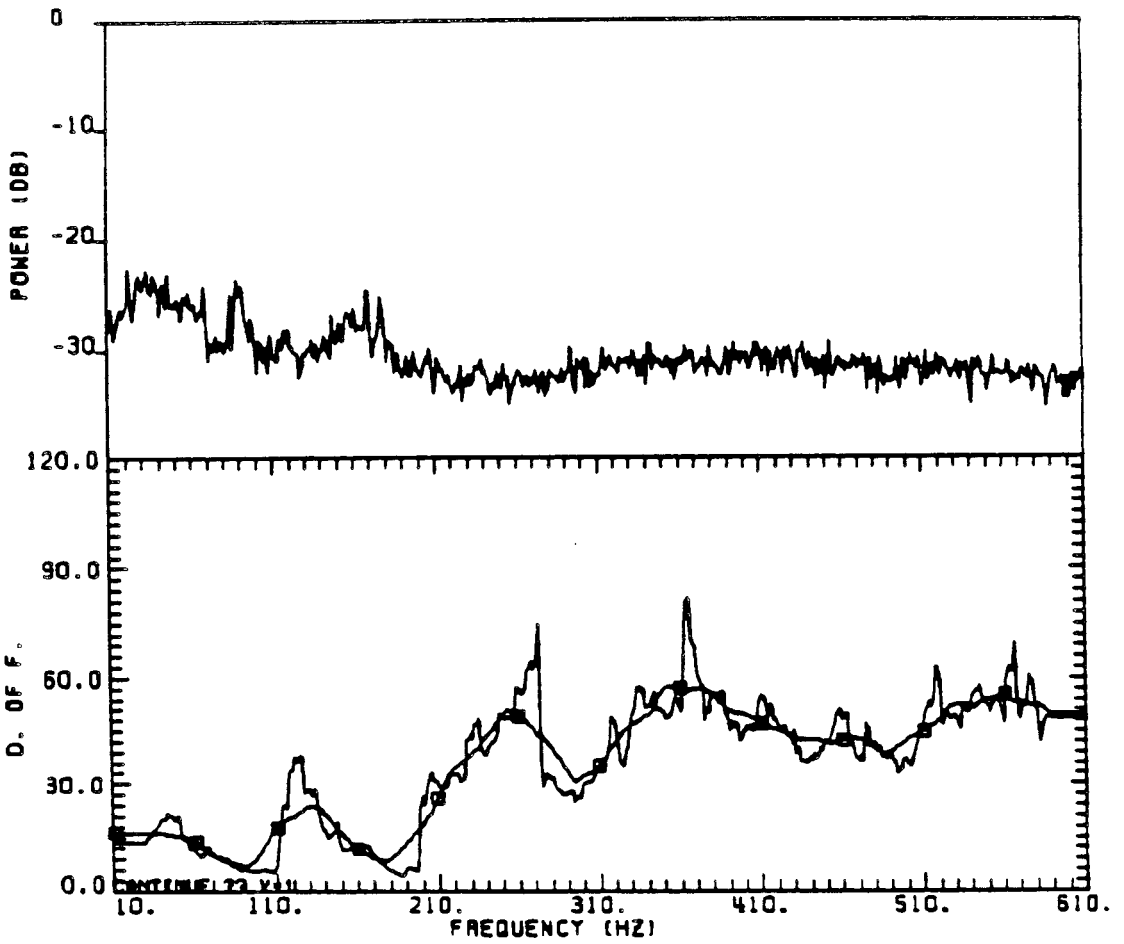


Figure 2 : Spectra and estimated number of degrees of freedom - adaptive beamforming.

A COMPARISON BETWEEN CONVENTIONAL AND ADAPTIVE BEAMFORMERS USING UNDERWATER ACOUSTIC DATA.

A C Smith\* and G C L Searle\*\*

This work compares the responses of adaptive and conventional acoustic array processors using data acquired from an underwater environment. The data from a horizontal planar array with omni-directional elements are processed using frequency domain and element space techniques to estimate the azimuthal noise anisotropy and to contrast the effectiveness of each processor. Three beamformers are represented: the uniform amplitude shaded beamformer, a non-uniformly shaded beamformer, and a fully adaptive processor which seeks to optimise array response by minimising the beampower.

As one examines the possible alternatives to increasing the measured signal-to-noise ratio or bearing resolution from an array of sensors, adaptive processing appears to be a logical way forward. This is mainly because of the processor's ability to reduce the effect of mobile interfering sources on the detection processes by automatically adjusting the array sensitivity pattern. The traditional (i.e. conventional) approach to array processing does not have these properties, but there is a price to pay for adaptation in terms of computational load. This work compares conventional and adaptive array processors, without too much regard to computational overheads, so as to see what adaptive array processing can do with real acoustic data. There is not a large amount of literature on the application of adaptive algorithms to data obtained from genuine underwater arrays (Refs 1-5) and, in consequence, questions continue to be asked relating to their implementation and the trade-offs which could be made to reduce the processor load and to increase their robustness towards errors.

It is not our intention to dwell on the mathematical details of array processing since these are given elsewhere (see, for example, reference 6 for an excellent tutorial paper) but some theory is given to explain the beamformers used here.

We will state, without proof, that for a maximum signal to noise beamformer with a unit sensitivity constraint in the look direction,  $\underline{c}$ , we have:

$$\underline{w}_{\text{-MLE}} = \frac{N^{-1} \underline{c}}{\underline{c}^T N^{-1} \underline{c}} \quad \dots(1)$$

where  $\underline{c}$  is a complex vector containing the steer terms of each array element and  $N$  is the noise-only covariance matrix.

\* Admiralty Underwater Weapons Establishment, Portland, Dorset, UK.  
(Now at RSRE, Satellite Communications Centre, Defford, WR8 9DU. UK.

\*\* Royal Australian Navy Research Laboratory, Sydney, Australia.

acoustic source in the vicinity of the array. Selected sections of trials data are transferred to magnetic disk. This permits analysis of the same data set by several beamforming techniques which would not otherwise be possible with the present tape transport system. During the time frame of each data set we expect the acoustic environment to change very little. Array rotation and source bearing changes are not significant.

In figure 1 we present an example of the kind of results that we have been obtaining from our data and this has been chosen to illustrate the paper because several features are clearly displayed. The figure shows frequency versus bearing for the three beamformers. The data are such that a broadband source is on a bearing of about  $90^\circ$  and a narrowband source on a bearing of about  $228^\circ$ . The frequency axis is linear in  $d/\lambda$  from 0 to 0.3.

The main points to be observed from this figure are:

- (a) The distinct sidelobe patterns of the UA and MDI beamformers and the lack of significant sidelobes of the ML beamformer.
- (b) The improved bearing resolution of the ML beamformer compared with the UA beamformer and, to a lesser extent, the MDI beamformer, particularly at the low end of the frequency spectrum.
- (c) The apparent increase in "detectability" using the ML beamformer, particularly at low frequencies and where a narrowband source is masked by the sidelobe response of the more powerful (broadband) source.

The greatest benefits of adaptive processing are to be seen at frequencies lower than the design frequency. However, at frequencies less than about four octaves below the design frequency of  $d/\lambda = \frac{1}{2}$  the MDI and ML processors, under the conditions described here, are not as consistent as at intermediate or higher frequencies. It is worth remarking here that because the MLE and MDI have been designed to optimize array response it follows that the beamformer will need to be supplied with equally "optimum" data. Such data are not available and small errors are inevitable. These will become more important as the size of the errors approach the same values as the differences between hydrophone responses and we believe that the poor responses of our data are attributable to this.

Finally we show, in figure 2, the power spectral density (dark histogram) and signal to noise (light histogram) for the beam in the direction of the narrowband sources for each of the three algorithms. Significant improvements in signal-to-noise ratio obtained by the MLE at  $d/\lambda$  of 0.04, 0.06, 0.16 and 0.27, where the narrowband radiators were operating.

### Summary

This paper has compared the performance of three array processors which operate in the frequency domain and element space: The conventional uniform amplitude and fixed weight beamformers, and the maximum likelihood estimator.

Each beamformer represents a distinct class of processor; uniform amplitude shading being the simplest and most robust, the maximum likelihood estimator representing an optimal processor in terms of signal-to-noise, and the maximum directivity index beamformer representing an intermediary class of fixed weight processors.

We have shown that, for the acoustic data considered in this work, the MLE improves bearing resolution, reduces sidelobe leakage and improves signal detectability. General observations would suggest that adaptive processing works very well, enabling significant enhancements, over similar conventional techniques, to be made. However, scenarios could be identified where adaptive processing may

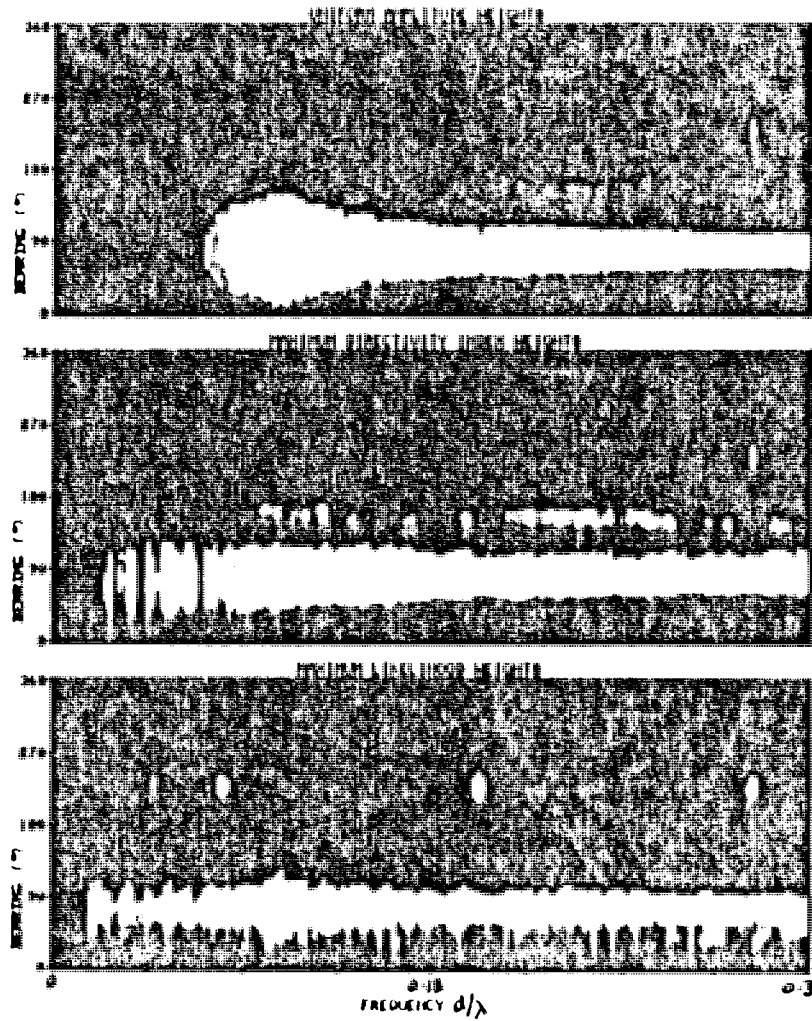


Fig 1: Azimuthal anisotropy versus frequency ( $d/\lambda$ ) for the three beamformers described in the text. White corresponds to high beampowers.

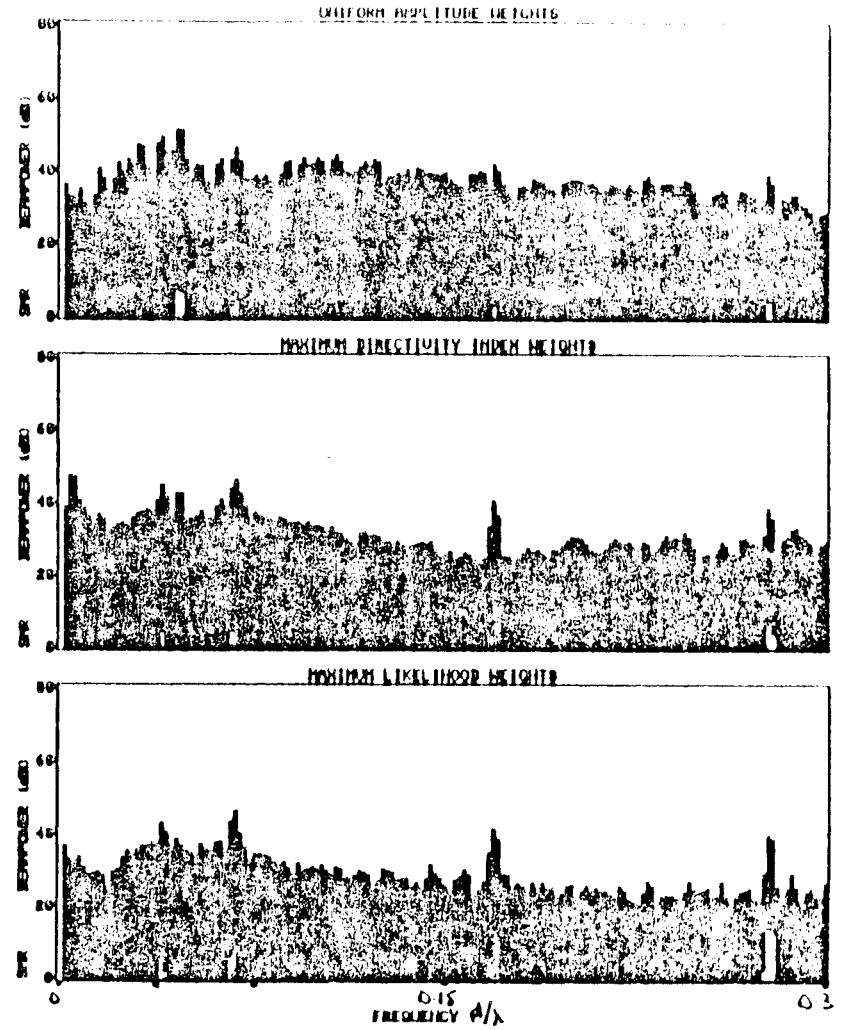


Fig 2: Power Spectrum for the beam at  $228^\circ$  versus frequency ( $d/\lambda$ ) for the three beamformers described in the text. The lighter histograms represent signal-to-noise ratio.

MISADJUSTMENT IN ADAPTIVE BEAMFORMING  
USING PERTURBATION SEQUENCES\*

Lal C. Godara  
Department of Systems Engineering  
Research School of Physical Sciences  
Australian National University, Canberra, ACT, 2601

Antonio Cantoni  
Department of Electrical and Computer Engineering  
University of Newcastle, N.S.W., 2308

### INTRODUCTION

The application of the adaptive Least Mean Square (LMS) algorithm to adaptive beamforming and its analysis has been studied by many authors. The algorithm is referred to as the constrained or unconstrained LMS algorithm depending upon whether or not the weights are subjected to constraints at each iteration.

The analysis of the unconstrained algorithm has been carried out in [1-5]. The analysis includes the transient behaviour of weights, the convergence and the transient behaviour of the covariance matrix of the weights and the misadjustment analysis. Analysis has been carried out when the algorithm is operating on broadband [1,2,3], narrowband real [5] and narrowband with complex data [4,5].

A constrained algorithm has been studied in [6-9]. The study of the convergence and the transient behaviour of the weights has been carried out in [7] for broadband data, in [9] for narrowband real and complex data and in [8] for the narrowband complex data when orthogonal perturbation sequences are used to estimate the required gradient. A misadjustment analysis of a constrained real algorithm has been carried out in [6] and bounds on the misadjustment are calculated. An approach similar to [6] is used in [9] to analyse a constrained algorithm for adaptive array processing and to calculate bounds on misadjustments when the algorithm operates on narrowband real and the narrowband complex data. The bounds on misadjustment for the perturbation case is presented in [8].

This paper presents an analysis of constrained algorithms used for adaptive antenna array processings and calculates the exact expressions for the misadjustments for the real, the complex and the perturbation case.

---

\* Work supported by the Radio Research Board, The Australian Research Grants Scheme and Department of Defence, Australia.

## 2. CONSTRAINED LMS ALGORITHM

Let a complex vector  $\underline{W}$  represent the  $L$  complex weights of an  $L$  element beamformer and a complex vector  $\underline{X}(t)$  represent the  $L$  complex signals derived from the beamformer [10].

Consider the constrained beamforming problem

$$\underset{\underline{W}}{\text{minimise}} \quad \underline{W}^H \underline{R} \underline{W} \quad (1)$$

$$\text{subject to} \quad \underline{W}^H \underline{C} = 1 \quad (2)$$

where  $\underline{R}$  is the complex array correlation matrix defined by

$$\underline{R} \triangleq E[\underline{X}(t)\underline{X}^H(t)] \quad (3)$$

and  $\underline{C}$  is a constraint vector. For a pre-steered array  $\underline{C}$  is a column vector of 1's.

It can be shown [7,11] that  $\hat{\underline{W}}$ , the solution of the optimization problem defined by (1) and (2) satisfies the equation

$$\hat{\underline{W}} = \underline{R}^{-1} \underline{C} / \underline{C}^H \underline{R}^{-1} \underline{C} \quad (4)$$

One real time constrained algorithm for determining the optimum weight vector  $\hat{\underline{W}}$  is

$$\underline{W}(n+1) = P[\underline{W}(n) - \mu \underline{g}(\underline{W}(n))] + \underline{C} / \underline{C}^H \underline{C} \quad (5)$$

where  $\underline{W}(n+1)$  denotes the new weight vector computed at the  $n^{\text{th}}+1$  iteration,  $\mu$  is a positive scalar which controls the convergence characteristics of the adaptive algorithm,  $\underline{g}(\underline{W}(n))$  is an unbiased estimate of the gradient of  $\underline{W}^H(n)\underline{R}\underline{W}(n)$  with respect to  $\underline{W}(n)$ , the idempotent projection matrix  $P$  is defined by

$$P \triangleq I - \underline{C}\underline{C}^H / \underline{C}^H \underline{C} \quad (6)$$

and  $I$  is the identity matrix.

2.1 Gradient Estimation The gradient of  $\underline{W}^H(n)\underline{R}\underline{W}(n)$  with respect to  $\underline{W}(n)$  is given by

$$\nabla_{\underline{W}}(\underline{W}^H \underline{R} \underline{W}) \Big|_{\underline{W}=\underline{W}(n)} = 2 \underline{R} \underline{W}(n) \quad (7)$$

There are a number of schemes for obtaining an unbiased estimate of this gradient [8,9,11,12]. Though in each case the estimated gradient is unbiased, the covariance of the estimated gradient obtained with each method is different and thus the transient and the steady state behaviour of the constrained algorithm is different in each case. The expressions for the covariance of the gradient estimated by different methods are summarised below and are valid under the assumption that  $\{X(\cdot)\}$  is an i.i.d complex Gaussian process.

A. Gradient Estimation Using the Complex Operations. The estimation of the required gradient by this method [5,9,11] requires complex multiplications and additions. If  $V_{\underline{g}_C}(\underline{W}(n))$  represents the covariance of the gradient estimated by this method for a given  $\underline{W}(n)$ , then

$$V_{\underline{g}_C}(\underline{W}(n)) = 4 \underline{W}^H(n) \underline{R} \underline{W}(n) \underline{R} \quad (8)$$

B. Gradient Estimation Using the Real Operations. The estimation of the required gradient by this method [5,9] is achieved using real multiplications and additions. If  $V_{\underline{g}_R}(\underline{W}(n))$  represents the covariance of the gradient estimated by this method for a given  $\underline{W}(n)$ , then

$$V_{\underline{g}_R}(\underline{W}(n)) = 8 \underline{R} \underline{W}^H(n) \underline{R} \underline{W}(n) + 4 \underline{R} \underline{W}(n) \underline{W}^H(n) \underline{R} \quad (9)$$

Both of the above methods are useful only when the signals on all the array elements are accessible. The following two schemes [8,12] use orthogonal perturbation sequences to estimate the gradient and do not require access to all the signals. The expressions for the variance of the gradient are given for a time multiplex perturbation sequence of length  $4L$ .

C. Dual Receiver System with Dual Perturbation. If  $V_{\underline{g}_2}(\underline{W}(n))$  represents the covariance of the gradient estimated by this method for a given  $\underline{W}(n)$ , then [8,12]

$$V_{\underline{g}_2}(\underline{W}(n)) = 2 \underline{W}^H(n) \underline{R} \underline{W}(n) \text{Diag}(\underline{R}) \quad (10)$$

D. Dual Receiver System with Reference Receiver. If  $V_{\underline{g}_3}(\underline{W}(n))$  represents the covariance of the gradient estimated by this method for a given  $\underline{W}(n)$  then [8]

$$V_{\underline{g}_3}(\underline{W}(n)) = 2\gamma^2 L [\text{Diag}(\underline{R})]^2 + 2 \underline{W}^H(n) \underline{R} \underline{W}(n) \text{Diag}(\underline{R}) \quad (11)$$

where  $\gamma$  is the perturbation step size.

### 3. MISADJUSTMENT RESULTS

The misadjustment is defined as

$$M \triangleq \lim_{n \rightarrow \infty} \frac{E[\underline{W}^H(n) \underline{X}(n+1) \underline{X}^H(n+1) \underline{W}(n)] - \hat{\underline{W}}^H \hat{\underline{R}} \hat{\underline{W}}}{\hat{\underline{W}}^H \hat{\underline{R}} \hat{\underline{W}}} \quad (12)$$

The results on the misadjustment are presented below for the constrained LMS algorithm when the gradient used in (5) is estimated by the methods described in the previous section. The detailed derivation of the results presented here can be found in [13].

Let  $\lambda_{\max}$  denote the maximum of  $\{\lambda_1, \dots, \lambda_{L-1}\}$  the non-zero eigenvalues of PRP.

Result 1: IF for a given  $\underline{W}(n)$  the variance of the gradient used in (5) is given by (8),

$$0 < \mu < \frac{1}{2\lambda_{\max}} \quad \text{and} \quad \mu \sum_{i=1}^{L-1} \frac{\lambda_i}{1-\mu\lambda_i} < 1 \quad (13)$$

THEN

$$M_c = \frac{\sum_{i=1}^{L-1} \frac{\lambda_i}{1-\mu\lambda_i}}{1 - \mu \sum_{i=1}^{L-1} \frac{\lambda_i}{1-\mu\lambda_i}} \quad (14)$$

Result 2: IF for a given  $\underline{W}(n)$  the covariance of the gradient used in (5) is given by (9),

$$0 < \mu < \frac{1}{\lambda_{\max} + \frac{\text{Tr} R}{2L}} \quad \text{and} \quad \frac{\mu \text{Tr}(R)}{2L} \sum_{i=1}^{L-1} \frac{1}{1-\mu\lambda_i} < 1 \quad (15)$$

THEN

$$M_2 = \frac{\frac{\mu \text{Tr}(R)}{2L} \sum_{i=1}^{L-1} \frac{1}{1-\mu\lambda_i}}{1 - \frac{\mu \text{Tr}(R)}{2L} \sum_{i=1}^{L-1} \frac{1}{1-\mu\lambda_i}} \quad (16)$$

Result 3: IF for a given  $\underline{W}(n)$  the covariance of the gradient used in (5) as given by (10),

$$0 < \mu < \frac{1}{\lambda_{\max} + \frac{\text{Tr}(R)}{2L}} \quad \text{and} \quad \frac{\mu \text{Tr}(R)}{2L} \sum_{i=1}^{L-1} \frac{1}{1-\mu\lambda_i} < 1 \quad (17)$$

THEN

$$M_3 = \frac{\left[ 1 + \gamma^2 \frac{\text{Tr}(R)}{\widehat{W}_H \widehat{R}_W} \right] \frac{\mu \text{Tr}(R)}{2L} \sum_{i=1}^{L-1} \frac{1}{1 - \mu \lambda_i}}{1 - \frac{\mu \text{Tr}(R)}{2L} \sum_{i=1}^{L-1} \frac{1}{1 - \mu \lambda_i}} \quad (18)$$

Result 4: IF for a given  $\underline{W}(n)$  the covariance of the gradient used in (5) is given by (11),

$$0 < \mu < \frac{1}{4\mu_{\max}} \quad \text{and} \quad \sum_{i=1}^{L-1} \frac{2\mu\lambda_i}{1 - 2\mu\lambda_i} < 1 \quad (19)$$

THEN

$$M_R = \frac{2\mu \sum_{i=1}^{L-1} \frac{\lambda_i}{1 - 2\mu\lambda_i}}{1 - 2\mu \sum_{i=1}^{L-1} \frac{\lambda_i}{1 - 2\mu\lambda_i}} \quad (20)$$

#### 4. DISCUSSION

At this stage the misadjustment produced by the different gradient schemes can be compared. The following observations are made from the results on the misadjustments presented in the previous section.

1. Comparing (16) and (18) one notes that in the case of dual receiver system with the reference receiver the misadjustment,  $M_3$ , is made up of two components. One of these components is equal to the misadjustment,  $M_2$ , of the dual receiver system with the dual perturbation. The second component is proportional to the square of the perturbation step size  $\gamma$  and can be made arbitrarily small by choosing smaller  $\gamma$  arbitrarily small.

2. A comparison of (14) and (20) reveals

$$M_c(2\mu) \equiv M_R(\mu) \quad (21)$$

that is, the misadjustments for the real and the complex case would be the same if the step size used in the complex case is double that of the one used in the real case. It is shown in [9] that for the small  $\mu$  the time constants associated with the weights are

$$T_i \approx \frac{1}{2\mu\lambda_i} \quad i = 1, 2, \dots, L-1 \quad (22)$$

Thus for the same misadjustments, the convergence time constants in the complex case would be one half that of the real case. That would mean that for the

same misadjustment the speed of the convergence of weights in the complex case is one half that of the real case.

3. It is interesting to observe that for a given  $\mu$  the misadjustment in the real and the complex case (unperturbed case) is only a function of the eigenvalues of PRP and thus is unaffected by the amount of the signal component in the system. On the other hand in the case when the gradient is estimated using perturbations the misadjustment is also a function of the desired signal. Note the presence of  $\text{Tr}(R)$  in (16) and (18).

The lowest value of  $M_2$  is  $\frac{M_c}{2}$  for a large array with very small input signal to noise ratio when all the steering vectors in the directions of noise sources are orthogonal to the constraint vector  $\underline{c}$ .  $M_2$  increases with the input signal power and is more than  $M_c$  for large input signal to noise power.

#### REFERENCES

- [1] Widrow, B. and McCool, J.B., "A Comparison of Adaptive Algorithms Based on the Methods of Steepest Descent and Random Search", *IEEE Trans. Antennas and Propagation*, Vol. AC-24, No. 5, Sept. 1976, pp. 615-637.
- [2] Widrow, B., McCool, J.B. et al., "Stationary and Non-stationary Learning Characteristics of the LMS Adaptive Filter", *Proc. IEEE*, Vol. 64, No. 8, Aug. 1976, pp. 1151-1162.
- [3] Senne, K.D., "Adaptive Linear Discrete-time Estimation", Technical Report No. 6778-5, June 1968, Syst. Theory Lab., Stanford University, Stanford, Cal. U.S.A.
- [4] Fisher, B. and Bershad, N.J., "The Complex LMS Adaptive Algorithm-transient Weight Mean and Covariance with Application to the ALE", *IEEE Trans. Acoust. Speech Signal Process.*, Vol. ASSP-31, No. 1, Feb. 1983, pp. 34-44.
- [5] Horowitz, L.L. and Senne, K.D., "Performance Advantage of Complex LMS Algorithm for Controlling Narrowband Adaptive Arrays", *IEEE Trans. Circuit System.*, Vol. CAS-28, No. 6, June 1981, pp. 562-576.
- [6] Moschner, J.L., "Adaptive Filters with Clipped Input Data", Technical Report No. 6796-1, June 1970, Inf. Syst. Lab., Stanford University, Stanford, Cal. U.S.A.
- [7] Frost, O.L., "An Algorithm for Linearly Constrained Adaptive Array", *Proc. IEEE*, Vol. 68, No. 8, Aug. 1972, pp. 926-935.

- [8] Godara, L.C. and Cantoni, A., "Analysis of the Performance of Adaptive Beamforming Using Perturbation Sequences", *IEEE Trans. Antennas Propagation*, Vol. AP-31, No. 2, March 1983, pp. 268-279.
- [9] Godara, L.C. and Cantoni, A., "On the Real and the Complex LMS Algorithms for Adaptive Array Processing", Technical Report EE8204, Dept. of Elect. and Computer Engg., University of Newcastle, N.S.W., 2308, Australia.
- [10] Godara, L.C. and Cantoni, A., "Signal Representation for Array Processing" Technical Report EE8203, Dept. of Elect. and Computer Engg., University of Newcastle, N.S.W., 2308, Australia.
- [11] Hudson, J.E., Adaptive Array Principles, New York, Peter Peregrins Ltd., New York and London, 1981.
- [12] Cantoni, A., "Application of Orthogonal Perturbation Sequences to Adaptive Beamforming", *IEEE Trans. Antennas Propagation*, Vol. AP-28, No. 2, March 1980, pp. 191-202.
- [13] Godara, L.C. and Cantoni, A., "Analysis of Constrained LMS Algorithm with Application to Adaptive Beamforming using Perturbation Sequences", Technical Report, EE8403, Dept. of Elect. & Computer Engg., University of Newcastle, N.S.W., 2308, Australia.

LEAKAGE OF INTERFERENCE IN ADAPTIVE BEAMFORMERS

D.R. Sweet

Weapons Systems Research Laboratory  
Defence Research Centre Salisbury

A B S T R A C T

The performance of a frequency-domain element-space adaptive beamformer and the Frost processor in cancelling narrowband interferences is investigated. The theoretical levels of narrowband leakage for the processors are first calculated, then results are given for runs on several real noise scenarios with characteristics approximately those of the theoretical scenarios. Some trends in leakage levels are observed and compared with theoretical trends.

1. INTRODUCTION

Adaptive beamformers cancel out interferences in non-look directions whilst maintaining the array response in the look direction. Except in certain ideal conditions, this cancellation is never complete. The leakage of narrowband interference lines into the look direction in particular may have undesirable effects such as causing false alarms and making classification of spectra difficult.

This report considers the performance of two processors, the frequency domain element-space (FD/ES) optimum beamformer(ref.1) and the Frost processor a time-domain element-space beamformer(ref.2). The theoretical performance of these processors in cancelling narrowband lines in some simple noise scenarios is first considered, then results are presented for leakage of narrowband interference lines into the look direction using real acoustic data. Where possible, comparisons between theoretical performance and performance using real data are made.

2. THE ALGORITHMS

2.1 Frequency-Domain/Element Space (FD/ES) Processor

In this processor, complex narrowband signals from the array elements are weighted and summed. The complex weights are adjusted to minimise

the average output power with the constraint of unity response in the look direction. The procedure is repeated at all the frequencies of interest.

## 2.2 Time-Domain/Element-Space (TD/ES) Processor (Frost Processor)

In this processor, real, broadband signals from the array elements are presteered in the look direction, passed through tapped-delay lines with variable weights and summed. The Frost processor minimizes the average output power with the constraint that signals from the look direction are passed undistorted.

## 3. THEORETICAL PERFORMANCE

Throughout this study, a 10-element array consisting of two concentric rings was considered. Cantoni and Godara(ref.3) obtained some theoretical results for the Frost processor using a simple noise scenario consisting of uncorrelated noise, isotropic noise, an octave-band interference (at  $107^\circ$  or  $180^\circ$ ) and up to three narrowband interference lines (at  $107^\circ$  or  $180^\circ$ ). Figure 1 shows a typical result - the look-direction is  $0^\circ$ , and the octave-band noise and narrowband interferences are all at  $107^\circ$ . 5 taps were used.

Cantoni and Godara observed the following trends in the TD case:

- (a) The visibility of lines is greater if there is a broadband interference in the same direction rather than in a different direction. Visibility is defined as the ratio of the total power at the line frequency to the noise power, expressed in decibels.
- (b) The visibility of lines is greater in directions in which the conventional response has a sidelobe, due to the fact that it is more difficult to null out interferences in these cases.
- (c) When the level of the narrowband lines is varied, the visibility passes through a peak (there is little leakage for very low line-levels, and for higher line-levels, the processor puts a high priority on nulling out the lines).
- (d) Visibility is greater when less than 5 taps are used, but is not noticeably less when more than 5 taps are used.

Theoretical results for the FD processor were obtained for the same scenarios as were considered above. In this case, the leakage lines were not discernible and typical visibilities were less than 0.1 dB.

## 4. PERFORMANCE USING REAL DATA

### 4.1 Detection of Leakage

- (a) FD If an isolated narrowband spike occurred in at the same frequency in two or more directions, the strongest spike was taken to be the target, and the weaker spikes were taken to be possible leakage lines. Power/azimuth plots were used to decide whether the line was due to sidelobe leakage or was from another source.
- (b) TD The theoretical results indicated that leakage was much less in FD processor than in the TD. Thus, any lines which appeared in the TD spectrum but not in the corresponding FD spectrum were assumed to be leakage lines. This was checked by ascertaining if there were stronger lines at the same frequencies but different azimuths.

### 4.2 Noise scenarios

The noise fields consisted of up to three of the following components:

- (i) A source with several strong, broad lines (the trials vessel).
- (ii) A projector source with a few stable narrowband lines.
- (iii) A broadband source, with or without superimposed lines.
- (iv) Other sources with narrowband lines.

### 4.3 Runs Performed

TD and FD beam spectra were obtained for the azimuths of the major sources in each of the noise scenarios. In cases where the sources were not well-separated in azimuth, a beam spectrum was obtained for an arbitrary azimuth well-separated from any sources. 5 taps were used in all TD runs, except in one scenario where up to 11 taps were used to check the variation in visibility with the number of taps.

### 4.4 Results

#### Frequency-domain

In all the scenarios considered, only one possible case of interference leakage was detected (apart from some instances of "main-lobe" leakage where the look direction was close to the interference direction). In this case, the conventional response had a rather high -5 dB sidelobe in the direction of the interference source, which was the trials vessel.

#### Time-domain

In the 14 scenarios considered, there was some leakage in all but three cases. This conforms with the theoretical prediction that interference

visibility is higher for the TD processor than for the FD processor. Figure 2 shows two TD beam spectra for a typical scenario in which there is a strong line source at  $48^\circ$  (the trials vessel), a broadband source at  $96^\circ$ , and a weak projector line at  $338^\circ$ . The lines labelled "A" and "B" at azimuth  $48^\circ$ , are clearly leaking into the spectrum at azimuth  $338^\circ$ . The FD spectra were the same as the corresponding TD spectra, except that the leakage lines at azimuth  $338^\circ$  are not evident.

#### Other observations on the results

1. Where the look-directions were close enough to observe main-lobe leakage, this was worse in the TD case than the FD case.
2. For the scenarios investigated, there was no definite evidence that the TD leakage of narrowband interferences was worse when they were associated with a broadband source, as was indicated by the theoretical results. However, because of the many factors influencing leakage level, this possibility cannot be discounted. One trend observed was that there was almost always some leakage when the interference was the trials vessel, which had a complex line spectrum. This suggests that any complex interference spectrum, whether it has a broadband component or not, has a tendency to leakage in the TD processor.
3. Increasing the number of taps from 5 to 11 did not noticeably decrease visibility. This is in line with theoretical results.
4. There was no noticeable correlation between TD leakage level and conventional sidelobe level.

#### 5. CONCLUSIONS

Some of the trends observed in theoretical leakage levels were also observed using real results. However, other trends such as the increase in leakage of lines associated with broadband sources and the correlation between leakage and conventional sidelobe level were not observed in the present results using real data. However, in complex real noise fields, many factors influencing leakage level are present, and extensive further studies are required to separate these effects.

## REFERENCES

- | No | Author   | Title   |
|----|--|---|
| 1  | D.J. Edelblute, J.M. Fisk<br>and G.L. Kinnison | "Criteria for optimum signal detection<br>theory for arrays"<br>J. Acous. Soc. Amer. Vol. 41,<br>pp 199-206, 1967.        |
| 2  | O.L. Frost                                     | "An algorithm for linearly-constrained<br>adaptive array processing"<br>Proc. IEEE, Vol. 60, pp 926-935, 1972.            |
| 3  | A. Cantoni and<br>L. Godara                    | "A study of element space antenna<br>array processors, Part III"<br>Tech. Rept. EE8223, University of<br>Newcastle, 1982. |

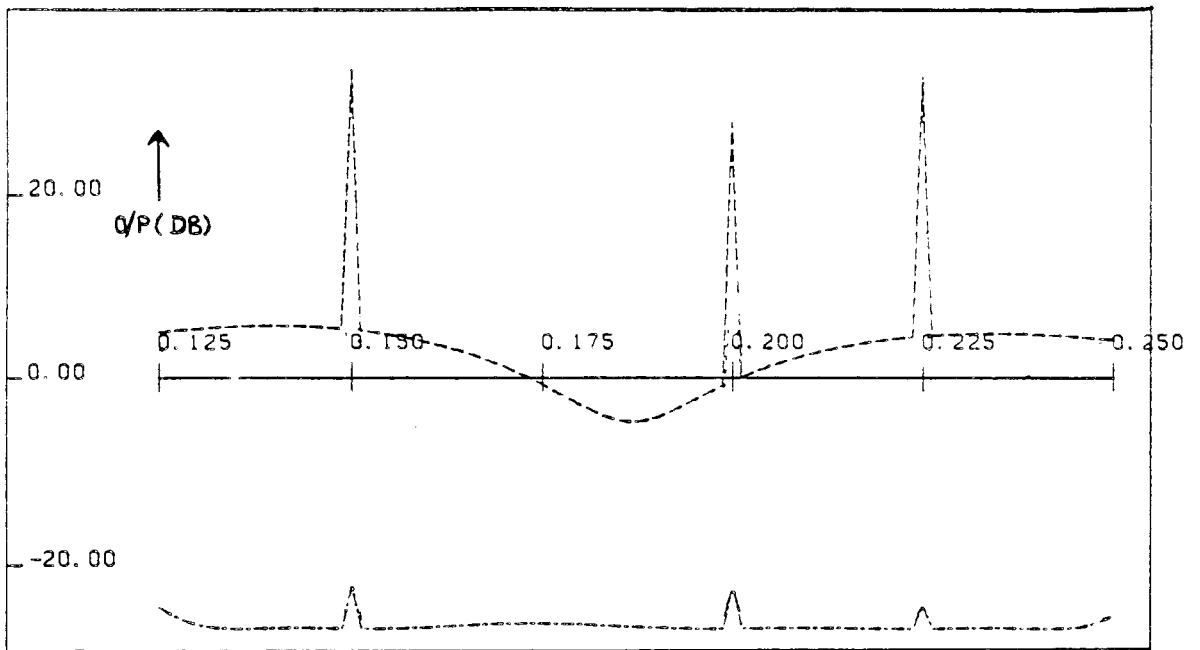


FIG. 1 - CONVENTIONAL (UPPER CURVE) AND OPTIMUM BEAM SPECTRA,  
FROST PROCESSOR

Look direction =  $0^\circ$ , Interference direction =  $107^\circ$   
No. of taps = 5

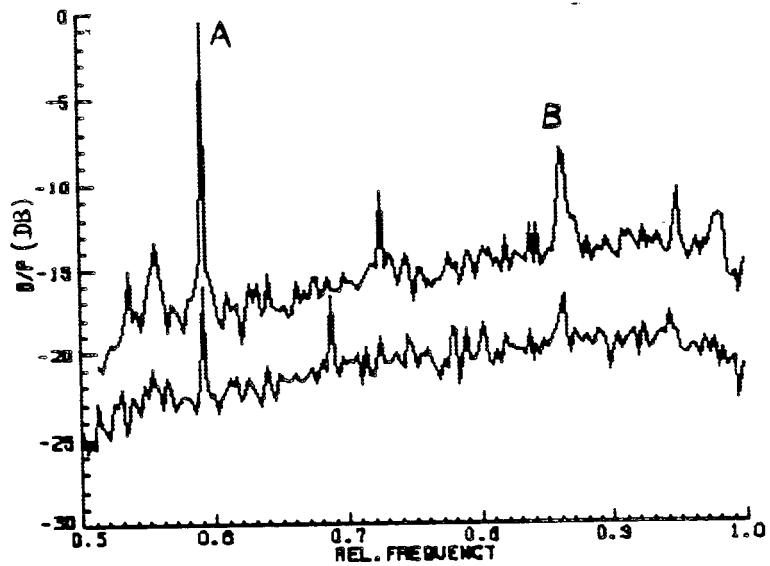


FIG. 2 - ADAPTIVE BEAM SPECTRA, TIME-DOMAIN PROCESSOR

Upper Curve (+ 5 dB offset): Azimuth =  $48^\circ$   
Lower Curve: Azimuth =  $338^\circ$

A NEW SET OF LINEAR CONSTRAINTS FOR  
BROADBAND TIME DOMAIN ELEMENT SPACE PROCESSORS

by

M.H. Er and A. Cantoni

Department of Electrical and Computer Engineering  
University of Newcastle, New South Wales, 2308, Australia

SUMMARY

In a Frost [1] processor, each sensor data is time shifted as for conventional beamforming to compensate for the misalignment between a look direction wavefront and the antenna array geometry. A set of linear constraints is then used to ensure that a desired frequency response characteristic in the look direction is achieved. Other forms of time domain broadband processors which make use of a fixed conventionally weighted array and an auxiliary, adaptive array have also been described in the literature [2]-[4]. In all these approaches, one practical drawback is that a new set of pre-steering delays is required for each look direction and consequently a new array correlation matrix needs to be computed for each look direction in order to obtain the optimal weights. Furthermore if the sensor outputs are sampled time series, then the only time delays available are integer multiples of the sampling interval. In general the required delays are not exact multiples of the sampling interval and there is a problem of generating the inter-sample values required to achieve pre-steering delays of sufficient accuracy. Interpolation of the sampled data could be used to

generate the required delayed signals.

The purpose of this paper is to introduce a new set of linear constraints for designing broadband time domain element space processors. Figure 1 shows the structure of an L-element partitioned broadband processor with (J-1) tapped delay sections.  $\hat{\underline{W}}_1^0$  ( $\gamma = 1$  in Figure 1) is the LJ-dimensional coefficient vector of the upper filter which achieves the closest approximation to the desired response over a frequency band of interest  $[f_L, f_u]$  in the look direction  $(\theta_0, \phi_0)$ . The lower filter consists of an L-channel tapped delay line with (J-1) delay sections per channel. The power response of the lower filter over a frequency band of interest is given by

$$\int_{f_L}^{f_u} H_L^*(f, \theta, \phi) H_L(f, \theta, \phi) df = \underline{W}^T Q_1 \underline{W} \quad (1)$$

where \* denotes conjugate operation and  $H_L(f, \theta, \phi)$  is the frequency response of the lower filter to a plane wavefront arriving in direction  $(\theta, \phi)$  defined by

$$H_L(f, \theta, \phi) = \sum_{k=1}^J \underline{s}^T(f, \theta, \phi) T(f) \underline{w}_k \exp[-j2\pi f(k-1)T] \quad (2)$$

where  $\underline{s}(f, \theta, \phi)$  is the L-dimensional vector defined by

$$\underline{s}(f, \theta, \phi) \triangleq [\exp(j2\pi f\tau_1), \dots, \exp(j2\pi f\tau_L)]^T \quad (3)$$

where  $\{\tau_\rho\}$  are the propagation delays between the wavefront and the sensor elements and  $T(f)$  is the  $L \times L$  dimensional diagonal matrix defined by

$$T(f) \triangleq \text{Diag}[\exp(-j2\pi fT_1), \dots, \exp(-j2\pi fT_L)] \quad (4)$$

The vector  $\underline{w}_k$  corresponds to the column of weights on the  $k^{\text{th}}$  tapped point defined by

$$[\underline{w}_k]_i = w_{(k-1)L+i}, \quad i = 1, 2, \dots, L, \quad k = 1, 2, \dots, J \quad (5)$$

To prevent signal suppression, the adjustable weights of the lower filter should, ideally, be constrained to have zero response over the frequency band of interest in the look direction and thus

$$\underline{W}^T Q_1 \underline{W} = 0 \quad (6)$$

Since  $Q_1$  is symmetric, it can be factorized as

$$Q_1 = \Gamma_1 \Lambda_1 \Gamma_1^T \quad (7)$$

where  $\Gamma_1$  is the  $LJ \times LJ$  dimensional eigenvector matrix given by

$$\Gamma_1 = [\underline{U}_1^1, \underline{U}_2^1, \dots, \underline{U}_{LJ}^1] \quad (8)$$

and  $\Lambda_1$  is the  $LJ \times LJ$  dimensional diagonal eigenvalue matrix given by

$$\Lambda_1 = \text{Diag}[\lambda_1^1, \lambda_2^1, \dots, \lambda_{LJ}^1] \quad (9)$$

where

$$\lambda_1^1 \geq \lambda_2^1 \geq \dots \geq \lambda_{LJ}^1 \geq 0 \quad (10)$$

If  $Q_1$  has rank  $n_1$ , then it is clear from (7)-(9) that the necessary

and sufficient conditions for (6) to be satisfied are

$$\underline{U}_i^T \underline{W} = 0, \quad i = 1, 2, \dots, n_i \quad (11)$$

With this approach, three types of pre-steering can be handled:

(a) No Pre-steering

In this case,  $T(f)$  is not included in (2).

(b) Coarse Pre-steering as Limited by Sampling Time  $T$

In this case,  $\{T_i\}$  is a set of time delays such that

$$\underline{S}^T(f, \theta_0, \phi_0) T(f) = \exp(-j2\pi f m_0 T) [\exp(j2\pi f \tilde{\tau}_1), \dots, \exp(j2\pi f \tilde{\tau}_L)] \quad (12)$$

for some integer  $m_0$  and  $0 \leq |\tilde{\tau}_i| < T$  for one form of discretization of  $\{T_i\}$  or  $0 \leq |\tilde{\tau}_i| \leq T/2$  for a rounded discretization of  $\{T_i\}$ .

(c) Exact Pre-steering

The time delays  $\{T_i\}$  are in this case adjusted so that

$$\underline{S}^T(f, \theta_0, \phi_0) T(f) = \exp(-j2\pi f \hat{T}) [1, 1, \dots, 1] \quad (13)$$

for some  $\hat{T}$ .

The elimination of exact pre-steering is important in digital implementation of antenna array processors and also offers computational advantages for determining the optimal weights. Furthermore the method presented also enables the processor to be made robust against various types of errors and mismatches between signal model and the actual scenario. For example the processor can be designed to allow for uncertainty in direction of arrival by replacing  $\hat{\underline{W}}_1^0$  by  $\hat{\underline{W}}_2^0$  which

ensures the closest approximation to the desired response over a frequency band of interest as well as over a spatial region of interest and by using a set of linear constraints of the form

$$\underline{U}_i^2 \underline{W} = 0, \quad i = 1, 2, \dots, n_2 \quad (14)$$

where  $\{\underline{U}_i^2, i = 1, 2, \dots, n_2\}$  are the  $n_2$  eigenvectors corresponding to the  $n_2$  nonzero eigenvalues of  $Q_2$  matrix which is defined by

$$Q_2 = \int_{\phi_0 - \Delta\phi/2}^{\phi_0 + \Delta\phi/2} Q_1 d\phi \quad (15)$$

So far, it has been assumed that  $Q_\gamma, \gamma = 1, 2,$  does not have full rank. When  $Q_\gamma$  has full rank or because in practice the eigenvalue evaluation will not yield exactly zero eigenvalues, one can impose  $n_0$  linear constraints of the form

$$\underline{U}_i^\gamma \underline{W} = 0, \quad i = 1, 2, \dots, n_0 \quad (16)$$

where  $n_0$  is chosen based on the percentage trace of  $Q_\gamma$  matrix defined by

$$\% \text{ tr} \triangleq \frac{\sum_{i=1}^{n_0} \lambda_i^\gamma}{\sum_{i=1}^{LJ} \lambda_i^\gamma} \quad (17)$$

Note that (16) can be thought of as a set of constraints which yield a small value of  $\underline{W}^T Q_\gamma \underline{W}$ . The value of  $n_0$  determines the number of degrees of freedom lost in the processor.

It follows from (16) that

$$\underline{W}^T Q_\gamma \underline{W} = \sum_{i=n_0+1}^{LJ} \lambda_i^\gamma (\underline{U}_i^\gamma \underline{W})^2 \quad (18)$$

and hence

$$\underline{W}^T Q_Y \underline{W} = \left( \sum_{i=n_0+1}^{LJ} \lambda_i^Y \right) \|\underline{W}\|_2^2 \quad (19)$$

Since  $\{\lambda_i^Y, i = n_0+1, \dots, LJ\}$  are the  $(LJ-n_0)$  smallest eigenvalues, it can be seen that (19) ensures a low gain with respect to  $\|\underline{W}\|_2^2$  and provided  $\|\underline{W}\|_2^2$  is not too large then  $\underline{W}^T Q_Y \underline{W}$  will be small.

The optimal weight vector which achieves the closest approximation to the desired response over a frequency band of interest as well as reduces the sensitivity of the processors to directional uncertainty and rejects non-look directional sources is the solution to the following constrained optimization problem.

$$\underset{\underline{W}}{\text{minimize}} \quad (\hat{\underline{W}}_Y^0 - \underline{W})^T R (\hat{\underline{W}}_Y^0 - \underline{W}) \quad (20a)$$

$$\text{subject to} \quad D^T \underline{W} = 0 \quad (20b)$$

where  $D$  is the  $LJ \times n_0$  dimensional matrix defined by

$$D \triangleq [\underline{U}_1^Y, \underline{U}_2^Y, \dots, \underline{U}_{n_0}^Y] \quad (21)$$

Examples of the frequency response and the optimal power estimate plots for the new processor with no pre-steering are shown in Figures 3 and 4 for illustration.

#### REFERENCES

- [1] O.L. Frost, "An Algorithm for Linearly Constrained Adaptive Array Processing", *Proc. IEEE*, Vol. 60, No. 8, August 1972, pp. 826-835.

- [2] L.J. Griffiths, "An Adaptive Beamformer Which Implements Constraints Using an Auxiliary Array Preprocessor", in Aspect of Signal Processing, Part 2, G. Taccoui [Ed.], D. Reidel Publishing Co., 1977, pp. 517-522.
- [3] C.W. Jim, "A Comparison of Two LMS Constrained Optimal Array Structures", *Proc. IEEE*, Vol. 65, No. 12, December 1977, pp. 1730-1731.
- [4] L.J. Griffiths and C.W. Jim, "An Alternative Approach to Linearly Constrained Adaptive Beamforming", *IEEE Trans. on Antennas and Propagation*, Vol. AP-30, No. 1, January 1982, pp. 27-34.

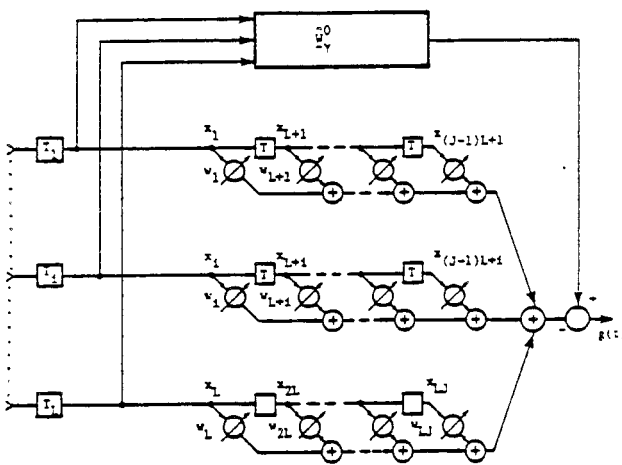


Figure 1

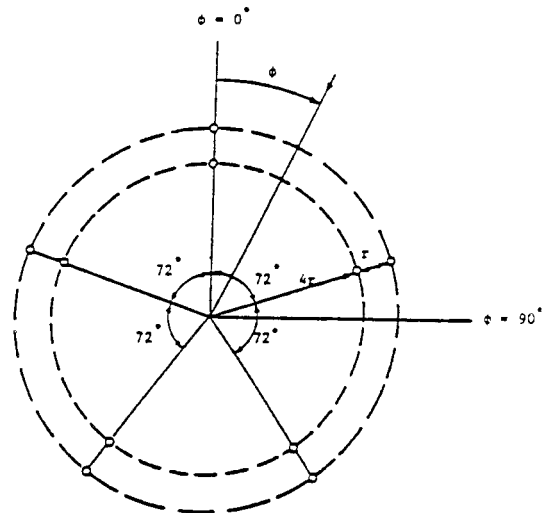


Figure 2

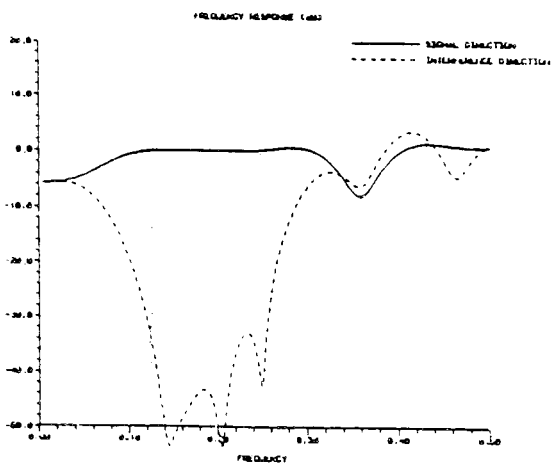


Figure 3

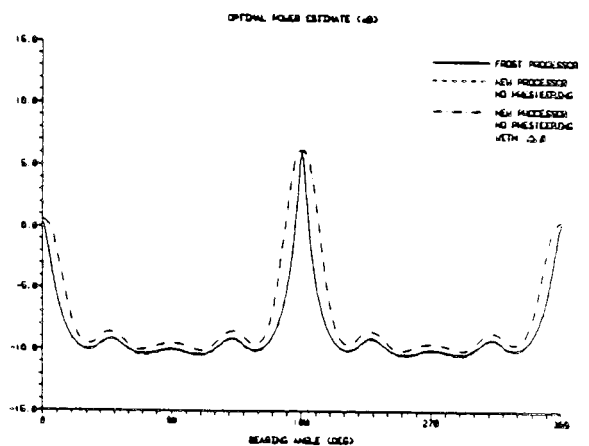


Figure 4

## G 1

### ON PHASE SHIFTER ERRORS IN AN ANTENNA ARRAY

Lal C. Godara

Department of Systems Engineering, Research School of Physical Sciences  
Australian National University, Canberra, ACT 2601, Australia.

#### INTRODUCTION

Phase shifters are commonly used in phased array radars [1] and adaptive arrays [2] to control the phases of narrowband signals received by or to be transmitted by antenna elements of an array. The phase shifters are chosen such that the narrowband signals received by all the elements from a given direction, referred to as the 'look direction', are phase aligned. In this situation the array beam is steered in the look direction.

Commonly used phase shifters are ferrite phase shifters and diode phase shifters [1, 3]. One of the important specification of these phase shifters which concerns an array designer is the root mean square (RMS) phase error.

The aim of this paper is to analyse the effect of these errors on the performance of an array beamformer, namely, the signal suppression and the reduction in the array gain.

#### 2. PRELIMINARY CONSIDERATION

Consider an array of  $L$  omnidirectional elements emerged in the far field of a sinusoidal point source of frequency  $f_0$  and power  $p_s$ . Let  $\tau_l$  be the time by which the signal on the  $l$ th element of the array incident from the look direction is delayed [4] and  $\alpha_l$ ,  $l = 1, 2, \dots, L$  be the phase delays to steer the array in the look direction. The phase delays are chosen such that the  $L$  output waveforms of the phase shifted elements due to a source in the look direction are identical. For example, the array is pre-steered in the look direction by choosing

$$\alpha_k = 2\pi f_0 \tau_k, \quad k = 1, 2, \dots, L \quad (1)$$

Let an  $L \times L$  dimensional diagonal matrix  $\hat{\Phi}_0$  be defined as

$$\hat{\Phi}_{0kk} \triangleq \exp(j\alpha_k) \quad (2)$$

Let  $\underline{W}$  denote the  $L$  weights of the processor shown in Figure 1 then for a given  $\underline{W}$  the mean output power of the processor is given by

$$P(\underline{W}) = \underline{W}^H \hat{\Phi}_0^H R \hat{\Phi}_0 \underline{W} \quad (3)$$

where  $R$  is the array correlation matrix given by

$$R = p_s \underline{S}_0 \underline{S}_0^H + \sigma_w^2 I + R_I \quad (4)$$

$R_I$  is the array correlation matrix due to interferences only,

$I$  is an identity matrix,  $\sigma_w^2$  is the white noise power on each element and  $\underline{S}_0$  is the steering vector defined as

$$\underline{S}_0 \triangleq [\exp(j2\pi f_0 \tau_1), \dots, \exp(j2\pi f_0 \tau_L)]^T \quad (5)$$

From (3) and (4) it follows that

$$\begin{aligned} P(\underline{W}) &= p_s \underline{W}^H \hat{\Phi}_0^H \underline{S}_0 \underline{S}_0^H \hat{\Phi}_0 \underline{W} + \underline{W}^H \underline{W} \sigma_w^2 \\ &\quad + \underline{W}^H \hat{\Phi}_0^H R_I \hat{\Phi}_0 \underline{W} \end{aligned} \quad (6)$$

Let  $\hat{\underline{W}}$  represent the weights of the processor shown in Figure 1 when it maximises the output SNR. These weights are referred to as the optimal weights and the processor with these weights is referred to as the optimal processor. An expression for the optimal weights is given in [5,6]. For the processor with unit response in the look direction it becomes

$$\hat{\underline{W}} = \frac{\hat{\Phi}_0^H R_N^{-1} \underline{S}_0}{\underline{S}_0^H R_N^{-1} \underline{S}_0} \quad (7)$$

where  $R_N$  is the correlation matrix of interference and white noise only.

From (6) the total output power  $\hat{P}$  of the optimal processor is

$$\hat{P} = p_s \hat{\underline{W}}^H \hat{\Phi}_0^H \underline{S}_0 \underline{S}_0^H \hat{\Phi}_0 \hat{\underline{W}} + \hat{\underline{W}}^H \hat{\underline{W}} \sigma_w^2 + \hat{\underline{W}}^H \hat{\Phi}_0^H R_I \hat{\Phi}_0 \hat{\underline{W}} \quad (8)$$

Substituting for  $\hat{\underline{W}}$ ,  $\hat{\Phi}_0$  and  $\underline{S}_0$  in (8) one obtains after manipulation the expressions for the output signal power  $\hat{P}_s$ , output white noise power  $\hat{P}_w$  and output interference power  $\hat{P}_I$  of the optimal processor as

$$\hat{P}_s = p_s \quad (9)$$

$$\hat{P}_W = \sigma_W^2 \beta \quad (10)$$

$$\hat{P}_I = \frac{\underline{S}_0^H \underline{R} \underline{N}^{-1} \underline{R}^H \underline{N}^{-1} \underline{S}_0}{(\underline{S}_0^H \underline{R} \underline{N}^{-1} \underline{S}_0)^2} \quad (11)$$

where

$$\beta \triangleq \frac{\underline{S}_0^H \underline{R} \underline{N}^{-1} \underline{R}^H \underline{N}^{-1} \underline{S}_0}{(\underline{S}_0^H \underline{R} \underline{N}^{-1} \underline{S}_0)^2} \quad (12)$$

The total output noise power  $\hat{P}_N$  of the optimal processor is given by

$$\hat{P}_N = \frac{1}{\underline{S}_0^H \underline{R} \underline{N}^{-1} \underline{S}_0} \quad (13)$$

### 3. RANDOM PHASE ERRORS

It is assumed that random phase errors which exist in the phase shifters can be modeled as stationary processes of zero mean and equal variances and are uncorrelated from each other.

Let  $\delta_\ell$ ,  $\ell = 1, 2, \dots, L$  represent the phase error in the  $\ell$ th phase shifter.

By assumption

$$E[\delta_\ell] = 0, \ell = 1, 2, \dots, L \quad (14)$$

and

$$E[\delta_\ell \delta_k] = \begin{cases} \sigma^2 & \text{if } \ell = k \\ 0 & \text{otherwise} \end{cases} \ell, k = 1, 2, \dots, L \quad (15)$$

Let  $\tilde{\alpha}_\ell$ ,  $\ell = 1, 2, \dots, L$  represent the phase delays of the actual phase shifters then

$$\tilde{\alpha}_\ell = \alpha_\ell + \delta_\ell, \ell = 1, 2, \dots, L \quad (16)$$

where  $\alpha_\ell$ ,  $\ell = 1, 2, \dots, L$  are the phase delays of error free phase shifters. Let a diagonal matrix  $\phi$  be defined as

$$\phi_{\ell\ell} \triangleq \exp(j\tilde{\alpha}_\ell), \ell = 1, 2, \dots, L \quad (17)$$

Substituting  $\phi$  for  $\phi_0$  in (8) and taking expectation over random phase errors one obtains an expression for the mean output power  $\hat{P}$  of the optimal processor with phase errors (OPPE)

$$\hat{P} = p_S \underline{W}^H \underline{E}[\phi \underline{S}_0 \underline{S}_0^H \phi] \underline{W} + \underline{W}^H \underline{W} \sigma_W^2 + \underline{W}^H \underline{E}[\phi \underline{R} \underline{R}^H \phi] \underline{W} \quad (18)$$

It follows from (18) that the output signal power  $\hat{P}_S$ , white noise power  $\hat{P}_W$  and the interference power  $\hat{P}_I$  of OPPE are given by

$$P_S^V = p_S \hat{W}^H E[\hat{\phi} H S_0 S_0^H \hat{\phi}] \hat{W} \quad (19)$$

$$P_W^V = \sigma_W^2 \hat{W}^H \hat{W} = \sigma_W^2 \beta^2 \quad (20)$$

$$P_I^V = \hat{W}^H E[\hat{\phi} H R_I \hat{\phi}] \hat{W} \quad (21)$$

Comparing (10) and (20) one notes that the output white noise power is not affected by the random errors in the phase shifters.

The effect of random phase errors on the output signal power and output interference power is now examined.

Substituting for  $\hat{\phi}$  and  $S_0$  in (19) using

$$\exp(z) = 1 + z + \frac{z^2}{2!} + \frac{z^3}{3!} + \dots \quad (22)$$

and assuming that the contribution of the higher order terms is negligibly small one obtains after rearrangement and manipulation [7]

$$P_S^V = p_S - p_S \sigma^2 (1 - \beta) \quad (23)$$

Note that in the absence of directional interferences  $\beta = \frac{1}{L}$

thus the output signal power of OPPE is got suppressed and the suppression of the signal power is proportioned to the input signal power and the variance of the random error. In the presence of directional interference  $\beta$  increases and thus the reduction in the signal power is less than otherwise.

Similarly the expression for the output interference power  $P_I^V$  of OPPE simplifies to

$$P_I^V = \hat{P}_I + \sigma^2 (\beta \hat{P}_I - \hat{P}_I) \quad (24)$$

where  $p_I$  is the total power of the directional interferences at the input of the processor.

ARRAY GAIN The array gain is defined to be the ratio of the output SNR to

the input SNR. If  $\hat{G}$  denote the array gain of OPPE then it follows from (20), (23) and (24) that

$$\hat{G} = \frac{\hat{G} (1 + \sigma^2 (\beta - 1))}{1 + \sigma^2 (\hat{G} \beta - 1)} \quad (25)$$

where  $\hat{G}$  is the array gain of the optimal processor. It follows from (25) that the array gain of the optimal processor with random phase errors is a monotonically decreasing function of the variance of the error. Now the following comparison between the effect of the random phase shifter errors and the effect of the random steering vector errors [8] on the performance of the optimal processor can be made

1. the output signal power decreases with the increase in the variance of the phase shifter errors if  $\beta < 1$ , where as in the case of the steering vector errors it is a monotonically increasing function of the variance of the errors. Note that for white noise only  $\beta = \frac{1}{L}$ ,
2. the output white noise power is not affected with the phase shifter errors,
3. the total output noise is a monotonically increasing function of the variance of the steering vector errors, where as the total output noise power decreases with the increase in the variance of phase shifter error if  $\hat{\beta}G < 1$  and
4. the array gains in both the cases are monotonically decreasing functions of the variance of random errors.

#### REFERENCES

1. Stark, L., Burns, R.W. and Clark, W.P., "Phase shifters for arrays", in Radar Handbook Ed by Skolnik, M.I., McGraw Hill, NY 1970.
2. Appelbaum, S.P. and Chapman, D.J., "Adaptive arrays with main beam constraints", IEEE Trans. Antenna Propagation, Vol. AP-24, No. 5, September 1976, pp. 650-662.
3. Mailloux, R.J., "Radar array theory and technology", Proc. IEEE, Vol. 70, No. 3, March 1983, pp. 246-292.
4. Godara, L.C. and Cantoni, A., 'Signal representation for array processing,' Technical Report No. EE8201, Department of Electrical and Computer Engineering, University of Newcastle, NSW 2308, Australia.
5. Reed, I.S., Malet, J.D. and Lawrence, E.B., "Rapid convergence rate in adaptive arrays," IEEE Trans. Aerospace Electronic Syst., Vol. AES-10, No. 5, Nov. 1974, pp. 853-863

6. Appelbaum, S.P., "Adaptive arrays", IEEE Trans. Antenna Propagation, Vol. AP-24 No. 5, September 1976, pp. 585-599.
7. Godara, L.C., "The effect of phase shifter errors on an adaptive array beamformer", to be published.
8. Godara, L.C., "The effect of weight vector errors on the performance of an antenna array", this Conference.

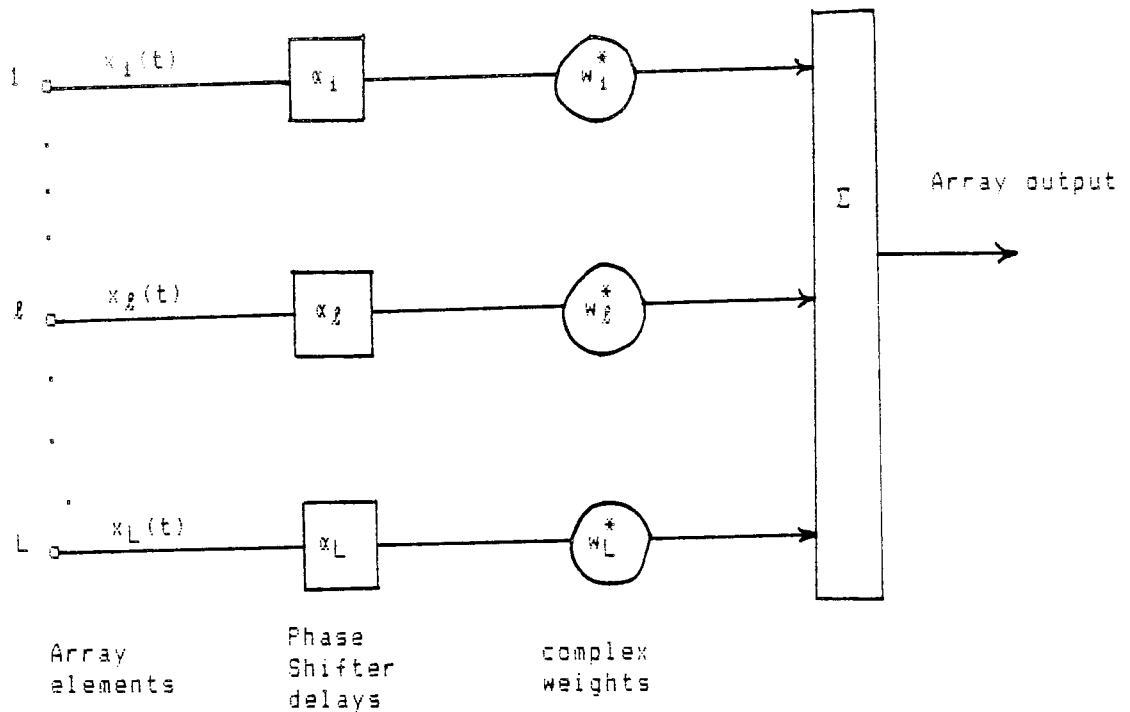


Figure 1: Beamformer Structure.

AN APPLICATION OF A NON-LINEAR TECHNIQUE TO THE PROCESSING OF  
UNDERWATER ACOUSTIC DATA

D.A. Gray

Weapons Systems Research Laboratory  
Defence Science and Technical Organisation  
Department of Defence  
GPO Box 2151 ADELAIDE South Australia 5001

INTRODUCTION

There has recently been interest in some alternative formulations of the optimum or maximum likelihood beamforming algorithm. Two such approaches have been the dominant eigen-vector and beam-space methods and in [1] it has been shown that both methods, if carefully applied, can give similar results to the usual element-space approach when beamforming with circular arrays. In view of some of the advantages of the beam-space method demonstrated in [1] and the fact that it can be applied to the outputs of an existing conventional time or frequency domain beamformer it is of interest to see whether the popular maximum entropy algorithm can also be formulated in beam-space and to compare this formulation with the more common element-space one.

To date a concise and simple formulation of the maximum entropy beamformer only exists for a linear array of equispaced receivers and, by analogy with time series analysis, the wave-number power spectrum at each frequency of interest can be expressed as a function of a set of parameters known as the prediction error filter coefficients. One such method [2] for obtaining these parameters is to solve the Yule-Walker equations using a spatial covariance function derived from the crosspower spectral matrix of receiver outputs [3]. Given only finite samples of the data the spatial covariance matrix is replaced by its estimate.

To formulate the maximum entropy method in beam-space we assume that the Fourier transformed outputs of a conventional time or frequency domain beamformer are available and derive an expression for the maximum entropy estimator of the frequency wave-number power spectrum as a function of the cross-power spectral matrix of these outputs. Intuitively when the system is overdetermined i.e. the number of beams is greater than or equal to the number of sensors then it would be expected that the crosspower spectral matrix of receiver outputs can be retrieved from that of the beam outputs and so the element space results can be fully recovered. However if the number of independent beams is less than the number of receivers then only an approximation to the element space results can be obtained and it is this case that is considered here

REVIEW OF THE ELEMENT-SPACE MAXIMUM ENTROPY PROCESSOR

If  $x$  denotes the complex vector of  $K$  receiver outputs at frequency  $f$  (note that any explicit dependence on frequency has been dropped) then  $R_x$ , the crosspower spectral matrix of receiver outputs, is given by

$$R_x = \langle xx^H \rangle$$

and is Toeplitz if the noise field is ergodic and homogeneous. From [2] the element-space maximum entropy wave-number power spectrum is given by

$$(R_x^{-1} \delta)_1 (z^H R_x^{-1} \delta \delta^H R_x^{-1} z)^{-1}$$

where  $\delta^H = (1, 0, \dots, 0)$  and  $z$  is the vector of phase delays determined by the wave-number values at which the spectrum is to be estimated. Note that in practice  $R_x$ , when replaced by its estimate is not necessarily Toeplitz and as discussed in [3] can be made so by generating a spatial covariance function formed by averaging along the diagonals of the estimated  $R_x$ . Furthermore to ensure statistically stable estimates of the power spectrum not all of the available spatial lags formed by such averaging along the diagonals should be used (see [3] for further details).

An example of the application of this method to underwater acoustic data is shown in figure 1 where an estimate of the frequency wave-number power spectrum obtained by a Fourier transform of the outputs of 32 receivers is compared with a maximum entropy one using 24 of the available 32 spatial lags.

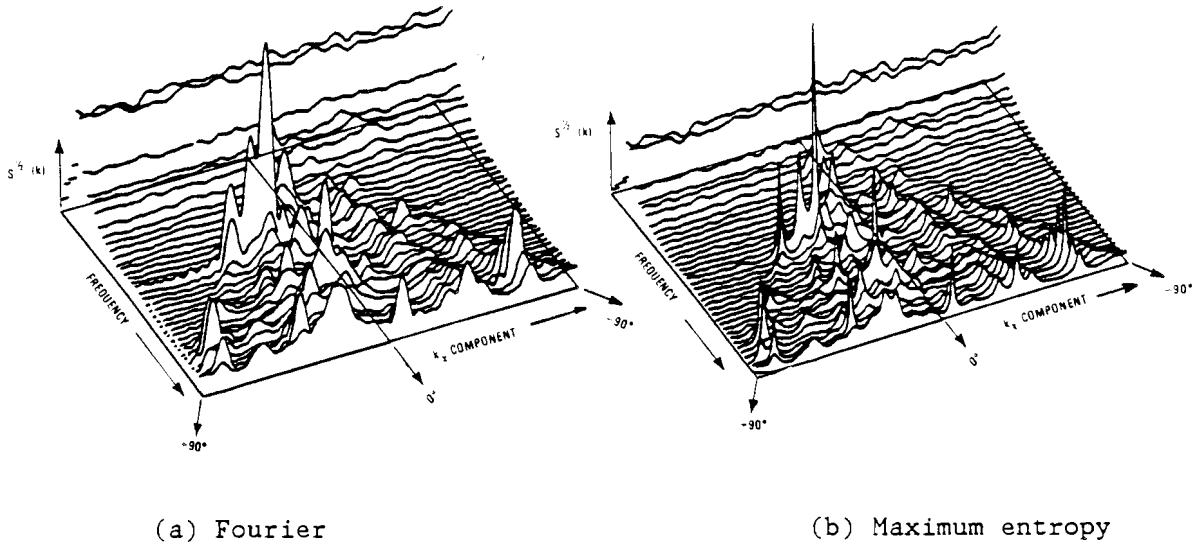


Figure 1 Fourier and maximum entropy estimates of the frequency wave-number power spectrum.

The results indicate the superior resolution of the maximum entropy method particularly in the presence of a strong interference.

#### DERIVATION OF THE BEAM-SPACE MAXIMUM ENTROPY ESTIMATES

It can readily be shown that the vector,  $y$ , of  $M$  conventional frequency domain beamformer outputs at frequency  $f$  is given by

$$y = V^H x$$

where  $H$  denotes Hermitian transpose of a matrix or vector and  $V$  denotes the  $K \times M$  matrix of phase delays defined by the chosen steering directions. It follows that the cross-power spectral matrix of beam outputs is given by

$$R_y = V^H R_x V. \quad (1)$$

To derive the maximum entropy estimator for a line array with receivers separated by a distance  $d$  we maximize the entropy, given by

$$\int_{-u}^u \ln S(k_x) dk_x$$

where  $u = \frac{1}{2d}$  and  $k_x = \sin(\theta)/\lambda$  is the component of the wave-vector along the array. The constraint commonly imposed [2] is that the inverse Fourier transform of  $S(k_x)$  equals the known spatial covariance function, i.e.

$$\int_{-u}^u S(k_x) \exp(2\pi i k_x \rho d) dk_x = (r_x)_\rho$$

Now if the  $R_x$ 's are not known or cannot be estimated, then the above constraint cannot be directly used. However (1) suggests that when the covariance matrix of beam outputs is known or can be estimated the following generalized constraint can be applied

$$\sum_{l=1}^K \sum_{m=1}^K V_{lj}^* \int_{-u}^u S(k_x) \exp(2\pi i k_x (l-m)d) dk_x V_{mn} = (R_y)_{jn}$$

Following Edwards and Fitelson [4] and introducing Lagrange multipliers then a solution to the maximum entropy beam-space problem is

$$S(k_x) = d (z^H V \alpha \alpha^H V z)^{-1}$$

where

$$(z)_j = \exp 2\pi i k_x (j-1)d = (z_0)^{j-1}$$

and

$$R_y \alpha = v_0 (V \alpha)_1^{-1}$$

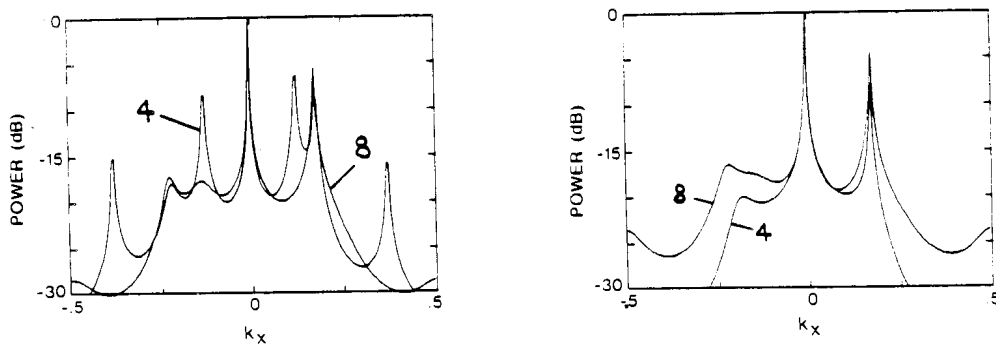
where  $v_0$  is the first column of  $V$ . This can be seen to be an appropriate generalization of the corresponding element space results and when  $M = K$  reduces to them.

A seemingly minor but important difference to the element-space derivation is that some of the zeros of the polynomial  $z^H V \alpha$  may lie on the unit circle e.g. this happens if one of the nulls of the polar responses of each of the presteered beams occur at a common value of  $k_x$ . Note that this would occur automatically if the beamsteering directions are chosen to be equispaced in  $k_x$ . This problem of extraneous spikes in the spectrum results from using an

insufficient number of beams i.e. from the fact that  $V_x$  does not span the complete  $K$  dimensional space. In general this singular behaviour is determined by

- (a) the number and spacing (either in angle or wave-number) of the chosen preformed beams; and
- (b) the shading coefficients used in forming the beams.

Some examples and a number of computer simulations suggest that shading the input beams can prevent such singularities occurring. If the wave-number power spectrum is to be estimated over the complete range of  $k_x$  then Gaussian shading of beams equispaced in  $k_x$  proved very effective. However if at a given frequency the spectrum is only to be estimated over the range of  $k_x$  corresponding to plane wave arrivals then Gaussian shading with equispacing in  $\sin \theta$  was found to be better.



(a) Unshaded

(b) Shaded

Figure 2 Beam Space Maximum Entropy Examples

The result of evaluating the above expression for the beam-space maximum entropy wave-number spectrum is shown in figure 2a for a linear array of 8 equispaced receivers for a noise field of two plane waves 10 and 15 dB w.r. to the isotropic noise level and at a frequency such that  $d/\lambda = .25$  where  $d$ , the separation of adjacent receivers has been scaled to unity. Two examples using 4 and 8 presteered beams were considered; in both cases the beams were equispaced over the region of  $k_x$  running from  $-0.5$  to  $0.5$ . Using 4 beams gives spurious peaks in addition to the correct peaks at  $k_x = 0$  and  $.16$ ; when 8 beams were used the full element space results were recovered and no spurious peaks observed. (N.b all plots have been normalized to a peak of unity.) Using Gaussian shading, figure 2b, effectively reduced these spikes but at the expense of increasing the width of the spectral peaks.

#### SUMMARY

The maximum entropy method has been used to estimate the frequency wave-number power spectrum of underwater acoustic data from a linear array of equispaced hydrophones and shows significant improvement in resolution over conventional processing.

A technique has been proposed which provides an estimate of the maximum entropy wave-number power spectrum using a set of preformed beams rather than

the receiver outputs. This approximation to the element space results improves as the number of beams used is increased. The spacing and shading of beams is a critical feature in the avoidance of spurious peaks which can occur in this formulation in a way similar to dominant eigenvalue methods.

#### REFERENCES

- (1) Gray, D.A. "Theoretical and Experimental Comparisons of Optimum Element, Beam and Eigen Space Array Processors." To appear in "Adaptive Methods in Underwater Acoustics" Ed. H.G. Urban, D. Reidel
- (2) McDonough, R.N. "Application of the Maximum-Likelihood Method and the Maximum-Entropy Method to Array Processing" Chap. 6, p.181 of 'Nonlinear Methods of Spectral Analysis' Ed. S. Haykin, Springer Verlag 1979
- (3) Gray, D.A. "Maximum Entropy Estimates of the Frequency Wavenumber Power Spectrum using a Linear Array of Equispaced Receivers" WSRL-0196-TR, February 1981, Weapons Systems Research Laboratory, Adelaide, South Australia
- (4) Edwards, J.A. and Fitelson, M.M. "Notes on Maximum-Entropy Processing" IEEE Trans. Info Theory 232 (1973)

## SYSTOLIC ARCHITECTURES FOR SONAR PROCESSING.

W. Marwood and A.P. Clarke

Weapons Systems Research Laboratory,  
 Defence Research Centre, Salisbury,  
 South Australia.

## 1. INTRODUCTION

Current sonar systems employ both time and space diversity to achieve a high level of operational performance. This, together with the complex geometry and relatively slow speed of sound propagation in the ocean, has imposed many constraints on the concomitant signal processing system. For example, low sonar operating frequencies and the use of wide-band processing force the use of broad-band beamforming. Further, ever-increasing numbers of hydrophone elements are being used for high spectral resolution and the signal processing system must be capable of forming in parallel large numbers of independent beams in order to attain an adequate angular cover as well as giving the spectral resolution. In addition, for towed systems in particular, the geometry of the array may fluctuate. The general effect of these three observations is to impose an enormous computing load on the signal processing system. American agencies have developed satellite-to-shore systems which can call on the number crunching power of super-computers like the Cray. In the Australian environment this is not possible and hence there is the necessity to look at parallel computers based on VLSI technology. If such systems are realisable then there is the added advantage that the system can be carried on small platforms such as helicopters and diesel-electric submarines.

The purpose of this paper is to indicate one possible architecture for implementing a limited class of passive broad-band beamformers. It is shown in this article that computing loads approaching hundreds of mega-flops can be achieved conceptually with a minimum of silicon area. It is also indicated that the systems can be made highly reliable by incorporating a limited form of self repair.

A paper by Whitehouse and Speiser [1] addresses the general question but does not give a clear indication of the power of systolic arrays for particular tasks. In contrast, this paper is concerned with a specific design and implementation.

## 2. SYSTOLIC ARCHITECTURES.

A form of distributed signal processing called a systolic array is to be considered. The systolic array is a one, two or higher dimensional array of identical processors. In each processor both the hardware and the executed program is identical. Each processor is connected to nearest neighbours only. Each processor receives data from its neighbours, computes data, and then passes data on to its neighbours at all times in synchronism with a master clock. In physiology, the word 'systole' is used for the heart contraction pumping blood. In the systolic array the system clock is the analogue of the heart.

In most sonar signal processing requirements the basic operations can be written in a matrix form. When this is realised it can be seen that each processor can consist of a cascaded sequence of processing blocks where each block is a systolic array executing a matrix operation. Hence the total implementation will consist almost entirely of systolic processing elements. Many examples are given in [2] and [3].

## 3. BEAMFORMING.

In conventional beamforming the observation of some propagating, coherent wave

in the ambient noise background of the ocean is enhanced by summing time-delayed and weighted hydrophone data. The weights are designed to achieve some specified side-lobe level from a particular array. The output in a given direction  $\theta$  is given by

$$b_{\theta}(t) = \sum_{n=2}^k w_n x_n(t - \tau_n(\theta)) \quad (3.1)$$

where  $x_n(t)$  is output from hydrophone  $n$

$w_n$  is a weight factor

$\tau_n(\theta)$  is a time delay to be applied to the  $n^{\text{th}}$  hydrophone to steer in the direction  $\theta$ .

In digital systems the  $x_n$  are sampled (usually at frequencies 5-10 times Nyquist) and samples from each hydrophone taken as near to the steered direction  $\theta$  as possible.

Figure 1 represents the beamforming task. This can be represented in matrix form

$$\text{tr}\{X.S(\theta)\} = b_{\theta}(t).$$

where  $X$  is the data buffer at time  $t$

and  $S(\theta)$  is a matrix that extracts data from  $X$  for summing.

Errors are possible due to sampling. Pridham and Mucci [4] suggest interpolation as a means of reducing this error. For steering over  $p$  angles it is then possible to write a matrix equation

$$\begin{bmatrix} b_1 \\ b_2 \\ \vdots \\ b_p \end{bmatrix} = \begin{bmatrix} r_1(\theta_1) & r_2(\theta_1) & \dots & r_k(\theta_1) \\ r_1(\theta_2) & r_2(\theta_2) & \dots & r_k(\theta_2) \\ \vdots & \vdots & \ddots & \vdots \\ r_1(\theta_p) & r_2(\theta_p) & \dots & r_k(\theta_p) \end{bmatrix} \odot \begin{bmatrix} x_1 \\ x_2 \\ \vdots \\ x_k \end{bmatrix} \quad (3.2)$$

where  $r_1, r_2, \dots, r_k$  are the  $k$  columns of  $S$  which are now occupied by

interpolation coefficients

$x_1, x_2, \dots, x_k$  are the  $k$  rows of  $X$

and  $\odot$  is an operation giving as the 'inner product' the sum over  $n$  of the scalar product  $r_n \cdot x_n$

#### 4. A FINITE-IMPULSE RESPONSE FILTER IMPLEMENTATION.

A finite impulse response filter of order  $N$  can be expressed as

$$y(n) = \sum_{k=0}^{N-1} h(k) x(n-k) \quad (4.1)$$

A direct form realisation of this algorithm utilising  $N$  systolic multiply-accumulate elements is shown in Figure 2. Operation of each element is defined by

$$c_i = a_i b_i + c_{i-1} \quad (4.2)$$

Each  $x(n)$  is broadcast to all elements, and the  $h(k)$  are entered serially into the linear array. The  $N$  coefficients are recirculated after initialisation of the array to minimise overheads. Operation of the filter is described in terms of the function of the first multiply-accumulate element. From the input sequence  $x_{i-N+1}, x_{i-N+2}, \dots, x_i$  the inner product

$$y(i) = \sum_{k=0}^{N-1} h(k) x(i-k)$$

is formed and output.

Terms of the output sequence  $\{y\}$  provided by this element are

$$y(i+jN) \quad j \text{ integral.}$$

Terms not provided by this element are

$$y(i+k+jN) \quad j \text{ integral and } 0 < k < N.$$

These terms are available from the remaining  $(N-1)$  elements in the structure of figure 2. Correct ordering of the output data sequence  $\{y\}$  is achieved by cyclically multiplexing the  $N$  outputs into a single sequence as shown in the figure. For large values of  $N$ , results are passed back along the array as in conventional systolic architectures, and re-ordered as necessary.

##### 5. A BEAMFORMER IMPLEMENTATION.

The matrix equation given in section 3 describes an interpolation beamforming algorithm. In this section a systolic architecture which implements this algorithm is described. A schematic of the beamformer is shown in figure 3. The formation of a single beam is considered first.

$$\begin{aligned}
& k \\
b_1(\theta_1) &= \sum_{i=1}^k r_i(\theta_1) \cdot x_i \\
& \\
& k \quad s \\
&= \sum_{i=1}^k \sum_{j=1}^s r_{i,j}(\theta_1) x_{i,j} \tag{5.1}
\end{aligned}$$

where  $s$  is the length of the data vector.

The inner summation is completed in  $s$  sample times by one multiply/accumulate element. Consider a linear structure in which the  $x_{i,j}$  are broadcast to  $k$  concurrent elements, and the appropriate  $r_{i,j}$  are provided to each element.

The array of systolic elements can compute the  $k$  inner products of (5.1) in  $s$  sample times. The  $k$  partial sums are then passed along the array and accumulated in an end element. This last element can be identical to all others if a multiplier of one is used. The beam sample is the result of this final accumulation.

Beam samples from this one element are computed every  $s$  sample times and can be represented as  $b_{i+j_s}$  for integral  $j$ .

To compute the remaining  $s-1$  samples not computed by the linear array, an additional  $(s-1)$  linear arrays are added to the structure. Operation is analogous to the case of the filter discussed in section 4. The  $x_i$  are broadcast to elements along the X-axis of figure 3 and the coefficients are pipelined across the array. Beam samples appear at the boundary elements in cyclical order as for the filter.

Additional beams are computed by replicating the two-dimensional structure described above, so generating a three dimensional systolic architecture. In the lower layers of the structure, all data is properly pipelined.

All operations are fully pipelined in this structure. Beam outputs are therefore available for all beams at every sample time. Pipelining delays necessitate a re-alignment of outputs. The maximum sample rate which can be achieved determined by the computation time of the multiply/accumulate element. For bit-serial floating-point elements this is of the order of one microsecond. As up to five elements can be placed on a 4 micron MPC chip it is clear that a beamformer as described is capable of implementation, and can have a computation rate well in excess of 100 mega-flops.

A practical implementation is feasible without modification for up to 16 sensors with sample rates approaching 1 MHz. For the sonar environment however, a practical implementation would multiplex the data through the array to match the computation rate to the sample rate.

## 6. RELIABILITY.

Redundant data paths can be implemented in both the FIR filter structure of section 4 and the beamformer of section 5. The use of multiply-accumulate elements with a self checking capability allows reliability and yield to be greatly enhanced for VLSI implementations. The approach is identical to that detailed in [5] and [6].

## 7. ACKNOWLEDGEMENT

The authors wish to thank Mr. A.B.Franks for the preparation of the figures in this paper.

## 8. REFERENCES

- [1] Speiser, J.M., Whitehouse, H.J. and Bromley, K.(1980). 'Signal Processing Applications for Systolic Arrays', Record of the 14th Asimolar Conference on Circuits, Systems and Computers, Pacific Grove, California, IEEE 80CH1625-3.
- [2] Pridham R.G. and Mucci R.A., 'A Novel Approach to Digital Beamforming' J. Acoust. Soc. Am., Feb 1978, pp425-434.
- [3] Whitehouse, H.J. and Speiser, J.M., 'Sonar Applications of Systolic Array Technology', presented at IEEE Eascon, Washington, D.C., Nov. 17-19, 1981.
- [4] Speiser, J.M. and Whitehouse, H.J., 'Parallel Processing Algorithms and Architectures for Real-time Signal Processing', SPIE Vol. 298, Real-time Signal Processing IV (1981), paper 298-03
- [5] Marwood, W. and Clarke, A.P. (1983). 'The Need and Possibility for the Design of Self Repairing Circuits', IREE and IEAust workshop 'Creating Integrated Systems' Adelaide.
- [6] Marwood, W. and Clarke, A.P. (1984). 'Reconfiguration Penalties in Arrays of Dynamically Reconfigurable Processing Elements', Pacific Asian Region Conference on VLSI, Melbourne, Australia.

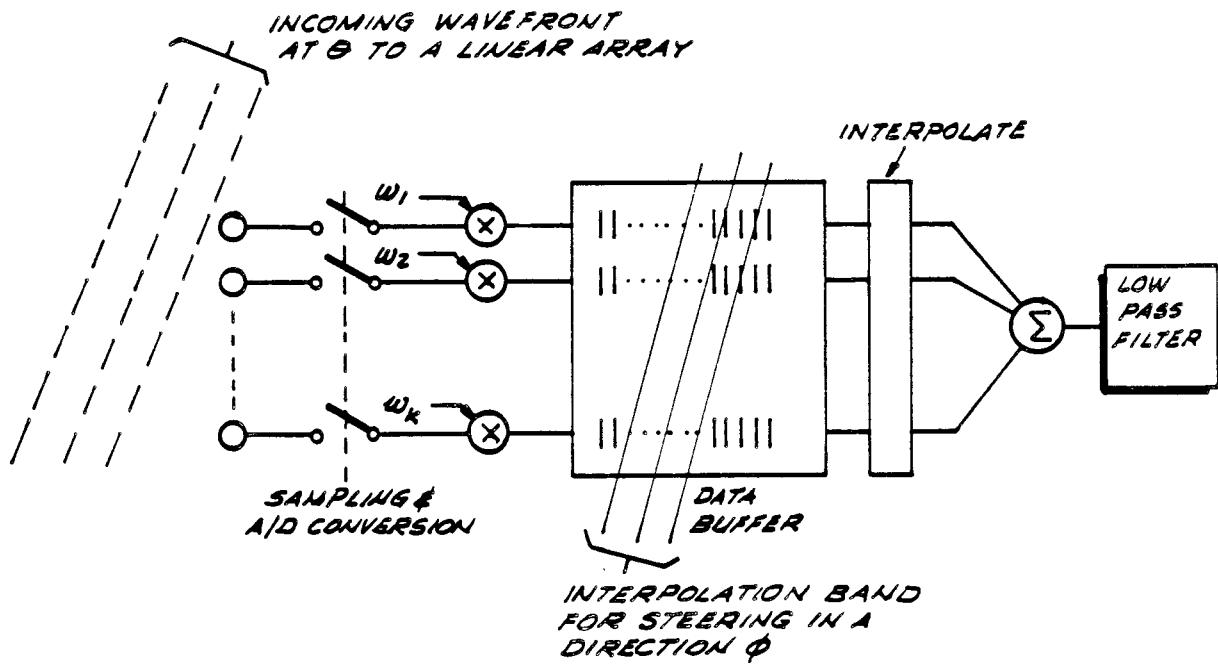
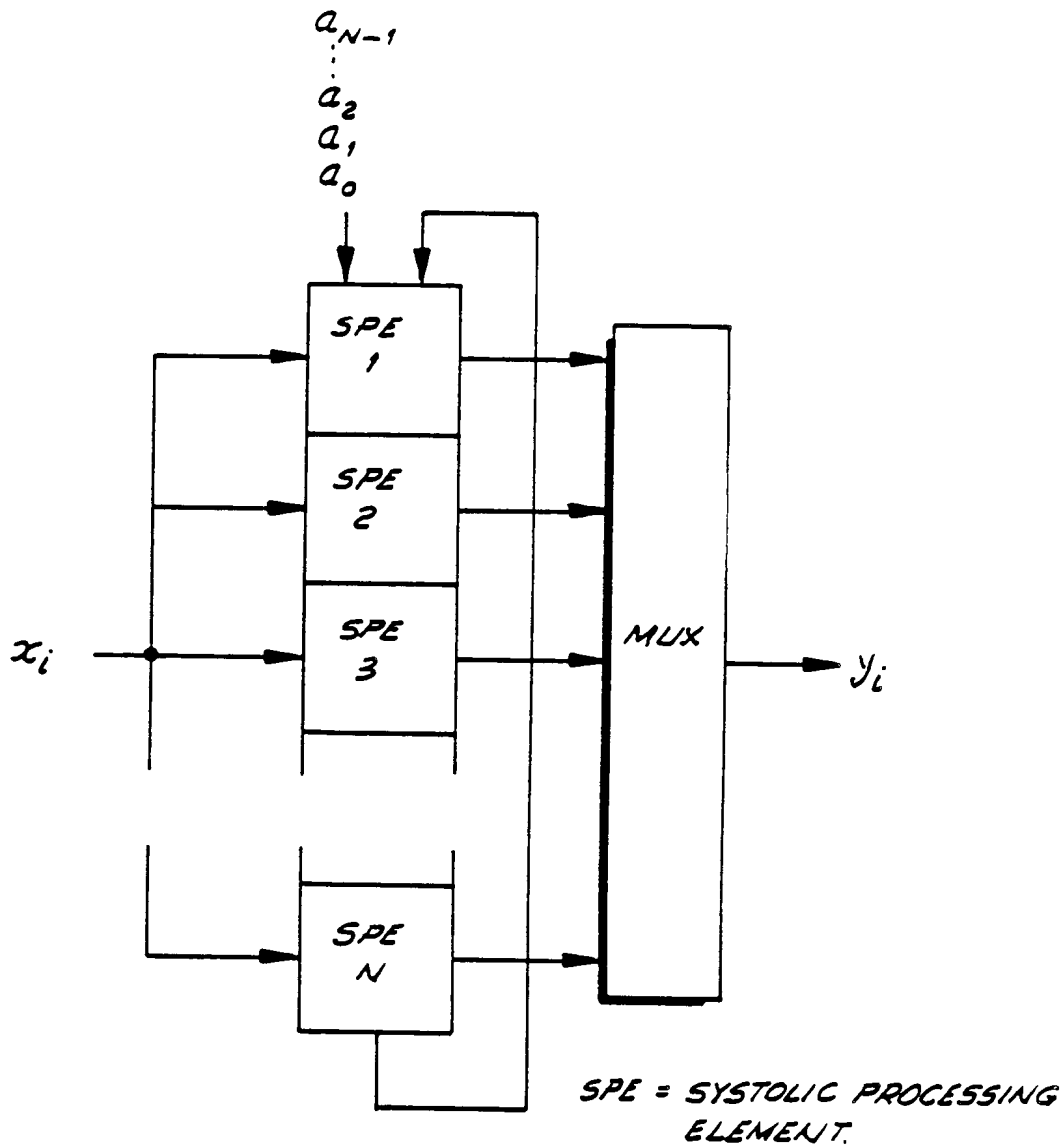
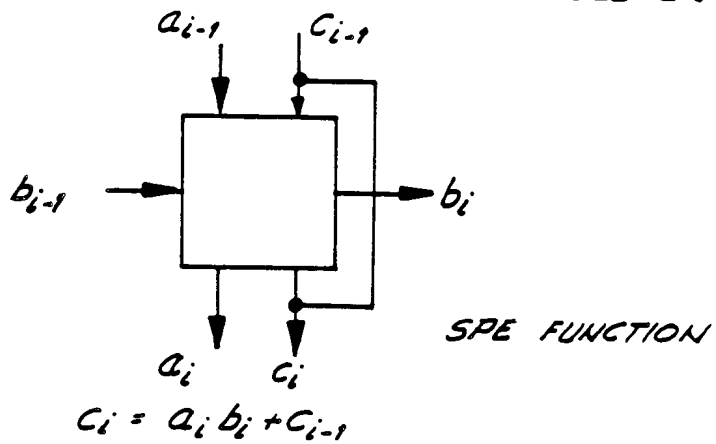


FIGURE 1.- A BEAMFORMER SCHEMATA FOR INCOMING WAVEFRONTS AT AN ANGLE  $\theta$  TO A LINEAR ARRAY OF  $K$  HYDROPHONES & A BEAM IS FORMED IN THE DIRECTION  $\phi$ .



SPE = SYSTOLIC PROCESSING ELEMENT.

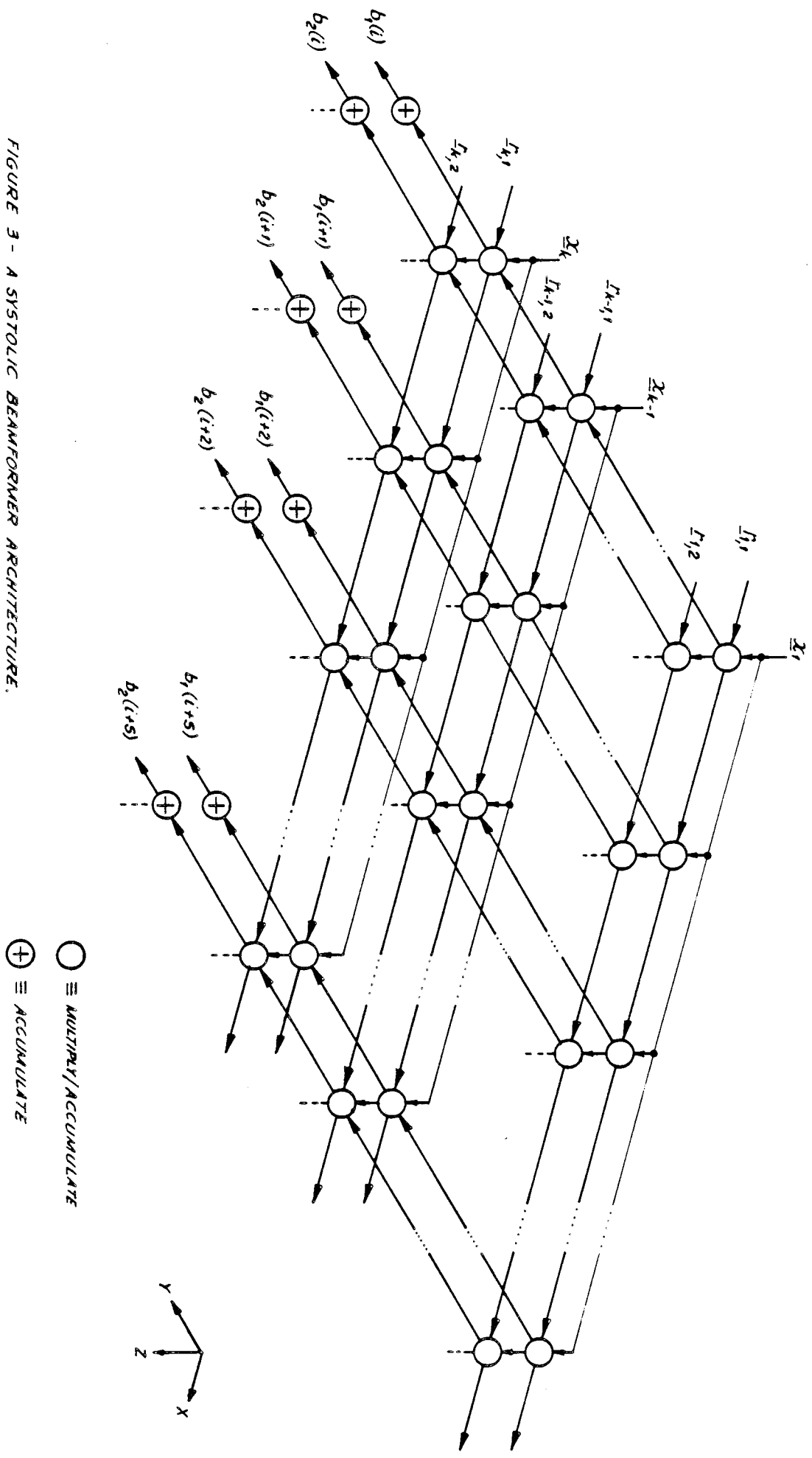


SPE FUNCTION

$$c_i = a_i b_i + c_{i-1}$$

FIGURE 2 - A FINITE-IMPULSE RESPONSE FILTER IMPLEMENTATION.

FIGURE 3 - A SYSTOLIC BEAMFORMER ARCHITECTURE.



## ROBUST ESTIMATION OF BEARING IN CORRELATED NOISE

C.L. Byrne\*, and A.K. Steele\*\*

\* Dept. of Mathematics, The Catholic University of America,  
Washington, DC 20064\*\* Weapons Systems Research Laboratory, Defence Research  
Centre Salisbury, South Australia

ABSTRACT Most nonlinear bearing estimators are unstable in the presence of correlated noise, phase errors and multi-path arrivals because they place too much emphasis on unstable eigenvectors of the cross-sensor correlation matrix. By implicitly reweighting the eigenvectors, without actually calculating them, we obtain stable, high resolution estimators, showing that important information has not been permanently lost due to perturbations. Comparison with the maximum likelihood estimator and eigenvector methods is made through simulations, illustrating the superior performance of the new, stable nonlinear method (SNLM).

1. INTRODUCTION

Because many of the well known nonlinear, high resolution bearing estimation procedures exhibit severe degradation when the data includes such perturbations as system phase errors or correlated arrivals, concern has been raised over the usefulness of these methods in practice, especially in correlated ambient noise environments. Indeed, the more basic question can be asked: Is there remaining in the perturbed data information sufficiently accurate for any nonlinear method to perform well? We show that the answer can often be affirmative and derive new, stable procedures that provide accurate resolution and localization of discrete sources in correlated noise, with high correlation between signals. The observed instability in other methods can be traced to flaws inherent in those methods and not to loss of accurate information in the data.

The methods presented here (and most other nonlinear methods) accept as data the matrix  $R$  of (time-averaged) single frequency cross-sensor correlations. The eigenvectors of  $R$  that correspond to the smaller eigenvalues (the "smaller" eigenvectors) are weighted more heavily in most nonlinear methods (through the use of  $R^{-1}$ ) and their null structure provides the information concerning source directions. These smaller eigenvectors break up into two classes, in the presence of correlated noise. Those eigenvectors corresponding to the smallest eigenvalues (the "smallest" eigenvectors) are nearly orthogonal to all steering vectors whose arrival angles lie within the region of noise concentration, therefore, their null structure is easily perturbed by phase errors. Because these smallest eigenvectors are most heavily weighted by most nonlinear methods these methods are unstable. However, those smaller eigenvectors not in this

\* Work done under contract with U.S. Naval Research Laboratory, Washington, DC  
\*\*Work done while on exchange at U.S. Naval Research Laboratory, Washington, DC

group are nearly unaffected by the phase errors, at least with regard to their null structure in the visible region, and thus retain all the information needed for high resolution processing. As the noise becomes increasingly correlated the number of stable eigenvectors decreases, so that eventually prewhitening is required, but for many correlated noise fields there are sufficiently many dependable eigenvectors of  $R$  to provide good bearing estimation; the examples below show this for a uniform line array oversampled up to five times the Nyquist rate.

The nonlinear method we present here is a generalization of Capon's maximum likelihood method (MLM) [1,2], which we call the stable nonlinear method (SNLM). Like the MLM, the SNLM employs  $R^{-1}$  and does not require explicit calculation of the eigenvectors of  $R$ . An understanding of the behavior of these eigenvectors is essential, though, and we consider this next.

## 2. THE EIGENVECTORS OF $R$

The improvement in resolution achieved by nonlinear methods, such as MLM, is best understood in terms of the eigenvectors of  $R$ ; more recent methods, based on explicit calculations of these eigenvectors (or generalized eigenvectors, when the noise is correlated) can provide high resolution for extremely low SNR, although they are more unstable [3-7].

Let  $R = S + Q$ , where  $S$  is the sum of  $J < N$  planewave rank one arrival matrices ( $N =$  number of sensors) and  $Q > 0$  is the noise-only correlation matrix. Let  $x_1, \dots, x_N$ ,  $\lambda_1 \geq \dots \geq \lambda_N > 0$  be the orthonormal eigenvectors and eigenvalues of  $R$ . When  $Q = I$  (uncorrelated noise) the vector  $x_n$ ,  $n \geq J+1$ , are orthogonal to each signal arrival vector. As  $Q$  begins to deviate from  $I$  the smallest eigenvectors ( $x_n$  for  $n$  near  $N$ ) begin to exhibit some of the properties of the smallest eigenvectors of  $Q$  itself. If  $Q$  corresponds to an isotropic noise field and the array is a uniform line array that is oversampled then the smallest  $x_n$  are nearly orthogonal to all the planewave arrival vectors in the visible region, while this is not the case for those  $x_n$  for  $n$  nearer to  $J + 1$ .

In each of the figures below we shall be concerned with the bearing response functions

$$1 / \sum_{n=L}^M \lambda_n^{-1} |e(\theta)^\dagger x_n|^2, \quad (1)$$

where  $e(\theta)$  is the usual steering vector associated with arrival angle  $\theta$ . In Figure 1 we have the bearing response function summed over the smallest 13 eigenvectors ( $L = 13$ ,  $M = 25$ ) of a 25 by 25 matrix  $R$ . Here the array is uniform, twice oversampled, with sensor spacing  $D = \lambda/4$ , a high isotropic noise and single planewave at broadside. Figure 2 shows the sum for the 11 eigenvectors  $x_n$ ,  $L = 2$ ,  $M = 12$ . In figures 1 through 4 the top curve is without phase errors; the other curves correspond to five independent simulations of random phase errors within  $\pm 5^\circ$ . Figures 3 and 4 show the effect on resolution; replacing the single planewave with two uncorrelated

ones, at  $\pm .0075 \pi/D$ , the smallest eigenvector ( $L=M=25$ ) of  $R$  fails to resolve, even when there are no phase errors (Fig. 3), while the sum for  $L = 8, M = 11$ , (Fig. 4) provides stable resolution.

### 3. THE STABLE NONLINEAR METHOD

The MLM estimator of bearing is

$$\text{MLM}(\theta) = 1/e(\theta)^\dagger R^{-1} e(\theta) = 1/ \sum_{n=1}^N \lambda_n^{-1} |e(\theta)^\dagger x_n|^2. \quad (2)$$

The SNLM has the same general form, but involves a different weighting of the  $x_n$ , specifically designed to de-emphasize both the smallest eigenvectors (the unstable ones) and the largest ones (that hinder resolution, particularly in the correlated arrival case):

$$\text{SNLM}(\theta) = 1/e(\theta)^\dagger R^{-1/2} (R + \alpha^2 R^{-1})^{-K} R^{-1/2} e(\theta) \quad (3)$$

or

$$\text{SNLM}(\theta) = 1/ \sum_{n=1}^N \left( \frac{\lambda_n^{K-1}}{(\lambda_n^2 + \alpha^2)^K} \right) |e(\theta)^\dagger x_n|^2. \quad (4)$$

Here  $K = 0, 1, 2, \dots$  and  $\alpha^2$  are parameters chosen by the user. We normalize  $R$  so that  $\text{trace}(R) = N$ . Then  $\alpha^2$  near 1 emphasizes the mid-range of eigenvalues. It is important that  $\alpha$  be greater than the smallest eigenvalues we wish to de-emphasize, but not as large as  $\lambda_J$ . By raising  $K$  we further reduce the weighting of all terms whose  $\lambda_n$  is not near  $\alpha$ .

In Figures 5 through 8 we have simulated a uniform line array of 25 sensors, oversampled by a factor of 5 ( $D = \lambda/10$ ). Isotropic noise is 30 dB above the uncorrelated noise, and two signals, at  $(.1 \pm .03) \pi/D$  each have power -3 dB relative to the total noise power. Figure 5 shows (top curve) the conventional estimator (linear), with and without phase errors (no discernable difference), below it the MLM for no phase errors, and below that MLM for the same five independent random sets of phase errors. Figure 6 shows the SNLM for the same case; from top to bottom we have  $K = 1, 4, 12$ . Here  $\alpha^2 = 6.0$  and each of the three graphs is actually the no-phase-error and the five phase-error cases, superimposed, showing almost perfect stability. Note that  $K = 0$  is MLM, so the  $K = 1$  case achieves stability with just one iteration beyond the MLM.

We show that the SNLM is not sensitive to the choice of  $\alpha$  in Figure 7, where  $K = 12$  and  $\alpha^2 = 6, 1$  and  $0.5$ .

When the signal arrivals are correlated most nonlinear methods fail, either by not resolving or by biasing the peak locations. In Figure 8 we show the MLM with and without phase errors (top curves) and the SNLM with and without errors (superimposed lower curves) with  $K = 12, \alpha^2 = 1.0$ . The two signals have a correlation coefficient of  $(0.9, 0^\circ)$ . The SNLM does show some bias in the estimated arrival angles, which becomes worse as the

signals become more highly correlated. The selection of  $\alpha$  is more critical when the signals are highly correlated since the high correlation forces one of the signal eigenvalues to approach the noise eigenvalues.

## CONCLUSIONS

Instability of many nonlinear bearing estimators in the presence of correlated noise, phase errors and partially correlated multi-path arrivals can be traced to excessively high weighting of unstable eigenvectors of the cross-section matrix,  $R$ . Stable nonlinear procedures (the SNLM) are able to overcome these difficulties by implicitly reweighting the eigenvectors. Resolution and localization are restored without explicit calculation of eigenvector.

## REFERENCES

- [1] J. Capon, "High-resolution frequency-wavenumber spectrum analysis," Proc. IEEE, vol. 57, no. 8, pp. 1408-1418, 1969.
- [2] \_\_\_\_\_, "Maximum-likelihood spectral estimation," in Nonlinear Methods of Spectral Analysis, S. Haykin, Ed. New York: Springer, 1979, pp. 155-179.
- [3] A. Cantoni and L.C. Godara, "Resolving the directions of sources in a correlated field incident on an array," J. Acoust. Soc. Amer., vol. 67, no. 4, pp. 1247-1255, 1980.
- [4] D.H. Johnson and S. Degraaf, "Improving the resolution of bearing in passive sonar arrays by eigenvalue analysis," IEEE Trans. Acoust., Speech, Signal Processing, vol. ASSP-30, no. 4, pp. 638-647, 1982.
- [5] R. Schmidt, "Multiple emitter location and signal parameter estimation," in Proc. RADC Spectral Estimation Workshop, Rome, NY, 1979, pp. 243-258.
- [6] D.H. Johnson, "The application of spectral estimation methods to bearing estimation problems," Proc. III, vol. 70, no. 9, pp. 1018-1028, 1982.
- [7] G. Bienvenu and L. Kopp, "Optimality of high resolution array processing using the eigensystem approach," IEEE Trans. Acoust., Speech, Signal Processing, vol. ASSP-31, no. 5, pp. 1235-1247, 1983.

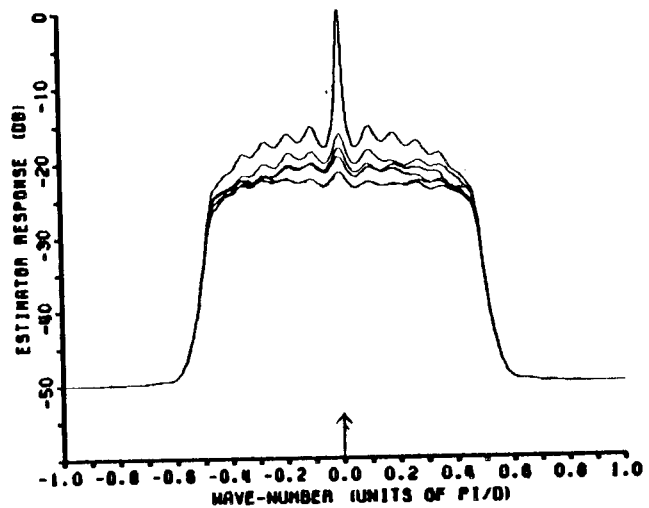


Fig. 1. Estimator response using eigenvectors 13 to 25; 1 signal.

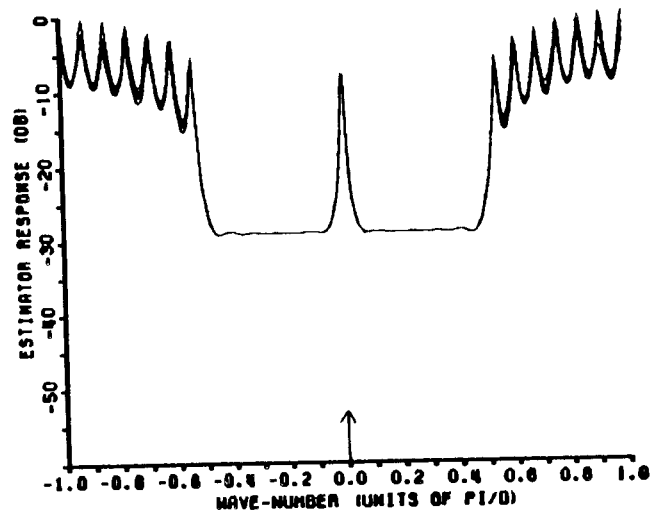


Fig. 2. Estimator response using eigenvectors 2 to 12; 1 signal.

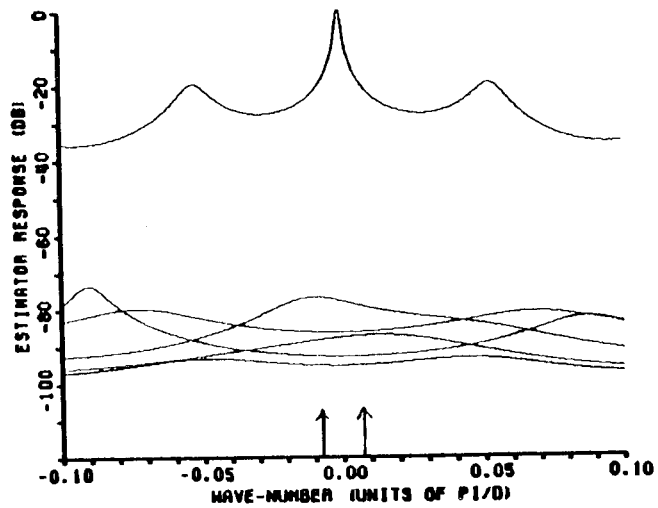


Fig. 3. Estimator response using eigenvector 25; 2 signals.

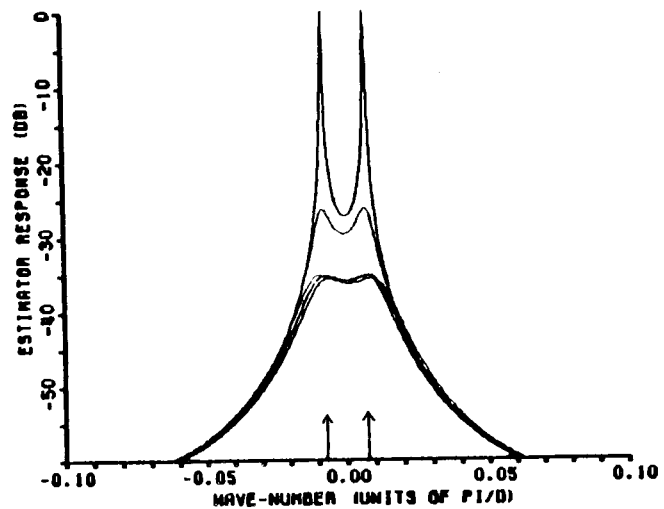


Fig. 4. Estimator response using eigenvectors 8-11; 2 signals.

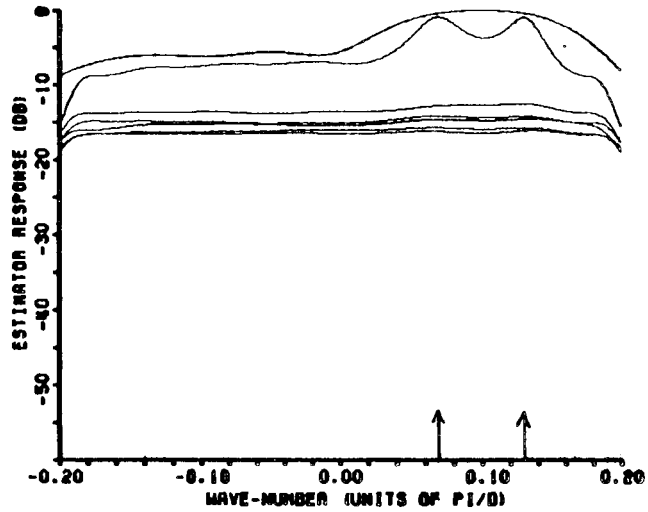


Fig. 5. Conventional and MLM estimators; 2 uncorrelated signals.

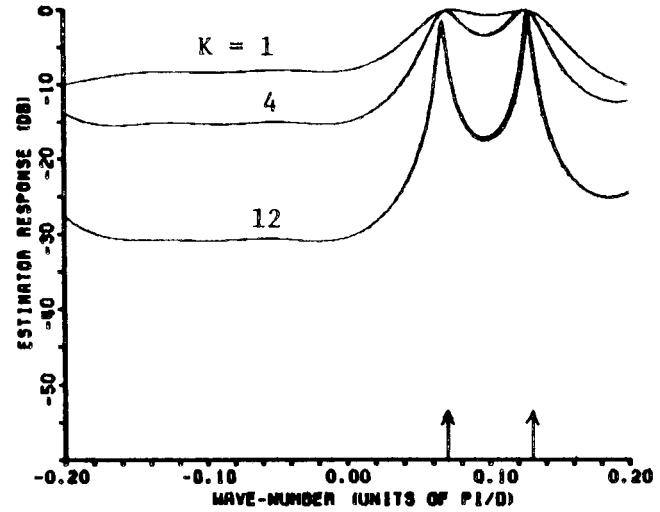


Fig. 6. SNLM estimators;  $K=1,4,12$  2 uncorrelated signals.

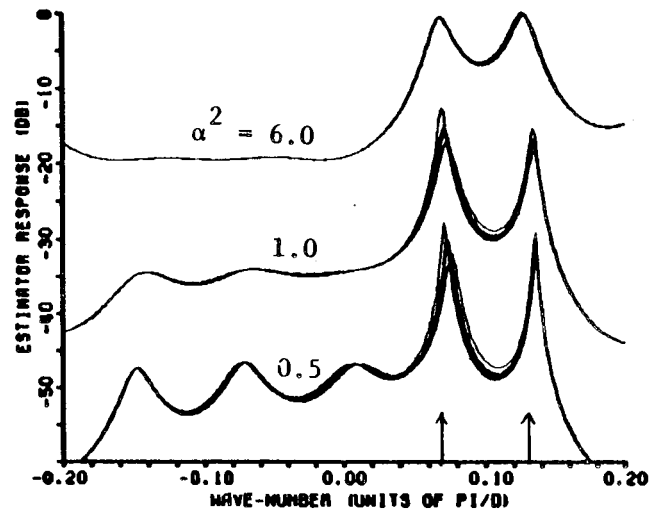


Fig. 7. SNLM estimators;  $\alpha^2=6,1,0.5$ ; 2 uncorrelated signals.

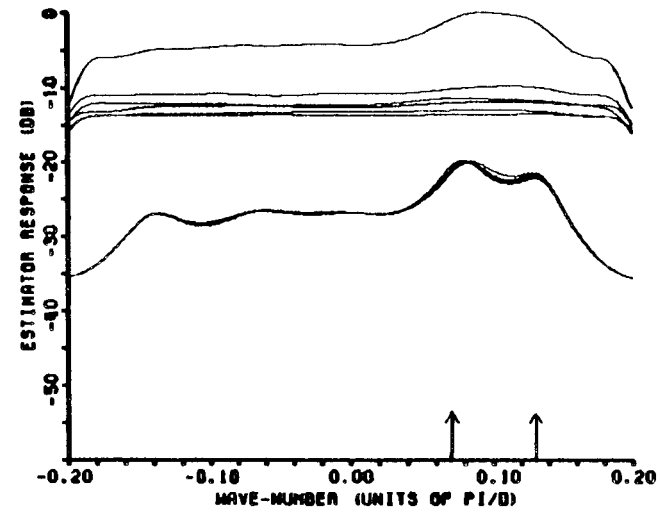


Fig. 8. MLM and SNLM estimators; 2 correlated signals.

## G 5. A HIGH SPEED SIDE SCAN SONAR BASED ON WIDE BAND CTFM

Dr.P.T.Gough	University of Canterbury,
M.J.Cusdin	Department of Electrical and
A.DeRoos	Electronic Engineering,
J.J.Sinton	Christchurch, New Zealand.

### ABSTRACT

The traditional continuous transmission frequency modulated (CTFM) sonar has been extensively modified by the inclusion of two local oscillators and two demodulators into the receiver which reduces the blind time (traditionally 10% of the sweep repetition period) to zero. As well, by adding a fixed offset to both the local oscillators and using an intermediate frequency (IF), the full transmitted bandwidth may be used producing up to a significant improvement in the speed of response for a fixed range resolution.

### 1 INTRODUCTION

Two types of underwater sonars are in current use: pulsed and modulated continuous wave sonars. A pulsed sonar transmits a short burst of sinusoidal pressure fluctuations and then waits for an echo reflected from an object in the insonified beam. The time delay between the pulse radiated and its returned echo is directly related to the distance between the transducer and the object (the range).

In contrast, a modulated continuous wave or continuous transmission sonar is always transmitting and always receiving so the transmission must be coded in some way to separate reflections from objects at different distances. The simplest coding used is the linear change in frequency with time from a high frequency  $f_h$  to a low frequency  $f_l$  in a fixed period of time  $T$  called the sweep period. This type of sonar is called a continuous wave or continuous transmission (CTFM or CWF) system.

### 2 TRADITIONAL CTFM SYSTEMS[1,2].

In any sonar there are only two or three items about the object that are of interest and are able to be measured: its distance from the transducer (the range), how big it is (the target strength), how close can it be to another object of comparable size and still be distinguished (the range resolution) and how often we get an independent estimate of these parameters (the response time). Note that in the pulsed sonar system, the response time is equal to the pulse repetition period as there is only one independent estimate of the range/target strength every pulse.

In the traditional CTFM sonar, the range is given by the difference between the frequency of the received echo and the frequency of the transmitted wave at that time. Although both the transmitted and received frequencies are changing with time, their frequency difference is not. It remains a function only of range. Figure 1 shows how the transmitted and received frequencies all change with time. Note that an object at maximum range  $R_m$  has a frequency difference of  $f_m$ . However, there is a portion of the sweep period  $T$  where the frequency difference vs range is not maintained and that is in the portion of time just after the flyback to the highest frequency. In this portion of the sweep period, the frequency difference is not related to the range of the object and so the receiver is normally gated off in this portion of the sweep (usually called the blind time). Unfortunately, the larger the maximum range  $R_m$  the larger the maximum frequency difference  $f_m$  and the greater the blind time. Traditionally blind time has been restricted to 10% of the sweep period which thus limits the maximum frequency difference  $f_m$  to 10% of the bandwidth  $f_h - f_l$ .

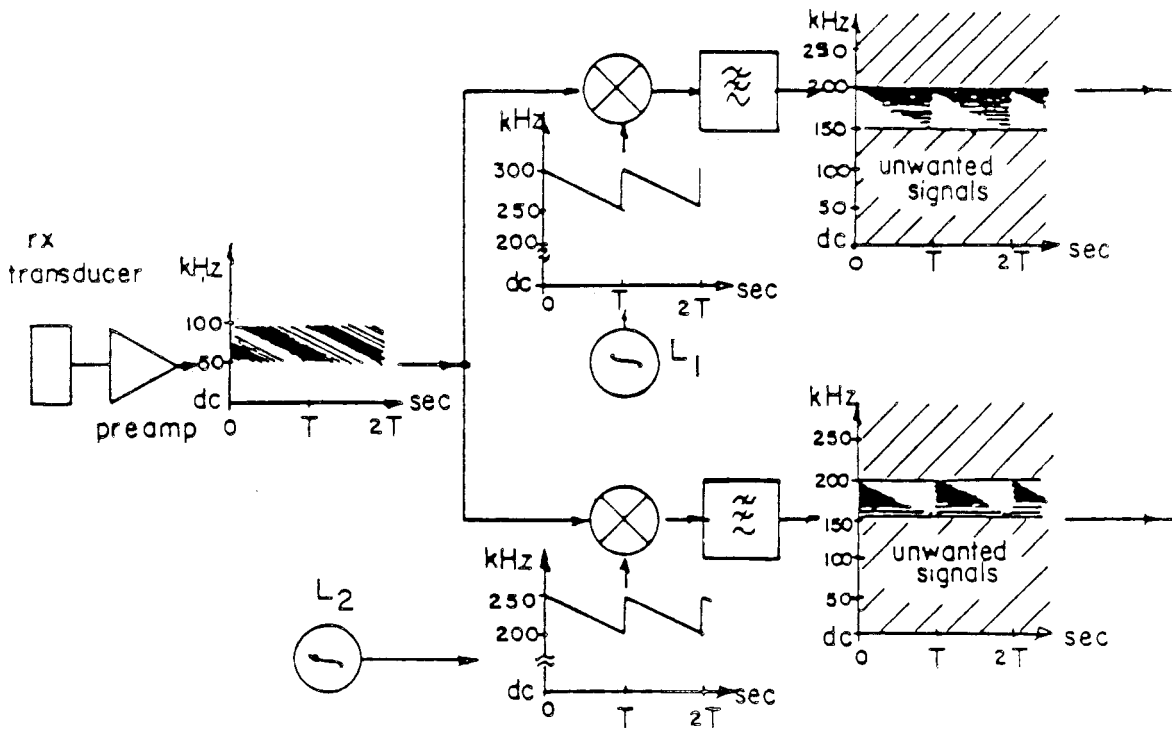


Figure 1. The block diagram schematic showing the double demodulation

The frequency difference is explicitly produced by demodulating the receiver echoes using a replica of the transmitted waveform as the local oscillator. Thus an object at a constant range now produces a constant frequency in the baseband frequency range DC to  $f_m$ . This signal is fed to a spectrum analyser to produce a standard A scan<sup>m</sup> output. That is, one of Target Strength versus Range.

The greatest limitation of the traditional CTFM sonar is the compromise between blind time and useful baseband. As the blind time is decreased, the proportion of  $f_m$  that may be used is also decreased. Thus for a fixed range resolution, the speed of response is also decreased - a real disadvantage if the target and/or sonar is moving, or the reflecting object has a fluctuating target strength. However, there is a method by which the full bandwidth of the sonar may be used without having any blind time at all. It requires two separate receiver demodulators and an IF stage.

### 3 DUAL DEMODULATION CTFM SYSTEM WITH AN INTERLACED IF [3,4]

To make the figures and the subsequent notation easier to follow, we introduce the actual frequencies we used. However, this does not preclude using this technique at any particular frequency band. The technique should work equally well from low frequency undersea mapping to high frequency medical imaging.

In the dual demodulation CTFM sonar built here, the one octave FM transmitted signal swept down the frequency band from 100 kHz to 50 kHz with a sweep repetition period of 500 msec. The echoes received by the hydrophone are amplified by a low noise preamp and then split into two parallel demodulation paths as indicated in figure 1. The upper path has a local oscillator  $L_1$  which has a 200 kHz offset from the transmitted signal. The wanted signals are thus demodulated into an IF band between 150 and 200 kHz with the strongest signals (the closest objects) at 200 kHz and decreasing in strength towards 150 kHz. Outside this IF band, that is from DC to 150 kHz and 200 kHz up, there are unwanted signals which are later filtered out.

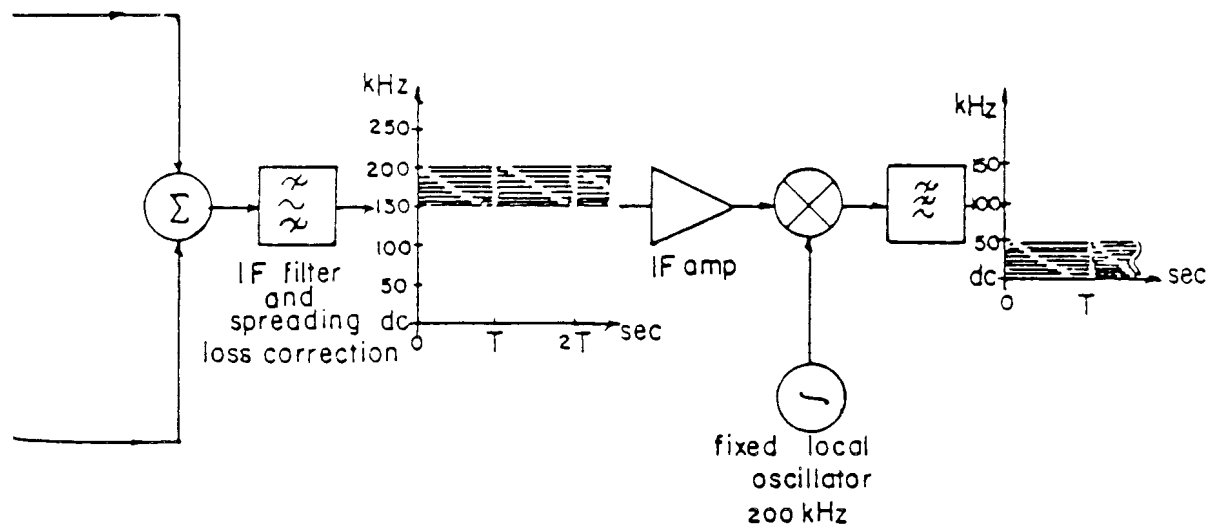


Figure 1 Continued.

The lower demodulation path has a local oscillator  $L_2$  with a 150kHz offset from the transmitted frequency. The wanted signals are also demodulated into the IF band 150 to 200kHz. The important item to note is that at any particular time the signals from each demodulator do not overlap in frequency. ie. they are perfectly interlaced as figure 1 shows. Since they are interlaced, they may be added to form a combined signal .

The combined signals are then passed through a IF filter (to reject the unwanted frequencies ) and range correction filter. The range correction filter ( having exactly the same effect as time varying gain in a pulsed sonar) ensures that equal strength targets have similar spectral amplitude irrespective of their range. Once the wanted signals have been rejected and the wanted signals range corrected, they are demodulated to baseband by a fixed local oscillator  $L_3$  at 200kHz. Thus the baseband now has the full range of frequency DC to 50kHz with no blind time what-so-ever. This has never been acheived before.

#### 4 SPECTRUM ANALYSER: RANGE RESOLUTION AND REPOSE TIME

Since the output of the CTFM sonar is a mixture of frequencies where the presence of a sinusoid is the indication of a reflecting object, some sort of spectrum analyser is required to turn the mixture of frequencies into a recognisable spectrum. A feature of any CTFM system is that the range resolution is not fixed by the form of the transmitted waveform, as it is in the pulsed sonar, but may be varied by altering the performance of the spectrum analyser. The spectrum analyser may be either based on the digital FFT, or on a bank of contiguous bandpass filters.

We selected the bank of filters spectrum analyser because it has a continuous output and was somewhat cheaper than a digital FFT with equivalent performance. The response time of the spectrum analyser is

primarily dependent on the bandwith of the individual filters that comprise the analyser and, as with all spectrum analysers, the bandwidth of the filters is equal to the spectral separation of their centre

frequencies.

In our sonar, the widest bandpass filter used in the spectrum analyser is 350Hz corresponding to a range resolution of 3m./filter, and so the response time of the sonar set to this particular range resolution is

$$t_r = 1/350 \\ = 2.8\text{msec.}$$

That is, we get a statistically independent estimate of the target strength and the range of all objects within the radiated beam every 2.8msec. even though the delay time of the echo from a target at maximum range is some 500msecs. The statistical independence is important as it is the probability density function of the amplitude in any one range resolution cell that enables us to distinguish a target lying on the sea floor from the general background reverberation or clutter. [5].

Since the demodulated waveform is periodic over the sweep period T, the narrowest bandpass filter that can be used in the spectrum analyser has a response time of T secs and a bandwidth of  $[1/T]$ Hz. Thus for our sonar the filter bandwidth could be as low as 2Hz corresponding to an approximate range resolution of 1.5cm/filter; however for other technical reasons, a minimum filter bandwidth of 6Hz was selected resulting in a range resolution of 5cm/filter and a response time of 167msecs.

#### 5 CONSTANT BEAMWIDTH AND POWER WITH FREQUENCY[6]

As the transmitted bandwidth covers a full octave spread (50 to 100kHz) a simple transducer would have a noticeable variation in beamwidth and sensitivity. To overcome the variation in beamwidth verses frequency the transmitting transducer is constructed in three concentric sections. At the higher frequencies only the inner section is activated and as the frequency is lowered the midsection and finally the outer section is activated. This corrects the variation in beamwidth verses frequency.

To overcome the variation in sensitivity verses frequency, the voltage applied to each section is carefully tailored to produce a flat overall response out of the receiver hydrophone with changing frequency.

The method by which the three waveforms are generated (one for each transducer section) is shown in figure 2. First the linear FM waveform is generated by standard direct digital synthesiser methods. A PROGRAMABLE COUNTER cycles down through the SINwave EPROM in shorter and shorter increments in address—thus producing the chirp waveform. In our sonar, the frequency changes from 100kHz down to 50kHz in a 500msec sweep repetition rate. This digital chirp waveform is passed to three multiplying digital to analogue converters (MDAC's) to produce three correctly tailored voltage waveforms  $V_1(t)$   $V_2(t)$  and  $V_3(t)$  to amplify and sent to each section of the transmitting transducer. The exact amplitude of the three waveform is determined by careful calibration tests and the correct digital equivalent stored in the amplitude EPROMs.

#### 6 COMPARISON WITH PULSED SONARS.

It is difficult to make fair comparisons between CTFM and pulsed sonars since they are often used for different purposes. However since our CTFM sonar was designed as a short range side scan sonar, it is reasonable to compare it with other short range side scan sonars. Table 1 shows some of the typical performance figures of three commercially available pulsed sonars as well as our CTFM sonar.

Several points are of interest in this table. Firstly, the CTFM sonar has a modest Source Level and so the sonar operates well below any cavitation limit. The CTFM sonar range resolution was actually measured at 10cm. (both walls of an aluminium pipe could be distinguished at a range of 100m.) and the SNR at 400m. range (with the filters set for a range resolution of 0.75m) was in theory anyway almost 14dB greater than that of the competition

This last claim requires some clarification. A recent publication[8] calculated the performance of several side scan sonars based on certain assumptions. These assumptions include the supposition that the SNR of a

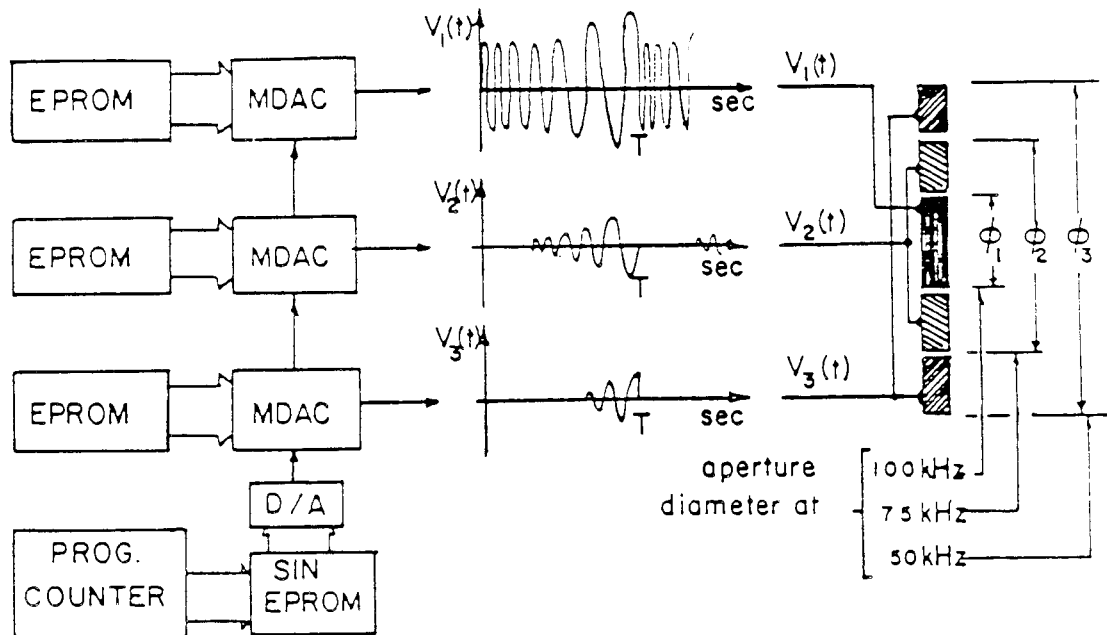


Figure 2 The three section direct digital frequency synthesiser and some typical waveforms.

non-chirped active sonar is given by

$$SNR = SL' + TS - 2TL - (NT - DI_r)$$

where  $SL'$  is the effective source level taking pulse dispersion into account,  $NT$  is the total sea state and thermal noise in the bandwidth of the sonar, with the remaining terms having their usual connotations.

The SNR of the Klein sonar was calculated using the following assumptions: range=400m,  $SL=228\text{dB}$ ,  $SL'=218\text{dB}$ ,  $DI_r=31\text{dB}$ ,  $BW=10\text{kHz}$ ,  $N_{ss}=N_{th}=25\text{dB}$ ,  $TS$  at 400m= $-28\text{dB}$ . Using these assumptions  $SNR=20\text{dB}$ .

When the sonar equation is used for a CTFM sonar, some extra factors must be considered. Firstly since the sonar is always transmitting, the amount of energy radiated into the environment is quite large as the duty cycle over a sweep period  $T$  is 100%. Secondly, the response time of the entire sonar is inversely proportional to the bandwidth of the individual filter which sets the range resolution. Thirdly in one sweep period, the rectified filter outputs may be averaged for several response times producing non-coherent intergration. So that finally for a CTFM sonar

$$SNR_{CTFM} = SL' + TS - 2TL - (NT - DI_r) + IF_R + IF_I$$

where  $SL' = SL$  as for a long pulse sonar

$$IF_R = 10 \log(1/BW_f \cdot \tau_e)$$

$BW_f$  = Bandwidth of the filters required to achieve a specific range resolution,

$$\tau_e = 2 \cdot \text{Range resolution} / c$$

$$\text{and } IF_I = E \log(T \cdot BW_f), \quad 5 < E < 7.3 \quad [8]$$

Consequently for our sonar where  $SL=191\text{ dB}$ ,  $TS$  at 400m= $-26\text{dB}$ , the individual bandwidth to achieve a range resolution of .75m  $BW_f=95\text{Hz}$ ,  $DI_r=26\text{dB}$ ,  $T=500\text{msec}$ ,  $c=1500\text{m/sec}$ ,  $E=6$ ,

$$SNR_{CTFM} = 33\text{dB}$$

a considerable improvement over that from any of the pulsed sonars. Unfortunately delivery schedules were such that we were unable to verify this figure experimentally.

One final point. In a pulsed sonar, improved range resolution is achieved by transmitting a shorter pulse and having a larger bandwidth system. Consequently, the SNR decreases with improved range resolution. In contrast, improved range resolution in a CTFM sonar is achieved by narrower bandpass filters which increases the SNR.

	Klein	EDO	Waverly	UofC/CTFM
Range Settings in m.	25-600	50-400	75-300	50-1km.
Max. Effective Range in sea water in m.	400	400	300	>800
Source Level in dB	228	218	No Data	191
Frequency in kHz.	100	100	110	100-50
Horizontal Beamwidth	1.	1.	1.5	constant 3.
Vertical Beamwidth	10.	25.	10.	constant 20.
Tx. Pulse length in msec.	0.1	0.1	0.1	NA
Effective pulse length due to dispersion in msec.*	1.0	1.0	1.0	NA
Effective Range Resolution in m.*	.75	.75	.75	variable 3m.to 10cm.
SNR at a range of 400m in dB	19	19	19	33 with range resolution set at 0.75m.

TABLE 1 \*Summary of performance figures.  
Estimate

## 6 CONCLUSIONS

The dual demodulation interlaced IF CTFM sonar has no blind time and, for a fixed range resolution, has the shortest response time and the best SNR performance of any available sonar. It is ideally suited to situations where there is movement of the sonar or of the target or variations in target strength due to medium fluctuations.

## REFERENCES

- [1] L.Kay, J.Brit.I.R.E., 19, pp105-110, 1959.
- [2] L.Kay, J.Brit.I.R.E., 20, pp785-796, 1960.
- [3] R.M.Hodgson & J.T.Boyes, Ultrasonics, 15, pp99-100, 1977.
- [4] P.T.Gough, A.Deroos & M.J.Cusdin, IEE part F, 131, pp270-274, June 1984
- [5] S. Haykin, Communication Systems, 2nd Ed, J.Wiley and Sons, N.Y.
- [6] R.Smith, PhD Thesis, University of Canterbury.
- [7] W.G.Russell-Cargill Ed., Recent Developments in Side Scan Sonar Techniques, Russell-Cargill, Sth Africa, 1982.
- [8] M.Skolnik, Introduction to Radar Systems, 2Ed, McGraw-Hill, NY, 1980

ACKNOWLEDGMENTS We gratefully acknowledge the assistance of Professor L. Kay as well as the advice and encouragement of W.Kennedy.

AUTHOR INDEX

	<u>Paper No.</u>		<u>Paper No.</u>
Akal, T.	A2	Diachok, O.	E5
Bannister, R.W.	B8	Douglas, P.	A5
Bao, X.L.	E6	Dunlop, J.I.	A5
Barrett, R.F.	F2	Edwards, D.	B1
Berman, D.	E5	Er, M.H.	F7
Browning, D.G.	B2	Ewans, K.C.	D2
Burgess, A.S.	D1	Ewart, T.E.	B4
Byrne, C.L.	G4	Fessenden, F.P.	C4
Cantoni, A.	F5, F7	Frisk, G.V.	A6, C5
Cato, D.H.	D3, D4	Godara, L.C.	F1, F5, G1
Chapman, N.R.	B3	Gordon, D.F.	B1
Clarke, A.P.	G3	Gough, P.T.	G5
Coleman, R.	E4	Gray, D.A.	F3, G2
Cusdin, M.J.	G5	Hall, J.C.	B8
Denbigh, P.N.	E3	Hall, L.H.	D6
Denham, R.N.	B5	Hall, M.	B7, C3
de Roos, A.	G5	Hamilton, E.L.	A1

AUTHOR INDEX (Cont'd.)

	<u>Paper No.</u>		<u>Paper No.</u>
Hays, E.E.	A6	Pedersen, M.A.	B1
Jenkins, C.	A7	Quill, A.F.	B6
Jensen, F.B.	A2, C1	Schmidt, H.	A2, C1
Jones, I.S.F.	E4	Searle, G.C.L.	F4
Kewley, D.J.	C4, D1	Sinton, J.J.	G5
Kibblewhite, A.C.	D2	Smith, A.C.	F4
Lam, S.F.	C4	Steele, A.K.	G4
Lawrence, M.W.	A4, A6	Sutton, G.R.	A3
Li, F.H.	E6	Sweet, D.R.	F6
Liu, B.S.	E6	Thompson, D.J.	B3
Lynch, J.F.	C5	Tindle, C.T.	C2
Macaskill, C.	B4	Tolstoy, A.	E5
Marrett, R.	D5	Tolstoy, I.	E5
Marwood, W.	G3		
Maxwell, J.G.H.	E4		
McMahon, D.R.A.	F2		
Mitson, R.B.	E1, E2		
Moore, B.	A3		
Payne, S.G.N.	B8		